Simplified Methodology for Indoor Environment Design

by

Jelena Srebric

M.E., Mechanical Engineering
University of Belgrade

Submitted to the Department of Architecture
in partial fulfillment of the
requirements for the Degree of Doctor of Philosophy
in the field of Building Technology

at the

Massachusetts Institute of Technology

September 2000

Signature of Author_____
Department of Architecture
August 1, 2000

Certified by_____
Qingyan Chen
Associate Professor of Building Technology
Thesis supervisor

Accepted by_____
Stanford Anderson
Chairman, Departmental Committee on Graduate Students
Head, Department of Architecture

Thesis Committee:
Leon R. Glicksman, Professor of Building Technology and Mechanical Engineering
Leslie K. Norford, Associate Professor of Building Technology

Simplified Methodology for Indoor Environment Design

by
Jelena Srebric

Submitted to the Department of Architecture
on August 1, 2000 in partial fulfillment of the
requirements for the Degree of Doctor of Philosophy
in the field of Building Technology

ABSTRACT

Current design of the building indoor environment uses averaged single parameters such as air velocity, air temperature or contaminant concentration. This approach gives only general information about thermal comfort and indoor air quality, which is limiting for the design of energy efficient and healthy buildings. The design of these buildings requires sophisticated but practical tools that are not currently available, and the objective of this thesis is to develop such a tool.

The development of the simple design tool had several phases. Each phase employed simplified models validated with measured data in order to assess model accuracy and reliability. The validation data was obtained from a state-of-the-art experimental facility at MIT.

Based on the collected data, we first developed simplified boundary conditions for the diffuser jet flow, which is the key flow element in mechanically ventilated spaces. The boundary conditions employ resultant momentum from the supply diffusers without modeling the detailed diffuser geometry. Although simple, the models can simulate airflow from complex diffusers commonly used for air-conditioning with reasonable accuracy.

Another simplification is the use of a zero-equation turbulence model to calculate indoor air distribution. The model uses the concept of eddy-viscosity and approximate turbulent viscosity with an algebraic equation. To test the turbulence model, an airflow program was developed. The program can simulate indoor airflow on a PC within several minutes, which is five to ten times faster than with the similar programs with a "standard" k-ε model.

Finally, the airflow program was coupled with an energy analysis program. The combined program simultaneously analyzes internal heat transfer and air movement as well as the heat transfer through the building envelope. The impacts on the thermal comfort in the occupied zone are quantified, and we found that the thermal comfort in most cases is not uniform. This has to be considered in designing radiative, convective, and hybrid heating and cooling systems for a building. The coupled program is an effective and economical design tool.

Thesis Supervisor: Qingyan Chen
Title: Associate Professor of Building Technology

ACKNOWLEDGEMENTS

To my advisor, Professor Qingyan (Yan) Chen, I would like to express my sincere thanks for his tireless support and guidance. He has always given me valuable ideas, suggestions and encouragement throughout the completion of the thesis. His knowledge and high standards in research has helped me to quickly build up my research experience and finish two ASHRAE projects that comprises a major part of my thesis.

I am also grateful to my thesis committee members, Professor Leon Glicksman and Professor Les Norford, whose valuable comments helped me to improve the thesis. My sincere thanks to Professor Glicksman for his help in my first ASHRAE project.

I thank Dr. Xiaoxiong Yuan , Yongqing Hu and Junjie Liu for their precious help in measurements that play an important role in my research. Also, I thank Tetsuya Hiramatsu from Asahi Glass Co., Ltd., and Haruo Hanibuchi from Sekisui House,Ltd. for sending me their measurement data that I used for the validation of the coupled program.

My special thanks to Dorrit Schuchter and Kathleen Ross for their logistic support that saved me a lot of time for my research. I would like to thank all my colleagues in the Building Technology Program for their collaboration and friendship.

DEDICATION

To my husband, brother and parents

Table of Contents

Chapter 4 Simulations for Commonly Used Air Supply Diffusers

Chapter 5 Validation of the Flow Program

Chapter 6 Coupling between the Flow Program and an Energy Analysis Program

Chapter 7 Conclusions and Recommendations

CHAPTER 1

INTRODUCTION

1.1 General Statement of Problem

Building systems constantly change along with their role in human society. Since the beginning of this century (1902) when W.H. Carrier designed a system to reduce and maintain air humidity at a certain level, air-conditioning became one of the most important building systems (McQuiston and Parker 1994). The development of air-conditioning enabled people to become independent of outdoor climate conditions and to shift most of their activities indoors. At present, people in developed countries spend 80% to 90% of their time indoors. Therefore, proper design of the indoor environment is crucial for human well being.

Design principles for the indoor environment have undergone several crucial revisions in the past thirty years. The first change occurred after the energy crisis in the early 1970s, and the later revisions occurred in the late 1980s. With the 1970s energy crisis, environment designers adopted principles of energy savings, since buildings consume more than one third of total energy in developed countries. As a result, buildings became better insulated and sealed, and ventilation rates were decreased to minimize energy use. Buildings that incorporate such energy conservation measures can provide an overall acceptable thermal comfort level for occupants. However, the reduction in ventilation rate requires the ventilation system to mix room air. The room air velocity and temperature in many such buildings are not uniform, or the thermal comfort level varies in different locations in a space.

On the other hand, indoor air quality (IAQ) in these buildings becomes poorer, since the internal pollution can not be diluted due to significantly reduced infiltration and supply of fresh air. The growing awareness of health risks from poor indoor air quality (Molhave 1982, Esmen 1985, Nero 1988) has prompted officials to triple the previously defined minimum of fresh air rate for each occupant as defined in ASHRAE (American Society of Heating, Refrigerating and Air-Conditioning Engineers, Inc.) Standard 62 (1989) for acceptable indoor air quality (Awbi 1991). Poor indoor air quality leads to building-related illnesses and symptoms as reviewed by Godish and Spengler (1996). Yet the majority of health problems reported in buildings (namely, nonspecific complaints often blamed on the so-called "sick building syndrome") have not been attributed to specific exposures. Available evidence suggests that multiple factors are involved in reported illnesses, including indoor air quality such as microbiological and chemical exposures not adequately characterized by current assessment approaches; physical conditions such as temperature, humidity, lighting and noise; and social/psychological stressors (NIOSH 1996).

Besides health problems, poor indoor climate negatively affects workers productivity in indoor environments, and causes significant economic losses. A majority of studies indicate an average productivity loss of 10% due to poor IAQ, and a conservative value of 6% is widely accepted (Dorgan et al. 1998). The overall economic

losses due to poor IAQ in US commercial buildings is estimated to be about $40 to $62.7 billion per year (Haymore and Odom 1993, Dorgan et al. 1998) in lost wages and productivity, administrative expenses, and health care costs. Note that not only poor IAQ, but also other environmental parameters such as thermal discomfort can adversely affect productivity (Wyon 1996).

The energy crisis and related problems with the poor IAQ and thermal comfort have stimulated the development of new technologies such as low energy cooling, passive solar systems, and building integrated photovoltaics (IEA 1998, NREL 1998). The US National Renewable Energy Laboratory (NREL 1998) estimated that current energy consumption could be reduced by 30% to 70% with new designs. This is very significant because the US spends $200 billion per year to heat, cool, light and operate private and commercial buildings. The new systems can provide better IAQ and thermal comfort while conserving energy in buildings. The new systems are very different from those used in the 1970s. Buildings with the new systems are more integrated with the environment, and use renewable energy and materials, and they take advantage of complex interactions between indoor and outdoor environments, such as climate conditions and indoor temperature stratification. Hence, the design of such systems requires sophisticated tools, which are not currently available.

1.2 Current Design Tools and Problems

The thermal comfort and indoor air quality are currently designed according to ASHRAE standards 55-1992 and 62-1999, respectively. To achieve a desired IAQ or thermal comfort level, the air distribution system supplies conditioned air to remove contaminants and to neutralize heat losses or gains indoors. Current designs use a single value for indoor air parameters that do not account for the fact of non-uniform distribution of indoor air. The current single value approach cannot:

- accurately estimate energy consumption in heating, ventilating and air-conditioning (HVAC) systems
- describe the non-uniform distribution of IAQ and thermal comfort level indoors.

Most energy analysis programs calculate energy consumption based on the assumption of uniform air temperature distribution in a room and an experimental correlation for convective heat transfer coefficients. However, the distributions of air temperatures and air velocities significantly impact energy calculation (Chen and Kooi 1988, Niu 1994, Nielsen and Tryggvason 1998). The energy calculation for spaces with highly stratified temperature fields such as atria with natural convection, offices with displacement ventilation, or rooms with radiant heating/cooling systems, is generally inaccurate. The enclosure walls of a room can have natural convection, forced convection and jet flows in different areas of the same space. To estimate the convective heat transfer coefficients for such a complex situation is difficult even for very experienced designers. Therefore, the prediction of the distribution of indoor parameters and heat transfer coefficients are essential for accurate estimation of energy consumption in buildings.

Furthermore, the air distribution system, such as a diffuser, directly influences the distribution of indoor air parameters. Consequently, the system has a direct impact on IAQ and thermal comfort distributions in the room. Prediction of jet flow from the diffuser is usually based on empirical formulae for velocity decay, velocity profile, jet trajectory, and jet separation distance for cold ceiling jets.

1.3 Methods for Indoor Environment Studies

To predict the distributions of air velocity, temperature, and contaminant concentrations, two basic methods are available: experimental measurements and computer simulations. The experimental measurements are normally considered more reliable than the computer simulations. Both methods have advantages and disadvantages for practical applications, which will be elaborated on in the following two sections.

1.3.1 Experimental Methods

The experimental methods were the only feasible approach to studying indoor air distributions in buildings with complex flow characteristics before the 1980s. Measurements can be performed *in-situ*, on small-scale models, and in environmental chambers. In-situ measurements are useful for performance evaluation of existing buildings and to provide feedback for designers. However, the data are not suitable for development of new design tools since many important factors cannot be controlled or measured in an actual environment. The measurements are normally performed in limited cases with relatively few data.

The small-scale models are not very suitable for room airflow studies since similarities between the model and prototype is difficult to achieve and in many cases impossible. The model and prototype must have the same Reynolds number (Re), Archimedes (Ar) number, and Prandtl (Pr) number for non-isothermal cases. Olson et al. (1991) showed that a 1:5 scale model could be built using refrigerant R-114. This model closely agreed with measurements made in a full-scale room that was geometrically similar to the model. Since only a 1:5 linear scale can be achieved the application of this technique to model large industrial facilities would require an unrealistic amount of refrigerant. Results from scale models using water did not provide good agreement with results for a full-scale room (Heiss 1987). The streamline patterns were very different and the water model produced laminar flow under conditions where the actual room was found to have turbulent flow. All the problems are the based on the fact that the scale of the flow and thermal phenomena leads to different scaling factors.

Environmental chambers are used to ensure controllable and reproducible thermal and airflow boundary conditions. A full-scale facility can simulate an actual space such as an office and contains furniture, human simulators and measurement instruments with data acquisition systems. The indoor parameters usually measured are air velocities, air velocity fluctuations, air temperatures, radiant temperatures and contaminant concentrations. Commonly used instruments for environmental measurements are hot-wire or hot-sphere anemometers, thermocouples, tracer-gases, and flow visualization

systems for airflow pattern observation. Airflow visualization is important since the measurements of low air velocities are often inaccurate, which presents one of greatest problems in airflow measurements at present.

Environmental chambers are useful but expensive. A chamber will have a scale problem if the chamber is used to simulate a large space, such as an atrium. In addition, the equipment used in most environmental chambers can produce significant errors, such as the measurements of low air velocity. Other more precise measurement equipment is available, such as supersonic anemometers and laser Doppler anemometers, but costs for these are very high for most researchers.

1.3.2 Computational Methods

The computer simulation solves numerically a set of partial differential equations for the conservation of mass, momentum (Navier-Stokes equations), energy, and species concentrations. The solution provides the field distributions of air temperature, velocity, relative humidity, and contaminant concentrations. This is called the Computational Fluid Dynamics (CFD) technique, and the most widely used method is the Reynolds Averaged Navier-Stokes (RANS) equation with turbulence models. The RANS solves the distributions of averaged air parameters in a space with a turbulence model. The use of a turbulence model is necessary to solve the flow parameters with the current capacity and speed of computers. However, the turbulence model approximates the airflow and leads to some uncertainties in the simulated results. The turbulence modeling method should be considered as an engineering approximation rather than a scientific law (Ferziger and Peric 1996). Hence, it is necessary to carefully evaluate the turbulence models performance and its assumptions through its applications to solve indoor airflow problems.

Different turbulence models are discussed in the literature. Some of them are mathematically complex and solve several additional governing differential equations for turbulence parameters, while the others may solve a simple algebraic equation for turbulence. Generally, more complicated turbulence models yield better results, but they require much more computing time and the calculations are less stable. Simple models such as algebraic equations are generally believed to produce incorrect solutions because they neglect important flow phenomena. In fact, a simple algebraic equation for turbulence (zero-equation model) may provide good results if it is carefully selected and calibrated (Wilcox 1993, Chen and Xu 1998, Nielsen 1998).

Compared with the experimental approach, the CFD methods are low cost because a modern PC can handle relatively complicated problems in an indoor space. The CFD results are informative and normally give three-dimensional special results in any given location in a room. Furthermore, an experienced designer can use a CFD program to obtain necessary information in a few hours. Therefore, CFD methods are becoming popular as a design tool, and are selected for the present investigation.

Nevertheless, CFD methods can only handle relatively simple air diffusers. For a complex diffuser, it is difficult to simulate it in the CFD methods. As discussed above, air supply diffusers play an important role in room air distribution. It is essential for the CFD methods to correctly simulate diffusers used in practice.

1.3.3 Simulation of Air Supply Diffusers

One common method of describing the flow and thermal characteristics of an air supply diffuser is by jet formulae. The formulae are empirical expressions for the jet decay, velocity profile, trajectory for inclined jets, and separation distance for cold ceiling jets. In general, the formulae have the same form but the coefficients used vary with the diffuser type. The coefficients lump the diffuser geometry influence on the jet performance, and their values are experimentally estimated (Kostel and Tuve 1955, Baturin 1972). The formulae operate under several basic assumptions: self-similarity of the jet profiles, linear jet spread, and preservation of initial jet momentum. However, these formulae do not account for room geometry, position and strength of internal heat sources, partitions and obstacles. In many cases, spaces are cluttered with objects and heat sources that have a significant impact on jet behavior (Heiselberg 1994, Nielsen J.R. 1996). Even in an empty space an air jet changes its behavior in the corners of the room (Nielsen 1974, Sandberg et al. 1991). The basic assumptions and additional boundary conditions limit the application of jet formulae. Also, for new diffusers the coefficient values have to be measured since the flow field strongly depends on diffuser geometry.

For design, the most important formulae are the jet velocity decay. Based on the decay, one can determine the jet throw, which is the distance from the diffuser to a place where the maximum jet velocity drops to a certain reference value called the terminal velocity. Since the maximum air velocity in the occupied zone should be less than 0.25 m/s (50 fpm), the air velocity is used as the terminal velocity. Early studies on indoor air distribution systems based on the throw (Kostel and Tuve 1955, Miller and Nevins 1972) developed a procedure for air diffuser selection (ASHRAE 1997). The throw can be determined from the decay jet formulae or from measurements. Diffuser manufacturers usually provide tables with measured isothermal jet throws and sometimes additional correction factors for cooling and heating conditions.

ASHRAE Standard 70 (1991) provides testing conditions for measuring isothermal and non-isothermal jet throw. However, the boundary conditions for non-isothermal measurements are not specified, and the setting of heat sources has to be reported. Consequently, the measured values of throw are valid only for the temperature difference between room air and the jet used for the test. This limitation shows that the throw measurements cannot effectively take into account a wide variety of thermal boundary conditions found in practice. For example, an experimental study (Heiselberg 1994) revealed that uniformly distributed heat sources have much weaker influence on the cold jet path than concentrated heat sources. The experiments show a deficiency of jet formulae for some practical applications.

Therefore, it seems necessary to develop a solid CFD method that simulates accurate complex diffusers. Literature studies (Jouini et al. 1994, Shakerin and Miller 1996, Hu et al. 1998) showed that combined experimental and computational approaches are most promising. They should be explored further.

1.4 Objective of the Present Work

The discussion in the previous sections indicate that detailed information on indoor airflow, such as the distributions of air velocity, air temperature, and contaminant concentration, is important to determine IAQ and thermal comfort. In addition, the convective heat transfer coefficient and air temperature distribution are needed to calculate accurate building energy consumption. The current experimental design tools are expensive and thus numerical simulation by CFD seems a good alternative.

This thesis aims to promote the numerical simulation approach for design of indoor environment. Nottage's remark (1951) that the study of room air distribution is primarily an experimental research does not hold anymore since recent developments in computational methods makes indoor environmental studies more realistic.

Many HVAC design engineers and architects do not have access to a large computer. Thus, it is important to develop a simple model to simulate indoor airflow on a personal computer. The model should calculate airflow patterns and the distribution of air velocity, temperature, and pressure. The flow program can then be coupled with an energy analysis program to simultaneously simulate airflow, thermal comfort, and energy consumption of HVAC systems. The flow program will also allow the temperature of interior walls to be predicted. The program also needs to accurately provide necessary information to properly size HVAC systems, to design air distribution systems and to assure acceptable comfort and IAQ conditions in the occupied zone.

The present investigation aims to identify a simple but reliable turbulence model that can provide detailed indoor air distribution information. With the model, one can simulate indoor airflow with brief training and a desktop computer. The program should be able to accurately simulate air supply diffusers commonly used in a room.

Therefore, the overall objective of this thesis is to develop and validate a simple design tool that can predict thermal comfort, IAQ, and energy consumption in a room with complex air diffusers. More specifically, the present study aims to:

- Develop a simple but reliable method to simulate eight complex air supply diffusers.
- Validate the simple diffuser simulation methods with experimental data measured from an environmental chamber.
- Develop a simplified airflow computer program that can calculate indoor air distribution as well as IAQ and thermal comfort. The program will be incorporated into a building energy analysis program to more accurately calculate energy consumption.

- Validate the simplified airflow program with measured data for different types of room airflow, such as forced, mixing and natural convection.
- Incorporate the simplified airflow program into an energy analysis program.
- Apply the coupled airflow and energy program for different building designs.

1.5 Outline of the Thesis

The thesis is divided into six additional chapters. Chapter 2 identifies a simple model for indoor environment modeling that provides distributions of indoor air parameters in a fast and reliable manner. A simplified airflow program has been developed and the chapter describes theoretical bases for the program. The focus is on the governing equations and the corresponding numerical techniques for their solution.

Chapter 3 also reviews modeling methods for airflow, but the focus is on supply diffuser modeling. The chapter presents a review of jet formulae, their capability to predict room air distribution, and simplified diffuser modeling for CFD. Diffuser modeling is crucial for the correct prediction of the room air distribution. Conventional methods for room air distribution design use jet formulae. Some simplified diffuser modeling methods use the jet theory to specify diffuser boundary conditions for CFD. The pros and cons of different modeling methods for practical applications are discussed.

In Chapter 4, simplified diffuser models are developed further because the results of numerical simulation strongly depend on the diffuser modeling. Two methods, box and momentum, are applied to simulate eight commonly used air supply diffusers. The diffuser modeling methods perform differently with different diffusers. Validation of the two methods by experimental data is performed. The chapter also presents methods to further develop diffuser modeling methods for practical applications.

Chapter 5 reports on the validation of a simple flow program with the zero-equation turbulence model for indoor airflow simulations. The validation uses measured data from a full-scale test chamber. The flow types studied include forced, natural, and mixed convection. The cases are complex three-dimensional airflow, and the simple flow program performs well. Numerical simulations can be preformed within a couple of minutes, and generally the agreement with measured data is good.

Chapter 6 discusses the procedure to couple the airflow program with an energy analysis program. The coupled program is developed and used to analyze five heating and cooling system designs. The program calculates the coupled energy/thermal comfort/air movement situations. The simulations showed that the simplified model produces realistic results that are representative of field conditions.

Finally, Chapter 7 summarizes the work presented in this thesis, and provides recommendations for further work.

CHAPTER 2

DEVELOPMENT OF A SIMPLIFIED FLOW PROGRAM

2.1 Introduction

This chapter reviews current methodologies used in computational studies of indoor environments. First, simplified models will be compared to select suitable methods for numerical simulations of room airflow. The method should provide parameters of design interests such as mean flow parameters, velocity, temperature and contaminant concentrations in a fast and reliable manner. Both speed and reliability are very important factors for design applications, and usually those two requirements contradict each other.

A simplified CFD with the zero-equation turbulence model is selected as a modeling tool to provide fast and reliable results for the applications that have been tested for. Since the zero-equation model is relatively new for indoor airflow simulations, the two-equation k-ε turbulence model will also be described and used as it is current industry standard for this type of simulation. Besides measured data, the widely used k-ε turbulence model seems to be a good base for validation of simplified methods that we will later introduce in the airflow modeling.

The model equations as well as the solution procedure will be presented. The solution procedure is iterative due to the complexity of the mathematical model.

2.2 Overview of Simplified Computer Models

The simplest mathematical models for calculating the distributions of indoor air velocity and temperature are probably the zonal methods. The zonal methods solve the conservation equation for mass and energy based on a number of approximations. The methods divide a given space into a number of grids, typically less than 10,000 grids. Then the zonal methods solve the mass and energy equations at the grid points to obtain a solution for the flow and thermal boundary conditions. The zonal methods are simple and easy to understand. It would be ideal if the method could produce reliable results.

One very simple zonal method (Lebrun and Ngendakumana 1987) fixes airflow patterns, and uses empirical laws for different flow components, such as jets, plumes, etc. The main limitation of this method is that knowledge of the airflow patterns is required. Therefore, the determination of the airflow patterns can be difficult even for an experienced designer. The method has limited applications.

Another popular zonal method is the network model (Walton 1989). This model determines flow within a space using Bernoulli's equation. It is a very effective approach for the simultaneous analysis of HVAC system, infiltration, and multi-room airflow problems. However, the method is unreliable if applied to a single space containing several different cells or sub-volumes.

The method proposed by Wurtz and Nataf (1994) calculates indoor air pressure using a degraded equation for the momentum. The airflow between two zones is determined by the pressure differential. Because of the poor representation of the momentum, the method does not work for pressure and buoyancy driven flows, i.e., flows created by temperature differences in the air.

The zonal model developed by Inard et al. (1996) calculates airflow in a room by dividing the indoor space into several zones. The model calculates the flow rate between the zones with small momentum through pressure distribution. Although the results are consistent with the experimental data, the model may not be applicable for high momentum flows.

Li et al. (1998) derived an analytical solution for a room with two effective openings and no bi-directional flow across openings. The solution has been extended to N-zones, and used as a validation tool for multi-zone pressure calculation obtained from a numerical simulation. This method can be applied only for simple flow patterns generated from the stack effect.

All the above models use discharge coefficients to calculate flow due to pressure or temperature differences. This reduces the reliability of the methods, since a general equation for the discharge coefficient has not been established. Application to a new geometry requires a more sophisticated simulation (CFD) or experiment to determine the discharge coefficients. Therefore, the zonal methods have limited applications.

The problems in determining the key simulation parameters for the zonal models stimulated development of a new simplified method. The method should provide parameters of design interests such as mean flow parameters, velocity, temperature and contaminant concentrations in a reliable and fast manner. The new method performs simplified CFD simulations as an inexpensive approach compared to the measurements and more reliable approach compared to the zonal models. The simplification is a new turbulence model specifically developed for room airflow (Chen and Xu 1998). The model is a zero-equation or algebraic turbulence model, which are the simplest turbulence models. The zero-equation model provides effective turbulence viscosity for Reynolds Averaged Navier-Stokes (RANS) equations, and forms a closed system of equations for the simplified CFD simulations.

In order to test the applicability of the simplified design approach, we have developed a flow program based on the model. The program subdivides the interior space into a number of cells as shown in Figure 2.1(a). For each cell, the conservation of mass is satisfied so that the sum of mass flows into or out of a cell from all its neighbors, Figure 2.1(b), is balanced to zero. Similarly the exchange of momentum from the flow into or out of a cell must be balanced in each direction with pressure, gravity, viscous shear, momentum, and energy transport by turbulent eddies. For turbulent flow, which normally exists in room flow, the challenge is to properly describe the turbulent transport

of momentum and energy in a simple algebraic form. The simple algebraic form must render correct results averaged over large cell spacing and for different flow situations.

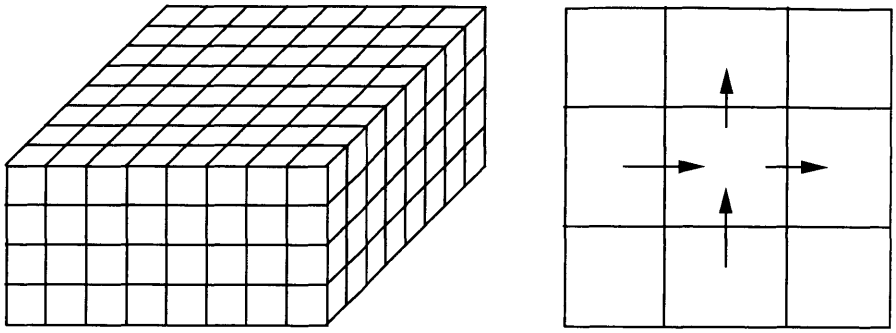

Figure 2.1. (a) Typical cell distribution used for room flow simulation with the simplified method and (b) sketch of mass balance within a cell

The next section gives the governing equations of mass, momentum, energy, and concentration along with the new form for the turbulent exchange used in the study. Also, a form of the two-equation turbulence model is the most widely used in practice and, hence, is suitable for comparison with the simplified method.

2.3 Governing Flow Equations

Most indoor airflows are turbulent. This is true even for flow in a clean room where the flow is often called "laminar". The nature of turbulence is complex and not yet fully understood. The turbulent flow is three-dimensional and random with many vortices (turbulent eddies) that enhance mixing in the flow field. The mixing decreases velocity gradients and dissipates kinetic energy of the fluid stream. The dissipation is irreversible, and kinetic energy is transformed to the internal energy of the fluid. Also, the enhanced mixing increases diffusion of mass and momentum, as well as temperature and concentration. Hence, the indoor airflow can have effective heat transfer and contaminant dispersion. To study the impact of turbulent mixing on thermal comfort and indoor air quality, partial differential equations that govern turbulent flow must be solved.

Indoor airflow is turbulent incompressible flow of Newtonian fluid, and the following transport equations describe the flow (tensor notation):

- Mass continuity:

$$\frac{\partial \rho}{\partial t} + \frac{\partial \rho \tilde{u}_i}{\partial x_i} = 0 \tag{2.1}$$

where ρ is the air density, $\tilde{u}_i$ is the instantaneous velocity component in x_i-direction, x_i is the coordinate (for i=1, 2, 3, x_i corresponds to three perpendicular axes), and t is the time.

- Momentum conservation:

$$\frac{\partial \rho \tilde{u}_i}{\partial t} + \frac{\partial \rho \tilde{u}_i \tilde{u}_j}{\partial x_j} = -\frac{\partial \tilde{p}}{\partial x_i} + \frac{\partial}{\partial x_j}\left[\mu\left(\frac{\partial \tilde{u}_i}{\partial x_j} + \frac{\partial \tilde{u}_j}{\partial x_i}\right)\right] + \rho\beta\left(T_o - \tilde{T}\right)g_i \tag{2.2}$$

where $\tilde{u}_j$ is the instantaneous velocity component in x_j-direction, $\tilde{p}$ is the instantaneous pressure, μ is the molecular viscosity, β is the thermal expansion coefficient of air, T_o is the temperature of a reference point, $\tilde{T}$ is the instantaneous temperature, and g_i is the gravity acceleration in i-direction.

- Energy conservation:

$$\frac{\partial \rho \tilde{T}}{\partial t} + \frac{\partial \rho \tilde{u}_j \tilde{T}}{\partial x_j} = \frac{\partial}{\partial x_j}\left(\frac{k}{c_p}\frac{\partial \tilde{T}}{\partial x_j}\right) + S_T \tag{2.3}$$

where k is the thermal conductivity of air, S_T is the thermal source, and c_p is the specific heat at constant pressure.

- Species concentration conservation:

$$\frac{\partial \rho \tilde{c}}{\partial t} + \frac{\partial \rho \tilde{u}_j \tilde{c}}{\partial x_j} = \frac{\partial}{\partial x_j}\left(\rho D \frac{\partial \tilde{c}}{\partial x_j}\right) + S \tag{2.4}$$

where $\tilde{c}$ is the instantaneous species concentration, D is the molecular diffusion coefficient for the species, and S is the species source.

Indoor airflow calculations use the Boussinesq approximation for thermal buoyancy, see Equation (2.2). This approximation makes air density a constant in all the governing equations and considers the buoyancy influence on air movement by the temperature difference.

The conservation Equations (2.1) to (2.4) must be solved numerically. The solution provides the field distributions of pressure, air temperature, velocity and contaminant concentrations. This is called the Computational Fluid Dynamics (CFD) technique. There are three CFD techniques: Direct Numerical Simulation (DNS), Large-Eddy Simulation (LES), and Reynolds Averaged Navier-Stokes (RANS) equations with turbulence models.

DNS solves the highly reliable Navier-Stokes equations without approximations. Therefore, DNS requires a grid resolution as fine as the Kolmogorov micro-scale for

small eddies. Since the Reynolds number for typical indoor airflow is approximately 10^5, the total grid number for solving the three-dimensional airflow is approximately 10^{11} to 10^{12}. Current super computers have grid resolution as fine as 512^3 which is approximately 10^8. Current computer capacity is still far too small to solve such a flow. In addition, the DNS method require very small time steps which make the calculation extremely time consuming. Using DNS for indoor environment simulation is not realistic in the near future. However, DNS can be used to develop new turbulent models (Xu et al. 1998).

LES was developed in the early 1970s by Deardorff (1970) for meteorological applications. He separated turbulent motion into large-eddies and small-eddies. The separation of the two did not significantly affect the evolution of large-eddies. LES solves the large-eddy motion by a set of filtered equations governing three-dimensional, time dependent motion. Turbulent transport approximations are used for small eddies and the small eddies are modeled independently from the flow geometry. The success of LES stems from the fact that the main contribution to turbulent transport comes from large-eddy motion. LES is also more realistic than DNS because LES can be performed on a large and fast workstation. Nevertheless, LES is still too time consuming because it calculates time-dependent flow, although the time and space steps can be larger than those for DNS. In addition, such a large and fast workstation is not available in most designers' offices.

The RANS method is fastest but may be the least accurate method. RANS solves ensemble-averaged Navier-Stokes equations by using turbulence modeling. In RANS, all unsteadiness is averaged and regarded as part of the turbulence (Ferziger & Peric 1996). The grid number used for the simulation is normally much less than that for LES or DNS. Most importantly, steady flow can be solved as time-independent. Therefore, computing costs are less than those for DNS and LES. However, turbulence modeling introduces an additional error into the calculation. Nevertheless, calculations based on RANS are popular and widely used in many designs since they give reasonably good results with an affordable computing effort. Even with more detailed calculations such as LES and DNS, the results should be averaged if used for design.

The first step in averaging the conservation equations is to decompose instantaneous variables to their mean and fluctuating parts. The mean parts are denoted with capital letters and fluctuating parts are denoted with $'$ superscript:

$$\tilde{u}_i = U_i + u_i' \qquad \tilde{p} = P + p' \qquad \tilde{T} = T + T' \qquad \tilde{c} = C + c' \qquad (2.5)$$

Figure 2.2 shows instantaneous values of velocity and temperature measured in a full-scale environmental chamber with a square mixing diffuser at the ceiling (for more details see Chapter 3). The results are for a period of 4.5 minutes sampled at 5 Hz. Two measurement points are selected to show how different airflow variables can be within the same space. Both measurement points are at the same vertical line (in the diffuser mid plane, 0.3m from its edge), but at different heights (h). The first measurement point is in the air jet region (h=2.40m) and the second one is in the occupied zone (h=1.10m) in the

room. The results show that the fluctuation and unsteadiness are much higher in the jet region than those in the occupied zone.

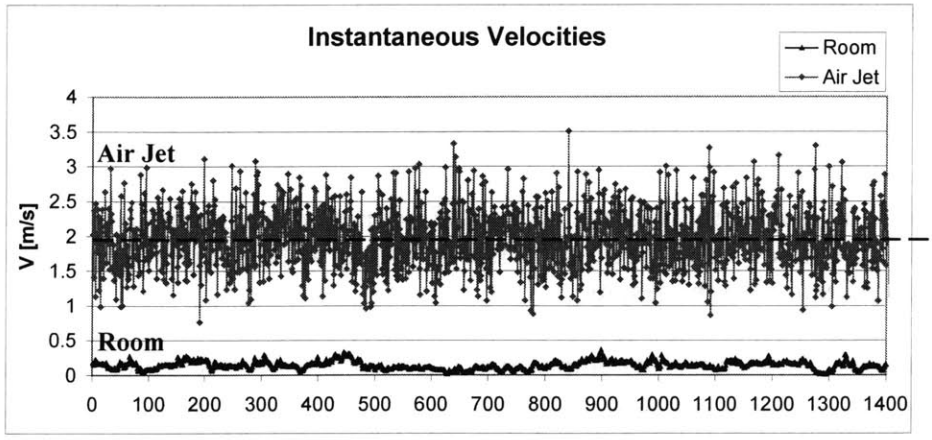

(a)

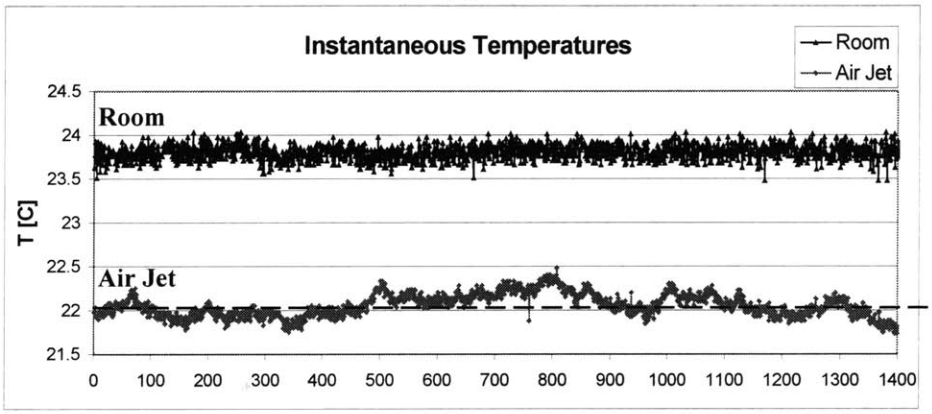

(b)

Figure 2.2 Instantaneous characteristics of air velocities (a) and temperatures (b) in a room with a square ceiling diffuser

A general variable can be introduced since any instantaneous variable can be represented as the sum of the average value and fluctuation around the average:

$$\tilde{\phi}(x_i, t) = \phi(x_i) + \phi'(x_i, t) \tag{2.6}$$

The averaging for statistically steady flow gives the mean value of the variables, and has the following integral form:

$$\phi(x_i) = \lim_{T\to\infty} \frac{1}{T} \int_0^T \tilde{\phi}(x_i, t)\, dt \tag{2.7}$$

The averaging time T has to be much larger than the time scale of turbulence to obtain results independent of the integration interval.

To evaluate the mean flow parameters for unsteady turbulent flow, ensemble averaging is used:

$$\phi(x_i,t) = \lim_{N\to\infty} \frac{1}{N} \sum_{n=1}^{N} \tilde{\phi}(x_i,t) \tag{2.8}$$

A measurement with the same initial and boundary conditions has to be repeated N times. The number of independent samples, N, has to be large enough to eliminate the influence of fluctuation on the results.

Equations (2.7) and (2.8) imply that the average of fluctuations is zero, i.e., $\overline{\phi'}(x_i,t) = 0$, where the line superscript denotes averaging. Therefore, by averaging the linear terms in the conservation equations we obtain the average of the variable as presented in equation (2.9). However, averaging of the nonlinear terms gives two terms (see equation (2.10)). The first term is a product of mean values, and the second term is an average of the fluctuation product, which is not zero since the fluctuations are correlated.

$$\overline{\tilde{\phi}}(x_i,t) = \overline{\phi(x_i) + \phi'(x_i,t)} = \overline{\phi}(x_i) + \overline{\phi'}(x_i,t) = \phi(x_i) \tag{2.9}$$

$$\overline{\tilde{u}_i\tilde{\phi}} = \overline{(U_i + u_i')(\phi + \phi')} = U_i\phi + \overline{u_i'\phi'} \tag{2.10}$$

Averaging the conservation Equations (2.1) to (2.4) gives the new system of equations called RANS equations:

$$\frac{\partial \rho U_i}{\partial x_i} = 0 \tag{2.11}$$

$$\frac{\partial \rho U_i}{\partial t} + \frac{\partial \rho U_i U_j}{\partial x_j} = -\frac{\partial P}{\partial x_i} + \frac{\partial}{\partial x_j}\left[\mu\left(\frac{\partial U_i}{\partial x_j} + \frac{\partial U_j}{\partial x_i}\right) - \rho\,\overline{u_i'u_j'}\right] + \rho\beta(T_o - T)g_i \tag{2.12}$$

$$\frac{\partial \rho T}{\partial t} + \frac{\partial \rho U_j T}{\partial x_j} = \frac{\partial}{\partial x_j}\left(\frac{\mu}{Pr_l}\frac{\partial T}{\partial x_j} - \rho\,\overline{u_j'T'}\right) + S_T \tag{2.13}$$

$$\frac{\partial \rho C}{\partial t} + \frac{\partial \rho U_j C}{\partial x_j} = \frac{\partial}{\partial x_j}\left(\frac{\mu}{Sc_l}\frac{\partial C}{\partial x_j} - \rho\,\overline{u_j'c'}\right) + S \tag{2.14}$$

where the coefficients for the viscous diffusion terms are rearranged:

$$\frac{k}{c_p} = \frac{1}{k/c_p} = \frac{\mu}{\mu k/c_p} = \frac{\mu}{\Pr}; \quad \rho D = \frac{1}{1/\rho D} = \frac{\mu}{\mu/\rho D} = \frac{\mu}{Sc},$$

Pr is the laminar Prandtl number, and Sc is the laminar Schmidt number.

The variables in the equations are the mean values (capital letters). Equations (2.12) to (2.14) contain additional terms $\rho\overline{u_i'u_j'}$ called Reynolds stresses, and $\rho\overline{u_i'\phi'}$ are called the scalar fluxes. The nonlinear terms in the original equations, (2.2) to (2.4), are on the right hand side. Here, the additional terms resulting from averaging are moved to the left side of the equation and grouped with viscous diffusion terms. The rearrangement of the diffusion terms is suitable for eddy-viscosity turbulence modeling.

2.4 The Eddy Viscosity Hypothesis

The Reynolds stresses and turbulence scalar fluxes have to be modeled in order to close the system of equations (2.11) to (2.14). The modeling of these additional transport terms is the main task of turbulence modeling. The eddy-viscosity turbulence models are based on the Boussinesq assumption in which the Reynolds stresses are proportional to the mean strain-rate, and the coefficient of proportionality is the turbulent (eddy) viscosity μ_t:

$$-\rho\overline{u_i'u_j'} = \mu_t\left(\frac{\partial U_i}{\partial x_j} + \frac{\partial U_j}{\partial x_i}\right) - \frac{2}{3}\delta_{ij}\rho k \tag{2.15}$$

where δ_{ij} is the Kronecker delta (when $i \neq j$, $\delta_{ij}=0$; and when $i=j$, $\delta_{ij}=1$), and k is the turbulence kinetic energy ($k = \frac{\overline{u_i'u_i'}}{2}$).

The second term on the right-hand side of Equation (2.15) represents the pressure diffusion caused by turbulence. The purpose of this term is to preserve equality for the equation when contracted for i = j = 1, 2, and 3. The three new equations have the form: $-\rho\overline{u_i'u_i'} = -\frac{2}{3}\rho k$, for i = 1, 2, and 3; and their sum gives $-2\rho k$ on both sides of the equality. Note that the mean-strain rate term is zero for i=j because of the mass continuity and, therefore, the eddy viscosity does not appear in the contracted equation. The eddy viscosity is a property of the flow field and depends on turbulence, while the molecular viscosity is a fluid property. Within the same flow field, the eddy viscosity is usually modeled as a variable parameter.

The scalar fluxes, turbulent heat and concentration fluxes are approximated as additional diffusion caused by turbulence (eddy-diffusivity):

$$-\rho\overline{u_j'T'} = \Gamma_{T,t}\frac{\partial T}{\partial x_j} \tag{2.16}$$

$$-\rho\overline{u_j'c'} = \Gamma_{C,t}\frac{\partial C}{\partial x_j} \tag{2.17}$$

where $\Gamma_{T,t} = \frac{\mu_t}{Pr_t}$, and $\Gamma_{C,t} = \frac{\mu_t}{Sc_t}$ are the turbulent diffusion coefficients for temperature and concentration, respectively; Pr_t is the turbulent Prandtl number, and Sc_t is the turbulent Schmidt number.

The modeling of eddy-viscosity and diffusivity is based on an analogy with laminar flow and molecular transport. Turbulent eddies are represented as molecules, which on a microscopic scale, collide and exchange energy. Although, the analogy is empirical and questionable (Wilcox 1993), the performance of the model is good for many practical applications. The performance depends particularly on the equation or equations used to define the distribution of eddy viscosity, which are called turbulence models.

With an eddy-viscosity model, the indoor airflow is described by the following time-averaged Navier-Stokes equations for the conservation of mass, momentum, energy, and species concentration:

- Mass continuity:

$$\frac{\partial \rho U_i}{\partial x_i} = 0 \tag{2.18}$$

where ρ is the air density, U_i is the mean velocity component in x_i-direction, and x_i is the coordinate (for i=1, 2, 3, x_i corresponds to three perpendicular axes).

- Momentum conservation:

$$\frac{\partial \rho U_i}{\partial t} + \frac{\partial \rho U_i U_j}{\partial x_j} = -\frac{\partial P}{\partial x_i} + \frac{\partial}{\partial x_j}\left[\mu_{eff}\left(\frac{\partial U_i}{\partial x_j} + \frac{\partial U_j}{\partial x_i}\right)\right] + \rho\beta(T_o - T)g_i \tag{2.19}$$

where U_j is the mean velocity component in the x_j-direction, p is the mean pressure, μ_{eff} is the effective viscosity, β is the thermal expansion coefficient of air, T_o is the temperature of a reference point, T is the mean temperature, and g_i is the gravity acceleration in the i-direction.

The last term on the right side of the equation is the buoyancy term. The turbulence influences are lumped into the effective viscosity as the sum of the turbulent viscosity, μ_t, and laminar viscosity, μ:

$$\mu_{eff} = \mu_t + \mu \tag{2.20}$$

- Energy conservation:

To determine the temperature distribution and the buoyancy term in Equation (2.19), the equation for energy conservation must be solved.

$$\frac{\partial \rho T}{\partial t} + \frac{\partial \rho U_j T}{\partial x_j} = \frac{\partial}{\partial x_j}\left(\Gamma_{T,eff}\frac{\partial T}{\partial x_j}\right) + \frac{q}{c_p} \tag{2.21}$$

where $\Gamma_{T,eff}$ is the effective diffusion coefficient for T, q is the thermal source, and c_p is the specific heat.

The effective diffusion coefficient for temperature is proportional to the effective viscosity since the eddy mixing is a source of turbulent diffusivity:

$$\Gamma_{T,eff} = \frac{\mu_{eff}}{Pr_{eff}} = \frac{\mu}{Pr} + \frac{\mu_t}{Pr_t} \tag{2.22}$$

Measurements have shown that Prandtl numbers are nearly constant for many flows and for the entire flow field (Peng 1996). The laminar Prandtl number is Pr=0.71, and the turbulent Prandtl number is Pr_t=0.9.

- Species concentration conservation:

$$\frac{\partial \rho C}{\partial t} + \frac{\partial \rho U_j C}{\partial x_j} = \frac{\partial}{\partial x_j}\left(\Gamma_{C,eff}\frac{\partial C}{\partial x_j}\right) + \rho C_S \tag{2.23}$$

where C is the species concentration, $\Gamma_{T,eff}$ is the effective diffusion coefficient for C, and C_S is the species source ($S=\rho C_S$).

The effective diffusion coefficient for concentration is analogous to the effective diffusion coefficient for temperature:

$$\Gamma_{C,eff} = \frac{\mu_{eff}}{Sc_{eff}} = \frac{\mu}{Sc} + \frac{\mu_t}{Sc_t} \tag{2.24}$$

Experiments have shown that the effective diffusion coefficient for concentration is almost the same as the effective viscosity (Peng 1996). Therefore, the laminar Schmidt number Sc=1.0, and the turbulent Schmidt number Sc_t=1.0.

Solution of equations (2.18) to (2.24) provides us with the distribution of indoor airflow parameters. This system of equations has only one unknown parameter, turbulent viscosity. The original time-averaged system of equations (2.11) to (2.14) has six unknown Reynolds stresses and three unknown scalar fluxes for each scalar variable. The eddy-viscosity (2.15) and eddy-diffusivity (2.16)-(2.17) assumptions reduced the problem encountered in the eddy (turbulent) viscosity modeling. The additional equation or equations used to calculate the eddy viscosity is called the eddy viscosity turbulence model.

2.4.1 Zero-Equation Turbulence Modeling

The zero-equation turbulence models are the simplest eddy viscosity models. The model has one algebra equation for turbulent viscosity, and no (zero) additional partial differential equations beyond the time-averaged equations for mass, momentum, energy and species conservation. In order to evaluate the Boussinesq eddy viscosity, Prandtl gave the mixing-length hypothesis (1925), which is the basis for zero-equation models.

Forming an analogy with the molecular transport of momentum, Prandtl postulated the mixing-length hypothesis in the following form:

$$\mu_t = \rho l_{mix}^2 \left| \frac{dU}{dy} \right| \tag{2.25}$$

where l_{mix} is the mixing length, ρ is the fluid density, and U is the average velocity.

The mixing length is an empirical variable defined as a transverse distance (free path) of small eddies (fluid lumps) over which their original momentum is preserved. The eddy-viscosity and mixing length are not physical properties of the fluid, but they are properties of the flow field. The product of the mixing length and the velocity gradient is called mixing velocity, which is also the property of the turbulent flow. Prandtl postulated that the mixing length near solid surfaces is proportional to the distance from the surface. This approximation gives good results only for a certain class of turbulent boundary layers (Wilcox 1993), such as free shear flows (jets, mixing layer, etc.). Calibration of the mixing length is always needed for complex flows.

One of problems with Prandtl's mixing length model is that the zero gradient for velocity results in zero turbulent viscosity (Karimipanah 1996). For example, the model gives zero turbulence viscosity in the middle of a pipe that has turbulent flow. Hence, researchers have developed new equations for both mixing velocity and eddy viscosity.

Much effort has been made to extend the applicability of the mixing length model. Van Driest (1956) devised a damping function to include wall-damping effects. The Van Driest's damping function was formulated as:

$$l_{mix} = \kappa y\left[1 - e^{\frac{-y+}{26}}\right] \tag{2.26}$$

where κ (=0.41) is the von Karman constant.

Clauser (1956) and Escudier (1966) made modifications to extend Prandtl's model to the defect layer. Corrsin and Kistlter (1954) and Klebanoff (1956) made an important modification to the model to include the intermittent phenomena in the boundary layer. The most important contributions to zero-equation models were made by Cebeci and Smith (1974), who proposed a two-layer, zero-equation model that includes almost all the above modifications, surface curvature, low-Reynolds-number effects, etc. Those models enjoyed wide popularity during the 1960's to the early 1980's. Wilcox (1993) described this model as "especially elegant and easy to implement." Baldwin and Lomax (1978) proposed a similar two-layer model that does not need to determine the boundary-layer edge in Cebeci-Smith's model.

Both models have been widely applied to many engineering applications (Ameri and Arnone 1994, Nikitopoulos and Michaelides 1995, Liu and Ikehata 1994). Although satisfactory results were obtained in channel and pipe flow, the Cebeci-Smith and Baldwin-Lomax models performed poorly in boundary-layer and separated flows, as most of the assumptions do not hold in these flows (Wilcox 1993). Zero-equation models can not adequately calculate turbulent heat transfer with variable property problems (Chyou and Sheicher 1992). While most engineers and scientists today are turning to more sophisticated turbulence models such as two-equation and Reynolds-Stress models, zero-equation models still deserve some attention because they are simple, cost-effective, and once calibrated, can predict mean-flow quantities fairly well.

Some zero-equation models may provide surprisingly good results. A constant viscosity model (one of the zero-equation models) can give much better results for swirling flow than the standard k-ε model. Also, Nielsen's study (1998) showed that, for the prediction of smoke movement in a tunnel, the constant eddy-viscosity model provides results closer to the measured data than the standard k-ε model.

However, none of the above zero-equation models are developed for room airflow, especially buoyancy-driven flows. It was, therefore, necessary to develop a zero-equation model for room airflow (Chen and Xu 1998).

In the Prandtl-Kolmogorov assumption, turbulent viscosity is the product of turbulent kinetic energy, k, and turbulent macroscale, l, which is a proper length scale for turbulence interactions:

$$\mu_t = C_v \rho k^{1/2} l \tag{2.27}$$

where $C_v = 0.5478$ is an empirical constant.

Depending on how one solves the unknown parameters k and l, eddy-viscosity models take different forms. The simple zero-equation model uses an algebra equation, and the complicated ones use multi-equations for turbulence transport. The following section (Chapter 2.4.2) will describe in more detail turbulence models that use two additional partial differential equations to close the system of conservation equations. Here, an additional assumption for Equation (2.27) will render a new zero-equation turbulence model developed for indoor airflow simulations (Chen and Xu 1998).

The turbulence kinetic energy in equation (2.27) can be expressed with turbulence intensity Ti and mean airflow velocity U:

$$Ti = \frac{\sqrt{\overline{u_i'^2}}}{U} = \frac{\sqrt{2k}}{U} \tag{2.28}$$

$$\mu_t = 0.5487 \rho \frac{Ti\, U}{\sqrt{2}} l \tag{2.29}$$

The average turbulence intensity for indoor airflow is assumed to be 10%. This value is a good estimate for the occupied zone in mixing ventilation, however it can be far from reality in the jet region. On the other hand, the zero-equation models perform very well for turbulent jets or other boundary layers if properly calibrated (Wilcox 1993). Chen and Xu (1998) used the assumption of uniform turbulence intensity and derived an algebraic function to express turbulent viscosity as a function of local mean velocity, U, and a length scale, l:

$$\mu_t = 0.03874 \rho U l \tag{2.30}$$

This equation has an empirical constant, a universal value of 0.03874 for different flows. The length scale, l, is the distance to the closest surface of the enclosure. The model (2.30) is an empirical equation.

Turbulence should be considered as an engineering approximation rather than scientific law (Ferziger and Peric 1996). Hence, the evaluation of the turbulence model's performance and justification of its assumptions is performed through its application in solving design problems. Therefore, Chapter 5 will focus on an evaluation of the zero-equation turbulence model for indoor airflow applications. Currently, the most popular turbulence models for indoor airflow modeling are the two-equation turbulence models. However, these models are more complex than the zero-equation turbulence model.

2.4.2 Two-Equation Turbulence Modeling

More complex forms of turbulence modeling require one or two additional partial differential equations to calculate parameters for the turbulent viscosity. The standard k-ε model (Launder and Spalding 1974) is the most widely used two-equation model in practice. The two additional transport equations, for turbulent kinetic energy k and turbulent energy dissipation ε, are added to the system of conservation equations. The turbulent viscosity is then evaluated without assumptions for length scale, which is difficult to estimate:

$$\mu_t = \rho C_\mu \frac{k^2}{\varepsilon} \tag{2.31}$$

where $C_\mu = 0.09$ is the empirical constant. The terms for the k and ε transport equations are given in Table 2.1.

Due to the complexity of turbulent flow, it is difficult to obtain a universal turbulence model for all types of indoor airflow. Many efforts in the recent past have been directed towards the identification of a suitable model for indoor environment simulation.

Chen (1995) evaluated the performance of five k-ε models: the standard k-ε model (Launder and Spalding 1974), a low-Reynolds-number k-ε model, a two-layer k-ε model, a two-scale k-ε model, and a renormalization group (RNG) k-ε model. Those turbulence models were used for the simulation of forced convection, natural convection, and mixed convection room airflow, as well as an impinging jet flow. Those flows are the basic elements of complex indoor airflow. Experimental data were used for the validation of the computed results. The results from the RNG k-ε model were slightly better than the standard k-ε model, and the other models were not stable. Therefore, Chen recommended the RNG k-ε model for indoor airflow simulations.

In another study, Muller and Renz (1998) tested the standard k-ε model, a low-Reynolds-number k-ε model and a Reynolds-stress model for the simulation of displacement ventilation. The low-Reynolds-number model provides the best overall agreement with measured data, but the other two models do not offer very different results.

On the other hand, Nielsen (1998) showed that the buoyancy term in the low-Reynolds-number k-ε model is most important for displacement ventilation. The damping functions, which are used to modify the standard k-ε model for near-wall laminar and transitional flows, have only a small influence on the results. The damping functions are the only difference between the low-Reynolds number k-ε model and the standard k-ε model.

A general conclusion from the above studies is that the turbulent models perform differently from one case to another, although all simulated flows are indoor airflows. In fact, no turbulent models performed superior to the standard k-ε model for indoor airflow simulations. The standard k-ε model is stable, easily implemented, widely validated, and reasonably accurate for many applications. This makes the standard k-ε model one of the most widely used turbulence models in practice. However, the standard k-ε model is not universal, and has provided erroneous results in many HVAC applications (Chen 1997).

The standard k-ε model has had problems in predicting strong buoyancy, separated flows, axisymmetric jets, swirl flows and heat transfer from a wall. Therefore, many modified k-ε models, such as the RNG k-ε model (Yakhot and Orszag 1986, Yakhot et al. 1992), have emerged to improve performance for certain classes of problems.

Compared to the standard k-ε model, the RNG k-ε model has an additional source term, R, in the equation for the turbulent energy dissipation, ε. This term improves flow prediction for regions with large strain rates, and the term is negligible for small strain rates. Therefore, the model can better predict separate flows, which are commonly present in indoor airflow. Recent studies (Chen 1995, Loomans 1998) have shown that the RNG k-ε model has better performance than the standard k-ε model for indoor airflow simulations. However, the RNG model assumes high Re numbers for the flow field, which is one of the assumptions that causes problems in modeling with the standard k-ε model. Modeling of the airflow field with the RNG model shows discrepancies that will be discussed further in Chapter 4.

The transport equations for all variables, including turbulence properties, can be written in terms of the general variable ϕ (defined in (2.6)):

$$\frac{\partial \rho \phi}{\partial t} + \frac{\partial \rho U_j \phi}{\partial x_j} = \frac{\partial}{\partial x_j}\left(\Gamma_{\phi,\text{eff}} \frac{\partial \phi}{\partial x_j} \right) + S_\phi \qquad (2.32)$$

The equation has transient, convection, diffusion and source terms.

Table 2.1 presents values for the variables, constants and source terms in the general transport equation (2.32) solved with the RNG k-ε turbulence model. The model constants are slightly different from the constants in the standard k-ε model.

The RNG k-ε model, as all other two-equation models, solves two additional differential equations for the turbulent transport processes. To solve the two equations requires considerable computing effort because of the highly non-linear characteristics of the equations. For example, the prediction of airflow in an office requires several hours of computing time on a fast PC. If a designer wants to use the CFD method to vary the design, such as to change HVAC equipment location, the huge computing time renders this process inefficient at the present, especially for conceptual designs. Therefore, the

zero-equation model is more suitable for design if the simplicity of the model does not lead to incorrect solutions of the transport flow equations.

In this study, both the zero-equation and RNG k-ε turbulence models will be used in different chapters. The reason for using these equations is that the simplifications for indoor airflow modeling will be introduced step by step. Therefore, we will start with existing practice that is based on two-equation turbulence modeling. Chapter 4 will use the RNG k-ε turbulence model to validate simplified modeling of diffuser boundary conditions. After validation of the simplified method for diffuser modeling, Chapter 5 will evaluate performance of the zero-equation model for various complex indoor airflows. Finally, Chapter 6 analyzes the zero-equation model and simplified diffuser boundary conditions for coupling the transport flow equations with energy analysis.

Table 2.1 The RNG k-ε turbulence model parameters

Equation	ϕ	$\Gamma_{\phi,eff}$	S_ϕ
Continuity	1	0	0
Momentum	U_i	$\mu+\mu_t$	$-\frac{\partial p}{\partial x_i}+\rho\beta(T_o-T)g_i$
Turbulent kinetic energy	k	$\mu+\frac{\mu_t}{\sigma_k}$	$P_k-\rho\varepsilon+G_b$
Dissipation rate of k	ε	$\mu+\frac{\mu_t}{\sigma_\varepsilon}$	$(C_{\varepsilon 1}P_k-C_{\varepsilon 2}\rho\varepsilon+C_{\varepsilon 3}G_b)\frac{\varepsilon}{k}+R$
Temperature	T	$\frac{\mu}{Pr}+\frac{\mu_t}{Pr_t}$	S_T
Concentration	C	$\frac{\mu}{Sc}+\frac{\mu_t}{Sc_t}$	S

$$\mu_t=\rho C_\mu\frac{k^2}{\varepsilon};\quad P_k=\mu_t\frac{\partial U_i}{\partial x_j}\left(\frac{\partial U_i}{\partial x_j}+\frac{\partial U_j}{\partial x_i}\right);\quad G_b=g_i\beta\frac{\mu_t}{Pr_t}\frac{\partial T}{\partial x_i}$$

$$R=-\rho\frac{C_\mu\eta^3(1-\eta/\eta_0)}{1+\beta'\eta^3}\frac{\varepsilon^2}{k};\quad \mu=S\frac{k}{\varepsilon};\quad S=(2S_{ij}S_{ij})^{1/2};\quad S_{ij}=\frac{1}{2}\left(\frac{\partial U_i}{\partial x_j}+\frac{\partial U_j}{\partial x_i}\right)$$

$$\eta_0=4.38;\quad \beta'=0.012$$

$$C_\mu=0.0845;\quad C_{\varepsilon 1}=1.42;\quad C_{\varepsilon 2}=1.68;\quad C_{\varepsilon 3}=1.0;\quad \sigma_k=0.7194;\quad \sigma_\varepsilon=0.7194$$

$$Pr=0.71;\quad Pr_t=0.9;\quad Sc=1.0;\quad Sc_t=1.0$$

2.5 Boundary Conditions

Boundary conditions are necessary for the mathematical solution of the transport flow equations. There are three types of boundaries of practical importance: free boundary, symmetry surface, and conventional boundary.

- Free boundary

The boundary surface may be adjacent to an inviscid stream. Examples are the air supply and exhaust. For a supply, the boundary conditions are:

$$\begin{aligned} U_i &= U_{supply} \\ T &= T_{supply} \\ k &= k_{supply} \\ \varepsilon &= \varepsilon_{supply} \\ C &= C_{supply} \end{aligned} \tag{2.33}$$

where subscripts "supply" are the parameter values at the supply outlet.

Pressure is normally given for an exhaust, and zero gradients normal to the surface are assumed as other parameters:

$$p = p_{exhaust}$$

$$\frac{\partial U_i}{\partial x_i} = 0, \quad \frac{\partial T}{\partial x_i} = 0, \quad \frac{\partial k}{\partial x_i} = 0, \quad \frac{\partial \varepsilon}{\partial x_i} = 0, \quad \frac{\partial C}{\partial x_i} = 0 \tag{2.34}$$

where $p_{exhaust}$ is the pressure at a return and x_i is the coordinate normal to the surface.

The supply equations (2.33) are suitable only for a slot opening. The next chapters of the thesis, 3 and 4, will provide methods for handling supply boundary conditions for more complex diffusers.

- Symmetry surface

If the x_i coordinate is normal to the symmetry surface, the following equations describe the boundary conditions of the surface:

$$\frac{\partial U_i}{\partial x_i} = 0, \quad \frac{\partial T}{\partial x_i} = 0, \quad \frac{\partial k}{\partial x_i} = 0, \quad \frac{\partial \varepsilon}{\partial x_i} = 0, \quad \frac{\partial C}{\partial x_i} = 0 \tag{2.35}$$

- Conventional boundary

This type of boundary includes wall, ceiling, and floor surfaces and the surfaces of furniture, appliances, and occupants. If the x_i coordinate is parallel to the surface, the boundary conditions are:

$$\tau = \mu_{eff} \frac{\partial U_i}{\partial x_j} \qquad (2.36)$$
$$q = h(T_w - T)$$

where τ is shear stress, and h is the convective heat transfer coefficient.

The convective heat transfer coefficient is determined from the following equation, which is similar to the Reynolds analogy:

$$h = \frac{\mu_{eff}}{Pr_{eff}} \frac{c_p}{\Delta x_j} \qquad (2.37)$$

Equations (2.36) and (2.37) can be used as wall boundary conditions for the laminar flows as well as for the turbulent flows. The zero-equation turbulence model applies directly to the specified equations. However, the RNG k-ε model developed for high Re numbers needs adjustment for the near wall region where the Re number is very small. The RNG k-ε model uses additional equations for the near-wall region, called wall functions (Tennekes and Lumley 1972). The wall functions are dimensionless velocity, temperature and concentration profiles in the wall boundary region. The wall boundary layer has three regions, the laminar sublayer ($0< y^+ \leq 5$), buffer zone ($5< y^+ \leq 30$), and inertial sublayer ($30 < y^+ \leq 130$), where y^+ is the dimensionless distance to the wall. The wall has a damping effect on the turbulent flow, and the layer closest to the wall has predominant viscous forces. In the buffer zone, viscous forces and Reynolds stresses have the same order of magnitude and neither can be neglected. Finally, the inertial sublayer is predominately turbulent.

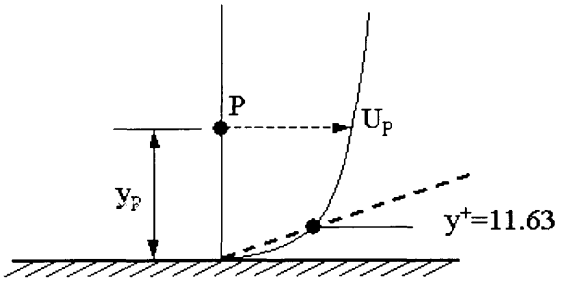

Figure 2.3 Velocity distribution near the wall

The wall functions give expressions for laminar and turbulent sublayers while the buffer zone is neglected. A near wall flow is considered laminar if $y^+ \leq 11.63$, and if $y^+ > 11.63$ the flow is turbulent. The wall function equations for velocity and temperature are:

$$\begin{aligned} u^+ &= y^+ \\ T^+ &= \mathrm{Pr}\, y^+ \end{aligned} \qquad \text{for } y^+ \leq 11.63 \tag{2.38}$$

$$\begin{aligned} u^+ &= \frac{1}{\kappa}\ln\left(E y^+\right) \\ T^+ &= \mathrm{Pr}_t\left[u^+ + E\left(\frac{\mathrm{Pr}}{\mathrm{Pr}_t} - 1\right)\left(\frac{\mathrm{Pr}_t}{\mathrm{Pr}}\right)^{1/4}\right] \end{aligned} \qquad \text{for } y^+ > 11.63 \tag{2.39}$$

$$u^+ = \frac{U_P}{u_\tau}, \quad u_\tau = \sqrt{\frac{\tau_w}{\rho}}, \quad y^+ = \frac{y_P u_\tau \rho}{\mu}, \quad T^+ = \frac{(T_w - T_P)u_\tau}{q}$$

where u^+ is the dimensionless mean velocity, U_P is the velocity parallel to the wall, u_τ is the friction velocity, τ_w is the wall shear stress, y^+ is the dimensionless wall distance, y_P is the distance to the wall, κ is the von Karman constant (κ=0.41), E is the roughness parameter (E=9 for hydraulically smooth walls with constant shear stress), T_w is the wall temperature, T_P is the air temperature, and q is the heat transfer rate.

In the viscous sublayer, the mean velocity profile is approximated as the linear function of wall distance (see Figure 2.3). At the wall surface (y=0), air velocity is zero (no-slip conditions) and air temperature is equal to the wall surface temperature. For the turbulent sublayer, the velocity profile is the log-law function.

Assumptions used to derive the wall functions restrict the application of these formulae to a certain class of flows. The assumptions are the Prandtl mixing hypothesis, the Boussinesq eddy-viscosity assumption, a fully developed flow, and no pressure gradients or other momentum sources (constant shear stresses). For the indoor airflow applications, the assumptions are acceptable and wall functions are widely used. However, predictions of the heat transfer in the near-wall region tend to be incorrect, and dependent on the distance to the wall y_P. Improved calculation of heat transfer is possible with improved temperature profile equations (Chen 1988) or use of equation (2.36) with a prescribed empirical value for the convective heat transfer coefficient h. A correct prediction of the wall boundary condition is crucial for indoor airflow simulations.

2.6 Numerical Methods

The governing equations (2.18) to (2.24) that employ the zero-equation turbulence model (2.30) and boundary conditions (2.33) to (2.37) forms a closed system of equations for the simplified airflow program. If instead of the zero equation model, the RNG k-ε turbulence model (Table 2.1) is used, then the wall functions (2.38) and (2.39) have to be added to the system of equations. The closed system fully describes the indoor airflow and has to be solved numerically. The following section describes the numerical methods for the solution of the nonlinear partial differential equations.

2.6.1 Integration and Numerical Schemes

The first step in the numerical procedure to solve the partial differential equations is the discretization of the solution domain. Two common discretization methods are the finite-volume method and the finite-element method. The finite-element method used to be popular because of its flexibility in defining complex geometry. However, the finite volume method requires less computing time, and with advanced grid generation techniques such as unstructured grid and body-fitted coordinates, it has become the most widely used discretization method.

The finite volume method divides space into a finite number of control volumes (cells). The transport equations are then applied to each of the control volumes. Figure 2.4(a) shows the notation convention for control volumes in a two-dimensional case, and the extension to the third dimension is straightforward. Also, the time is divided in intervals and treated as a fourth dimension. In Figure 2.4, the capital letters denote the centers of control volumes, and the lower case letters the control volume interfaces. The scalar variables, such as P, T, k, ε and C, are calculated in the center of a control volume, and assumed to be the same within the control volume. In order to avoid numerical problems, the velocity components are solved at the cell interfaces. This discretization procedure is called the staggered grid distribution. The staggered grid allows the pressure source term in momentum equations to be calculated as a gradient between two neighboring control volumes. The following discretization equations will be derived for the cell center (scalar variables), and have a similar form with different notations for the cell interface (velocity components).

Integration of the general transport equation (2.32) over a control volume gives the following expression:

$$\int_V \frac{\partial \rho \phi}{\partial t} dV + \int_V \frac{\partial \rho U_j \phi}{\partial x_j} dV = \int_V \frac{\partial}{\partial x_j}\left(\Gamma_{\phi,eff} \frac{\partial \phi}{\partial x_j}\right) dV + \int_V S_\phi dV \qquad (2.40)$$

Each term in the above equation will be integrated separately and then combined in the final discretization equation.

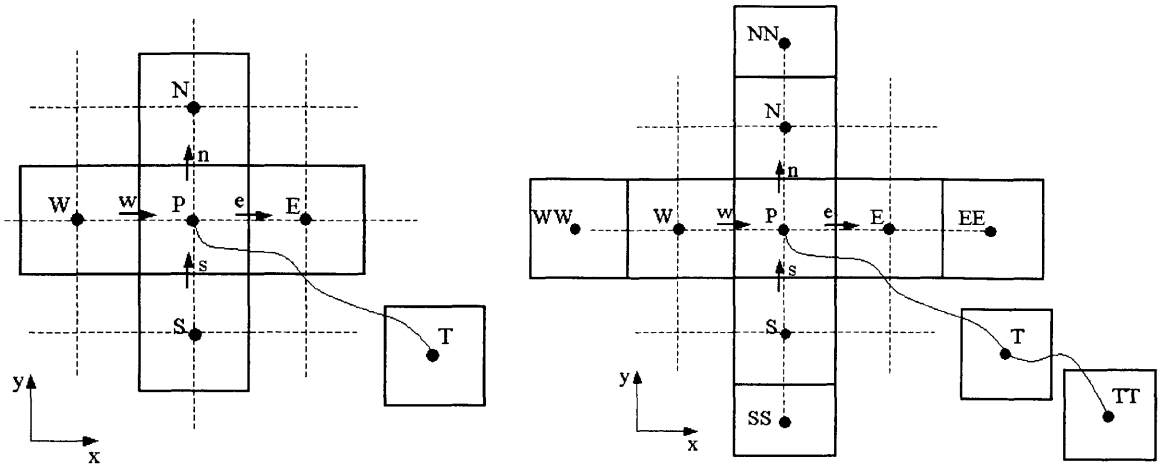

(a) (b)

Figure 2.4 Discretization of the calculation domain (a) upwind scheme, (b) quick scheme

Integration over the control volume for the unsteady terms is:

$$\int_V \frac{\partial(\rho\phi)}{\partial t} dxdydz = \frac{\rho\phi_P - \rho\phi_{P,old}}{\delta t} V_P \qquad (2.41)$$

where V_P is the cell volume, ϕ_P is the value of a scalar variable at the present time, $\phi_{P,old}$ is the value of a scalar variable at a previous time step, and δt is the time interval.

Since the control volume forms a closed surface, the volume integral can be transformed into the surface integral (Gauss theorem). The assumption of a uniform value for the integral variable inside the control volume is extended for the cell surfaces. Therefore, integration of the convection terms gives:

$$\int_A [(\rho U\phi)_e - (\rho U\phi)_w] dydz = (\rho U\phi A)_e - (\rho U\phi A)_w = F_e\phi_e - F_w\phi_w \qquad (2.42)$$

$$\int_A [(\rho V\phi)_n - (\rho V\phi)_s] dxdz = (\rho V\phi A)_n - (\rho V\phi A)_s = F_n\phi_n - F_s\phi_s \qquad (2.43)$$

$$\int_A [(\rho W\phi)_h - (\rho W\phi)_l] dxdy = (\rho W\phi A)_h - (\rho W\phi A)_l = F_h\phi_h - F_l\phi_l \qquad (2.44)$$

where F_i (i=e,w,n,s,h and l) is the convective flux, and the notation (Figure 2.4) is e (east) for +x, w (west) for –x, n (north) +y, s(south) for -y, h (high) for +z, and l (low) for –z.

The solution of the convection term integrals is based on the approximation of the convective fluxes called the differencing scheme. The fully implicit upwind scheme is

simple and stable, and adopts the value in the nearest cell upstream of the fluid motion for the interface value of a scalar variable. The upwind differencing scheme for the convection term is:

$$F_e\phi_e - F_w\phi_w = \|F_e,0\|\phi_P - \|-F_e,0\|\phi_E - (\|F_w,0\|\phi_W - \|-F_w,0\|\phi_P) \quad (2.45)$$

$$F_n\phi_n - F_s\phi_s = \|F_n,0\|\phi_P - \|-F_n,0\|\phi_N - (\|F_s,0\|\phi_S - \|-F_s,0\|\phi_P) \quad (2.46)$$

$$F_h\phi_h - F_l\phi_l = \|F_h,0\|\phi_P - \|-F_h,0\|\phi_H - (\|F_l,0\|\phi_L - \|-F_l,0\|\phi_P) \quad (2.47)$$

where $\|x,y\| = \max(x,y)$ and has a maximum of two numbers in the brackets. Table 2.2 shows formulae for the convective fluxes, and conveniently uses velocity values at the cell interface.

Table 2.2 Formulae for the coefficients in convection and diffusion terms

Cell Face	Convective Flux F	Diffusive Coefficient D	Diffusion Coefficient Γ
e	$\rho U_e A_e$	$\frac{\Gamma_e A_e}{x_E - x_P}$	$\frac{\Gamma_E + \Gamma_P}{2}$ or $\frac{2\Gamma_E\Gamma_P}{\Gamma_E + \Gamma_P}$
w	$\rho U_w A_w$	$\frac{\Gamma_w A_w}{x_P - x_W}$	$\frac{\Gamma_W + \Gamma_P}{2}$ or $\frac{2\Gamma_W\Gamma_P}{\Gamma_W + \Gamma_P}$
n	$\rho U_n A_n$	$\frac{\Gamma_n A_n}{y_N - y_P}$	$\frac{\Gamma_N + \Gamma_P}{2}$ or $\frac{2\Gamma_N\Gamma_P}{\Gamma_N + \Gamma_P}$
s	$\rho U_s A_s$	$\frac{\Gamma_s A_s}{y_P - y_S}$	$\frac{\Gamma_S + \Gamma_P}{2}$ or $\frac{2\Gamma_S\Gamma_P}{\Gamma_S + \Gamma_P}$
h	$\rho U_h A_h$	$\frac{\Gamma_h A_h}{z_H - z_P}$	$\frac{\Gamma_H + \Gamma_P}{2}$ or $\frac{2\Gamma_H\Gamma_P}{\Gamma_H + \Gamma_P}$
l	$\rho U_l A_l$	$\frac{\Gamma_l A_l}{z_P - z_L}$	$\frac{\Gamma_L + \Gamma_P}{2}$ or $\frac{2\Gamma_L\Gamma_P}{\Gamma_L + \Gamma_P}$
t	$\frac{\rho V_P}{\delta t}$	-	-

Integration of the diffusion terms results in the following formulae:

$$\int_A \left[\left(\Gamma\frac{\partial\phi}{\partial x}\right)_e - \left(\Gamma\frac{\partial\phi}{\partial x}\right)_w\right] dydz = D_e(\phi_E - \phi_P) - D_w(\phi_P - \phi_W) \quad (2.48)$$

$$\int_A \left[\left(\Gamma \frac{\partial \phi}{\partial y} \right)_n - \left(\Gamma \frac{\partial \phi}{\partial y} \right)_s \right] dxdz = D_n(\phi_N - \phi_P) - D_s(\phi_P - \phi_S) \tag{2.49}$$

$$\int_A \left[\left(\Gamma \frac{\partial \phi}{\partial z} \right)_h - \left(\Gamma \frac{\partial \phi}{\partial z} \right)_l \right] dxdy = D_h(\phi_H - \phi_P) - D_l(\phi_P - \phi_L) \tag{2.50}$$

where the diffusion coefficients are arithmetic or harmonic averages for the two adjacent cells (see Table 2.2).

Finally, the source term can be also integrated and then linearized as follows:

$$\int_V S dxdydz = SV_P = S_\phi \tag{2.51}$$

$$S_\phi = S_C + S_P \phi_P \tag{2.52}$$

The final discretization equations with unsteady, convection, diffusion and source terms is:

$$a_P \phi_P = a_E \phi_E + a_W \phi_W + a_N \phi_N + a_S \phi_S + a_H \phi_H + a_L \phi_L + a_T \phi_{P,old} + S_C \tag{2.53}$$

$$a_P = a_E + a_W + a_N + a_S + a_H + a_L + a_T - S_P \tag{2.54}$$

where the coefficient formulae are given in Table 2.3.

Equations (2.54) and (2.54) are valid for several differencing schemes such as upwind, central, hybrid, and power-law. The upwind scheme is the first-order scheme, and hence is prone to numerical diffusion. The order of scheme accuracy is determined from the Taylor series truncation error. The use of higher order schemes such as the quick scheme (third order) reduces numerical diffusion, but also induces less numerical stability. The quick scheme (Quadratic Upstream Interpolation for Convective Kinetics, Leonard 1979) uses more neighbor cells (see Figure 2.1(b)), hence the final discretization equation is:

$$\begin{aligned} a_P \phi_P = {} & a_E \phi_E + a_W \phi_W + a_{EE} \phi_{EE} + a_{WW} \phi_{WW} + a_N \phi_N + a_S \phi_S + a_{NN} \phi_{NN} + a_{SS} \phi_{SS} + \\ & a_H \phi_H + a_L \phi_L + a_{HH} \phi_{HH} + a_{LL} \phi_{LL} + a_T \phi_{P,old} + a_{TT} \phi_{P,old,old} + S_C \end{aligned} \tag{2.55}$$

$$\begin{aligned} a_P = {} & a_E + a_W + a_{EE} + a_{WW} + a_N + a_S + a_{NN} + a_{SS} + \\ & a_H + a_L + a_{HH} + a_{LL} + a_T + a_{TT} - S_P \end{aligned} \tag{2.56}$$

where the coefficient formulae are given in Table 2.3.

Table 2.3 The coefficients for Upwind and Quick differencing schemes

Coeff.	Upwind Scheme	Quick Scheme
a_E	$D_e + \|\|-F_e,0\|\|$	$D_e - \left\|\left\|\frac{3}{8}F_e,0\right\|\right\| + \left\|\left\|-\frac{6}{8}F_e,0\right\|\right\| + \left\|\left\|-\frac{1}{8}F_w,0\right\|\right\|$
a_{EE}	-	$-\left\|\left\|-\frac{1}{8}F_e,0\right\|\right\|$
a_W	$D_w + \|\|F_w,0\|\|$	$D_w - \left\|\left\|-\frac{3}{8}F_w,0\right\|\right\| + \left\|\left\|\frac{6}{8}F_w,0\right\|\right\| + \left\|\left\|\frac{1}{8}F_e,0\right\|\right\|$
a_{WW}	-	$-\left\|\left\|\frac{1}{8}F_w,0\right\|\right\|$
a_N	$D_n + \|\|-F_n,0\|\|$	$D_n - \left\|\left\|\frac{3}{8}F_n,0\right\|\right\| + \left\|\left\|-\frac{6}{8}F_n,0\right\|\right\| + \left\|\left\|-\frac{1}{8}F_s,0\right\|\right\|$
a_{NN}	-	$-\left\|\left\|-\frac{1}{8}F_n,0\right\|\right\|$
a_S	$D_s + \|\|F_s,0\|\|$	$D_s - \left\|\left\|-\frac{3}{8}F_s,0\right\|\right\| + \left\|\left\|\frac{6}{8}F_s,0\right\|\right\| + \left\|\left\|\frac{1}{8}F_n,0\right\|\right\|$
a_{SS}	-	$-\left\|\left\|\frac{1}{8}F_s,0\right\|\right\|$
a_H	$D_h + \|\|-F_h,0\|\|$	$D_h - \left\|\left\|\frac{3}{8}F_h,0\right\|\right\| + \left\|\left\|-\frac{6}{8}F_h,0\right\|\right\| + \left\|\left\|-\frac{1}{8}F_l,0\right\|\right\|$
a_{HH}	-	$-\left\|\left\|-\frac{1}{8}F_h,0\right\|\right\|$
a_L	$D_l + \|\|F_l,0\|\|$	$D_l - \left\|\left\|-\frac{3}{8}F_l,0\right\|\right\| + \left\|\left\|\frac{6}{8}F_l,0\right\|\right\| + \left\|\left\|\frac{1}{8}F_h,0\right\|\right\|$
a_{LL}	-	$-\left\|\left\|\frac{1}{8}F_l,0\right\|\right\|$
a_T	F_T	F_T
a_{TT}	-	F_{TT}

The quick scheme also preserves the upwind principle for the evaluation of the cell variables, but reduces the discretization error by accounting for more neighbor cells. The interface value of the scalar variable is the weighted value of the two cells upstream of the fluid motion. However, for some calculations (see chapter 5.2.1) the numerical instability with the quick scheme is difficult to control. Also, using the solution procedure with the quick scheme is a much slower process than with the upwind scheme, but due to its higher accuracy the quick scheme is popular.

2.6.2 The Solution Procedure

The solution procedure for the system of discretized transport equations is iterative because the equations are coupled and the convection terms in momentum equations are non-linear. Also, the pressure field does not have a transport equation, and therefore the pressure source term in the momentum equations must be calculated. The pressure field can be obtained indirectly from the continuity equation since the calculated velocities from the momentum equation have to satisfy mass continuity. Only the correct values of the pressure field will provide correct values of velocities that satisfy the mass continuity. The solution procedure starts with the initial guessed fields for calculated variables (velocity, pressure, turbulent quantities, temperature and concentration). First, the guessed pressure field p* is used to calculate velocity components, which are denoted u*, v* and w*. Then, the pressure field has to be corrected in a way that the velocity field satisfies the continuity equation. The correct pressure p is linked to the pressure correction p' in the following form:

$$p = p^* + p' \tag{2.57}$$

In a similar way, the velocities can be defined as:

$$u = u^* + u' \qquad v = v^* + v' \qquad v = v^* + v' \tag{2.58}$$

where u', v', w' are the velocity corrections.

The velocity correction equation has the same form as the final discretization Equation (2.53) or (2.55). However, the terms that represent the influence of the neighbor cells are neglected since that would ultimately involved the entire flow field into the velocity and pressure correction for each particular cell. Therefore, the velocity correction equation contains only the source term based on the pressure correction:

$$u'_e = \frac{A_e}{a_e}(p'_P - p'_E) \qquad v'_e = \frac{A_n}{a_n}(p'_P - p'_N) \qquad w'_h = \frac{A_h}{a_h}(p'_P - p'_T) \tag{2.59}$$

The neglected terms should not influence the final solution; the correction for velocity and pressure is done to reach the correct solution. Substituting the velocity correction, Equation (2.59), in the mass continuity equation gives the pressure correction equation in the same form as the general transport equation that uses the same solver as the other calculated variables:

$$a_P p'_P = a_E p'_E + a_W p'_W + a_N p'_N + a_S p'_S + a_H p'_H + a_L p'_L + S_C \tag{2.60}$$

where S_C is the source term is the mass continuity based on the "starred" velocities.

$$S_C = \dot{m}^*_w - \dot{m}^*_e + \dot{m}^*_n - \dot{m}^*_s + \dot{m}^*_t - \dot{m}^*_l$$

Solving the pressure correction gives values for the corrected pressure field p. Next, the velocity corrections (equation (2.59)) and velocity components can be solved. After the pressure and velocity fields are calculated, the other scalar variables are also calculated. The iterations continue with the calculated values as new guesses for variables. The procedure is repeated until the convergent solution is reached. This is the Semi-Implicit Method for Pressure-Linked Equations (SIMPLE) algorithm (Patankar and Spalding 1972).

The SIMPLE algorithm has been successfully used for many calculations. However, the calculation of the pressure correction ignores the influence of the neighboring velocity corrections and as a result slow convergence can occur due to severe pressure corrections. Examples of algorithms that are more economical than the original SIMPLE algorithm are SIMPLEC (Van Doormaal and Raithby 1984) and SIMPLET (Sheng et al. 1998). The former takes into account the first neighboring velocity corrections, and the later incorporates the temperature correction suitable for buoyancy-driven flows.

Due to the non-linearity of convection terms in the transport equations, solution procedures can be unstable. The variables must be solved simultaneously, and the progress towards a solution has to be simultaneous. To control the rate of change for the calculated variables, relaxation factors are used. Two relaxation techniques are available: linear relaxation and false-time step. Both relaxation factors serve to control the change in variable calculations and, hence, decrease the numerical instability. The form of the linear relaxation is:

$$\phi_P^{new} = \alpha\phi_P^n + (1-\alpha)\phi_P^{n-1} \tag{2.61}$$

where α is the linear relaxation factor (a number between 0 and 1), ϕ_P^{new} is the new value for the variable after n iterations, ϕ_P^n is the calculated variable after n iterations, and ϕ_P^{n-1} is the calculated variable after n-1 iterations. Therefore, the new value of the variable is $\alpha \times 100\%$ of the current value and $(1-\alpha)\times 100\%$ of the previously stored value. An extreme value of the relaxation factor, α=0 prevents the calculation of the variable, and α=1 neglects the value from the previous iteration ϕ^{n-1}. The lower the values of α are, the slower the calculation of ϕ, but the more stable the calculation is.

The false time step relaxation has the same form as the transient term given by equation (2.41):

$$\frac{\rho\phi_P^{n-1} - \rho\phi_P^n}{\delta t_f} V_P \tag{2.62}$$

where δt_f is the chosen value of the false time step. This term is treated as a source and is added to both sides of the general transport equation. Consequently, this relaxation does not influence the final solution, but the smaller values of δt_f create a slower solution

procedure. An extreme value of the false time, $\delta t_f=10^{-10}$ prevents calculation of the variable, and $\delta t_f=10^{+10}$ does not affect the calculation. Calculation with this relaxation is sometimes called pseudo-transient, and it is effective for buoyant flows, highly swirling flows, and other flows where governing equations cause stability problems (Versteeg and Malalasekera 1995).

A general problem with relaxation factors is that they depend on a solved case, and therefore their values have to be estimated and corrected during calculations. The relaxation only influences the calculation procedure and the final solution of a problem is independent of relaxation factors. The criterion for ending the numerical procedure is called the convergence criterion. Usually, the residual of the continuity equation must be smaller than a certain predefined value.

Finally, the numerical solution should be independent of grid distributions, initial variable distributions, and relaxation factors.

2.7 Discussion and Summary

This chapter gives an overview of mathematical and numerical modeling used to develop simplified airflow programs. The current methods for building simulations, zonal models and CFD, divide the calculation domain into number of grids and solve conservation equations. However, the zonal model does not solve the momentum conservation problem, and this causes several problems. The flow patterns have to be estimated from other methods such as the jet theory (see Chapter 3), and also, the momentum due to pressure or temperature differences is fixed with discharge coefficients obtained from CFD or measurements. CFD is a more reliable tool, but requires significant computing effort, which is currently prohibitive for the early-stage design of buildings. The simplified airflow program should be able to significantly decrease computing time.

Currently, the most appropriate CFD method for the indoor airflow modeling is RANS with turbulence modeling. RANS is the fastest CFD method and provides reasonably good solutions for indoor airflow simulations. A turbulence model consists of several additional conservation equations for the turbulent properties. The simplest zero-equation models use a single algebra equation. Nevertheless, turbulence modeling is an approximation, and therefore justification for the assumptions introduced must be validated with measured data (Chapter 4). Another important approximation for numerical simulations of the indoor environment is the modeling of the supply diffuser jet flow. This modeling is also based on several assumptions such as momentum similarity, and the applicability of the modeling has to be validated with experimental data (Chapter 5). Chapter 3 reviews diffuser jet flow characteristics, and methods for diffuser jet modeling in CFD simulations.

CHAPTER 3

TURBULENT JETS AND ROOM AIR DISTRIBUTION

3.1 Introduction

For mechanically ventilated rooms, air distribution strongly depends on the performance of air supply diffusers. The prediction of diffuser flow characteristics is challenging since the jet flow from the diffuser is complicated due to the complex diffuser geometry and the effects of confined space. Jet formulae are commonly used to describe the flow and thermal characteristics of supply diffusers. The jet formulae are empirical expressions for jet velocity and temperature decay, profiles, trajectory for inclined jets and separation distance for cold ceiling jets. Researchers (Nottage 1951, Kostel and Tuve 1955, Miller and Nevins 1972, Baturin 1972) have spent many decades developing the jet formulae, and today the approach is the most widely used to design room air distribution systems.

This chapter first reviews the formulae, and then applies the formulae to several diffuser jets. Some diffuser jets can be successfully predicted with the jet formulae, but not all of them. Also, other experimental studies (Sandberg et al. 1991, Heiselberg 1994, Tavakkol et al. 1994, Karimipanah 1996) have revealed similar deficiencies and limitations in the application of jet formulae for air distribution design.

A relatively new approach for designing room air distribution is CFD simulations of the indoor environment. This approach is becoming more popular due to its flexibility in testing different room layouts and supply air jet parameters. However, numerical simulations of the diffuser jets are still difficult to perform, especially for very complex diffusers such as multi-nozzle and valve diffusers. Different simplified methods for numerical modeling of the supply diffuser jets will be presented in the last section of this chapter, and their pros and cons will be discussed.

3.2 Jet Flow Definition and Classification

Jet is a flow motion with tangential separation at its boundaries. This separation exhibits discontinuity in velocity, temperature or species concentration, but not in static pressure distribution. Due to instability of tangential separation, the jet flow generates eddies. Large and small eddies are responsible for momentum, energy and species transfer along the jet stream as well as across the jet. The interaction of large eddies with small eddies and irrotational fluid increases the jet volume and decreases jet velocity. This behavior is in accordance with momentum conservation, and the phenomenon is known as a jet entrainment. As surrounding air is entrained, the jet stream slows and the jet diffusion in the surrounding environment increases.

Another important characteristic of turbulent jets is the jet initial momentum preservation. Since the static pressure is constant and equal to the pressure in the surrounding environment, the jet momentum in the axial direction is preserved:

$$M_x = M_0 = \int_0^A \rho u^2 dA = \rho U_0^2 A_0 \tag{3.1}$$

where M_x is the jet momentum at distance x from the jet source, M_0 is the initial jet momentum, A_0 is the effective area of the supply device, U_0 is the initial jet velocity and ρ is the air density. For a plane turbulent jet momentum conservation can be shown by integrating the momentum equation. However, for practical applications such as in diffuser jets, the effective area of the supply device may be difficult to determine.

For HVAC applications in indoor environments, diffuser air jets are classified according to the most important parameters for jet diffusion, such as jet temperature and distance to the nearest enclosure surface. The jet can be isothermal if the jet temperature is the same as the room air temperature or non-isothermal if is the temperatures are different. With respect to the distance from enclosure surfaces, a jet can be free or attached. When an air diffuser is installed close to the side walls, floor or ceiling, the jet attaches to the surface due to the Coanda effect. The attachment occurs since on the wall side the jet has a restricted entrainment and forms a zone of lower air pressure that drags the jet towards the wall. On the other hand, a free jet has unrestricted momentum diffusion and room air entrainment. In practice, a jet can be treated as a free jet if the enclosure is big enough to have a minimal impact on the jet trajectory and spread.

For a free turbulent air jet, the growth rate of the jet's thickness can be represented as a linear function of distance x from the jet's virtual origin (see Figure 3.1). This result is obtained from experimental measurements that showed the jet stream velocity profiles are self-similar in different cross-sections along the jet. Prandtl (1925) assumed that the mixing length is constant at any jet cross-section. A dimensionless analysis of the self-similar velocity profiles with the Prandtl's assumption shows linear growth of the jet boundary. Similar assumptions were used for wall jets with the conclusion of liner jet growth. The assumptions hold only in certain jet regions.

For indoor air distribution, an air jet is normally divided into four zones (ASHRAE 1997) as shown in Figure 3.1:

- Core
- Transitional
- Main
- Terminal

In the core zone, the centerline velocity U_m is equal to the initial jet velocity U_0. The core region usually extends approximately four diameters or widths of the supply opening. The transitional region can be neglected for circular jets or plane jets when the aspect ratio (width/height of square opening) is smaller than 13.5 (Awbi 1991). For most commonly used supply diffusers, the first two zones are relatively small compared to the

third or main jet zone. In the main jet zone, the flow is fully developed, and the velocity profiles are self-similar and can be described with non-dimensional jet profiles.

A fully developed jet flow is very important for HVAC engineering applications because diffuser jets usually enter the occupied space within their main zone (third zone). Therefore, the main zone is a subject of study by many researchers (Li et al. 1993). Actually, not only jet velocity profiles, but also jet temperature and concentration profiles tend to be self-similar in the main zone. Within a jet, heat and mass transfer are more intense than momentum transfer. This phenomenon contradicts Prandtl's mixing-length theory, which assumes the momentum and heat transfer mechanisms are the same. However, measurements (Schlichting 1979) have shown that for jets and wakes, the temperature profiles are wider than the velocity profiles. Taylor's vorticity-transfer theory can provide a theoretical explanation. According to the theory, the turbulent mixing motion causes an exchange of vorticity rather than momentum, and heat is transferred by diffusion. Consequently, for the temperature and concentration profiles, the core region fades faster. The main zone for temperature and concentration develops faster than that for momentum (Grimitlyn and Pozin 1993). The fully developed region has many formulae to define the jet flow parameters such as velocity and temperature, which are key design parameters for the air distribution systems.

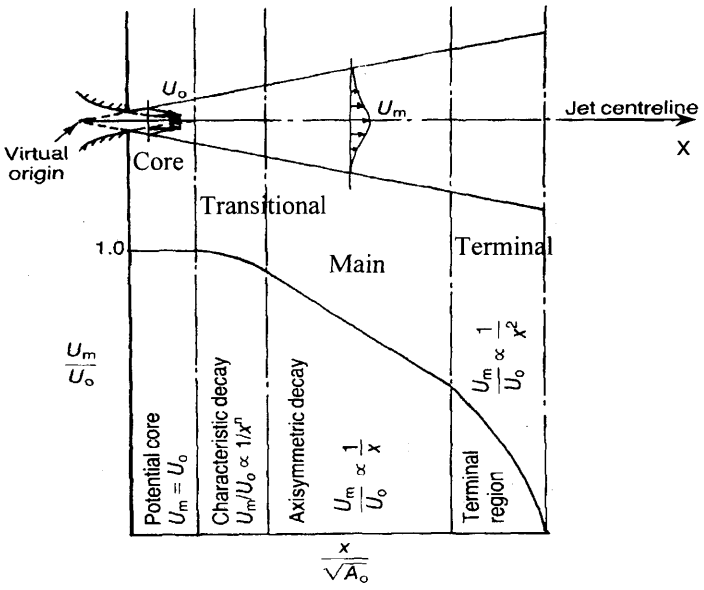

Figure 3.1. Jet zones and characteristic velocity profiles (log-log plot, Awbi 1991)

Finally, in the terminal region, jet velocity decay is very rapid, and jet velocities become the same order as room airflow velocities. In the terminal region, jet separation may occur in a cold air distribution system, which can cause draft problems. The theory of the terminal jet region is still under development, and no formulae are available to describe jet degradation.

3.3 Jet Formulae

Early studies of jet flow were based primarily on jets issued from simple supply devices such as orifices, nozzles or rectangular openings. Basic jet equations are for the profiles and decay of jet velocity and temperature. Also, mathematical expressions for jet entrainment flow and kinetic energy are available. The jet equations are extended for diffusers with more complex geometry such as vortex, square and round ceiling diffusers. Hence this chapter will review those formulae and then evaluate them by applying them to several commonly used supply air diffusers. The review starts with the formulae for jet profiles.

3.3.1 Jet Profiles

Jet profiles represent distributions of jet velocity or temperature in a cross section in the fully developed jet region. Figure 3.2 shows two jet profiles for free and attached jets. The profiles can be expressed by dimensionless formulae with scaling factors for velocity and length.

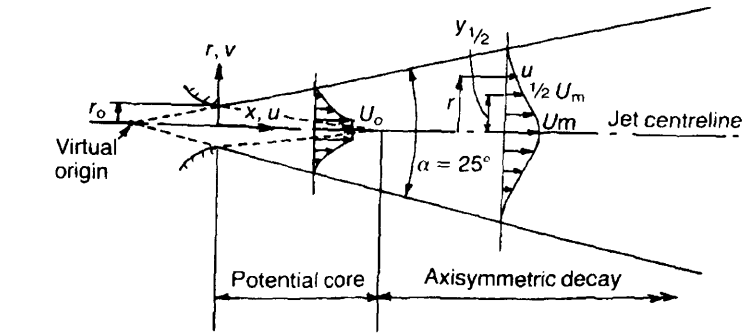

(a)

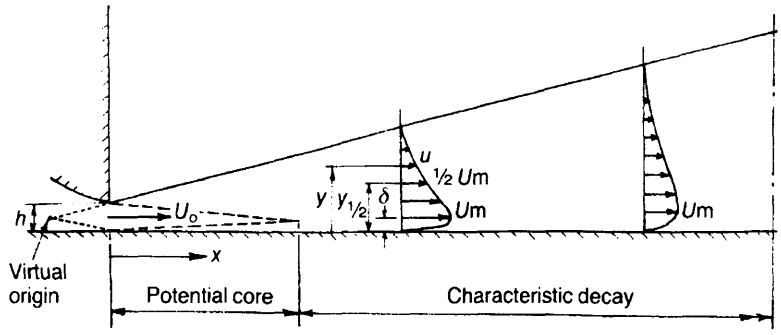

(b)

Figure 3.2. Jet velocity profiles for
(a) free axisymmetric jets (b) attached jets (Awbi 1991)

In case of a free jet, the scaling factor for velocity is the centerline velocity U_m and that for length is a half-width of the jet spread $y_{1/2Um}$, which represents a distance from the centerline to a position where the jet velocity is half of U_m (see Figure 3.2(a)).

For attached jets, the velocity scale is maximum velocity U_m in the jet cross section, and the length scale is a half-width of jet spread $y_{1/2Um}$, which is a distance from the wall to a position where the jet velocity is a half of the maximum velocity (see Figure 3.2(b)). The following presents jet formulae for velocity and temperature profiles for different jets. The formulae have been used in simplified diffuser simulations to generate boundary conditions for the diffusers.

- Isothermal jet in the main zone

For isothermal plane (linear) jets, Rajaratnam (1976) developed a formula for velocity profile:

$$\frac{u}{u_m} = \exp\left[-0.693\left(\frac{y}{y_{1/2Um}}\right)^2\right] = \exp\left[-69.3\left(\frac{y}{x}\right)^2\right] \tag{3.2}$$

where $y_{1/2Um} = 0.1\,x$.

Huo et al. (1996) presented another equation:

$$\frac{u}{u_m} = \exp\left[-\frac{y^2}{2\,(0.082\,x)^2}\right] = \exp\left[-74.4\left(\frac{y}{x}\right)^2\right] \tag{3.3}$$

The two equations, if rearranged, have the same form with slightly different coefficients. The difference is small and negligible in practical applications.

For isothermal axisymmetric jets, Huo et al. (1996) used

$$\frac{u}{u_m} = \exp\left[-\frac{y^2 + z^2}{2\,(0.082\,x)^2}\right] \tag{3.4}$$

Figure 3.3(a) shows an axisymmetric jet velocity profile described by Equation (3.4) at distance x=0.45m (1.5ft) from the jet origin. This Gaussian profile is typical for free jets and is called a "top hat" profile. Figure 3.3(b) represents an experimental observation (Rajaratnam 1976) for wall jets: the top hat profile is observed in a horizontal plane, while in the vertical plane, a velocity profile can be described by an erf function. The experiments (Rajaratnam 1976) also showed that jet growths in a horizontal plane is four to five times faster than that in a vertical plane due to unrestricted momentum and vorticity diffusion in the horizontal plane, while diffusion in the vertical plane is bounded by the wall.

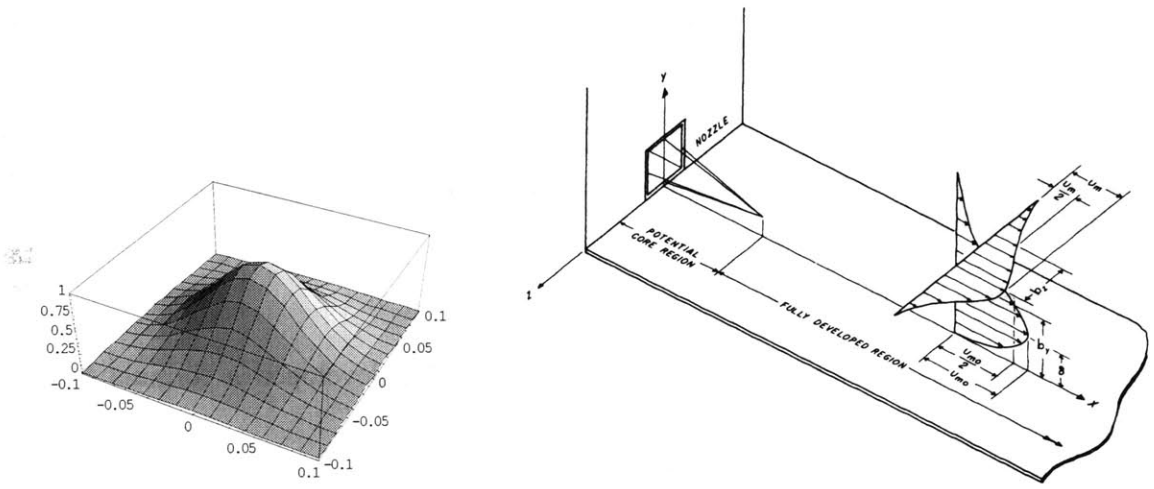

Figure 3.3. Jet velocity profiles for three-dimensional (a) free jets and (b) wall jets

- A non-isothermal jet in the main zone

For isothermal attached jets, Verhoff (1963) proposed:

$$\frac{u}{u_m} = 1.48\eta^{1/7}\left[1 - erf(0.68\eta)\right] \tag{3.5}$$

where $\eta = \dfrac{y}{y_{1/2Um}}$, $y_{1/2Um} = 0.073(x + 12\,b)$ (Rodi 1982).

Equations (3.3), (3.4), and (3.5) can be used as simplified diffuser models to obtain jet profiles for boundary conditions in CFD simulations. If the jet is close enough to the diffuser and is not yet disturbed by the surroundings (enclosure, heat sources), the profiles obtained with the equations may be appropriate to describe the diffuser jet characteristics. However, the profiles apply only to the main jet region, and not to core or transitional regions. Even the application to the main jet region is limited since the surrounding environment may play an important role in jet development. For example, jet may be developed to neither free nor attached one. Section 3.3 provides more analysis on the application of a jet equation for diffusers with validation by measured data.

For non-isothermal jets, the jet temperature distribution is another important characteristic in room air distribution design. The temperature profile formula is usually normalized by a scaling factor temperature T_m. The T_m can be either the centerline temperature for free jets or the lowest temperature at given jet cross sections for wall jets. Reichardt (1944) studied plane free jets and discovered that the temperature profiles are similar to velocity profiles. He found that the temperature profiles could be represented as a square root of velocity profiles. His results confirm Taylor's vorticity-transfer theory,

and demonstrate that the heat diffusion is higher than the vorticity diffusion. The temperature profile in the jet's main region is calculated by:

$$\frac{T - T_r}{T_m - T_r} = \sqrt{\frac{u}{u_m}} \tag{3.6}$$

where T_r is the average room temperature. For mixing ventilation, T_r equals the return air temperature.

Experimental studies show that the temperature profile is not a good estimate for jet temperatures in HVAC applications (Nielsen 1992, Amiri et al. 1996) probably because of the thermal impact from many concentrated heat sources in the vicinity of a jet.

The length scale, $y_{1/2Um}$, velocity scale, U_m, and temperature scale, T_m, are needed to close the system of equations. At present, $y_{1/2Um}$ is assumed to be a linear function of x, the distance from the jet origin. An experimental study (Knappmiller 1994) for cold ceiling jets showed that the assumption of linear jet spread is not a good one. Knappmiller (1994) proposed a bi-linear model for the half-width jet spread. The cold jet spreads slowly close to the diffuser, and faster in the area closer to the separation point. The model provided good results for the cases he studied. However, a general expression is not available since the jet spread in the area close to the separation point could not be correlated with supply boundary conditions.

The U_m and T_m can be expressed by the jet decay formulae. For design purposes, velocity decay formulae are more effective than the velocity distribution formulae because designers need to estimate the maximum velocity in the occupied zone. The following section discusses the jet decay formulae.

3.3.2 Jet Decay

The jet decay formulae were developed from the hypotheses of initial jet momentum M_0 preservation and the similarity of dimensionless profiles. Abramovich (1963) showed that velocity decay for a plane jet is proportional to $1/\sqrt{x}$, and for an axisymmetric jet is proportional to $1/x$. The decay equations also contain a constant coefficient that depends on a diffuser's type and can be determined experimentally. The following paragraphs summarize some of the dimensionless results for the jet's main region. More jet formulae can be found in the literature (Awbi 1991, Grimitlyn 1993, Li et al. 1993, Zhivov 1993, Livtchak et al. 1994, ASHRAE 1997).

- Velocity decay in the jet main region:

  For isothermal axisymmetric free jets

$$\frac{u_m}{u_0} = K_1 \frac{\sqrt{A_0}}{x} \tag{3.7}$$

where u_0 is the initial jet velocity, A_0 is the diffuser effective area, x is the distance from diffuser, K_1 is the centerline velocity decay constant, K_1=7.0 for orifice jets (Rodi 1982), K_1=5.7 for compact jets, K_1=1.1 for radial jets, and K_1=2.0 for incomplete radial jets (Li et al. 1993).

In Equation (3.7), coefficient K_1 lumps together all important effects for jet velocity decay. The coefficient is a function of diffuser type, and the high value of K_1 indicates a slow jet decay or a jet with low shear stress. The correct selection of K_1 is crucial for the determination of jet decay. The current design guidelines use a constant for K_1 (ASHRAE 1997). The measurements have shown that K_1 is not a constant and depends on many factors such as jet confinement, deflection (see section 3.5.3), and the Reynolds number when jet velocity is low (lower than 6 m/s (1200 fpm), Re < $5x10^4$) (Malmstrom et al. 1997).

For isothermal plane (linear) free jets

$$\frac{u_m}{u_0} = K_1 \sqrt{\frac{H_0}{x}} \tag{3.8}$$

where H_0 is an effective width of the diffuser; different experimental studies give different centerline decay coefficients for plane free jets K_1=2.2 (Li et al. 1993), K_1=2.3 (Rodi 1982), and K_1=2.35 (Whittle 1986).

For isothermal attached jets, the jet velocity decay is slower than for the free jets. ASHRAE (1997) recommends use of the same decay formulae as for the free jets, but the centerline velocity decay constant K_1 should be multiply by 1.4 to account for the slow velocity decay of attached jets.

Inclined non-isothermal jets require more complex jet formulae to account for buoyancy forces that influence the jet trajectory and decay. The Archimedes number, as a dimensionless ratio of the buoyancy force to the inertia force, is a suitable indicator of non-isothermal jet behavior. Non-isothermal jets issued horizontally (α_0=0°) or inclined ($\alpha_0 \leq \pm 45°$) can be calculated by (Shepelev 1978):

$$\frac{y}{\sqrt{A_0}} = \frac{x}{\sqrt{A_0}} \mathrm{tg}\alpha_0 \pm \psi \frac{K_2}{K_1^2} \mathrm{Ar}_0 \frac{x}{\sqrt{A_0}} \tag{3.9}$$

$$\mathrm{Ar}_0 = \frac{g\sqrt{A_0}(T_0 - T_r)}{u_0^2 T_r} \tag{3.10}$$

where y is the vertical distance from the jet origin, x is the horizontal distance from the jet origin, α_0 is the angle of inclination measured from the horizontal axis x, ψ is the experimental constant, ψ=0.47, K_2 is the centerline temperature decay constant, K_2=1.7 for linear and radial jets, K_2=3.4 for compact jets (Li. et al. 1993), Ar_0 is the Archimedes number based on the air supply parameters, g is the gravitational acceleration, and T_0 is the supply air temperature. The sign ± in the Equation (3.9) depends on the y-axis orientation and the direction of the buoyancy force (cold or heated jet). The jet trajectory is an average result since its fluctuation has been observed. The fluctuation may influence the accuracy of the formula (Zhivov 1993).

- The temperature decay for non-isothermal free jets

  For non-isothermal axisymmetric free jets

$$\frac{T_m - T_r}{T_0 - T_r} = K_2 \frac{\sqrt{A_0}}{x} \frac{1}{K_n} \tag{3.11}$$

where T_m is the centerline jet temperature, and $K_n = \left[1 \pm \frac{2.5K_2}{K_1^{\,2}} A_r \left(\frac{x}{\sqrt{A_0}}\right)^2\right]^{1/3}$ for vertically discharged jets, and K_n = 1 for horizontally projected jets (Li. et al. 1993).

For non-isothermal plane (linear) free jets

$$\frac{T_m - T_r}{T_0 - T_r} = K_2 \sqrt{\frac{H_0}{x}} \frac{1}{K_n} \tag{3.12}$$

where $K_n = \left[1 \pm \frac{2.5K_2}{K_1^{\,2}} A_r \left(\frac{x}{H_0}\right)^{3/2}\right]^{1/3}$ for vertically discharged jets, and K_n = 1 for horizontally projected jets (Li et al. 1993).

The velocity decay formulae for non-isothermal jets discharged horizontally are the same as those for the isothermal jets. For the vertically projected non-isothermal jets Equations (3.7) and (3.8) have to be multiplied by the coefficient K_n, which accounts for the gravitational effect.

For an attached non-isothermal jet, the separation distance for cold ceiling jets is an important design parameter since the cold jet may drop and enter the occupied zone. Kirkpatrick and Elleson (1996) recommended the following formula for determining the separation distance:

$$x_s = a C_s K_1^{1/2} \left(\frac{\Delta T}{T} \right)^{-1/2} Q^{1/4} \Delta P^{3/8} \tag{3.13}$$

where x_s is the separation distance, a is the constant (for IP units a=11.91 for SI units a=48.04), C_s is the separation coefficient (C_s=1.2), K_1 is the velocity decay constant, ΔT is the room-jet temperature difference, T is the average absolute room temperature, Q is the volume flow rate, and ΔP is the diffuser static pressure drop.

The higher the jet flow rate and the initial jet momentum, M_0, the longer the separation distance. The last two terms in Equation (3.13) show that the separation distance is linearly proportional to the flow rate ($x_s \sim Q$) since the static pressure drop is proportional to the square of the flow rate ($\Delta P \sim Q^2$).

The jet formulae provide important insight into jet behavior. The following section discusses whether the jet formulae can be used to calculate the flow characteristics with eight commonly used diffusers. The calculations are validated with measured data.

3.4 Application of Jet Formulae to Diffuser Jets

The jet formulae describe in a simple way jet flow from many different supply diffusers. The formulae have been developed from extensive experimental work, under laboratory conditions that in most cases use large empty spaces. In order to test whether the jet formulae can be used to describe boundary conditions in CFD simulations for supply air diffusers, it is important to assess their performance for different commonly used diffusers (Srebric et al. 2000b). The formulae should be reliable for the design of air distribution systems. For design applications, the jet formulae should be able to predict air parameters in the jet region that enters an occupied zone. However, the CFD applications need jet formulae to predict airflow in the vicinity of a diffuser. This section evaluates the performance of the jet formulae in the vicinity of diffusers, for their potential to be incorporated in CFD simulations.

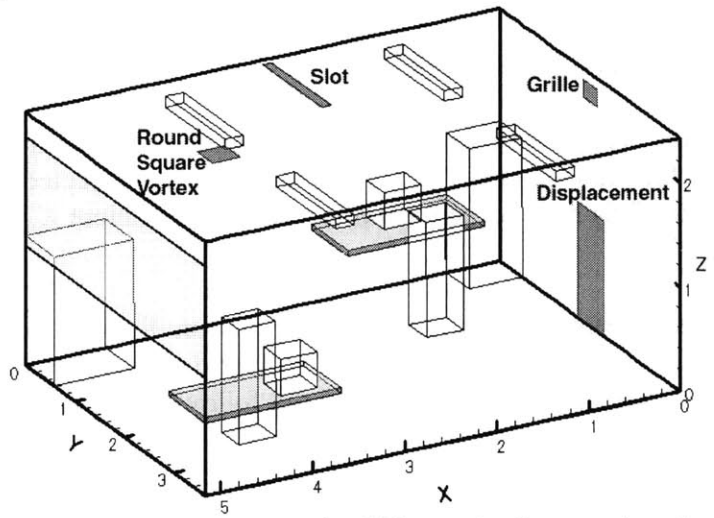

Figure 3.4 Positions of the supply diffusers in the test chamber

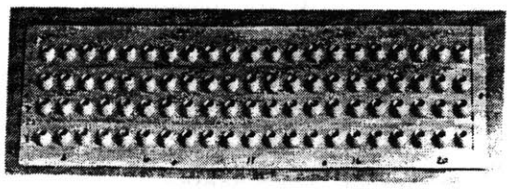

(a)

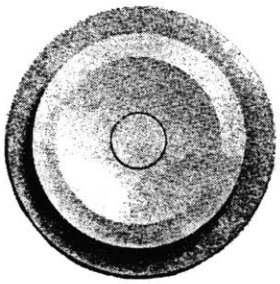

(b)

(c)

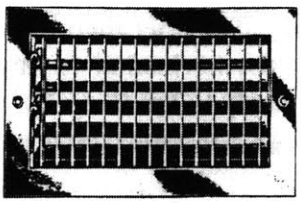

(d)

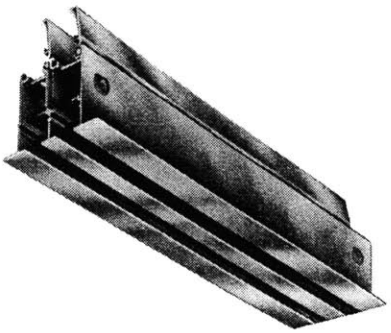

(e)

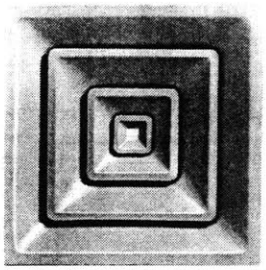

(f)

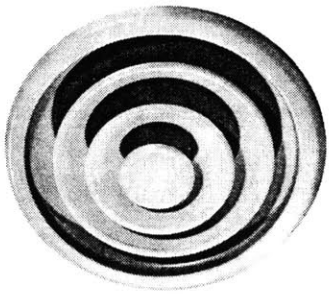

(g)

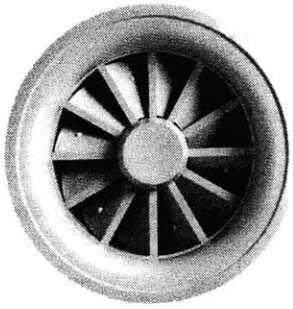

(h)

Figure 3.5 Commonly used air supply diffusers: (a) nozzle, (b) valve, (c) displacement, (d) grille, (e) slot, (f) square ceiling, (g) round ceiling, and (h) vortex

The jet formulae described in Section 3.3 will be used to predict flow characteristics from eight commonly used air supply diffusers installed in a full-scale environmental chamber. The diffusers are nozzle, valve, slot, displacement, round, square, vortex, and grille diffuser (see Figure 3.5). Experimental data on air velocity and temperature distributions are available for these diffusers, and it can be used to validate the results obtained with the jet formulae. Figure 3.4 shows the positions of some of the diffusers installed in a full-scale environmental chamber. The chamber layout represents a small office space with two workstations. The other diffusers, nozzle and valve, have been tested in different full-scale environmental chambers.

- Nozzle diffuser

The nozzle diffuser (IEA 1993) was tested under isothermal and non-isothermal conditions for the jet that was discharged below the ceiling. The jet discharge angle was 40^{o} from the horizontal towards the ceiling. Although the jet attached to the ceiling at approximately 0.2 m (0.66 ft), it does not immediately develop into a normal attached jet. At 1.0 m (3.3 ft) from the diffuser, the jet flows parallel to the ceiling but the jet profiles cannot be described by Equation (3.5) for attached jets. However, Figure 3.6 shows that the jet at 2.2 m (7.2 ft) is attached, and its profile can be predicted with the jet formula. On the other hand, the jet decay equations presented in section 3.3.2 could not be used to evaluate the maximum jet velocity since K_1,the centerline velocity decay constant, was not calibrated for this application.

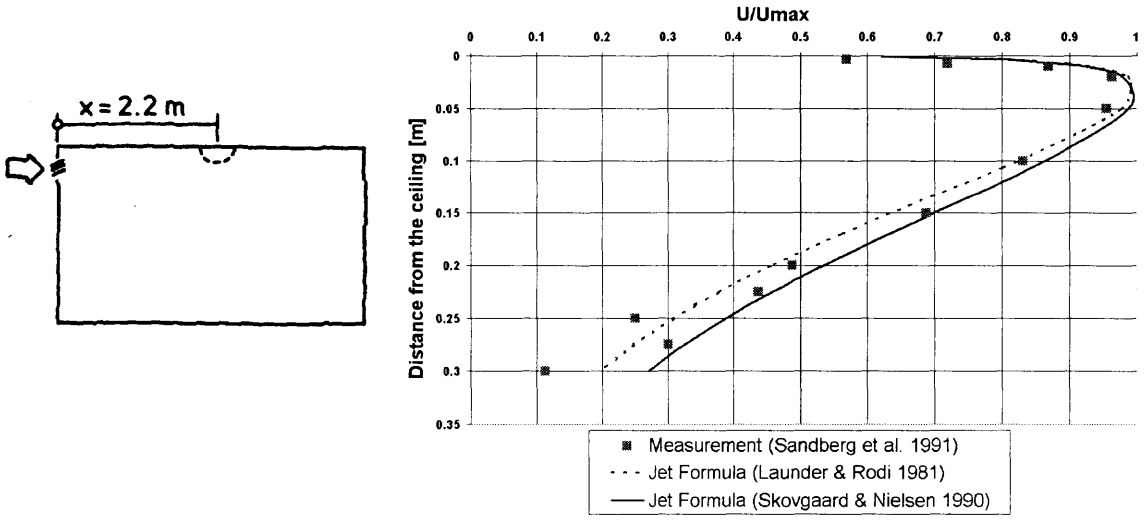

Figure 3.6 Attached jet developed at the ceiling 2.2 m (7.2 ft) from the nozzle diffuser

- Valve diffuser

The valve diffuser discharges a conical jet from the ceiling straight downward to the floor. The cone angle is around 60^{o}. The conical jet merges in a single jet a short distance from the diffuser. No jet formulae are available for this valve diffuser.

- Displacement diffuser

The displacement diffuser is the only non-mixing supply diffuser examined in this investigation. This diffuser supplies fresh air at the floor level. The air supply velocities are lower than 0.5m/s (100fpm), and the air supply temperatures are lower than the ambient air. The heat sources create thermal plumes and the airflow from the occupied lower zone to upper room zone. The low-velocity cold jet enables temperature and contaminant stratification. For high cooling loads the basic principle of displacement ventilation can be violated and the mixing between layers can be established. Therefore, the displacement ventilation is suitable for the low cooling loads (~25-40 W/m^2). The maximum cooling load can be 120 W/m^2, and the diffuser must have a large surface area.

Figure 3.7 shows the development of jet flow in front of the displacement diffuser. The jet drops immediately to the floor in the front of the diffuser because of the low air supply velocity and buoyancy effect. The jet then spreads over the floor and reaches the opposite wall. In front of the diffuser, the jet velocity profile changes along its trajectory. Close to the diffuser no jet formulae can be used since the jet is in a transition region. Only after 0.9 m (3.0 ft) does the jet form an attached jet. Figure 3.8(a) shows good agreement in the jet region between the jet formula (Equation (3.5)) and measured data (Livchak 1999) for the velocity profile at 1.2 m (4.0 ft) from the diffuser. However, the jet formulae can predict only velocities in the jet region that is less than 0.2 m (0.66 ft) above the floor, because the velocities above the region are influenced by the room conditions. In fact, the velocity profile above the jet region represents the backward airflow towards the displacement diffuser.

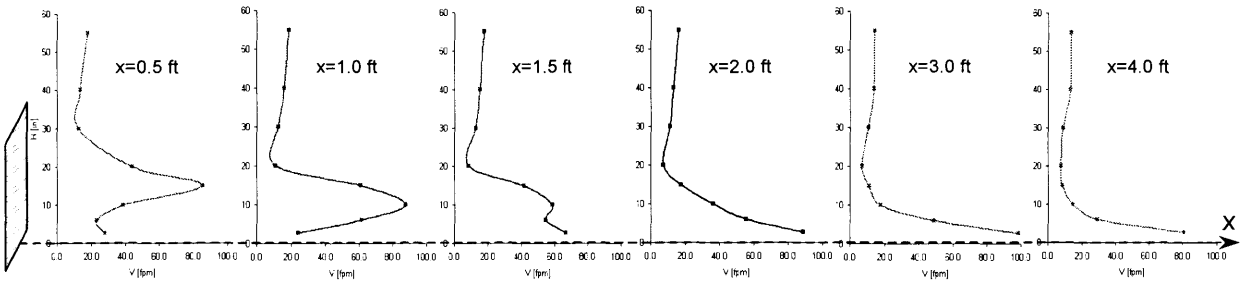

Figure 3.7. Development of the wall jet in front of the displacement diffuser

The velocity decay formula (3.7) for isothermal jets has to be modified for the displacement diffuser for non-isothermal flows. Nielsen (1992) used the same formula but with a different centerline velocity decay constant, K_1. K_1 should depend also on the Archimedes number, Ar. This approach requires extensive measurements to establish the K_1 as a function of Ar for different types of diffusers.

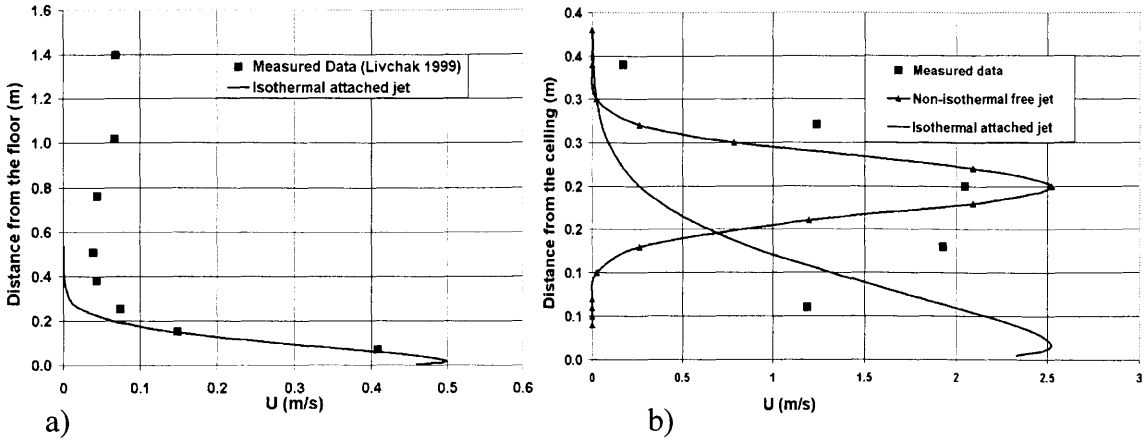

Figure 3.8. The velocity profile predicted by jet formulae for
(a) displacement diffuser (x=1.2 m), and (b) grille diffuser (x=0.45 m)

The extensive measurements might be worthwhile if the jet formula could also predict temperature distribution. However, the temperature profile does not exhibit similarity as desired, probably due to the influence of internal heat sources. The temperature profile deviated from that predicted by Equation (3.6), increasing with increased distance from the diffuser. Nevertheless, Jacobsen and Nielsen (1992) found that equation (3.6) is the best fit for their data. Another study (Amiri et al. 1996) with plane-attached non-isothermal jets also found a similarity in terms of velocity profiles but could not find suitable jet formulae for the temperature profiles since the temperature profiles were not similar. Figure 3.9 shows dimensionless velocity and temperature profiles obtained in their study. It seems that, for HVAC supply diffusers, the jet temperature profiles cannot be predicted accurately with the formulae.

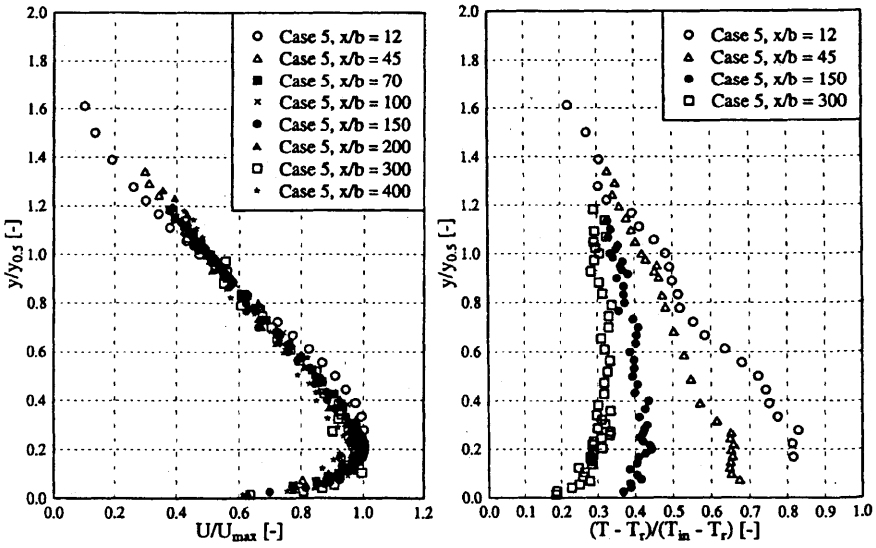

Figure 3.9 Measured velocity and temperature profiles for a slot opening at a different distance x from the opening (b=0.01 m) (Amiri et al. 1996)

- Grille diffuser

The next diffuser studied is a grille diffuser. The grille diffuser generated a jet through deflection vanes that were adjusted in this case to issue a straight horizontal jet. The diffuser was installed 0.11 m below the ceiling as shown in Figure 3.4. The jet from the diffuser was attached to the ceiling through the Coanda effect. Figure 3.8(b) shows the measured velocity profile at 0.45 m (1.5 ft) from the diffuser with an airflow rate of 5 ach. Similar profiles were measured at 0.6m (2 ft) and 0.8m (2.6 ft) from the diffuser. The results indicate that the jet is neither attached nor free. Therefore, both the attached and free jet formulae failed to predict this jet flow.

The partially attached jets in HVAC applications have been observed before (Karimipanah 1996). Nasr and Lai (1998) give a review of experimental studies for partially attached plane jets that eventually develop into fully attached jets. They called them offset jets. Figure 3.10 shows a jet similar to the grille diffuser, where the jet is placed close to the ceiling. Two characteristic parameters are x_a, the distance from the diffuser to a point where the jet attaches to the ceiling, and x_w, where the jet develops into a fully attached jet. Between x_a and x_w the jet is only partially attached. For an isothermal plane jet located parallel to a ceiling (offset jet) the following experimental formulae are available to determine x_a (Awbi 1991) and x_w (Nielsen 1997):

$$\frac{x_a}{h} = 0.73\frac{D}{h} - 2.3 \qquad \text{for } \frac{D}{h} \in (3,37) \tag{3.14}$$

$$\frac{x_w}{h} = 2.1\frac{D}{h} + 10 \qquad \text{for } \frac{D}{h} \in (5,25) \tag{3.15}$$

where D and h are shown in Figure 3.10.

The above equations (3.14) and (3.15) are valid for only a certain range of *D/h*. For the grille diffuser studied, *D/h*=0.65, which is beyond the valid range. Therefore, the formula is not valid for the diffuser. Our measurements confirmed that the jet was not attached even at 0.8 m (2.6 ft) from the diffuser.

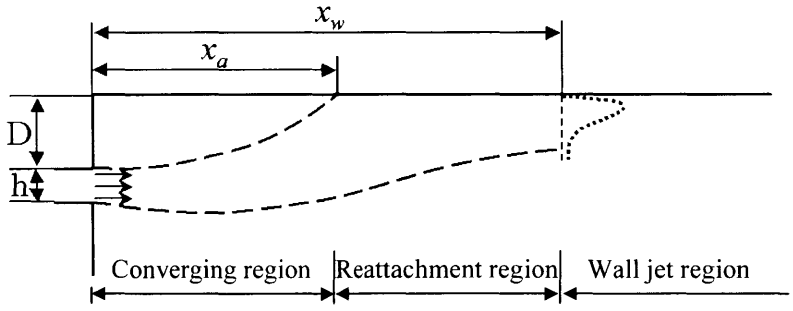

Figure 3.10 Jet trajectory and regions for an offset jet

A cold jet would separate at a certain distance from the diffuser. In order to avoid a draft created by the jet, it is important to determine the separation distance. For the grille diffuser with three different flow rates (3, 5 and 8 ach), the separation distance was estimated by smoke visualization and jet formulae (3.13). The formula needs the diffuser static pressure drop as input. Many diffuser catalogues provide such pressure drop information for a certain range of discrete airflow rates, and the formula is very sensitive to the pressure drop. We have applied the formula to the grille diffuser for those flow rates with known static pressure drops. The calculated separation distance for 8 ach was approximately 0.35 m (14") longer than that observed by smoke. This discrepancy probably comes from the velocity decay coefficient that could only be roughly estimated.

Figure 3.11 in the lower right corner illustrates the separation distance estimated by smoke (dashed lines). The figure also shows dimensionless temperature profiles for the grille diffuser at the middle vertical cross-section. The results indicate a very uniform temperature distribution in the lower part of the room, although the difference is significant in the upper part of the room. The difference is especially evident at the region close to the diffuser. In this case, a 3 ach ventilation rate can still create a reasonable amount of mixing in the occupied zone, although the jet separated from the ceiling very early. However, the velocity distribution in the occupied zone, especially near the floor, is rather different with different ventilation rates, because the separation distance and airflow pattern are different.

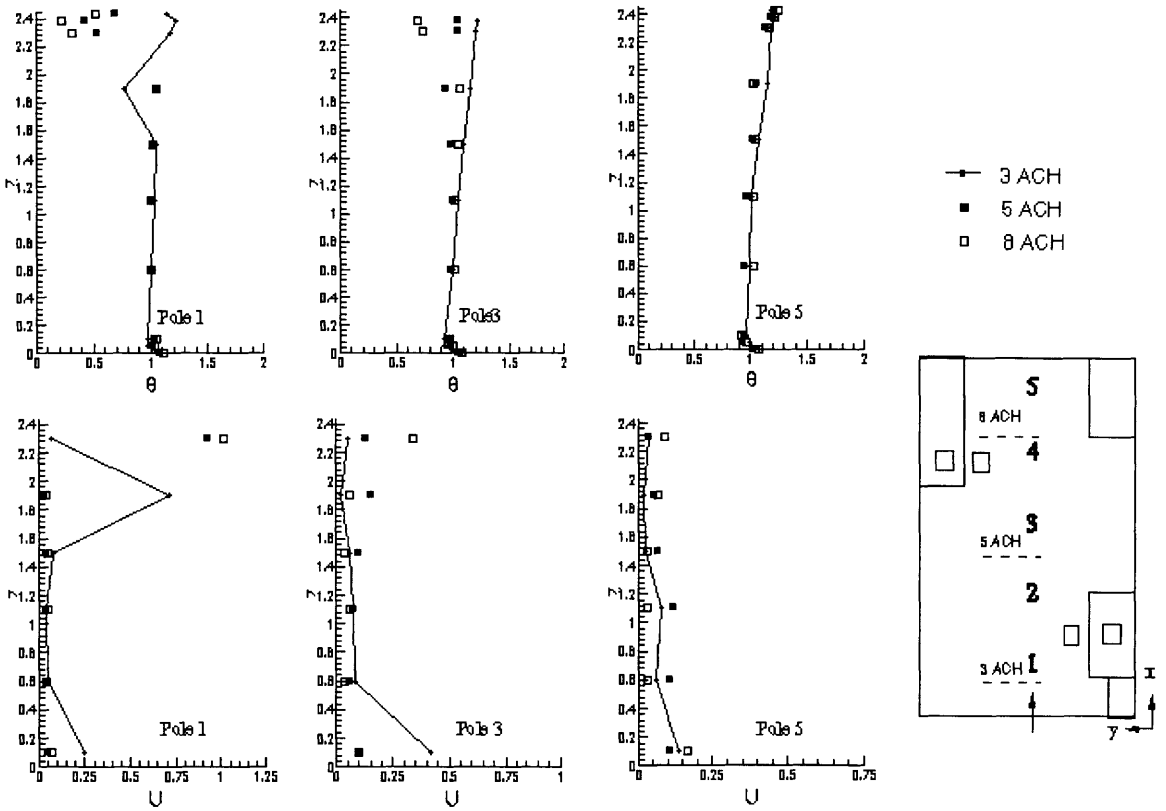

Figure 3.11 Dimensionless temperature and velocity profiles for the grille with different flow rates, $\theta=(T-T_{in})/(T_{out}-T_{in})$ and $U=V/V_{in}$

- Slot diffuser

The slot diffuser was installed in the proximity of two enclosure surfaces (the ceiling and side wall). The blades in the diffuser were adjusted to discharge horizontal jet to the right side of the room where several concentrated heat sources were placed (see Figure 3.4). The initial jet flow was 45° downwards, but after a short distance the jet attached to the ceiling and the north wall. The attachment was probably also pushed by the thermal plumes from the heat sources. Very similar to the results for the grille diffuser as shown in Figure 3.8(b), neither the free jet formula nor the attached jet formula can correctly simulate the velocity profile along the jet.

The jet envelope is a three dimensional surface that in some cross section exhibit both attached and free jet shape as shown in Figure 3.12. The figure shows two jet velocity profiles in the horizontal cross sections at 0.46 m (1.5 ft) from the diffuser. The profile closer to the ceiling (0.06 m or 2.4") has the shape similar to the free jets, while the profile further from the ceiling (0.42 m or 1.4 ft) shows attachment to the north wall. Between those two extreme positions, the jet gradually changes its shape from free to attached one. This type of change no formulae can predict.

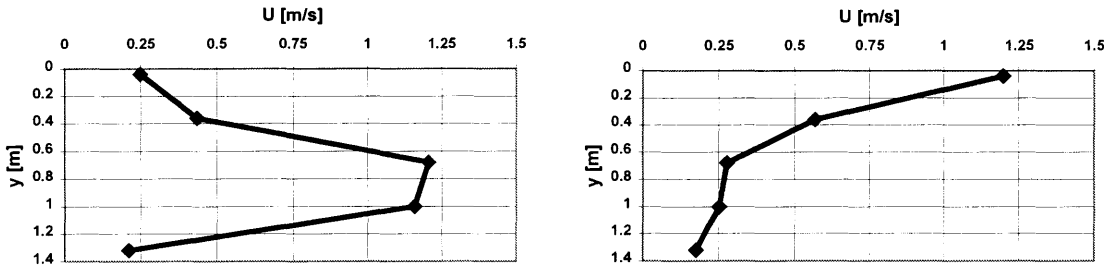

(a) (b)

Figure 3.12 The measured jet velocity profiles in the horizontal cross sections at 0.46 m in front of the slot diffuser at (a) 0.06 m and (b) 0.42 m from the ceiling (y is a distance from the north wall)

- Square, round and vortex ceiling diffusers

The square, round, and vortex ceiling diffusers can be classified as the same type. The diffusers discharge the air horizontally in a radial direction, the four directions, and a radial direction with swirl, respectively. The wall jet formula can predict the jet velocity profile if measured data are available to calibrate the formula coefficient. For example, Figure 3.13 shows a good agreement between measured and calculated velocity profile in the middle cross section for the square ceiling diffuser. The measured data are used to obtain the length scale $y_{1/2U_m} = 0.073(x + 0.2)$ for the jet profile formula (3.5). Similar analysis can be applied to the jet region close to the round ceiling diffuser, but we did not have enough data to calibrate the length scale formula. On the other hand, the formula cannot be applied to the region close to the vortex diffuser due to the geometric character of the diffuser.

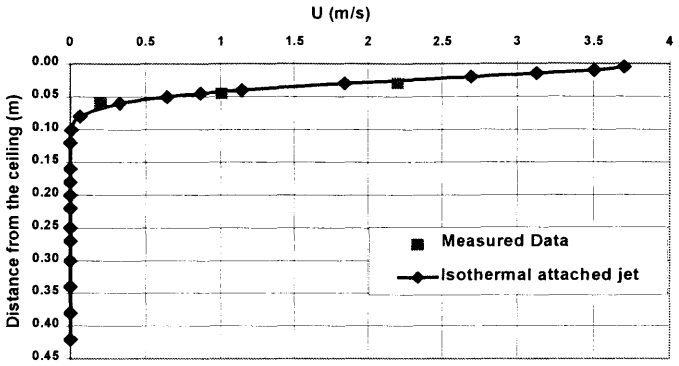

Figure 3.13 The velocity profile predicted by jet formulae
for the square ceiling diffuser (x=0.17 m)

The square, round, and vortex ceiling diffusers had the same position in the test chamber and the same thermal and flow boundary conditions. Therefore, it was interesting to examine the resulting temperature and airflow fields with the different ceiling diffusers. Figure 3.14 compares the dimensionless temperature and velocity profiles measured at five poles in the test chamber. The figure in the lower right corner shows the pole positions where the profiles were measured. Although the diffusers were very different, the temperature profiles were the same in the occupied zone. The smoke visualization showed that the airflow patterns differed only in the region close to the ceiling. In fact, all three diffusers had jets attached to the ceiling. The difference of the normalized velocities in Pole 5 is smaller than that in Pole 3. This indicates that the vortex diffuser has higher jet entrainment and faster velocity decay.

The studied jet flows have shown some of problems usually encountered in practical applications of the jet formulae. The jet profile formulae can be applied only to free and attached jets if the length scale formula is available for the studied diffuser. Furthermore, the jet formulae for velocity and temperature decay normally include the decay coefficients (K_1 and K_2) that depend on the diffuser type, internal heat sources, and the proximity of enclosure surfaces. Therefore, it is difficult to determine the coefficients. Even if the decay jet formulae can be used, it is more reliable for determining the velocity and temperature decay within a small distance from the jet origin (the diffusers) where jet is not disturbed by internal configuration.

Nevertheless, the jet formulae can provide insight into the physical processes of diffuser jets, such as the jet diffusion and entrainment rates. Since the formulae are simple and easy to use, they deserve considerable attention in design of air distribution systems.

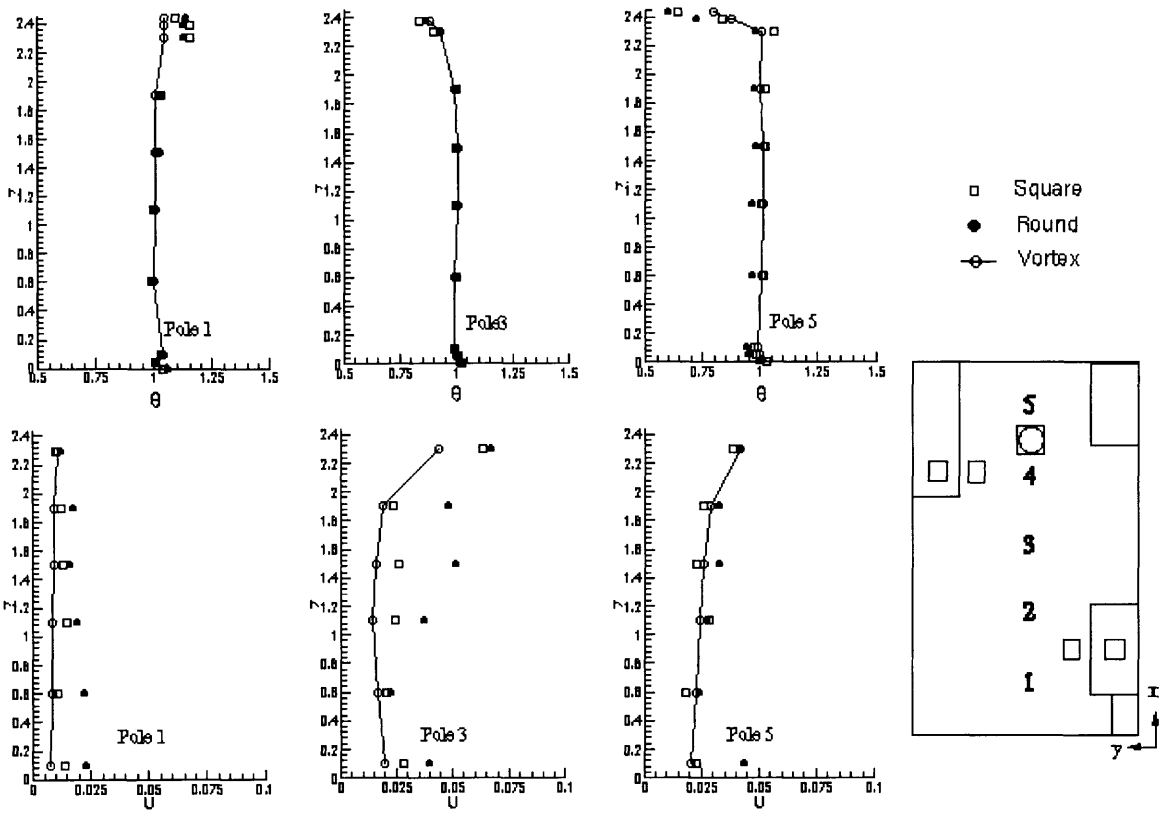

Figure 3.14 Dimensionless temperature and velocity profiles for the square, round and vortx ceiling diffusers $\theta=(T-T_{in})/(T_{out}-T_{in})$ and $U=V/V_{in}$

3.5 Tools for Room Air Distribution Design

The previous section shows that some of the jet formulae can be used to calculate velocity and temperature distribution along a jet. The formulae are therefore of value for designing room air distribution because the jets have a significant impact on air distribution. If the maximum velocity and temperature can be determined in the occupied zone by using the formulae, thermal comfort conditions in the room will be known. This section will discuss how to use the jet formulae to design various air distribution systems.

An air distribution system should provide fresh air, dilute contaminants, and heat or cool a space. According to the airflow pattern created, the air distribution system is either mixing or displacement ventilation. Mixing ventilation creates high momentum from its supply devices, removes the contaminants by mixing pollutants with fresh air, and enhances heat transfer by forced convection. The air distribution system is primarily uniform except in the jet region and the regions close to the heat and contaminant sources. On the other hand, displacement ventilation is mainly buoyancy driven with very low momentum from the diffuser and it removes pollutants and heat gains by displacing contaminated air by fresh air without mixing. Thus, the indoor air distribution is non-uniform and this creates stratification in room air. The stratified distribution of

temperature and pollutant concentrations makes the displacement ventilation more efficient for cooling and contaminant removal than the mixing ventilation.

The different principles of displacement and mixing ventilation require different design approaches. The following sections first review current design approaches, and then discuss problems and limitations.

3.5.1 Mixing Ventilation

The jet formulae are the basic tools for mixing ventilation design. To ensure an acceptable level of thermal comfort and indoor air quality, designers use the jet formulae to predict the jet development in a space. The following parameters are used for designing a mixing ventilation system:

- Isothermal throw
- Maximum jet velocity in the occupied zone
- Separation distance for cold ceiling jets

The jet throw is a distance from the diffuser where the maximum jet velocity drops to a certain reference value called terminal velocity, which is in most cases 0.25 m/s (50 fpm). The throw can be determined from the jet decay formulae or from measurements. From Equation (3.7), the throw for the terminal velocity of 0.25 m/s, $T_{0.25}$, is:

$$T_{0.25} = x = K_1 \sqrt{A_0} \frac{u_0}{0.25} \tag{3.16}$$

where the centerline velocity decay constant K_1 varies from 1.1 to 7.0 (see section 3.3.2).

Many diffuser manufacturers usually provide tables with measured isothermal jet throw and sometimes additional correction factors for cooling and heating conditions. ASHRAE Standard 70 (1991) gives the instructions for the throw measurements, and recommends test room dimensions and diffuser positions. The recommended room is an empty space for the measurements of maximum isothermal throw. However, the boundary conditions for non-isothermal measurements are not specified. The setting of heat sources is arbitrary and has to be reported with the measured data according to the standard. The report should contain a detailed description of the test setup and the method of maintaining thermal loads. The measured non-isothermal throw is valid only for the tested heat fluxes. According to the design guidelines, the jet throw should be equal to the characteristic length, which depends on diffuser positions and type. The characteristic length is a distance from the diffuser to the place where the jet impinges on a wall or collides with other jets (ASHRAE 1997).

The purpose of performing the throw calculation is to ensure that maximum air velocity in the occupied zone is less than 0.25 m/s (50 fpm). Hence, direct calculation of the maximum air velocity in the occupied zone seems even better. An ideal solution is to

use a single formula to calculate the maximum velocity (Nielsen 1991). Some diffuser manufacturers provide diagrams to calculate the maximum jet velocity as a function of characteristic length and supply flow rate. However, the diagrams can be only used for free jets or wall jets before they deflect in the closest room corner. The next section (3.5.3) will describe jet deflection in corners and other complex phenomena that probably cannot be incorporated in a general formula for maximum velocity in the occupied zone.

Only a simple case, where jet can travel with no obstacles or deflections directly to the occupied zone, can use the velocity decay formula to evaluate the maximum air velocity. The reason for this is that the enclosure walls have crucial influence on the jet development and its parameters in the occupied zone. The throw measurements are performed in a test facility whereby the walls do not intercept with the jet. Therefore, measured throw data are a more reliable design criterion than measured maximum velocity in the occupied zone.

Separation distance is another design criterion for cold ceiling jets. The jet separation should be greater than the room characteristic length, otherwise, the cold jet may separate and cause draft problems. According to Equation (3.13), the separation distance, x_s, is proportional to the airflow rate Q, the temperature difference between jet and room ΔT, and the centerline velocity decay constant K_1. The shortest separation distance for design calculation should use the minimum flow rate the diffuser can deliver. The difference between the two extreme decay constants (for the compact jets from grille diffuser, K_1=5.7, and for the radial jets from circular ceiling diffuser, K_1=1.1) leads to a factor of 2.4 variation in the separation distance x_s.

Applying isothermal jet formulae to non-isothermal jets is possible if the buoyancy force is negligible compared to the momentum force. In fact, the momentum force is higher than the buoyancy force in the area close to a diffuser. With an increase of distance from the diffuser, the buoyancy force may become stronger than the momentum force. The local Archimedes number Ar_x seems to be a good criterion for the evaluation of non-isothermal jet behavior. The non-isothermal jets can be treated as isothermal jets if (Grimitlyn and Pozin 1993):

- Plane (linear) jets

$$\mathrm{Ar}_x = \frac{K_2}{K_1^2}\mathrm{Ar}_0\left(\frac{x}{H_0}\right)^{3/2} \le 0.15 \tag{3.17}$$

- Axisymmetric and radial jets

$$\mathrm{Ar}_x = \frac{K_2}{K_1^2}\mathrm{Ar}_0\left(\frac{x}{\sqrt{A_0}}\right)^{2} \le 0.1 \tag{3.18}$$

where x is the distance from the diffuser, K_1 is the centerline velocity decay constant, and K_2 is the centerline temperature decay constant (see Chapter 3.3.2 for more details).

Diffuser selection for non-isothermal conditions uses data for the isothermal jet throw although the buoyancy force cannot be neglected. The reason is that the non-isothermal throw depends on thermal boundary conditions. It is difficult to establish a database for non-isothermal throw design due to the huge number of possible thermal boundary conditions. Nevertheless, for cold jets a throw distance can be chosen from tables (ASHRAE 1997) to maximize the Air Diffusion Performance Index (ADPI) defined in ASHRAE 113-1990. ADPI specifies desired values for the local air velocities and temperature for people to feel comfortable in sedentary (office) occupations. In fact, the purpose of the room air distribution design is to create indoor air parameters in order for room occupants to feel comfortable. The ADPI criterion applies only for cooling conditions in mixing ventilation.

3.5.2 Displacement Ventilation

The displacement ventilation design cannot use criteria used for the mixing ventilation. The isothermal throw criterion is not suitable for the displacement ventilation, because the thermal plumes from heat sources are equally necessary for the displacement airflow field as the diffuser jet flow. Although the wall jet formulae for velocity agree with the measurements, the temperature distribution or stratification cannot be predicted (see section 3.4). Recently developed design guidelines for displacement ventilation (Chen et al. 1999) offer a design procedure. The design has to provide a temperature gradient lower than 3 K (5°F) between the head and foot level of a person.

Since the velocities in the occupied zone are very low with the displacement ventilation (see Figure 3.8(a)), low temperature stratification becomes a crucial design requirement. Therefore, a method for designing a displacement air distribution system should be able to reliably determine air temperature distribution in a space.

3.5.3 Limitations and Problems

The current methods for designing room air distribution system are primarily based on throw tables provided by diffuser manufacturers and jet formulae. This section will summarize the most important limitations and problems with the methods. The jet throw is normally measured under isothermal conditions in a large, empty room. The room should be sufficiently large so that it will not interfere with the jet development. The jet formulae are also developed for the jet main region in an empty room. Therefore, the jet formulae can not consider the following factors:

- The influence of room confinement on air distribution, such as
    - Non-stagnant environment
    - Corner deflection

- Jets with multiple attachments and partially attached jet

- Internal heat sources (distribution, temperature stratification)
- Internal partitions and obstacles

The room confinement influences jet development and its parameters in several ways. The stagnant environment assumption is not valid because the confined space creates a momentum exchange between the jet and the surrounding air. The exchange leads to a reverse flow in the environment, which influences jet development (Grimitlyn and Pozin 1993, Grimitlyn 1996, Karimipanah 1996). The confined jets have a higher rate of spread, and lower maximum velocities than jets in "infinite" enclosures. Therefore, the throw for an enclosure is lower than the one measured in test settings. Also, the jet regions are shorter for smaller enclosures (Tavakkol et al. 1994).

In a confined space, velocity decay is not a linear function of the distance from the jet origin. The jet decay formulae shown in section 3.3.2 cannot predict the centerline jet velocities (Sandberg et al. 1991). Grimitlyn and Pozin (1993) proposed a confinement correction factor, K_c, for the centerline decay constants, K_1 and K_2, that is a function of the diffuser type and area factor (free jet area divided by the room's cross sectional area at the same distance from the diffuser). The function has a Gaussian curve shape ($0< K_c <1$). Additional corrections are needed when a jet has a relatively high cross section compared to the room section because the position of exhaust openings becomes important due to the size of the recirculation zone.

Another important phenomenon in confined spaces is jet corner deflection (Sandberg et al. 1991). In a room's corners, the pressure increases and the jet decelerates due to an adverse pressure gradient. The jet then deflects and continues to flow along the perpendicular surface. After each deflection in a corner the jet first accelerates due to the higher pressure and reaches a maximum velocity and then decelerates before reaching the next corner. The jet deflection does not occur only in "long" rooms where a jet enters the terminal zone before reaching the opposite wall. Sandberg's experimental results for velocity decay along the room perimeter (see Figure 3.15) show a jet's redevelopment. Therefore, it is difficult to establish simple formula to connect supply air velocity with the maximum air velocity in the occupied zone. Currently, no jet formulae can predict jet flow with the corner deflections.

Jets with multiple attachments and partially attached jets are another group of problems that cannot be modeled with the available jet formulae. A jet issued close to two enclosure surfaces attaches to both surfaces as discussed in section 3.4. The jet profiles are different from those attached to a single surface. A partially attached jet develops neither attached nor free jet characteristics. The incomplete attachment is due to a large distance between the diffuser and the attached surface or due to the buoyancy that reduces the Coanda effect.

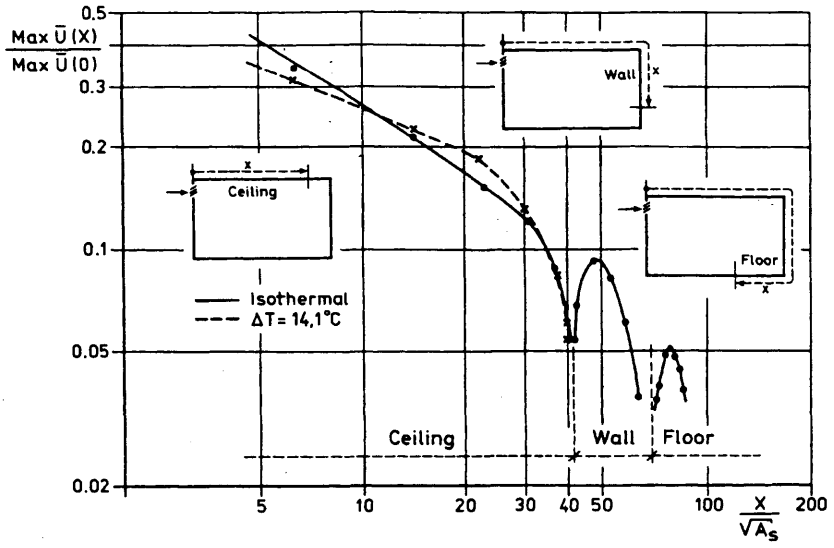

Figure 3.15. Maximum jet velocity along the perimeter of a room (Sandberg et al. 1991)

Internal heat sources can significantly impact non-isothermal jet behavior. The jet formulae for the jet trajectory, temperature decay and separation distance use the Archimedes number to account for buoyancy forces. In those formulae, the local temperature stratification is neglected and the room is assumed to have a single averaged air temperature. However, air temperature stratification could influence a jet's trajectory (Murakami et al. 1991). Heiselberg (1994) studied the impact of heat source distribution on the jet trajectory and found that concentrated heat sources have a greater impact on jet trajectory than distributed sources. A concentrated heat source close to the cold jet origin slows down the cold jet drop to the occupied zone. The distribution of heat sources is also a possible explanation for the disagreement between the measured temperatures and the calculated ones by the jet temperature formula (Nielsen 1992). A temperature formula has been developed for an empty space and cannot predict the profiles in a confined room with many heat sources (Jacobsen and Nielsen 1992, Amiri et al. 1996). In general, the jet velocity formulae perform better than the temperature formulae. A possible explanation is that the jet is the only momentum source in most indoor spaces but there are many heat sources.

Indoor environments usually contain many objects such as furniture, partitions, and equipment that may obstruct airflow in an occupied zone. An isothermal study (Nielsen J.R. et al. 1996) demonstrates that the obstacles in an occupied zone reduce the air flow velocity level in the entire room, and therefore the overall flow momentum is reduced. Also, the velocity profiles in the occupied zone have lower gradients, and even the ceiling attached jet has lower centerline velocities. If an obstacle in the jet's path is big enough, it can cause local jet separation (Awbi 1991). The jet can reattach if the obstacle is farther than a certain critical distance from the jet origin. The most severe influence of the obstacles on jet flow development is internal partitions such as acoustical screens for cubicles. A study for a typical office partition with a single supply and exhaust ceiling opening (Jouini et al. 1994) shows that the partition can prevent air

circulation in half of the space. Jet formulae are available for an obstacle in the jet path (Awbi 1991), but the jet formulae for more general cases with internal obstacles and partitions are not available.

These problems with jet formulae reduce their reliability and accuracy for designing room air distribution systems. Extensive experimental work must be performed to establish new formula coefficients for more complex cases. However, an attempt to lump so many factors into a single coefficient may be unsuccessful. Since room airflow is a result of the interaction of flow elements in the space, an approach to designing air distribution systems has to be universal for all flow elements. For example, partially attached jet flow usually depends not only on the diffuser's position in the confined space, but also on the cooling load, heat source distribution, and jet discharge angle. A universal approach for integrating all flow elements in a space for room air distribution design is the Computational Fluid Dynamics (CFD) method described in Chapter 2.

Older air distribution design guidelines are developed from the results obtained from small-scale and full-scale experimental chambers, while newer guidelines (Kirkpatrick and Elleson 1996, Chen et al. 1999) also use CFD results in their development. CFD replaces experimental measurements to collect data for the development of jet formulae and design guidelines. Using CFD as a design tool itself is an effective alternative. Therefore, the following sections will review current approaches and problems for CFD studies of room air distribution and diffuser jets.

3.6 Numerical Studies of Room Air Distribution

Several factors have contributed to the popularization of CFD study for indoor jet diffusion. The factors are limited boundary conditions treated with jet formulae and measurements, the development of computer technology, and the need for more effective air distribution systems. CFD study offers flexibility by imposing different boundary conditions for new air distribution systems. Although CFD is a popular tool for room airflow prediction, complex diffuser boundary conditions are difficult to impose. A large international research effort (Moser 1991) identified the simulation of air supply devices as one of the five most difficult problems in applying CFD to study room airflow. This has prompted researchers to bypass the CFD application in the design of room air distribution.

The reliability and accuracy of CFD simulation depends on several factors such as the turbulence model, the numerical scheme, and boundary condition modeling. Correct modeling of the supply air boundary condition is most crucial because the supply air momentum moves air in a space. Since a diffuser is much smaller than a room, to model the same detail for the diffuser and the room would require a very different length scale in the CFD modeling. Since the diffuser determines the initial jet flow characteristic, several researchers (Emvin and Davidson 1996, Chen 1996) have chosen to simulate detailed diffuser geometry. To model detailed diffuser geometry would require millions of grid cells, which need large amounts of computer capacity. On the other hand, to use the room length scale would ignore the details in the diffuser, which could introduce

errors in the numerical simulation. Therefore, an alternative solution is to develop a simplified but reliable method to simulate a diffuser while allowing the use of a room-length scale in CFD simulations.

3.7 Simplified Diffuser Boundary Conditions

Simplified methods to model diffuser airflow employ resultant momentum from the supply diffusers without modeling the detailed diffuser geometry. Those methods can be grouped (Fan 1995) in two basic categories:

- momentum modeling at the air supply devices
- momentum modeling in front of the air supply devices

The momentum modeling approach at the supply device imposes initial jet momentum, M_0, as a boundary condition for CFD simulations. On the other hand, the approach for momentum modeling in front of the supply device uses the momentum downstream from the diffuser, M_x. The approach that applies the momentum modeling at the air supply devices is relatively easy to use. This advantage is very important if the approach is used for indoor air distribution design since complex methods may introduce more problems than benefits in practice. On the other hand, the approach that models momentum in front of the air supply device uses jet formulae or measured data. Although this approach can apply some existing knowledge, the formulae can be applied only in special cases or when measurements have been performed. The special cases for using jet formulae are fully developed free or attached diffuser jets, assuming that formulae are available for that type of diffuser. Unfortunately, for many practical applications jets are neither free nor attached, and transition region tends to be big. Furthermore the jet's main region is already being influenced by room airflow. Therefore, application of the momentum modeling in front of the diffuser requires measurements in many cases.

To illustrate how the approach for momentum modeling at the supply device works, we use the following study conducted in the IEA Annex 20 as an example. The IEA study used a Hesco nozzle diffuser as shown in Figure 3.16. The diffuser has 84 nozzles arranged in four rows. Although each nozzle can be rotated freely, the study fixed all nozzles in one position: 40^{o} towards ceiling. The IEA study employed momentum modeling at the supply device with the following three variations:

- basic model (Heikkinen 1991)
- slot model (Heikkinen 1991)
- momentum model (Chen and Moser 1991)

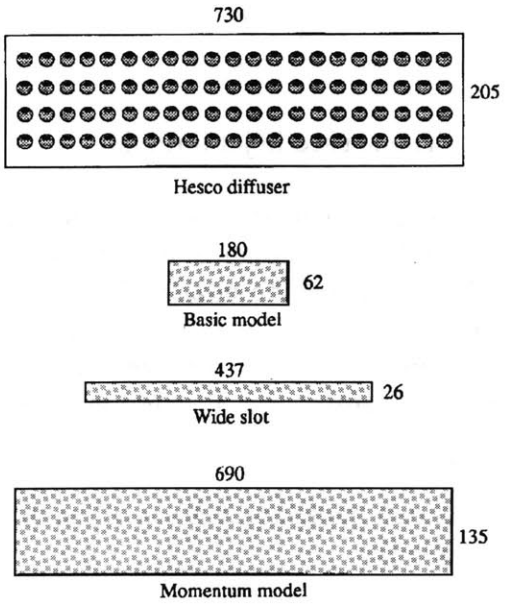

Figure 3.16 The approach for momentum modeling at the supply device

The basic model (Heikkinen 1991) concentrates all the nozzle openings into a simple slot, which has the same effective area and velocities as the diffuser as shown in the second figure in Figure 3.14. The model is easy to implement, and reasonably predicts room airflow patterns. However, by comparing the computed results with the measured data, the jet profiles and decay are not well predicted (Ewert et al. 1991). This method simulates the diffuser with a very small jet area, which limits jet spreading. Another study (Chen and Moser 1991) indicated that the basic method is not suitable for non-isothermal airflow.

Heikkinen (1991) proposed a wide-slot model (the third figure in Figure 3.16), which is a modification of the basic model. The diffuser was again presented with the same effective area, but the aspect ratio was different. The opening was wider in order to simulate a wider spread of the jet in the core region and higher jet entrainment. With the wide-slot model, the mixing in the core region was over-predicted and jet penetration was higher. Therefore, the wide-slot method is ineffective. It is unlikely that the model would yield satisfactory results for other type of diffusers.

Chen and Moser (1991) developed the momentum method that de-couples momentum and mass boundary conditions for the diffuser in CFD simulation. The diffuser is represented in the CFD study with an opening that has the same gross area, mass flux and momentum flux as a real diffuser (the last figure in Figure 3.16). This model enables specification of the source terms in the conservation equations over the real diffuser area. The air supply velocity for the momentum source term is calculated from the mass flow rate $\dot{m}$ and the diffuser effective area A_0:

$$U_0 = \frac{\dot{m}}{\rho A_0} \tag{3.19}$$

Note that the A_0 is the same as the one used in jet formula.

The momentum method has been validated with measured data for the nozzle and displacement diffusers. The model performance is very good for the displacement diffuser (Yuan et al. 1999). However, for the nozzle diffuser, the initial jet mixing and maximum jet velocities are over-predicted (Heikkinen 1991, Chen and Moser 1991). The application of it to displacement and nozzle diffusers indicates that the momentum method may be suitable for some diffusers but it is not universal. The method deserves further attention, and will be used in Chapter 5 for the other six types of diffusers.

The approach for momentum modeling in front of the diffuser has also been used in many studies. Its variation includes:

- box model (Nielsen 1989, 1997),
- prescribed velocity model (Nielsen 1989), and the
- diffuser specification model (Huo et al. 1996)

The box model (Nielsen 1989, 1997) represents the diffuser boundary conditions in an imaginary box surface around the diffuser. The flow field within the box is ignored. An example of the box method shown in Figure 3.17 illustrates how the method imposes boundary conditions for a nozzle diffuser. One of the box surfaces uses jet profiles as boundary conditions while the others use a free boundary with zero gradients for flow parameters (see section 2.4). To specify the boundary conditions, suitable jet formulae should be applied or air velocity, temperature and gas concentration profiles must be measured. Results obtained from the box method are in good agreement with measured data (Nielsen 1997). However, in another study (Heikkinen 1991) the box method over-predicted the maximum jet velocity more than other simplified methods. Another problem with the box model is determining the box size. The box should be sufficiently large to have the boundaries in the fully developed jet region where the velocity and temperature profiles are similar. On the other hand, the box has to be small enough to avoid the impact of room air recirculation and thermal plumes on the jet.

To avoid the problem with the box size and the specification of temperature and gas concentration profiles, Nielsen (1989) developed the prescribed velocity model. The model also uses jet theory or measured data for the diffuser's flow specifications, but the space between the diffuser and the profile location is included in the calculation domain. At the supply opening, the boundary conditions are specified with the basic model. In a small volume placed in front of the diffuser, the calculated profiles are fixed and updated as boundary conditions (see Figure 3.17). The update can be on two velocity components in two perpendicular planes (Nielsen 1989) or one velocity component in one plane (Heikkinen 1991). The results show better agreement with the measured data than the basic model (Skovgaard and Nielsen 1991, Svidt 1994).

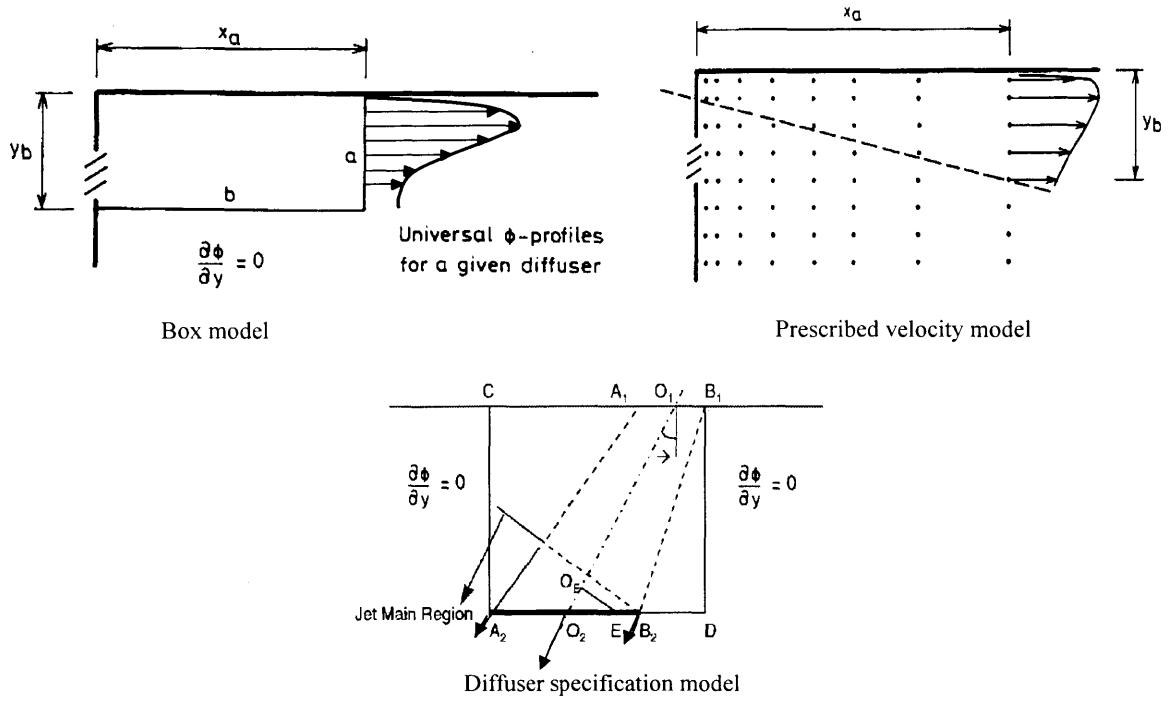

Figure 3.17 Methods for momentum modeling in front of the diffuser

The diffuser specification model (Huo et al. 1996) is another modification of the box model. The model uses the jet formulae (jet profiles, decay and trajectory); no measured data are needed to specify the boundary conditions. The use of the jet formulae has the advantage of employing existing knowledge, and the disadvantage of inheriting the problems described in section 3.5.3. For example, the partially attached jets that are common in air distribution systems cannot be simulated, and many diffusers do not have jet formulae coefficients. The method was tested for two two-dimensional and one three-dimensional airflow systems. The comparison with the measured data was mostly qualitative. The box size has to be carefully determined for the same reason as for the original box method. If the method is for more general applications further validation is needed.

The above literature review reveals that no simplified method is clearly superior. Nevertheless, it is possible to select models that are more general in their theory. From the first group of methods, which model diffusers at the air supply diffuser, the momentum method seems most promising. From the second group of methods, which model resulting flow fields in front of the diffusers, the box method seems most appropriate. The following section explains why the two methods are most appropriate.

The momentum method appears more favorable since it has shown some good results. The basic model was eliminated because many studies have demonstrated that the model does not predict the room airflow parameters (Ewert et al. 1991, Svidt 1994,

Cheong et al. 1999). Also, the wide slot method is not general enough as described above.

The momentum method performed better than the other two methods for modeling at the diffuser surface in Heikkinen's (1991) study that compared the simplified models. The momentum method, according to Heikkinen, could be used more generally, but further validation is necessary. Emvin and Davidson (1996) applied the following four methods to simulate a nozzle diffuser: basic, momentum, box (simplified methods) and full resolution method, the later of which is a detailed simulation of the diffuser geometry. They concluded that no simplified method provides satisfactory results. Furthermore, they have been especially critical of the momentum method due to possible numerical errors. The next chapter provides detailed analysis and recommends solution for numerical problems with the momentum method.

Emvin and Davidson (1996) used the full resolution method since they were not satisfied with performance of the simplified methods. The full resolution method uses the local grid refinement to geometrically represent all of the nozzles. They used three levels of refinement, and gave each nozzle a 2x2 grid distribution. Figure 3.18 shows their result for the basic model and the full resolution model. In this case, the basic model provides the correct flow pattern compared to the smoke visualization, but the velocity magnitudes are incorrect. However, the full resolution method obviously did not correctly predict the airflow pattern since there was no recirculation zone in the upper left corner. Therefore, the application of the full resolution model may not be a reliable design tool even though the computing effort is significant. The simplified methods are still more desirable due to the low computing effort needed and diffuser modeling.

The box method in the second group of simplified models does not require calculations of the areas close to the diffuser, where very fine grids might be required to properly simulate the jet development and initial mixing. This provides for faster calculations and better numerical stability. The disadvantage of specifying an additional profile for temperature and concentration for the box method can be overcome by performing heat and species balance at the box boundaries. The box method requires measured data in some cases. If it can produce more accurate results, the approach is recommended. On the other hand, the prescribed velocity method requires calculations in the area close to the diffuser, and needs a measured velocity profile if jet formulae are not available. Finally, the diffuser specification method uses only jet formulae and hence cannot model some important design cases. Also, this method is a special case of the box method. Therefore, the box method is selected in the group that models the jet momentum in front of the diffuser.

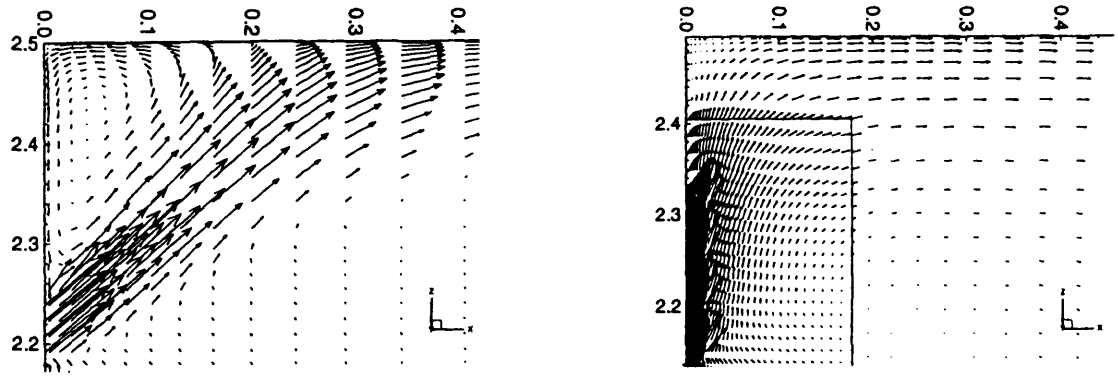

Figure 3.18 Computed results (a) with the basic model and (b) with the full resolution model (Emvin and Davidson 1996)

The box and momentum methods will be further studied and validated for the eight diffusers tested for the jet formulae applications (see Section 3.4). The CFD simulations of supply diffusers should be developed further to become a reliable air distribution design tool since the current design methods have limitations as discussed in this chapter. Chapter 4 will be devoted to the development of simplified diffuser modeling for CFD.

CHAPTER 4

SIMULATIONS OF COMMONLY USED AIR SUPPLY DIFFUSERS

4.1 Introduction

This chapter reports the results for different types of air supply diffusers simulated by imposing simplified boundary conditions for them. The computed results are then validated with the measured data of the airflow parameters obtained from a full-scale environmental chamber. The aim of the study is to propose a simple method with good accuracy in presenting complex diffusers. Section 3.6 has reviewed the simplified methods available in the literature and found that two methods, the momentum and box methods, are promising and have good potential for further study. Therefore, the two methods are used in this chapter.

The momentum method specifies mass, momentum, energy and concentration at the supply diffuser surface, while the box method specifies the profiles of those parameters at a certain distance in front of a diffuser. Both methods avoid detailed representation of the diffuser geometry and model a resulting flow. The simulations with the simplified diffuser modeling should provide information on indoor airflow parameters. It is similar to the jet formulae described in Chapter 3 that model different diffusers to determine resulting airflow field. However, the CFD simulations used in this chapter would provide more detailed information.

To predict jet behavior, the jet formulae assume a constant jet momentum along its path of development. Namely, the formulae assume the initial jet momentum M_0 is the same as the momentum M_x at position x from the diffuser. However, the jet flow in front of the diffuser can involve momentum losses due to jet mixing. In fact, if a diffuser issues several separate jets, such as the nozzle diffuser, the jets will merge in front of the diffuser as one shown in Figure 4.1. Close to the diffuser surface, the jets are separated by low-pressure recirculation zones that are characteristic for the converging region of this jet flow. The jets then merge in one, and form combined single jet. Figure 4.1 shows how two parallel plane jets issued from the two slot openings merge and develop into one (Lai and Nasr 1998). For diffusers, the size of the converging and merging regions can be smaller than the grid size used in CFD. Therefore, the recirculation and corresponding momentum loss cannot be accounted for in a CFD calculation. The momentum method would not be able to account for the loss, while the box method excludes the problem because the method does not solve flow in the regions.

The box method avoids some of the problems the momentum model has, but on the other hand requires much more time for imposing the boundary conditions. The current box method also needs some measured data for all the parameters simulated. Therefore, the momentum method is preferred, as it is easier to implement in a CFD simulation. The box method will be recommended for the diffusers that the momentum method might not be able to simulate.

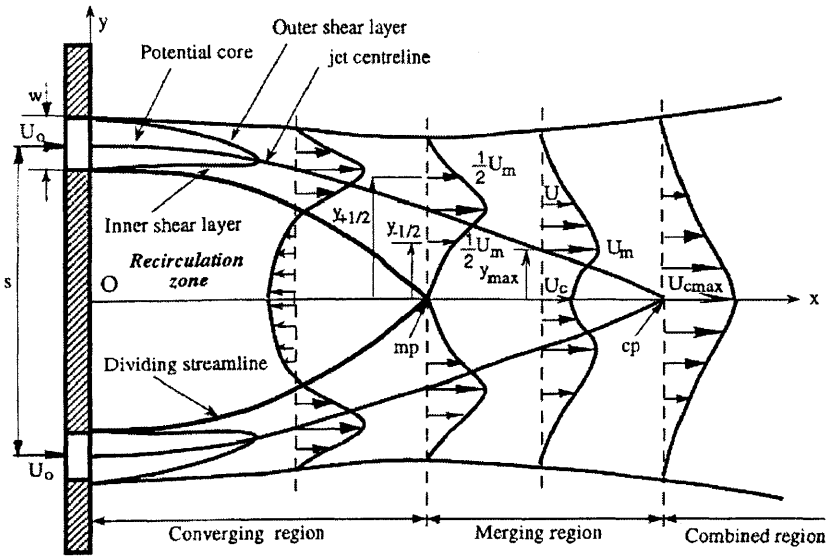

Figure 4.1 The development of two parallel plane jets (Lai and Nasr 1998)

The momentum method requires the following data when it is used in a CFD simulation:

- airflow rate
- discharge jet velocity or effective diffuser area
- supply turbulence properties
- supply temperature and contaminate concentration

In the same CFD simulation, the box method needs the information on:

- distribution of air velocities
- turbulence properties
- distributions of temperature and contaminate concentration

In order to test the two methods to obtain solid conclusions, many different diffusers commonly used in real air distribution systems should be studied. Different types of diffusers generate different airflow distributions, and may have fundamental differences in the jet flow structure. Therefore, it is not sufficient to validate the simplified methods with only two or three types of the diffusers. The current study will investigate the following eight different diffusers:

- Nozzle diffuser
- Slot (linear) diffuser
- Valve diffuser
- Displacement diffuser

- Round ceiling diffuser
- Square ceiling diffuser
- Vortex diffuser
- Grille diffuser

Chapter 3 has described the performance of jet formulae for the prediction of airflow in rooms with those eight diffusers. In general, the application of jet formulae to predict jet flow in confined spaces is difficult and sometimes impossible. CFD simulation of supply diffusers may provide more general and reliable jet flow from a diffuser and room air distribution.

To ensure a general presentation of the diffusers on the market, the eight diffusers are selected from six different manufacturers. The manufacturers are Hesco (Switzerland), Stork Air (The Netherlands), Krueger (AZ), Metal Air (FL), Halton (KY) and Trox (Germany). The manufacturer catalogues provide diffuser geometry, installation instructions, throw data, pressure drop and noise criteria. Some of the catalogues also have additional information on diffuser aerodynamic performance and effective area that is an important parameter for our study.

The CFD validation should use accurate data. Some fine measured data for the nozzle diffuser (IEA 1993), the valve diffuser (Chen and Jiang 1996), and the displacement diffuser (Yuan et al. 1999, Livchak 1999) seem sufficiently good and therefore are used in the present investigation. For the other five diffusers, we have performed detailed measurements in our environmental chamber. Also, the measurements for the displacement diffuser have been repeated as a check on our experiment. The following section discusses how the data are obtained from our chamber.

4.2 Full-scale environmental test facility

The airflow pattern and the distributions of air velocity and temperature were measured in a full-scale environmental test facility as shown in Figure 4.2. The facility consists of a well-insulated box (thermal resistance = 30 ft^2 °F h/Btu or 5.3 m^2K/W) with a partition wall that divides the box into a test chamber and a climate chamber. Each chamber has a separate air-handling system. The wall between the test and climate chambers has a double-glazing window as wide as the room. The temperature, relative humidity, and air supply rate was controlled in both chambers. The climate chamber was used to simulate the outdoor climate. The test chamber, 17 ft (5.16 m) long, 12 ft (3.65 m) wide, and 8 ft (2.43 m) high, simulates the indoor environment. The six diffusers can be installed in the chamber at positions shown in Figure 4.3, where the dashed lines denote cross sections of middle planes in the chamber.

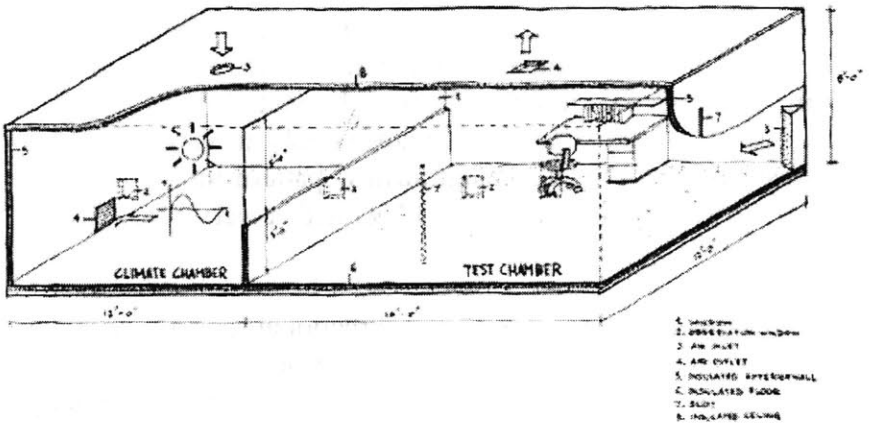

Figure 4.2 Dimensions and sketch of the test chamber

The major measuring equipment of the test facility used for the present study includes:

- A flow visualization system by smoke for observing air flow patterns
- A hot-sphere anemometer system for air velocity and temperature measurements
- A thermocouple system for measuring wall and air temperatures
- A tracer-gas system for measuring concentration

The test chamber has two long vertical slots and several observation windows on the walls. Light penetrates through the slots and forms a thin light sheet. By injecting smoke into the room, the airflow pattern was observed through observation windows normal to the light sheet. The test facility has two types of smoke sources, a theater fog

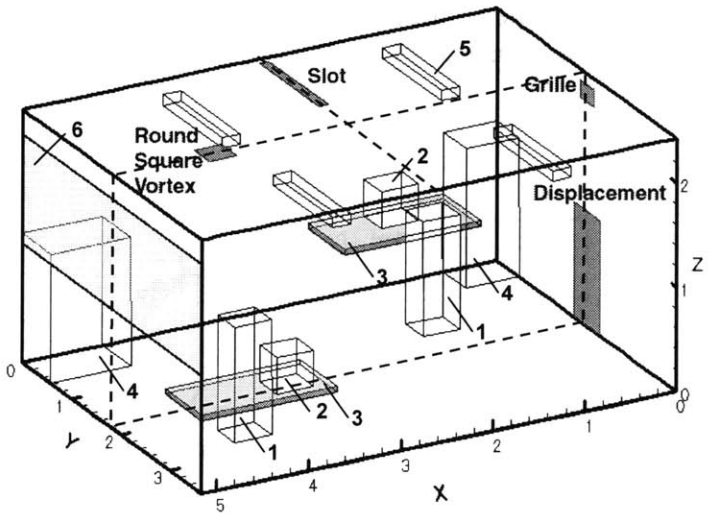

Figure 4.3 Positions of the supply diffusers in the test chamber
(person - 1, computer - 2, table - 3, cabinet - 4, fluorescent lamp - 5, window - 6)

generator and an air current kit. The theater fog generator produces smoke with a temperature far above the environmental temperature. The smoke was cooled through a long tube before entering the room to approach neutral buoyancy. This generator produced a large amount of smoke to observe how supply air was distributed in the room. However, this was not ideal for visualizing airflow pattern in a particular area. The air current kit remedied the problem. The kit generated a very small amount of smoke locally.

The hot-sphere anemometers with omni-directional sensors are widely used for air velocity, velocity fluctuation, and air temperature measurements. The test chamber has 30 hot-sphere anemometers for simultaneous measurements of the air velocity. This device has two velocity sensors, heated and unheated, shown in Figure 4.4. The heated sensor generates natural convection that could be the same order of magnitude as the measured velocity itself. The convection has a negative impact on the data accuracy. Lower overheating temperatures for the sensor have positive impact on accuracy due to decreased natural convection, but at the same time negative impact on the dynamic response of the instrument (Popiolek 1998). Besides the natural convection and dynamic response, other important characteristics of low-velocity anemometers are static calibration (accuracy and positioning), directional sensitivity, accuracy of temperature compensation, sampling rate, upper frequency and impact of the probe protection (Melikov et al. 1998). All of these characteristics are important for the velocity and temperature measurement accuracy. The appendix A gives a detailed evaluation of measurement accuracy for the hot-sphere anemometers presented in Figure 4.4 and used in our experiments (Melikov 2000).

ASHRAE Standard 55 specifies the low-velocity range to be between 0.05 and 0.5 m/s (10 and 100 fpm) and requires an accuracy for the mean velocity measurements of ±0.05 m/s (±10 fpm). Typical air velocities in the occupied zone are often lower than 0.25 m/s (50 fpm) because of the comfort requirements. With the accuracy defined by the ASHRAE standard, the data measured by the anemometers could have high measurement

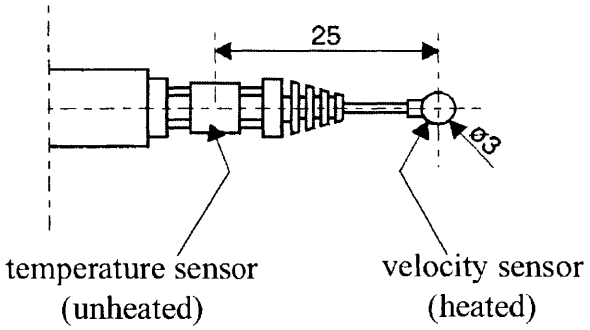

Figure 4.4 The hot-sphere anemometer with omni-directional sensor (dimensions in mm)

uncertainty. New requirements and guidelines for low velocity measurements have been developed and suggested for inclusion in future standards (Melikov et al. 1998). Regardless of the problems, hot-sphere anemometers are still widely used instrument for air velocity and temperature measurements. The reason is relatively low cost of hot-sphere anemometers compared to the other available instruments such as laser Doppler anemometers.

The repeatability of the velocity measurements with our anemometers is 0.01 m/s (2 fpm) or ±2% of readings. Since the probe size is relatively large (3mm, 1/8 in), the probes are not sensitive to high frequency velocity fluctuation. The errors of velocity fluctuation measurements are difficult to estimate. The measuring errors for air temperature are ±0.8 °F (±0.4 K), including the errors introduced by the data acquisition systems. The wall and air temperature measurements with the thermocouples and data logger system have the same errors as the anemometers. The measurements of air temperature either by anemometers or thermocouples are reliable. The air temperature fluctuations are small in the steady-state condition that should be reached before the measurements take place. An important consideration for temperature measurements is the radiation effect. The surface of probes should be highly reflective in order to minimize the radiation from enclosure surfaces to the temperature sensors. Our sensors are vacuum covered with a special aluminum coating that also increases their resistance to contamination.

The tracer-gas system is a gas analyzer controlled by a microprocessor. The gas analysis is based on a photoacoustic infrared detection method that enables measurements of different tracer gases that absorb infra red light. The study uses 1% of SF_6 mixture with air because the background concentration of SF_6 in atmosphere is almost zero. The gas detection threshold is around 10^{-3} ppm. The system accuracy is ensured by compensation of temperature fluctuations, water vapor and interference caused by other gases. The repeatability for concentration measurements is 1% of measured value.

4.3 Experimental Conditions

The full-scale environmental test facility and its major measuring equipment described in the previous section are used to measure air distribution in the chamber with the six diffusers. The hot-sphere anemometers are attached to movable poles. Each of five poles supports six anemometers that measure air velocities and temperatures in 30 points simultaneously. Additionally, two thermocouples are affixed to the poles to measure air temperatures near the floor and ceiling. A total of 40 thermocouples are attached to the floor, ceiling, window and walls to measure the surface temperatures. The tubes for sampling the tracer gas (SF_6) are also fixed to the poles at the same location as that for the anemometers.

The test chamber is arranged to simulate a two-person office. Each has a computer, a table and some furniture. Our experiment was conducted for a summer condition. The air temperature in the climate chamber is controlled to be 35°C (95°F). The measurements are conducted under steady-state conditions by stabilizing the room

thermal and fluid conditions for more than 12 hours before recording the data. The data were collected in one plane through the entire chamber as well as close to the diffusers. Figure 4.5 presents positions for the five poles that carried anemometers and tracer gas sampling tubes for the measurements through the entire chamber. The measurements for the displacement, square, round vortex and grille diffuser had poles positioned in the shown middle cross section (Figure 4.5(a)). On the other hand, the poles for the slot diffuser measurements were positioned in a plane closer to the diffuser as shown in Figure 4.5(b).

The flow boundary conditions for supply and return diffusers are given in Table 4.1. The flow rates are in the range usually applied for mechanical ventilation of small office spaces. The supply velocities for the same flow rates vary from diffuser to diffuser since the effective areas of diffusers are different. Table 4.2 presents values of the internal heat sources that are the same for all experiments. However, the return air temperatures vary since the total internal heat gains are not constant. The variable part of the cooling load is a result of the different flow conditions and slightly different temperatures on the wall and window between the climate chamber and the test chamber. The cooling load (see Table 4.3) depends on the flow rates, diffuser position and jet flow conditions.

In order to simulate indoor air quality, each human simulator had a point source of tracer gas (SF_6) attached to the center of the simulator's top surface. The tracer gas is used to simulate contaminants released from the two occupants. The SF_6 flow rate for each person is $0.03128 \times 10^{-6}\ m^3_{SF_6}/s$.

With the described experimental facility, one could measure the airflow pattern and the distributions of air velocity, temperature, and tracer-gas concentration. The detailed data are available in a report (Chen and Srebric 2000). The data are useful to validate the two methods that simulate the six diffusers.

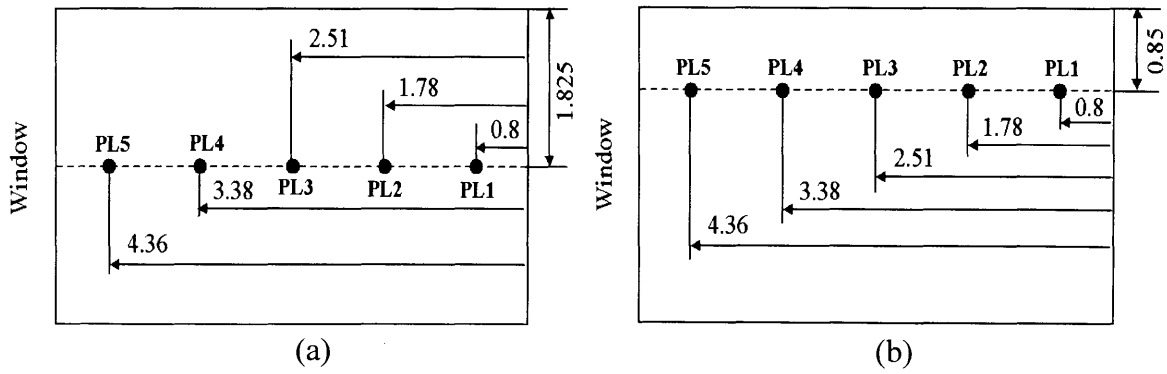

Figure 4.5 The pole positions (in meters) for the measurements in the middle of the chamber for (a) five diffusers (b) slot

Table 4.1 Flow boundary conditions for different experiments

Diffusers	Air Exchange Rate ACH (cfm)	Supply Air Velocity fpm (m/s)	Supply Air Temp in Duct °F (°C)	Supply Air Temp from Inlet °F (°C)	Exhaust Air Temp °F (°C)
Slot (Linear)	9.2 (249)	768 (3.90)	61 (16.20)	61 (16.31)	70.5 (21.4)
Displacement	5.0 (135)	70 (0.35)	55 (13.00)	57 (14.00)	72 (22.2)
Round Ceiling	5.0 (135)	705 (3.58)	61 (16.06)	61 (16.27)	76.6 (24.8)
Square Ceiling	4.9 (132)	1024 (5.20)	58 (14.50)	58.5 (14.70)	75.4 (24.1)
Vortex	5.1 (138)	1476 (7.50)	61 (16.35)	61 (16.35)	76.6 (24.8)
Grille	8.0 (216)	429 (2.18)	61 (16.23)	61 (16.33)	72 (22.3)
	5.0 (135)	276 (1.40)	59 (15.06)	59.5 (15.25)	76 (24.5)
	3.0 (81)	169 (0.86)	51 (10.62)	51 (10.71)	77.5 (25.3)

Table 4.2 Internal heat sources that are constant for all experiments

Internal Heat Sources*	Btu/hr (W)
Each human simulator	256 (75)
Computer 1**	590 (173)
Computer 2	368 (108)
Each fluorescent lamp	116 (34)
TOTAL	1935 (567)

*the climate chamber temperature was controlled at 95°F (35°C)
**(close to the window)

Table 4.3 Total heat transfer for different experiments

Diffusers	Cooling Load Btu/h (W)	Internal Heat Sources Btu/h (W)	Heat Gain from Partition* Btu/h (W)
Slot (Linear)	2515 (737)	1935 (567)	580 (170)
Displacement	2395 (702)	1935 (567)	460 (135)
Round Ceiling	2286 (670)	1935 (567)	351 (103)
Square Ceiling	2474 (725)	1935 (567)	539 (158)
Vortex	2276 (667)	1935 (567)	341 (100)
Grille	2525 (740)	1935 (567)	590 (173)
	2484 (728)	1935 (567)	549 (161)
	2296 (673)	1935 (567)	361 (106)

*Partition is the surface that simulates external wall and window.

4.4 Turbulence Modeling for Jet Flow Simulations

The turbulence modeling for different airflow simulations has been discussed in Chapter 2. The RNG k-ε turbulence model is used in this investigation. The reason is that the two-equation turbulence models are most popular for indoor environment simulations. According to Chen (1995), the RNG k-ε turbulence model is the best among several turbulence models he tested for indoor airflow.

For the two-equation turbulence models, the turbulence parameters needed at the supply are the kinetic energy k_0 and dissipation rate ε_0. Joubert et al. (1996) studied the influence of the supply turbulence boundary conditions on the CFD simulations. They applied three different formulations for the supply turbulent kinetic energy and dissipation rate, and found no influence on the simulation results (mean velocity and turbulent kinetic energy). They also studied the impact of different supply turbulence intensity (Ti = 4%, 9%, 14% and 37.4%) and also found no impact on the calculation results. This is indeed good news, since in most cases the inlet turbulence parameters are not known. In our simulations, the following formulations of the supply turbulence parameters are used:

$$k_0 = \frac{3}{2}(\mathrm{Ti} \times U_0)^2 \tag{4.1}$$

$$\varepsilon_0 = \frac{C_\mu^{3/4} k_0^{3/2}}{l_0} \tag{4.2}$$

where U_0 is the supply velocity, Ti =10% is the turbulence intensity, C_μ = 0.09 is the empirical constant, and l_0=0.1L is the length scale. L normally equals to the characteristic length of the diffuser such as the width of the slot diffuser.

Joubert et al. (1996) also studied the influence of the supply jet profiles on the calculated parameters. Two different supply velocity profiles, flat and parabolic (top-hat), gave the same mean velocities and airflow pattern. However, the profile shape influences the calculated values of the turbulent kinetic energy. Furthermore, another study of the jet flow with LES and DNS (Jacobitz et al.1997) have shown that even the fluctuations of the supply velocity are important factor for the calculation of the turbulent kinetic energy. Therefore, more accurate calculations of the turbulent kinetic energy require LES or DNS that uses time-dependent supply velocity profiles. This approach is not realistic for the design at present due to high computing power and significant calculation time. Nevertheless, the airflow pattern and mean velocities are not influenced by the supply jet profile. Therefore, our study will use the averaged flat profiles as the approximation for the supply velocity from complex diffusers.

4.5 Diffuser Simulations

4.5.1 Nozzle Diffuser

The nozzle diffuser is the one used for validation exercises in International Energy Agency (IEA) Annex 20 project (Air Flow Patterns within Buildings, 1993). The diffuser consists of 84 small round nozzles arranged in four rows in an area of 0.71 m × 0.17 m (28 in. × 6.7 in.). Each nozzle has a diameter of 11.8 mm (1/2 in), and the total airflow area for all nozzles is 0.0092 m^2 (0.1 ft^2). The flow direction of each nozzle is adjustable. The IEA study adjusted all the nozzles 40° upwards (see Figure 4.6(a)). The test room is 4.8 m (15.8 ft) long, 3.0 m (9.8 ft) wide, and 2.5 m (8.2 ft) high. The supply diffuser and exhaust diffusers are installed close to the ceiling in the center of the shorter wall as shown in Figure 4.6(b). The exhaust size is 0.2 x 0.3 m^2 (0.66 x 0.98 ft^2). The supply and exhaust diffuser position creates a symmetrical airflow within the room with the symmetry plane running through the diffuser.

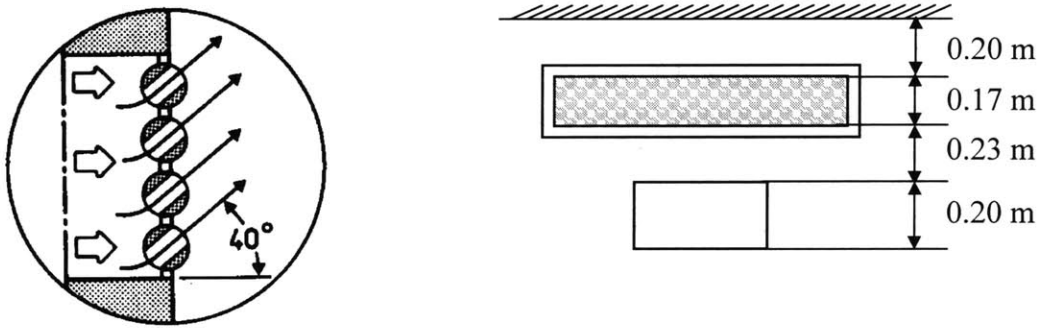

(a) (b)

Figure 4.6 The position and orientation of the nozzle diffuser installed in the IEA study

The measurements have been performed under isothermal and non-isothermal conditions in the symmetric plane. The isothermal case was measured by several research groups (Ewert et al. 1991, Sandberg et al. 1991, Heikkinen 1991). Our study uses the data from Ewert et al. (1991), since the data were obtained by a laser Doppler anemometer (LDA). LDA is more reliable than omni-directional hot-film or hot-sphere anemometers. Also, LDA measures more detailed flow information, such as the velocity components in three directions with which the flow direction can be determined. The velocity direction measured by LDA is more precise than that with the smoke visualization.

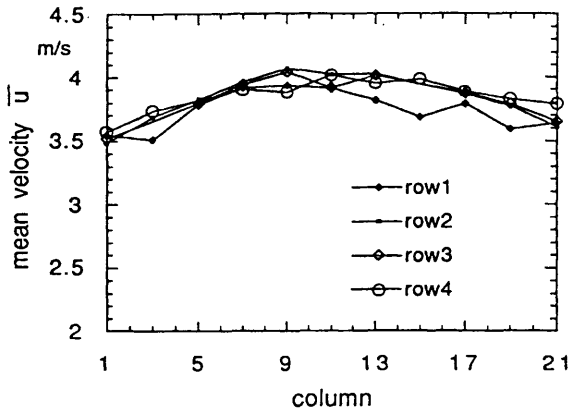

Figure 4.7 The discharged velocities measured for each of the 84 nozzles (4 rows of 21 nozzles) (Ewert et al. 1991)

The supply airflow rate was 0.0315 m^3/s (67 cfm), corresponding to an air change rate of 3 ACH. The maximum jet velocity at the supply plane was on average 3.8 m/s (760 fpm), see Figure 4.7. The decay of this supply velocity is very fast due to the merge of the 84 small jets. This merging phenomenon is similar to that with the two parallel plane jets as shown in Figure 4.1, but the distance between openings is much smaller. Figure 4.8 presents the measured velocity and flow pattern visualization in the symmetry plane (Heikkinen 1991). The size of the recirculation zone is approximately 0.2 x 0.2 m (0.66 x 0.66 ft). The maximum jet velocity drops to 1.5 m/s (300 fpm) in approximately 0.1 m (0.33 ft) from the diffuser, where the small jets already are combined into a large one. The momentum loss measured in front of the diffuser is approximately 14% of the total momentum (Heikkinen 1991). Hence, the momentum is not conserved.

The measurements along the room perimeter show that the jet develops into the attached jet at a certain distance from the diffuser. Figure 3.6 shows an excellent agreement between the attached jet profile as computed and the measured data. However, the profile is at a distance of 2.2 m (7.2 ft) from the diffuser. The distance is too large if the box method should be used since the box would cover a half of the ceiling length.

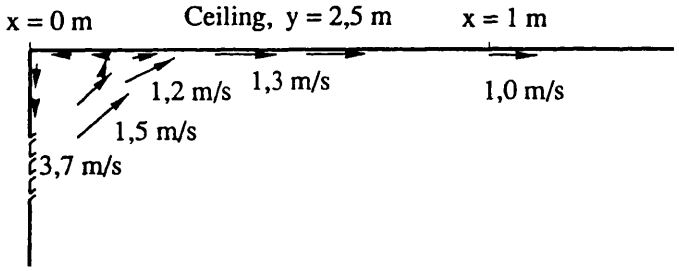

Figure 4.8 Airflow pattern visualized with smoke in the symmetry plane (Heikkinen 1991)

Our study uses the momentum method to simulate the nozzle diffuser with a supply airflow rate of 0.0315 m^3/s (67 cfm) and discharge velocity of 3.8 m/s (760 fpm) directed 40° towards the ceiling (see Figure 4.9(a)). The simulations have been performed for a half of the room since the airflow is symmetric. Figure 4.10(a) shows the calculated flow field in the area close to the diffuser with momentum method and a grid resolution of 50×32×35. There is no recirculation in the upper left corner, and the jet spreads very rapidly in the region after the attachment to the ceiling. In contrast, the experiment shows in Figure 4.8 a recirculation due to the Coanda effect on the left upper corner. We have further calculated with finer grid resolutions, for the entire room, and for just a small flow domain close the diffuser. All of the simulations fail to predict the recirculation.

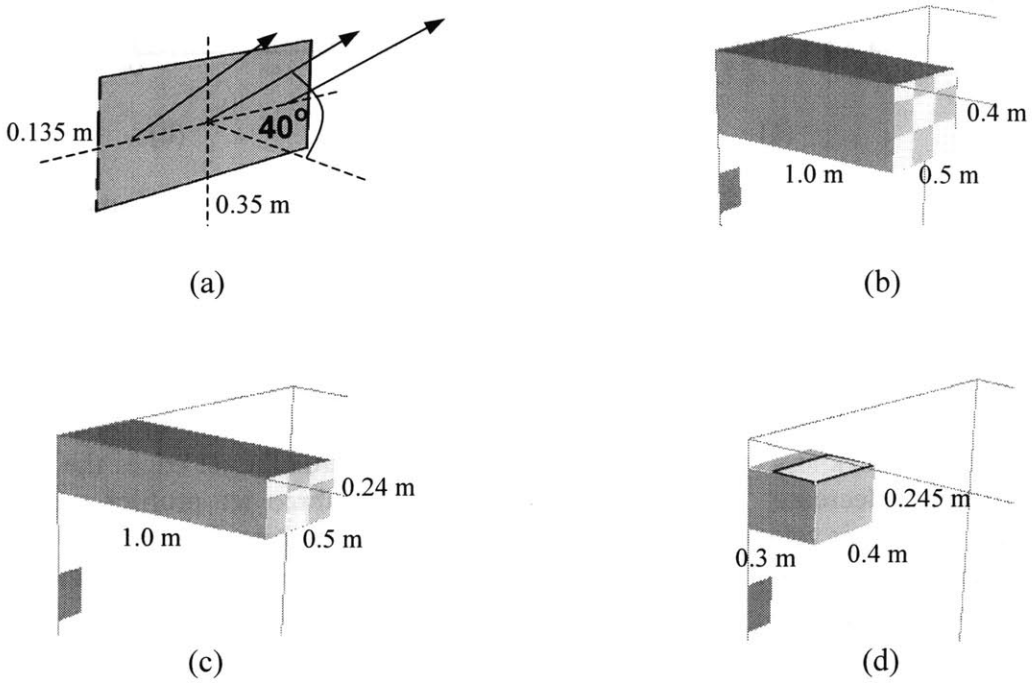

Figure 4.9 Simulation of the nozzle diffuser with (a) the momentum method (b) the box method (c) the small box and (d) the tiny box method

If the box method is used, the box is normally larger than the domain with the recirculation. Therefore, the calculation with the box method does not need to handle this flow area that is difficult to predict. However, the box method needs measured data to set the boundary conditions since the air jet formulae do not work for this diffuser and cannot be used to generate boundary conditions for the CFD simulation. The reason why the jet formulae do not apply is because the jet is not fully attached in the vicinity of the diffuser. Although the jet can develop to a fully attached jet at a distance of 2.2 m (7.2 ft) from the diffuser, the box would cover a quarter of the room that is too large. With such a large box, the impact of the room size, internal heat load, internal obstacles, etc. on the airflow cannot be accurately account for.

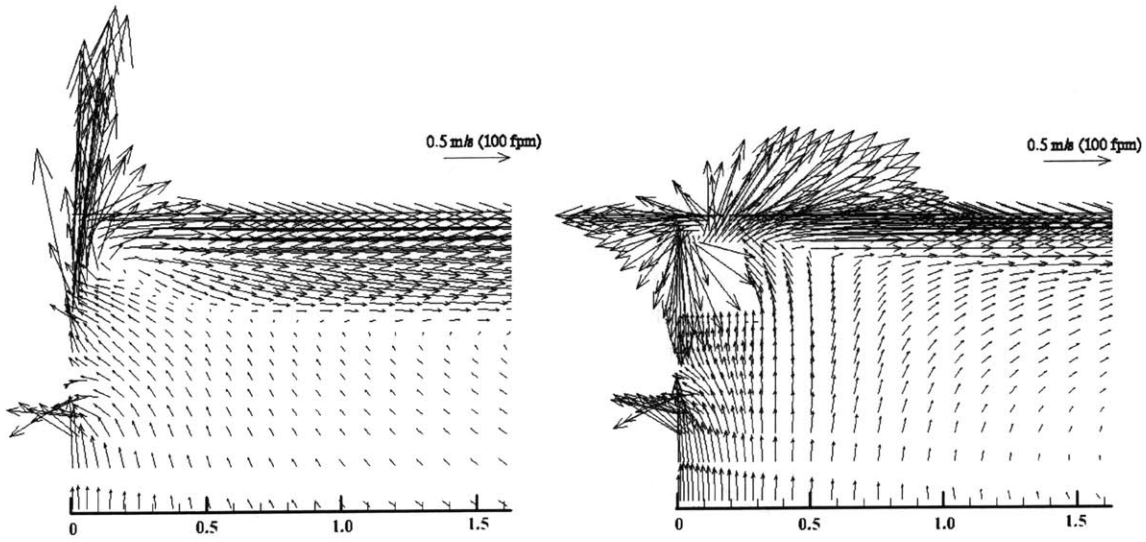

(a) (b)

Figure 4.10 The calculated flow field with (a) the momentum method (b) the tiny box method

The measured velocity as shown in Figure 4.11 is used to set the boundary conditions for the box method. The velocities are measured close to the ceiling at 1.0 m (3.3. ft) in front of the diffuser. The presented profiles shows that the jet had highest velocities and thickness in the symmetry plane, and towards the jet edges the velocities and thickness decrease. For our box simulations, the three jet profiles are used to calculate supply air velocities for the supply box patches illustrated in Figure 4.9(b). The supply box surface has 3×3 supply patches that use averaged profile velocities for the represented area.

The box size used is only 1.0 m × 0.5 m × 0.4 m that is small and is the same as the one other researchers used (Nielsen 1988, Heikkinen 1991, Ewert et al. 1991). With the box size, the velocity profile in the front surface is described as the boundary conditions for the CFD simulation. The boundary conditions for all the variables at all other surfaces are assumed to be zero-gradient. Figure 4.12 shows a good agreement between the calculated results and the measured data at 2.2 m (7.2 ft) from the diffuser. Note that comparison between the calculated results and the experimental data at 1.0 m from the diffuser is not possible, because the box size is the same as the distance. The figure shows also the profiles calculated with the momentum method. Although the method fails to predict the recirculation, it can predict even better velocity profiles.

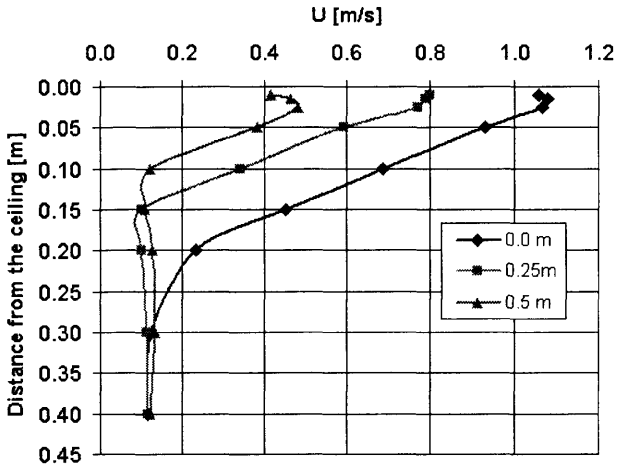

Figure 4.11 The measured velocities 1.0 m (3.3 ft) in front of the diffuser and at certain distance from the symmetry plane (0, 0.25 and 0.5 m; 0, 0.82, 1.64 ft)

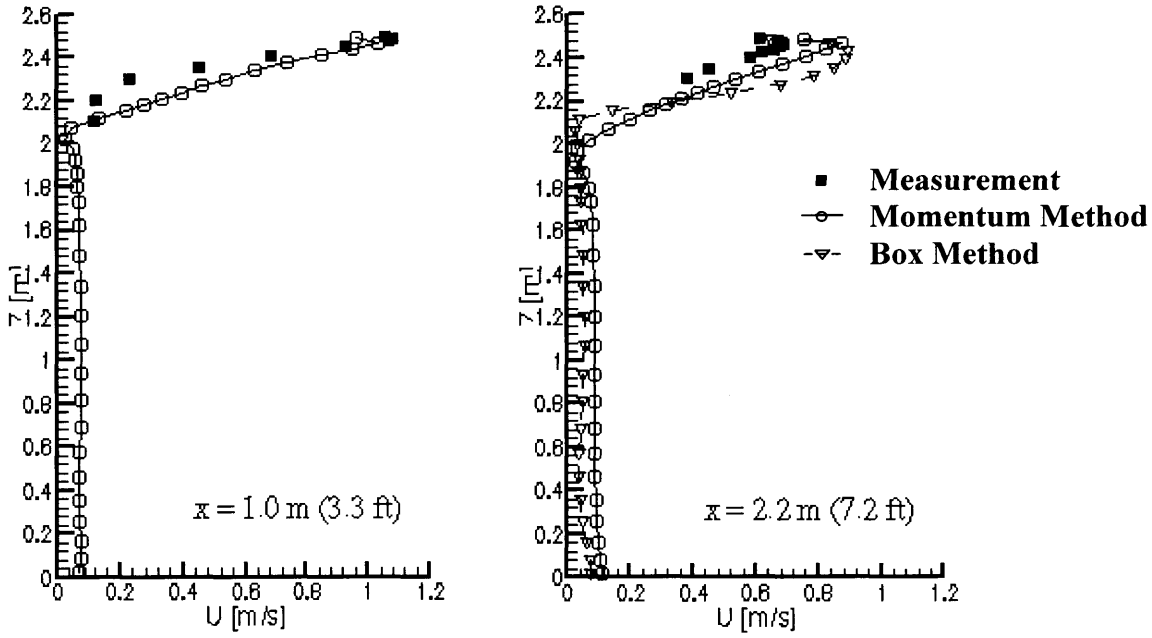

Figure 4.12 The comparison of the calculated and measured velocity profiles for the nozzle diffuser at the two positions in the symmetry plane

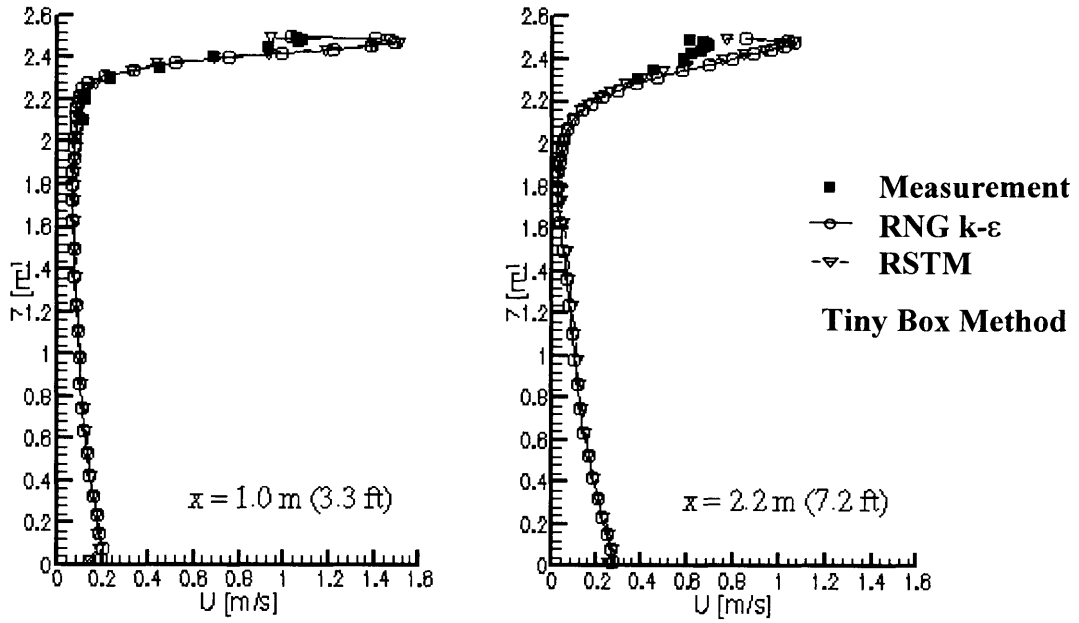

Figure 4.13 The comparison of the measured velocity profiles and that calculated with RNG k-ε model and RSTM in two sections of the room with the nozzle diffuser

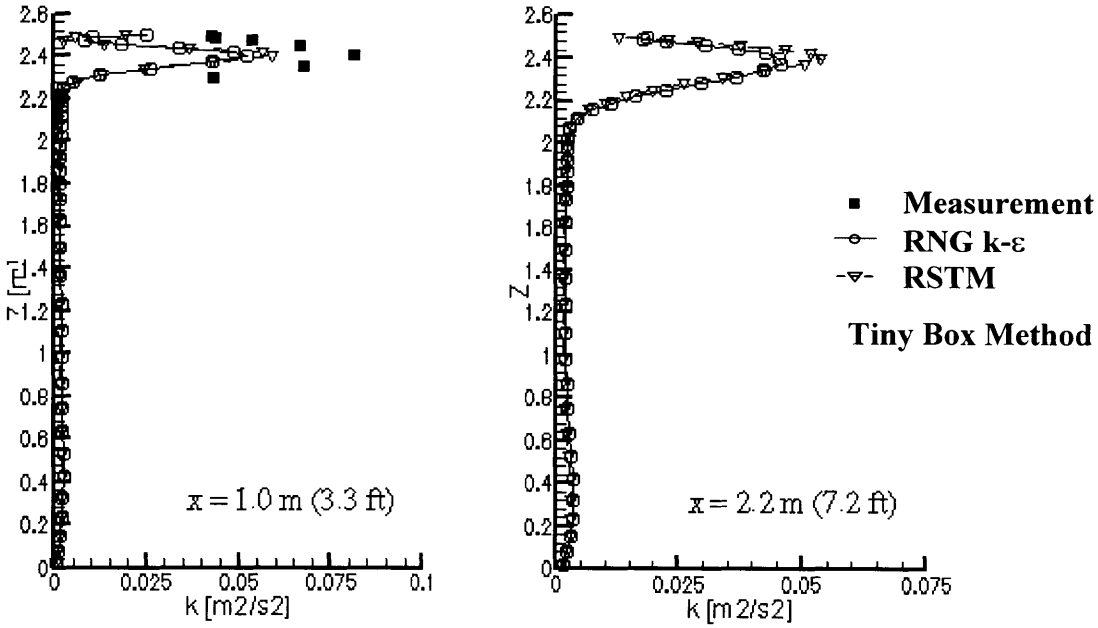

Figure 4.14 The comparison of the measured turbulent kinetic energy and that calculated with RNG k-ε model and RSTM in two sections of the room with the nozzle diffuser

The calculated velocity profile with the box method is different from the measured one. The reason for the discrepancies might be too large box dimensions. Therefore, the next simulation used smaller box that neglects lower part of the measured velocity profiles as shown in Figure 4.9(c). The justification for this approximation is that the jet center is responsible for most of the momentum transport. Consequently, the small box gave the same velocity profile as the bigger one, and the results are not presented here. The disagreement between measured and calculated results indicates that the major problems for the over-prediction of the jet velocity profile have not been solved. The possible reason for the poor prediction of the velocity profiles is probably still large box that covers significant part of the calculation domain.

In order to further study the impact of the box size on the numerical simulations, a tiny box is used (0.3 m x 0.4 m x 0.25 m) as shown in Figure 4.9(d). The box is so small that one has to impose velocity profile at the top surface of the box as the boundary conditions for the CFD simulation. In fact, the velocity profile is only imposed on the front part of the top surface where the flow is outwards. At the front part of the top surface, the flow direction of 45^{o} upwards with a uniform air supply velocity is 0.9 m/s. The supply velocity used for the tiny box was estimated from the smoke visualization since no measured data is available. The airflow pattern calculated with the tiny box has a recirculation in the upper left corner of the approximately same size as the one estimated with the smoke visualization. This is the only method discussed so far that is able to predict correctly the airflow pattern close to the diffuser. Figure 4.15 further compares the computed velocity profile with the measured one in two sections at the symmetry plane of the room. The agreement between the computed and measured results is excellent.

The current investigation used the RNG k-ε model and upwind scheme. We have also tested other numerical schemes and turbulence models. The other differencing schemes tested are hybrid and quick. The hybrid scheme gave the same results as the upwind scheme since the local Pe (Peclet) numbers were high, and the convection terms dominated the momentum transport. The quick scheme was very unstable for this simulation. Even with very patient adjustments on the relaxation factors. Obviously, different differencing schemes did not improve the calculated results. The study also used a Reynolds stress turbulence model (RSTM). The model produced slightly different turbulent kinetic energy (Figure 4.14) in the jet region from that by the RNG model. Otherwise, the two turbulence models perform the same in this case.

The supply velocity for the tiny box was only estimated from the smoke visualization since for that region nobody measured detailed jet parameters. The jet maximum velocity was over-predicted for approximately 25% for both velocity profiles (see Figure 4.13). Therefore, the supply velocity has been decreased for 25%, and with the new value of 0.9 m/s, results agree very well with the measured data as presented in Figure 4.15. Both jet profiles have been successfully predicted. Therefore, the tiny box is appropriate for nozzle diffuser simulation since the airflow pattern and jet profiles is are correctly simulated, and the tiny box data can be used for simulations of different diffuser

installation positions. The valuable experience in developing an appropriate box size for nozzle diffuser will be used for the following slot (linear) diffuser simulations.

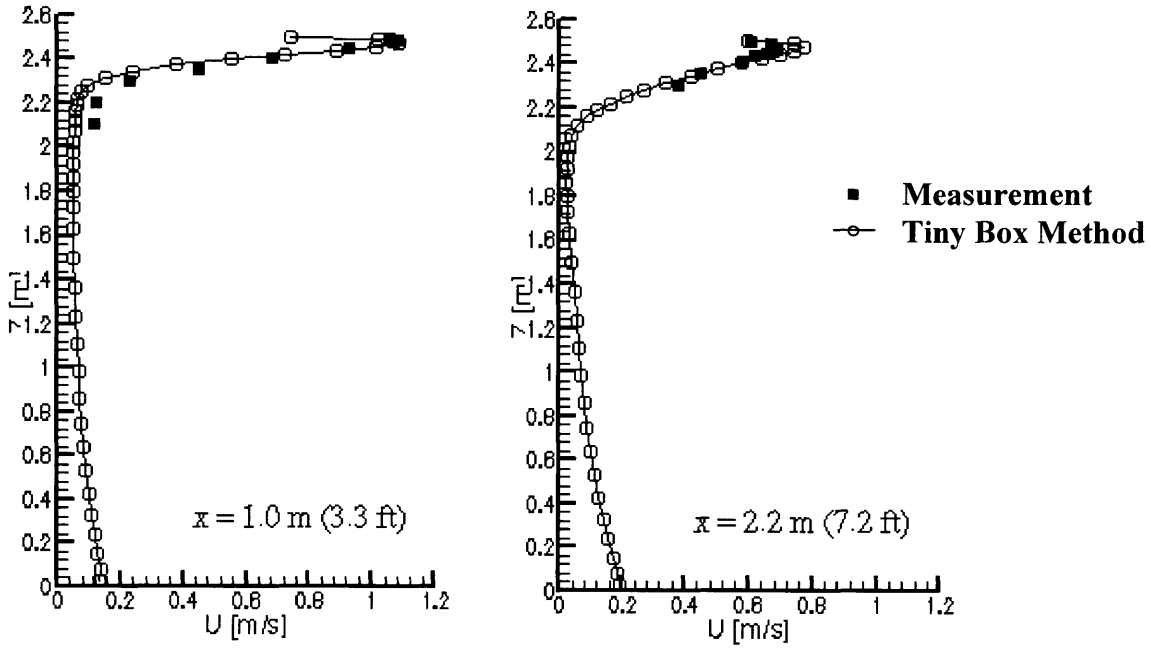

Figure 4.15 The comparison of the calculated and measured velocity profiles for the nozzle diffuser at two positions in the symmetry plane

4.5.2 Slot (Linear) Diffuser

The second diffuser studied is a slot (linear) diffuser, measured under summer cooling conditions. Table 4.1 shows the supply airflow boundary conditions of which the supply airflow rate is 250 cfm. The flow rate is in the middle of the recommended operation range for the diffuser. Figure 4.16 shows the opening dimension, opening position and the distance between the diffuser and the closest side wall. The diffuser was installed in the ceiling, 0.15 m (6") from the side wall. The diffuser in this position generated a jet attached to both the ceiling and the side wall. For this type of jet, the formulae for attached jets to a single surface cannot be used.

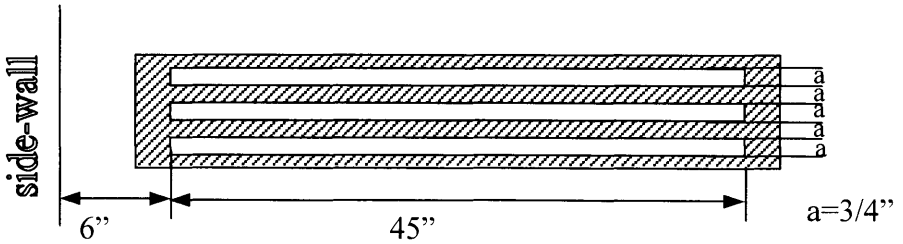

Figure 4.16 The slot (linear) diffuser dimensions and installation position

In fact, the diffuser has three openings that discharge parallel plane jets. The jets merged in a short distance from the diffuser because of the small separation distance (3/4") between the openings. According to the manufacturer's catalogue, the jet will be discharged horizontally without separation as shown in Figure 4.17. Our smoke visualization illustrates that the jet was about 45° downwards to the rear wall before it is reattached to the ceiling at 20 cm (0.65 ft) from the diffuser. Because the jet attached to the upper sidewall as well, the overall jet flow is towards the upper right corner of the room (Figure 4.3).

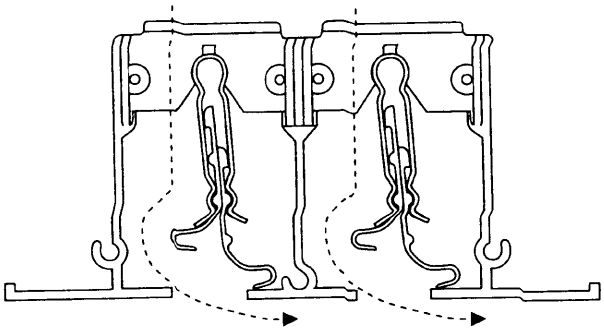

Figure 4.17 The airflow pattern from the slot diffuser manufacturer's catalogue

In order to simulate the jet flow, both the momentum and box methods were used. The momentum method set the initial jet at 45° downwards over an area of 0.1 m × 1.15 m (0.33 ft × 3.8 ft) as shown in Figure 4.18(a). The validation of the calculated results with the measured data for the air velocities and temperatures is presented in Figure 4.19 and Figure 4.20, respectively. The calculations used three different grid resolutions. The grid sensitivity is evident in the area near the ceiling close to poles 3, 2 and 1, where the flow is dominated by the jet. Finer grid resolution gives a thinner jet with higher jet maximum velocity that is in better agreement with the velocity data. Unfortunately, the calculated jet temperature with finer grid resolution is not in good agreement with the data in the jet region. The reason is not yet clear.

On the other hand, the investigation used different numerical schemes, because using finer grid resolution does not seem to be helpful. With the quick scheme, the calculated velocity is in better agreement with the data than that with the upwind scheme (see Figure 4.21 and Figure 4.22). However, the use of the quick scheme requires several times longer computing time. In addition, the numerical stability is much lower than that with the upwind scheme. Nevertheless, the calculated temperature in the jet region with the quick scheme does not agree better with the data. In fact, we latter found that the problem, which disappears with the box method, is related to the complex mixing in front of the diffuser.

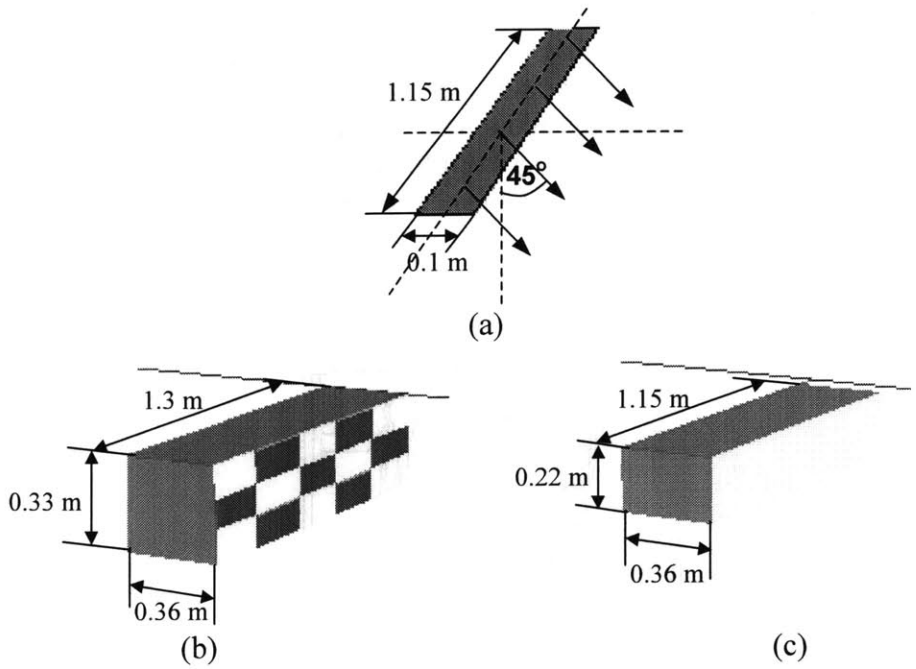

Figure 4.18 Simulation of the slot diffuser with (a) the momentum method (b) the box method, and (c) the tiny box method

Figure 4.23 shows further that the computed tracer gas concentration with the momentum method is in reasonable agreement with the measured data. It is interesting enough to note that even the sharp gradient in pole 1 is well predicted, where the tracer gas source is closely located. Normally a point source creates a locally high gradient of tracer gas concentration that is difficult to predict numerically. Note that, with the momentum model, the supply boundary condition from the diffuser can be easily defined for the tracer gas concentration. This is done through specifying the concentration directly at the inlet.

With the box method, the measured data were used to specify the boundary conditions for the diffuser in the CFD simulation, since no jet formulae are available. This study has used two types of box methods. The first method uses the measured data of the air temperature and velocity at 0.36 m (1.2 ft) downstream from the diffuser. At this position, the jets have been merged into an attached one. The box shown in Figure 4.18(b) covers the downstream section, because our measurements in the opposite direction found very low air velocities (an average 0.3m/s (60 fpm) at 0.06m (0.2 ft) from the diffuser). Obviously, the low velocity is due to jet entrainment. The experiment measured the air velocity and temperature at 15 points on the box front surface. The data are used directly as the boundary conditions for the CFD simulation. The other box surfaces are modeled as a zero-pressure boundary as described in Chapter 2.

Figure 4.24 presents velocity profiles calculated with the box method for three different grid resolutions. The calculated results agree very well with the measured data. It seems that the discrepancy between the computed and measured results for poles 4 and

5 is larger than those shown in the other poles. In fact, the discrepancies are the same because poles 4 and 5 use a smaller coordinate scale. Most of the discrepancies are within the error bar. The figure also shows that the discrepancy for the maximum jet velocity is within 10% and the jet spread is the same for different grid resolutions as indicated in pole 2. Please note that the upper part of pole 3 is within the box. Therefore, zero velocity is plotted in the figure, while the measurement shows a large velocity.

Figure 4.25 shows the computed and measured temperature profiles. The computed profiles are in excellent agreement with the data in both jet and recirculation regions. In this case, the box method can accurately describe the boundary conditions for the diffuser. The CFD simulation can give a very good result with the method. The study also found no grid dependency for this particular case, because the flow stream line is almost parallel to the grid lines that is less likely to generate numerical diffusion.

However, the box method needs the distribution of tracer gas at the box surface. The tracer gas distribution is not uniform in front of the diffuser, which makes the specification of the tracer gas boundary conditions very difficult. The concentration measurements require more labor than the velocity and temperature measurements. As a result, this method is unlikely to be practical. Therefore, we did not simulate the tracer gas concentration with the box method.

The above results conclude that the specification of the boundary conditions for CFD simulation with the box method requires substantial effort in measurements and CFD modeling. This investigation also used the same tiny box (the second box method) for the slot diffuser as the one used for the nozzle diffuser. The peripheral jet velocities at the front surface of the box are neglected if they are low than 0.4 m/s (80 fpm). Figure 4.9(c) shows the size of the tiny box. The averaged air velocity over the entire supply surface is used as the boundary condition for CFD modeling. The temperature and tracer gas concentrations at the front surface of the box are obtained from the energy and species balance. The balance calculation will be detailed in section 5.6.

The results with the tiny box method exhibit rough agreement with the measured data in the occupied zone, but the method fails to predict the jet flow due to the flat velocity profile used at the supply surface. Figure 4.26 shows clearly the flat jet velocity profile at pole 2 that is already 0.45 m (1.5 ft) in front of the box. The flat velocity profile has also a significant impact on the calculated temperature jet profile (Figure 4.27). Nevertheless, the balance treatment for the temperature and concentration can be used in the CFD simulation to predict reasonably good temperature and concentration profiles as shown Figure 4.27 and Figure 4.28. In fact, the momentum method exhibits similar problems. To improve the results, the measured velocity profiles should be used in both the momentum and tiny box methods. Of course, the effort in that direction would cost more because of the need in more data. The results with the momentum method, the box method, and the tiny box method conclude preliminarily that the accuracy in simulation boundary conditions for a complex diffuser is proportional to the labor in describing the diffuser. There is always a trade-off between accuracy and labor for this particular diffuser.

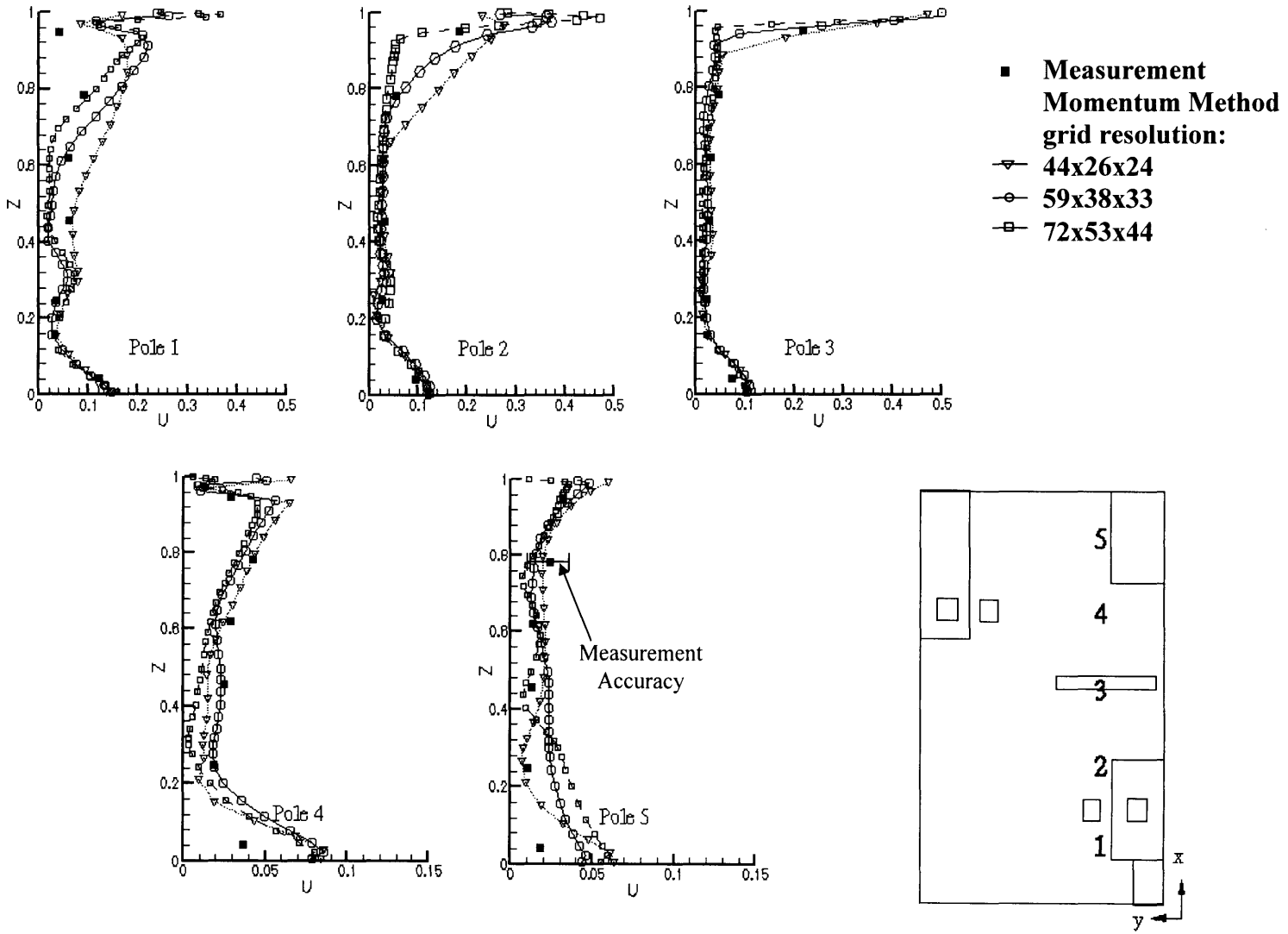

Figure 4.19 The comparison of the calculated and measured velocity profiles for the slot diffuser at five positions in the room Z=height/total room height (H), U=velocity/supply velocity (U_0), H=2.43m, U_0=3.9m/s

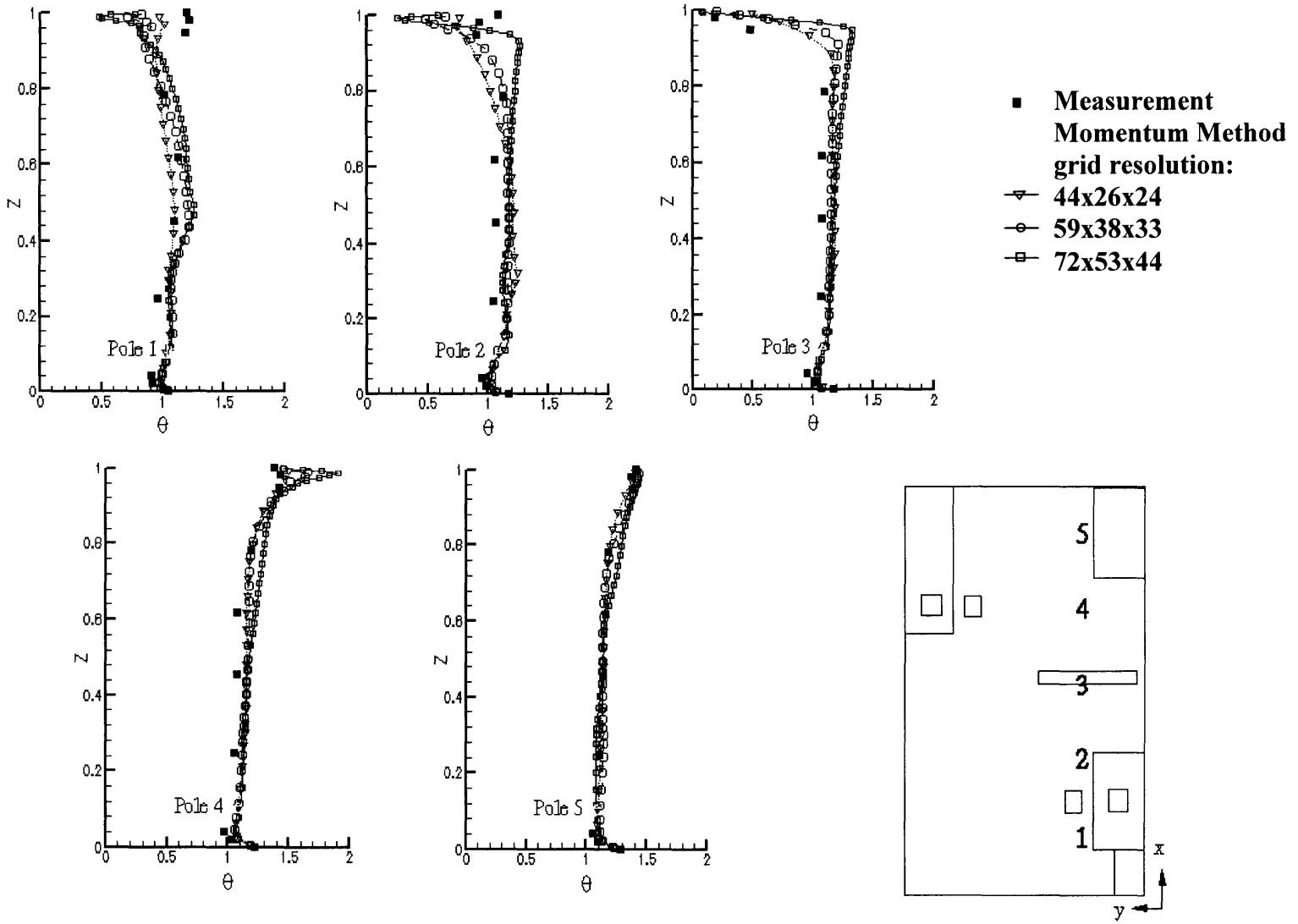

Figure 4.20 The comparison of the calculated and measured temperature profiles for the slot diffuser at five positions in the room, Z=height/total room height (H), $\theta=(T-T_{in}/T_{out}-T_{in})$, H=2.43m, $T_{in}=16.2^{o}C$, $T_{out}=21.4^{o}C$

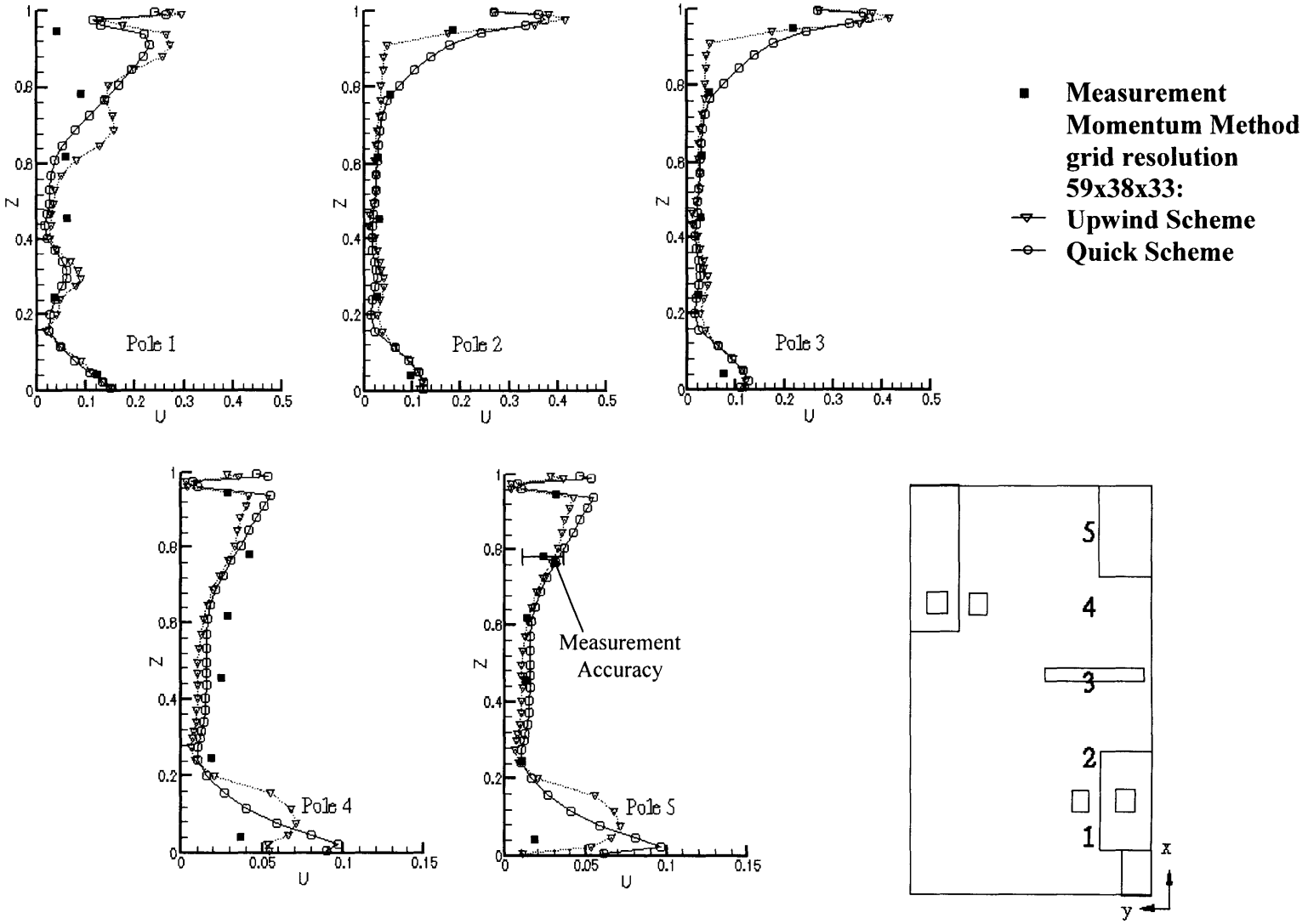

Figure 4.21 The comparison of the calculated and measured velocity profiles for the slot diffuser at five positions in the room Z=height/total room height (H), U=velocity/supply velocity (U_0), H=2.43m, U_0=3.9m/s

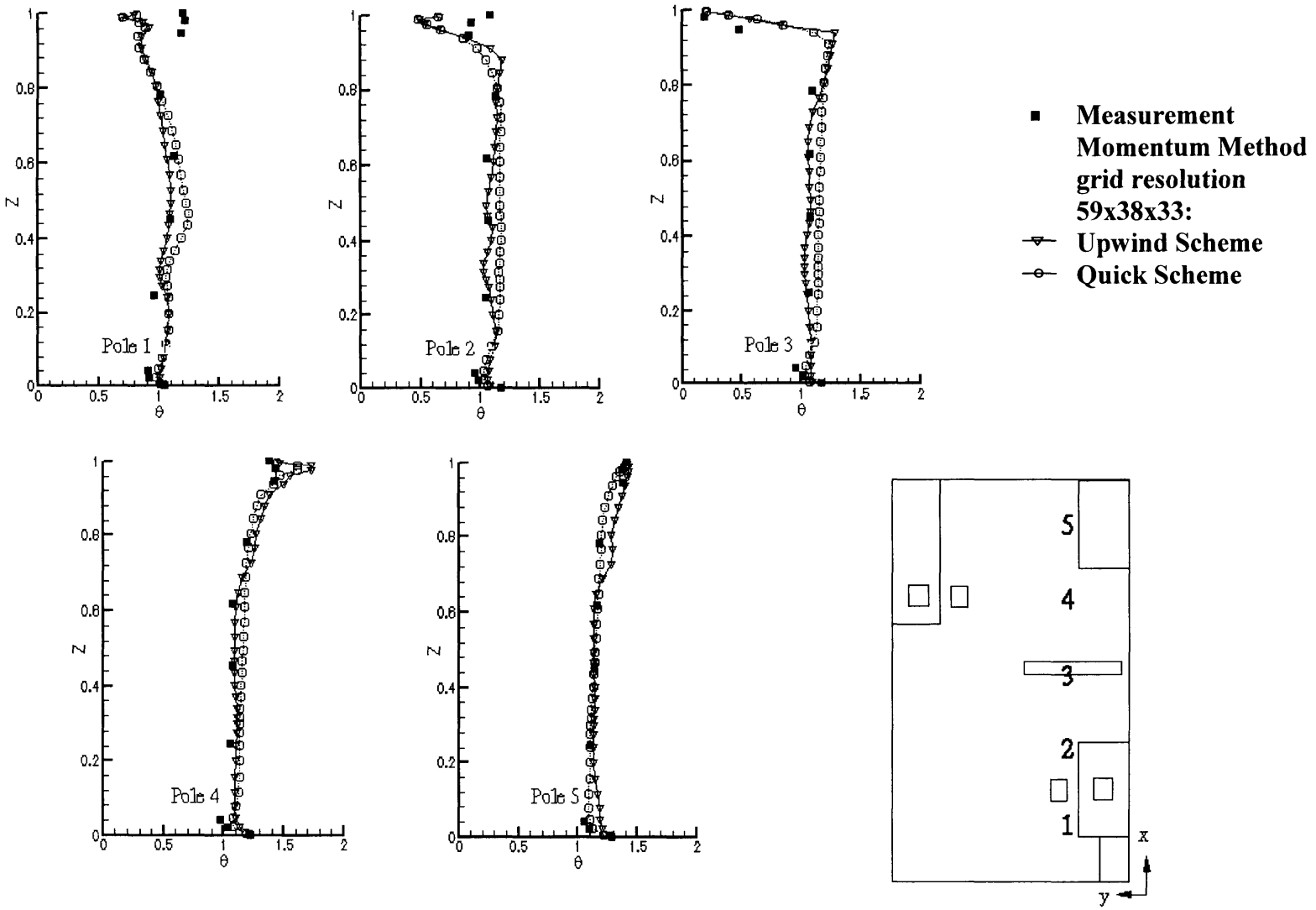

Figure 4.22 The comparison of the calculated and measured temperature profiles for the slot diffuser at five positions in the room, Z=height/total room height (H), $\theta=(T-T_{in}/T_{out}-T_{in})$, H=2.43m, $T_{in}=16.2^{o}C$, $T_{out}=21.4^{o}C$

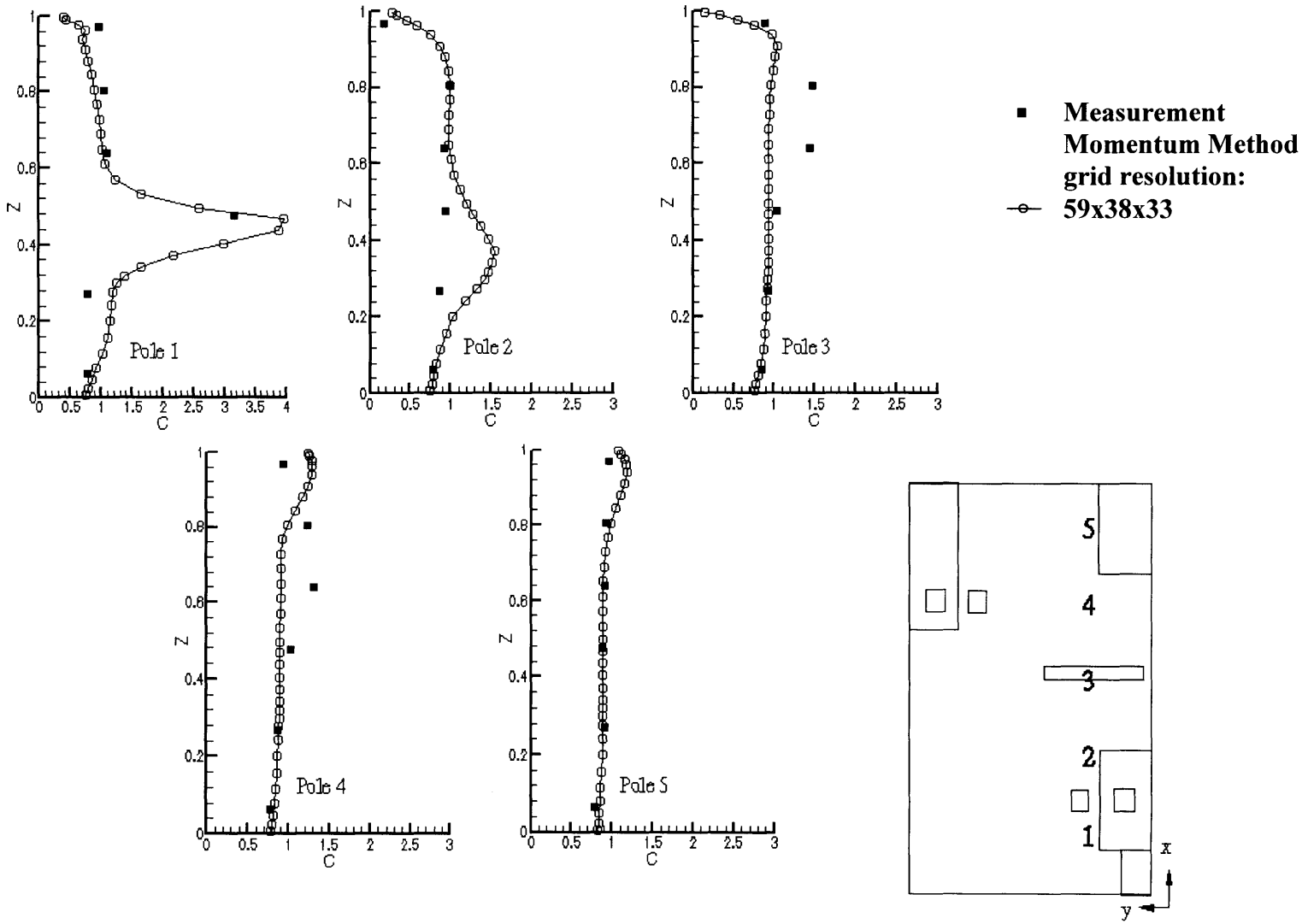

Figure 4.23 The comparison of the calculated and measured SF_6 concentration profiles for the slot diffuser at five positions in the room, Z=height/total room height (H), $C=(c-c_{in}/c_{out}-c_{in})$, H=2.43m, c_{in}=0.04489 ppm, c_{out}=1.0078 ppm

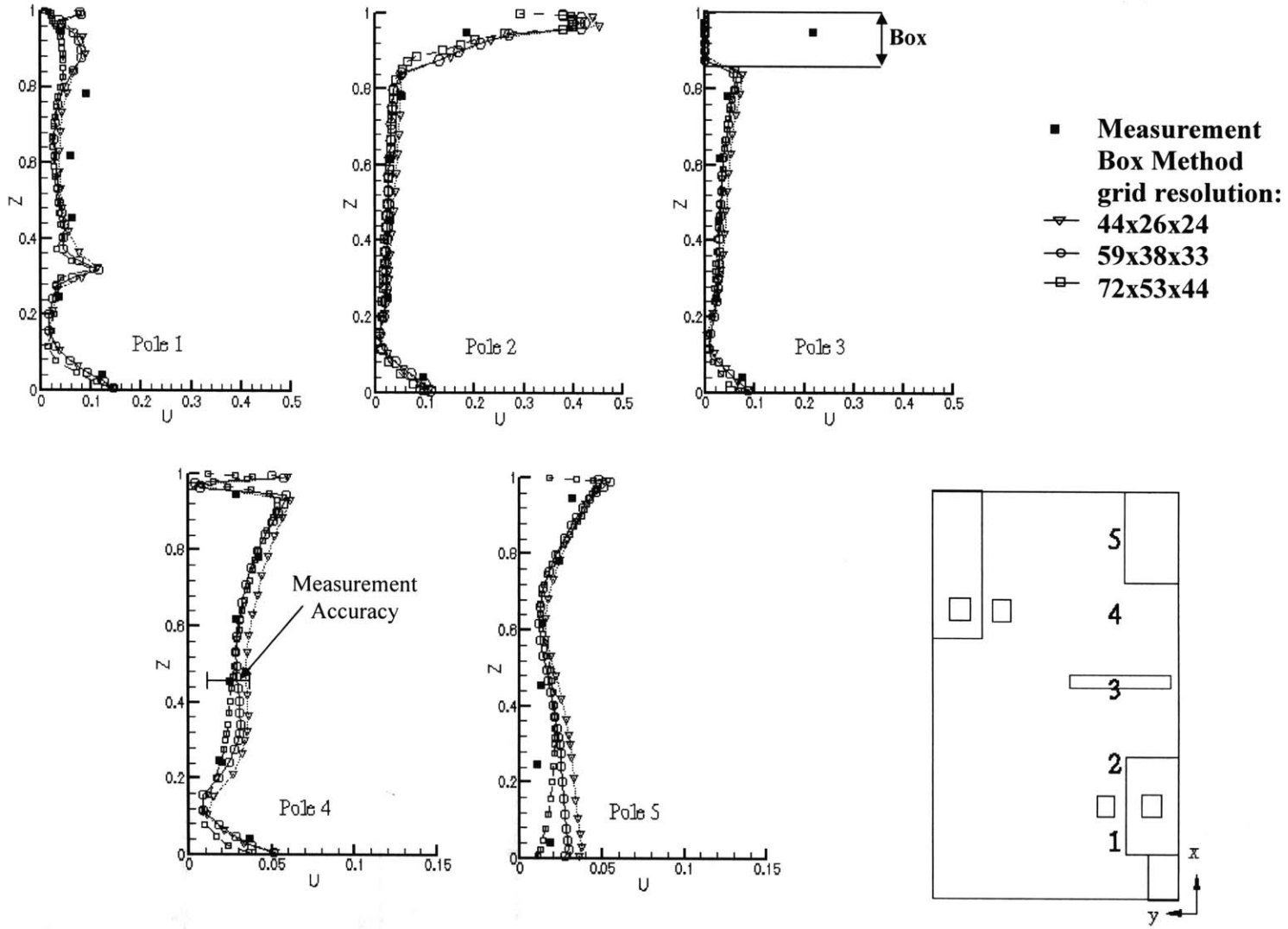

Figure 4.24 The comparison of the calculated and measured velocity profiles for the slot diffuser at five positions in the room
Z=height/total room height (H), U=velocity/supply velocity (U_0), H=2.43m, U_0=3.9m/s

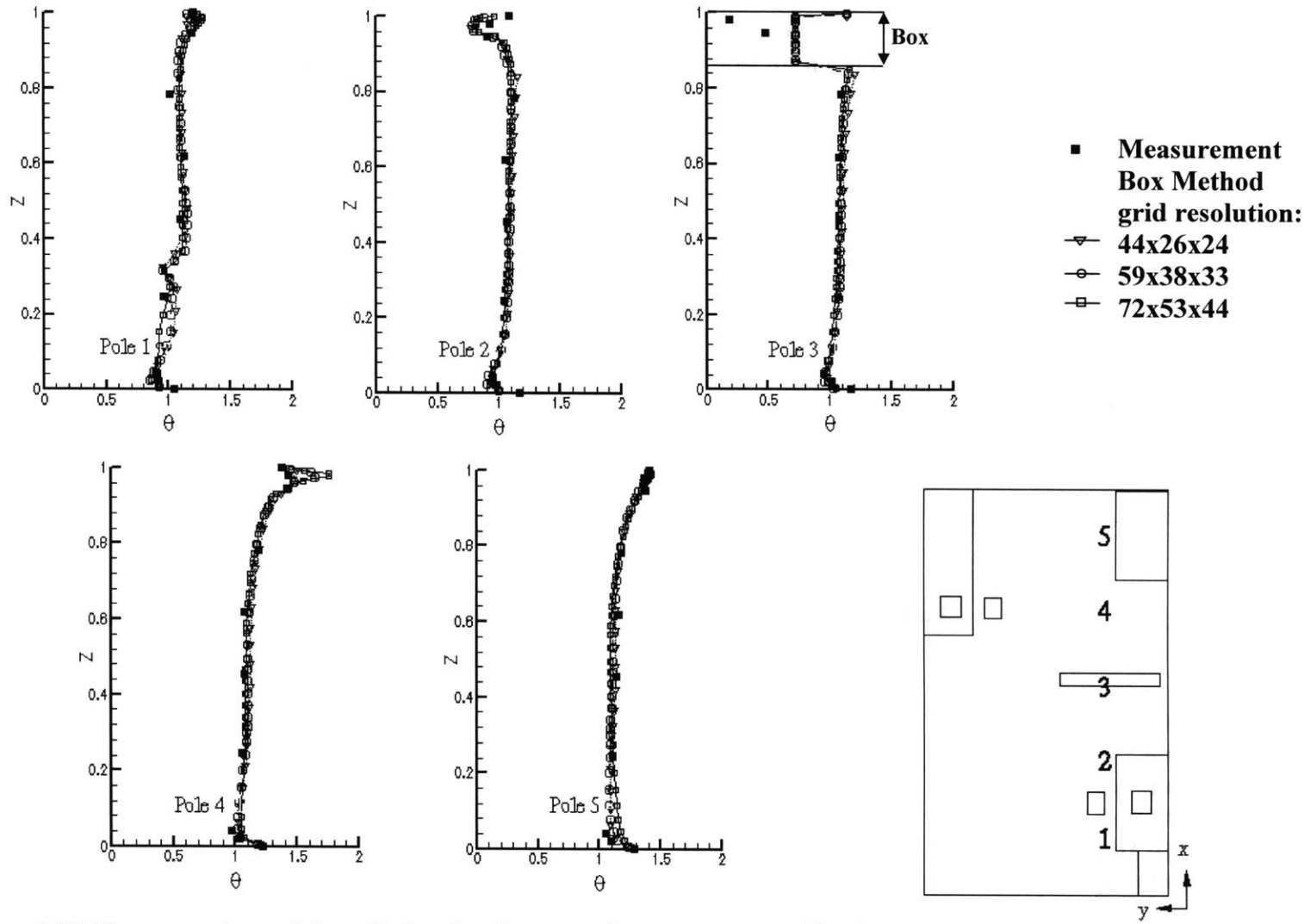

Figure 4.25 The comparison of the calculated and measured temperature profiles for the slot diffuser at five positions in the room, Z=height/total room height (H), $\theta=(T-T_{in}/T_{out}-T_{in})$, H=2.43m, $T_{in}=16.2^{o}C$, $T_{out}=21.4^{o}C$

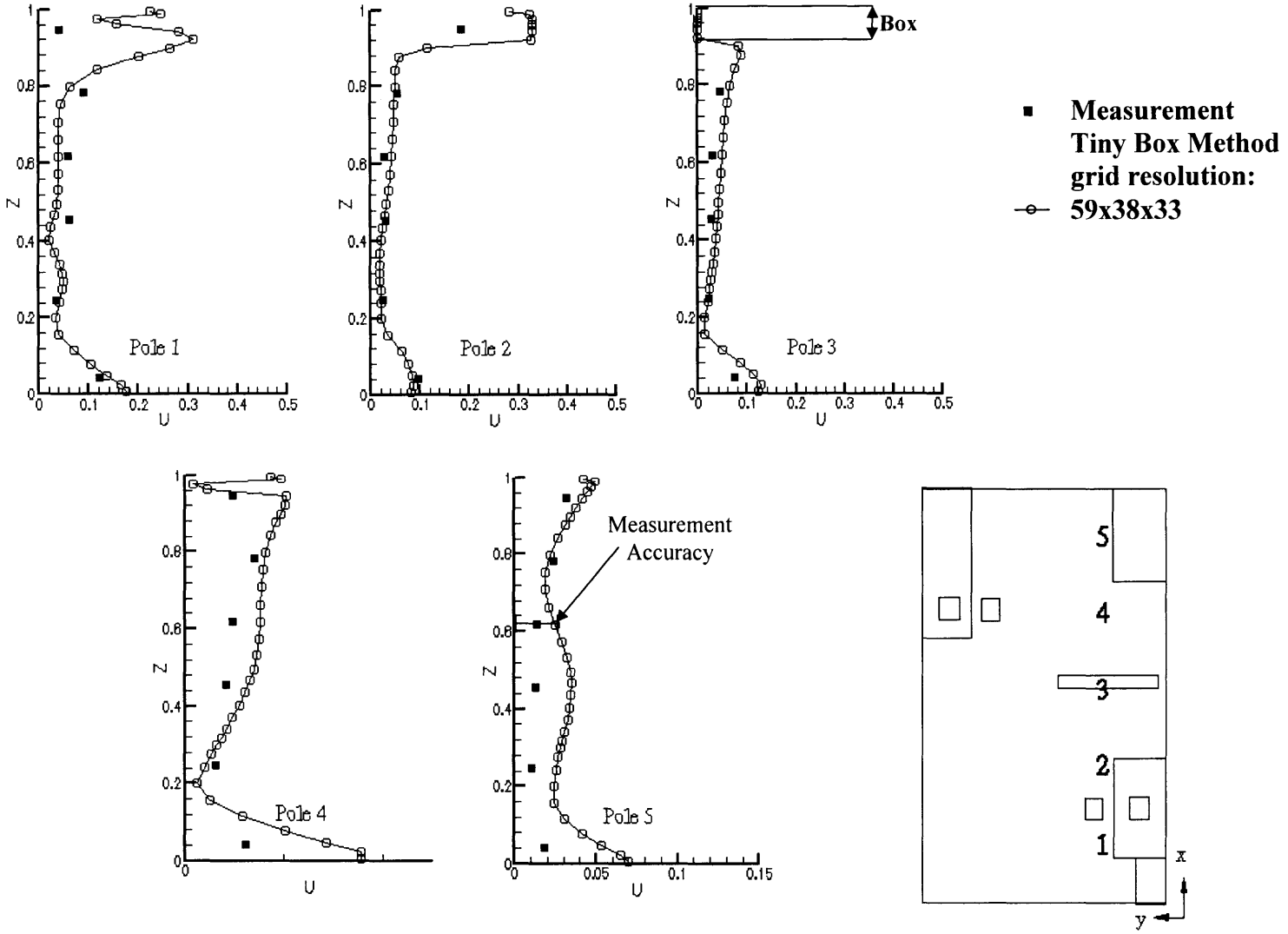

Figure 4.26 The comparison of the calculated and measured velocity profiles for the slot diffuser at five positions in the room Z=height/total room height (H), U=velocity/supply velocity (U_0), H=2.43m, U_0=3.9m/s

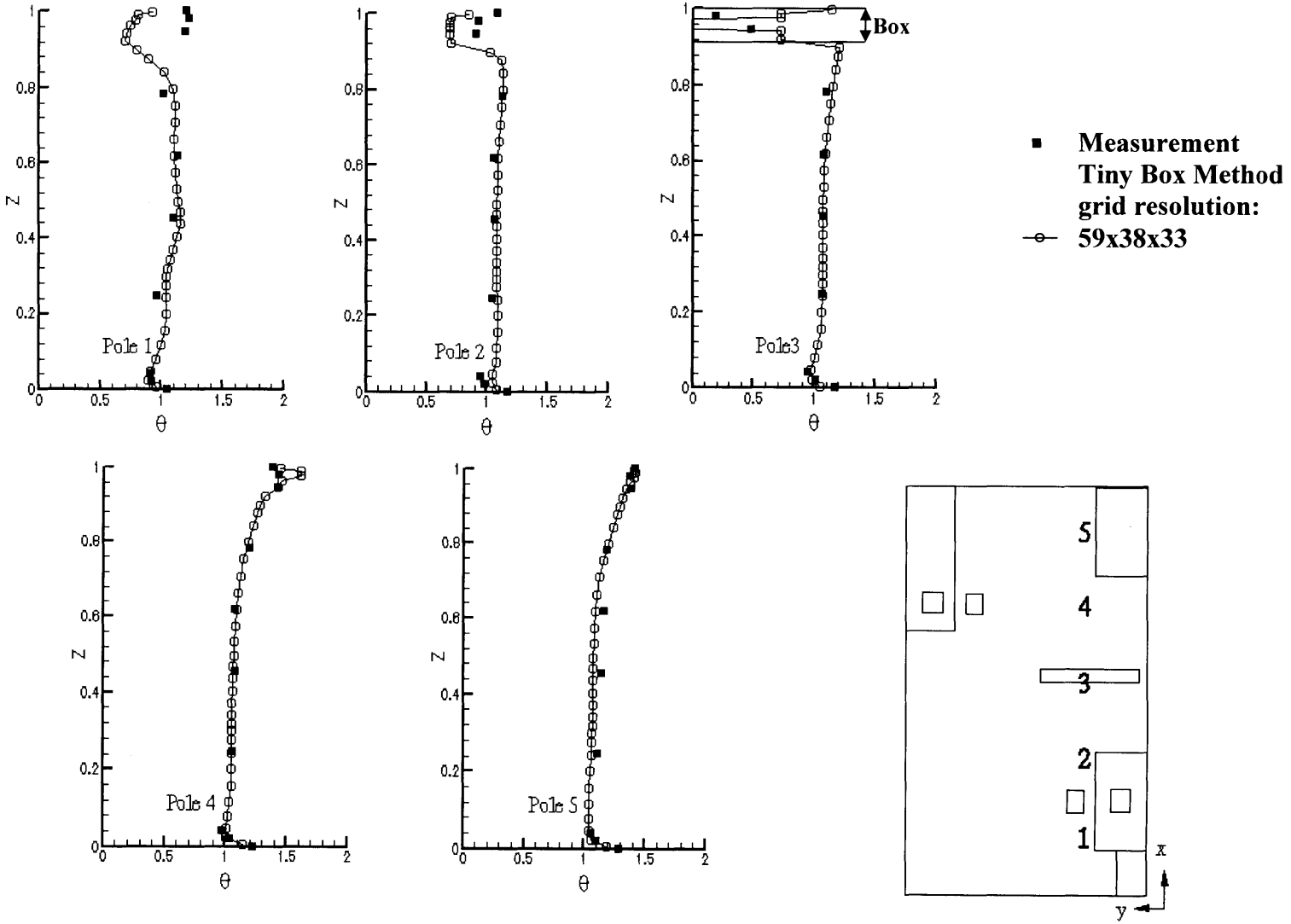

Figure 4.27 The comparison of the calculated and measured temperature profiles for the slot diffuser at five positions in the room, Z=height/total room height (H), $\theta=(T-T_{in}/T_{out}-T_{in})$, H=2.43m, $T_{in}=16.2^{o}C$, $T_{out}=21.4^{o}C$

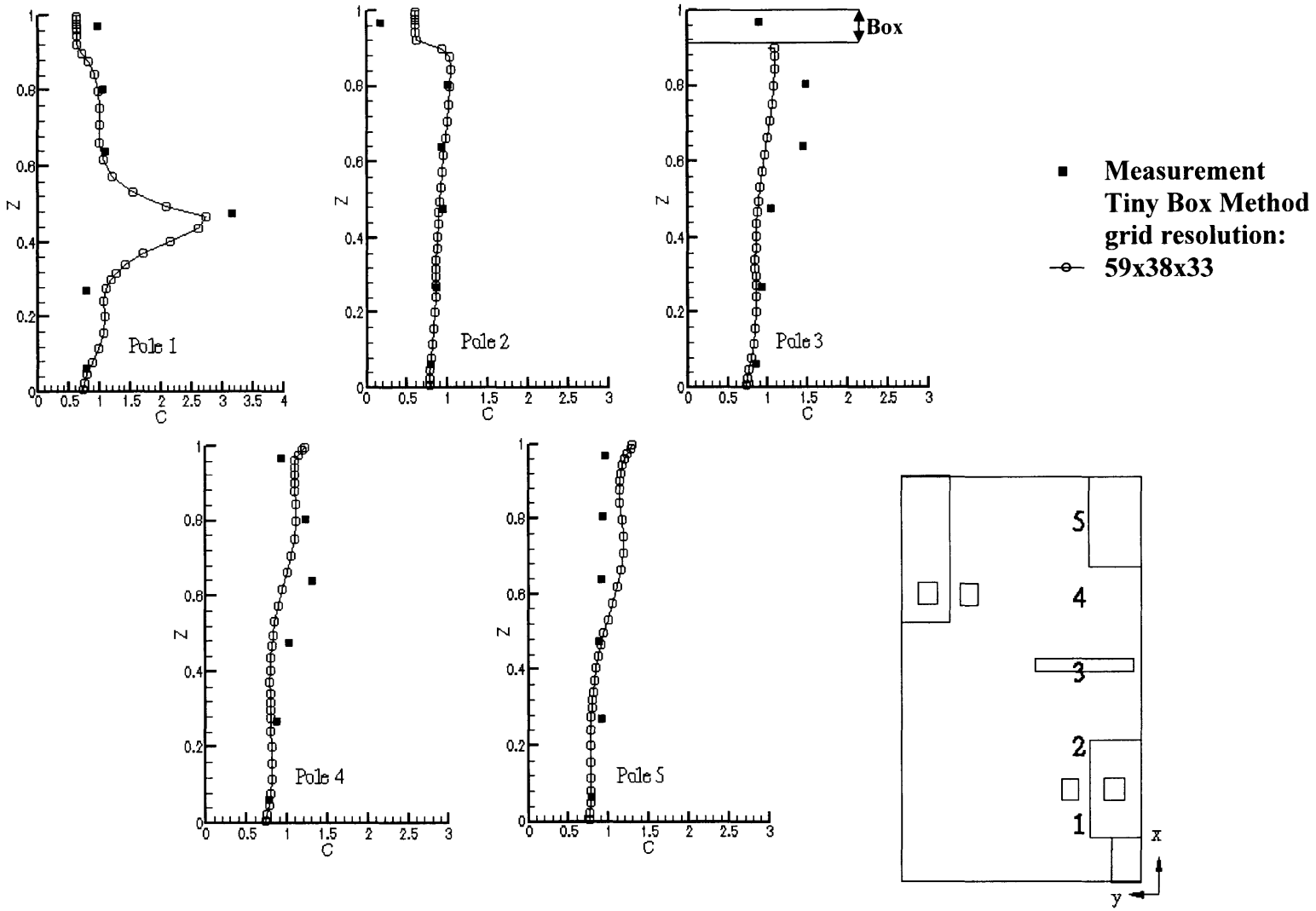

Figure 4.28The comparison of the calculated and measured SF_6 concentration profiles for the slot diffuser at five positions in the room, Z=height/total room height (H), $C=(c-c_{in}/c_{out}-c_{in})$, H=2.43m, c_{in}=0.04489 ppm, c_{out}=1.0078 ppm

4.5.3 Valve Diffuser

Another diffuser studied is a valve diffuser that has a complex geometry as shown in Figure 4.29(a). The diffuser consists of a coaxial cylinder and an inner cone (valve). The relative position of the valve to the cylinder, *s*, is a key parameter for the diffuser effective area. A small *s* means a small effective area and a high discharge jet velocity.

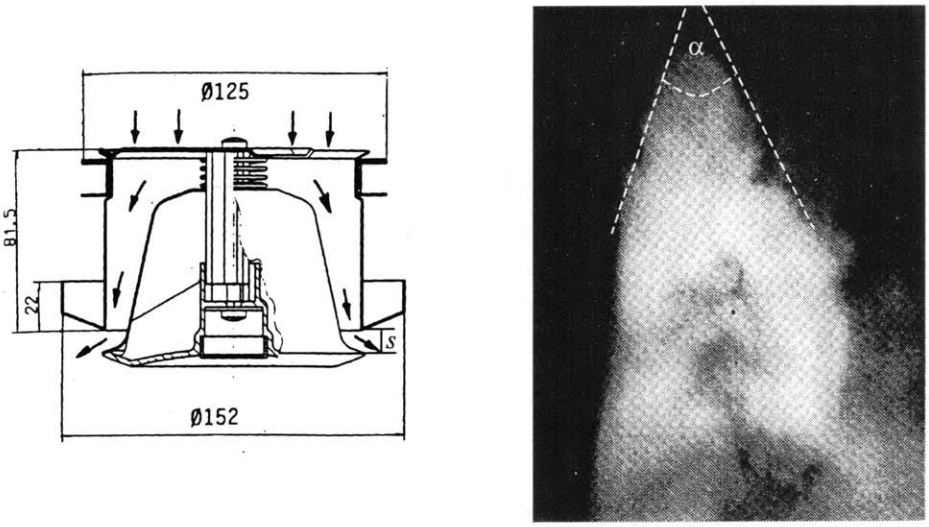

(a) (b)

Figure 4.29 Valve diffuser (a) geometry and (b) airflow pattern by smoke visualization

Chen and Jiang (1996) provided measured velocity for s = 11.5 mm (0.45 in) with the supply airflow rate of 40 m^3/h (23.5 cfm) in the vicinity of the diffuser. The corresponding average discharge velocity is 5 m/s (1000 fpm). The measurements were carried out under isothermal airflow conditions in an empty chamber. The chamber size is 3.41 m (11.2 ft) long, 2.36 m (7.7 ft) wide, and 2.36 m (7.7 ft) high. The diffuser was installed in the ceiling to discharge vertically downward flow. Figure 4.29(b) shows jet flow pattern with smoke visualization. The diffuser produced a conical jet at its origin then, after a certain distance, the jet merges into an axisymmetric one. The jet has a very high entrainment rate and its mass flow rate increases by approximately 8 times at 0.18 m (0.6 ft) below the diffuser.

To predict the jet from the diffuser, Chen and Jiang (1996) simulated the airflow through the diffuser and its vicinity. They used three different grid systems in order to correctly model diffuser geometry and the airflow pattern. The first grid system used cylindrical coordinates with small steps to represent the curved surfaces. The simulation gave a completely wrong airflow pattern due to the excessive turbulence energy predicted in the slope surface of the diffuser cone. Their calculated jet was attached to the ceiling though the smoke visualization displays a downward flow. The other two grid systems used are body-fitted coordinates and unstructured grid. Both of them gave a good

prediction of the airflow pattern, as shown in Figure 4.30, and the pressure drop through the diffuser. The calculations predicted a small recirculation below the diffuser after which the conical jet merges in one. However, both the body-fitted coordinates and the unstructured grids require more substantial effort than the cylinder coordinates in the CFD grid generation.

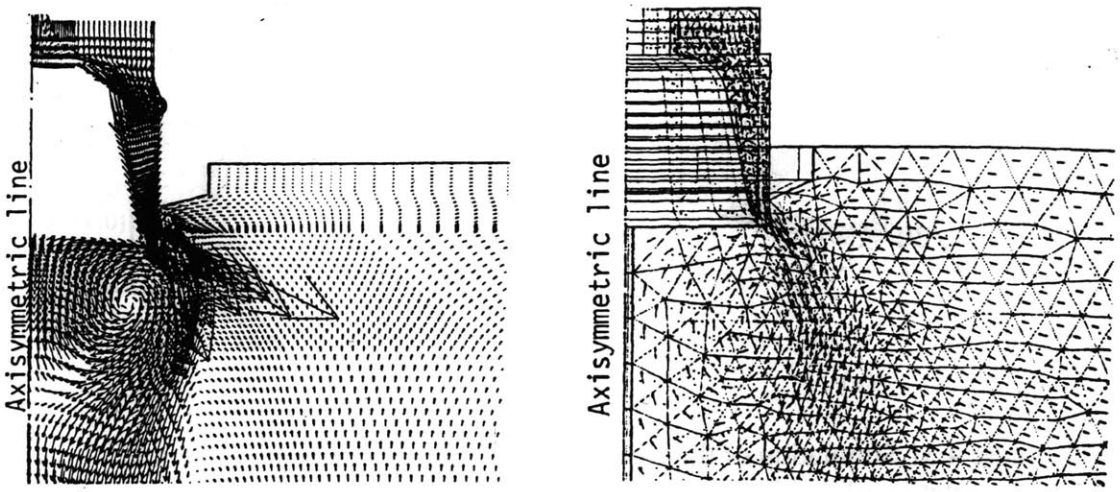

(a) (b)

Figure 4.30 Computed air velocities with (a) the body-fitted coordinates (b) the unstructured grid (Chen and Jiang 1996)

The detailed simulation of the diffuser by Chen and Jiang (1996) is not feasible for practical design, if there are multiple diffusers in a complex room. This study will test the momentum and box methods with the Cartesian coordinates. Figure 4.31(a) presents the simplified diffuser geometry used in the momentum method and the corresponding supply velocity direction. From the smoke visualization, the jet cone angle α is estimated to be approximately 60° as shown in Figure 4.29(b). Obviously, the method is much easier to use than those used by Chen and Jiang (1996). However, the momentum method has to use the smoke visualization to estimate the discharge angle. Further, the simplifications introduce some problems. The predicted results with the momentum method are very sensitive to the α. When $\alpha \leq 60^{\circ}$, the calculated jet does not spread very much. However, when $\alpha > 60^{\circ}$, the calculated jet attaches to the ceiling. The predictions obviously do not agree with that observed with the smoke visualization. Therefore, the valve diffuser cannot be correctly simulated with the momentum method. Nevertheless, if the momentum method is applied for only a small volume around the diffuser, it can give an important correct size for the box method.

Figure 4.31(b) shows the airflow pattern predicted with the momentum method when it is applied to only a part of flow domain (0.7 m × 0.7 m × 0.7 m) around the diffuser. The simulation provides detailed flow structure that otherwise might not be easy seen from the visualization. The flow pattern looks similar to that with the body-fitted

coordinates and unstructured grids. The recirculation zone below the diffuser is around 0.11 m (0.36 ft), which is approximately the same size as the one predicted with the unstructured grid. After that region, the jet merges into one and continues to grow downwards. If the box method should be used, the box size should be larger than this region that includes the recirculation. Otherwise, the box method could not give a good prediction of the airflow pattern. For example, with a smaller box in which the box front surface is 0.045 m from the diffuser, the box method gives a wrong airflow pattern that shows the jet is attached to the ceiling.

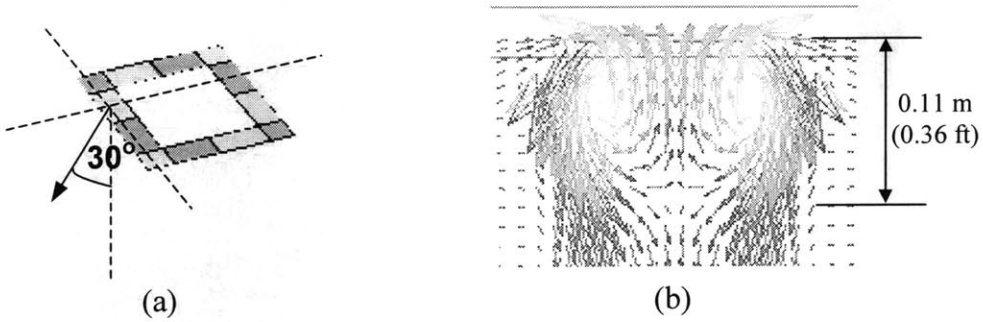

Figure 4.31 Simulation of the valve diffuser with the momentum method
(a) representation of the diffuser geometry, and (b) the calculated airflow pattern

The box size that can successfully simulate the airflow pattern with the valve diffuser is 0.175 m (0.57 ft) from the diffuser as illustrated in Figure 4.32. The figure shows the box covers 3×3 points where the measured velocity is available.

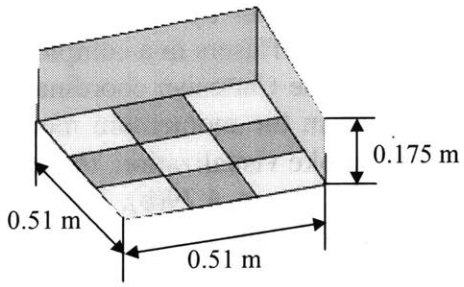

Figure 4.32 The box used to simulate the valve diffuser

Figure 4.33 and Figure 4.34 show the calculated airflow pattern in the chamber. The calculation found a small recirculation zone along the jet axis close to the floor that can also be clearly seen in the smoke visualization. In the recirculation zone, the smoke is lighter. The jet spreads much faster in the narrower room section (Figure 4.33) than that in the wider room section (Figure 4.34). The reason is not clear. The two dashed lines in Figure 4.33 and Figure 4.34 display positions where the measured data are available. The measured air velocity at the two markers on line 1 is around 0.5 m/s (100 fpm), and at the two markers on line 2 around 0.13 m/s (26 fpm). The calculated velocity agrees very well with the data. From the airflow pattern predicted and the limited comparison between the

calculated and measured velocities, it seems that the box method can simulate the flow from the valve diffuser.

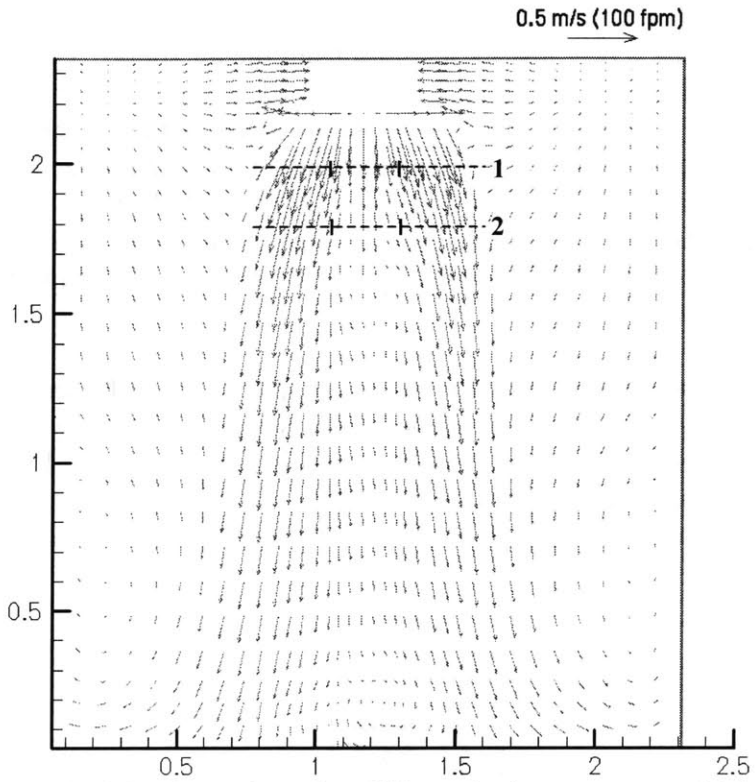

Figure 4.33 The velocities from the valve diffuser in the narrower middle cross section

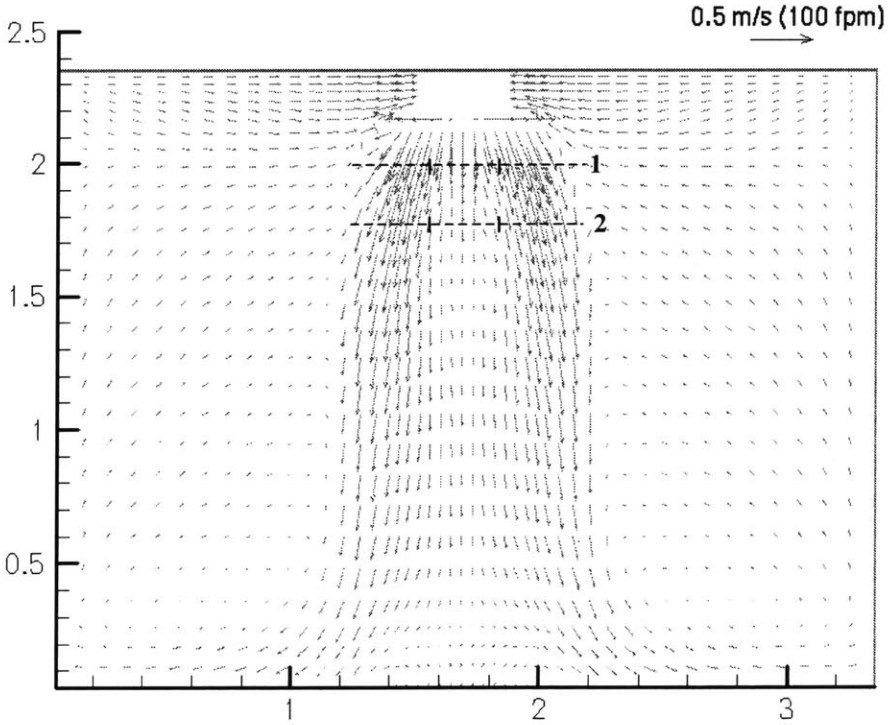

Figure 4.34 The velocities from the valve diffuser in the wider middle cross section

4.5.4 Displacement Diffuser

This section will report the results how to simulate a displacement diffuser. The displacement diffuser has a very low momentum from the air supply. Our simulation has used the momentum method because the box method is not suitable for the diffuser. Because the buoyancy force is at least in the same order as the momentum force, the airflow pattern from the jet does not correspond to any classic catalogue of jets defined in conventional textbooks. The jet rapidly changes its type and shape as shown in Figure 3.7. The jet depends also strongly on the heat sources in the room. If the box method is used, it is difficult to determine the box size and to estimate the impact of the room airflow on the low velocity jet.

Figure 4.35 presents the geometry of the displacement diffuser. The airflow is discharged horizontally from the front surface. The supply air velocity is 0.35 m/s (70 fpm), the airflow rate is 0.0768 kg/s (135 cfm), and the temperature is 13.0°C (55°F). In the experiment, the supply air temperature was adjusted to be very low in order to study how the low supply temperature can affect the thermal comfort in the occupied zone.

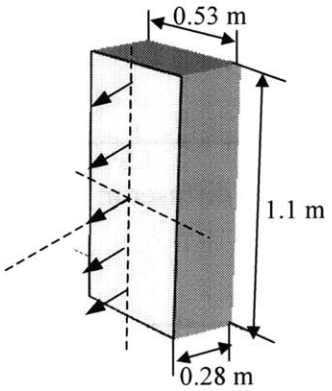

Figure 4.35 Simulation of the displacement diffuser with the momentum method

Figure 4.36 presents a comparison of the calculated and measured air velocities at five positions in the room. The results show that the air velocities are low even in the jet region (lower than 0.35 m/s (70 fpm)). In the other part of the room, the air velocities are mostly lower than 0.1 m/s (20 fpm). Since there are slow and unsteady recirculations in the lower part of the room, it was difficult to obtain reliable velocity in the area. Hence, the agreement between the computed and measured results is reasonably good. Because the low velocities would not cause a draft problem, it is important to correctly predict room air temperature stratification in displacement ventilation system design. Figure 4.37 shows a very good agreement between the calculated and measured air temperatures. This is especially evident in the jet region (pole 1).

However, the results for the tracer gas concentration shown in Figure 4.38 indicate some discrepancies between the computed profiles and the data. The discrepancies are large in the lower part of the room. We found that the tracer gas

concentration distribution is difficult to predict, since the results are very sensitive to tracer gas source location. In addition, the source is nearly a point source while the CFD computations have to simulate it as a volume source. Further, the initial momentum from the source is also difficult to simulate. All of these should contribute to the discrepancies found in this study. In fact, the study conducted by Yuan et al. (1999) had the same problem. Despite the discrepancies in the tracer gas concentration prediction, the CFD simulations with the momentum method are capable for indoor airflow predictions in a room with a displacement diffuser.

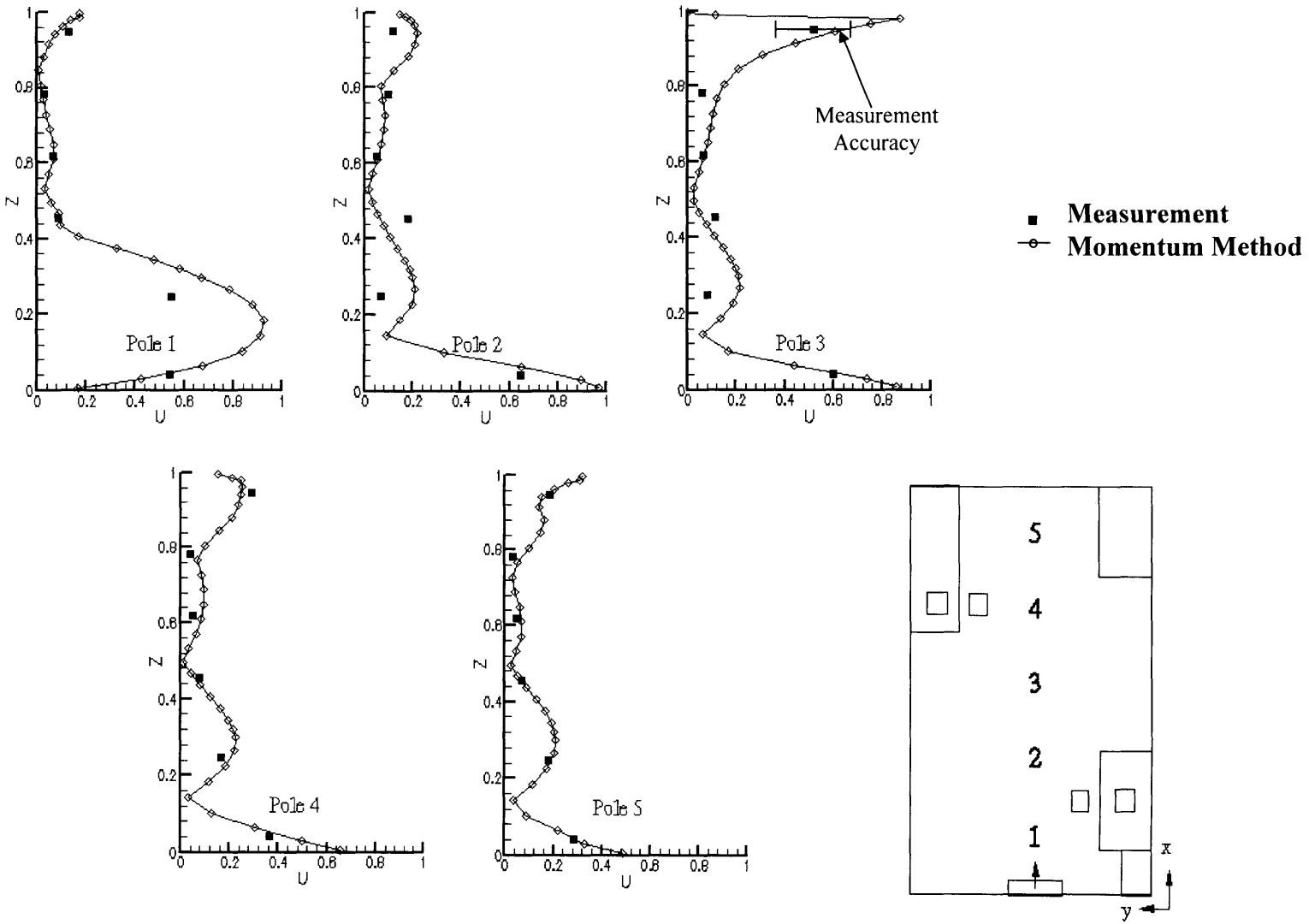

Figure 4.36 The comparison of the calculated and measured velocity profiles for the displacement diffuser at five positions in the room, **Z**=height/total room height (H), U=velocity/supply velocity (U_0), H=2.43m, U_0=0.35m/s

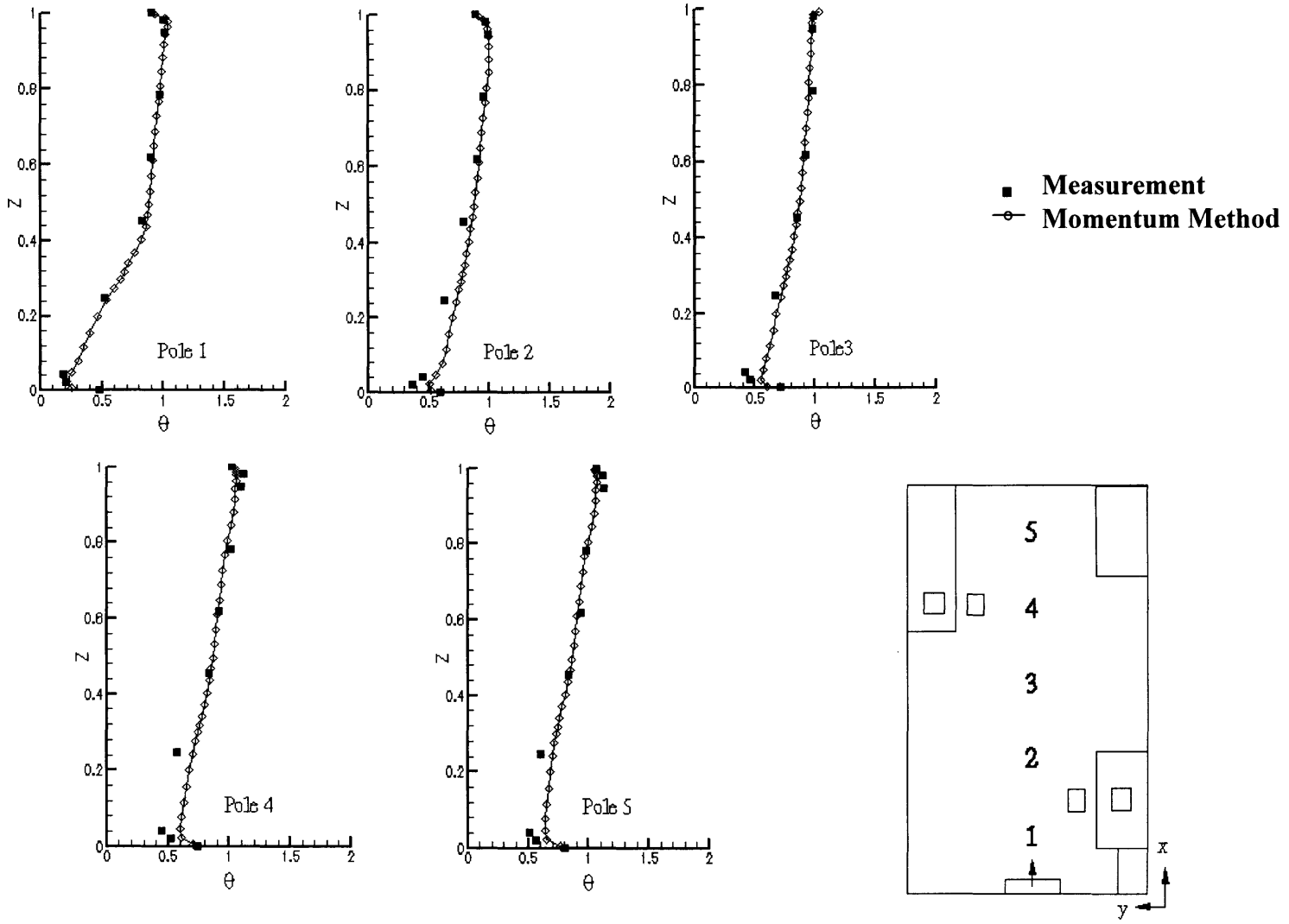

Figure 4.37 The comparison of the calculated and measured temperature profiles for the displacement diffuser at five positions in the room, Z=height/total room height (H), $\theta=(T-T_{in}/T_{out}-T_{in})$, H=2.43m, $T_{in}=13.0^{o}C$, $T_{out}=22.2^{o}C$

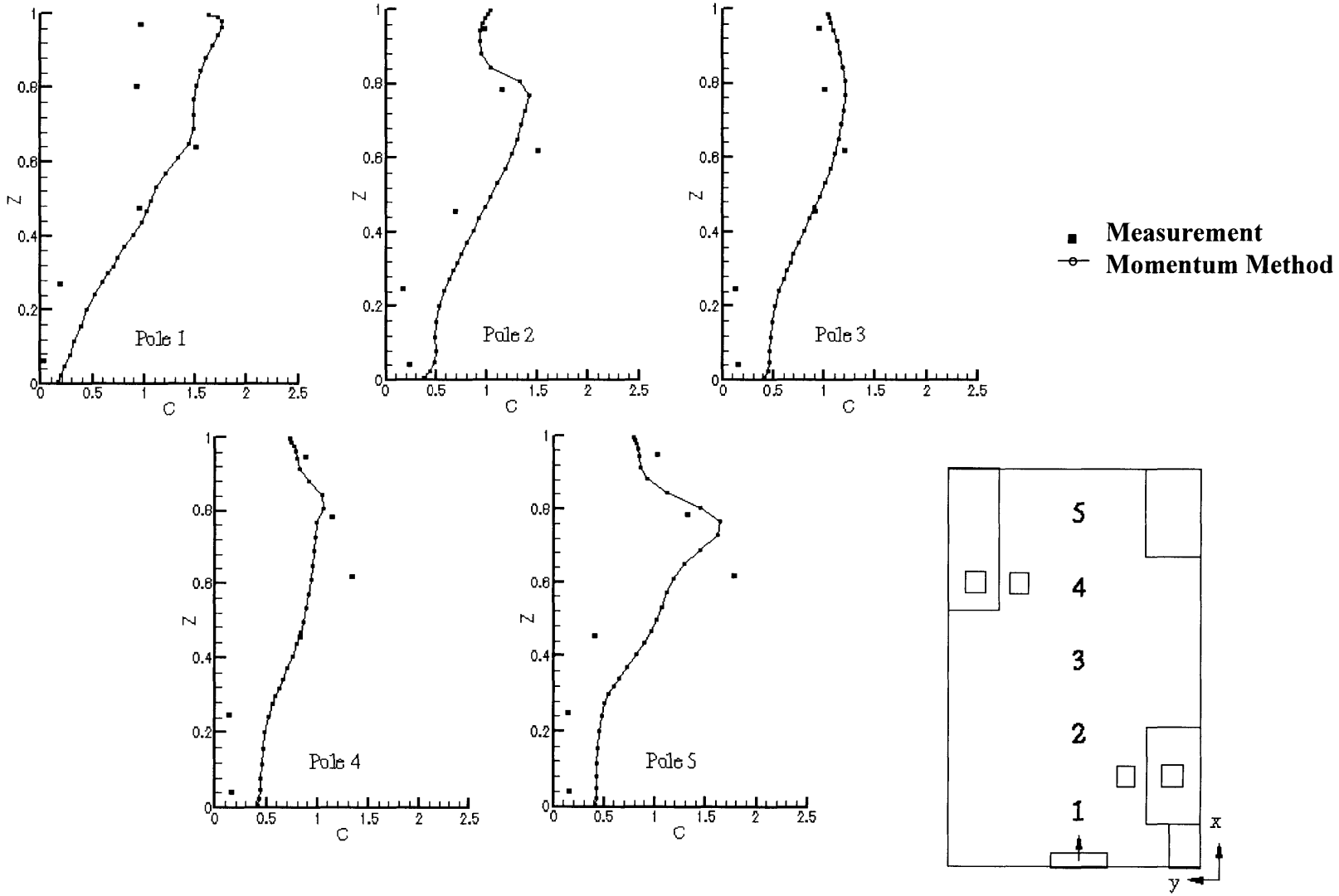

Figure 4.38 The comparison of the calculated and measured SF_6 concentration profiles for the displacement diffuser at five positions in the room, Z=height/total room height (H), $C=(c-c_{in}/c_{out}-c_{in})$, H=2.43m, c_{in}=0.04489 ppm, c_{out}=1.0078 ppm

4.5.5 Square Ceiling Diffuser

The square ceiling diffuser is one the most widely used diffusers in the U.S. The diffuser discharges jets in four cross and four diagonal directions as shown in Figure 4.39.

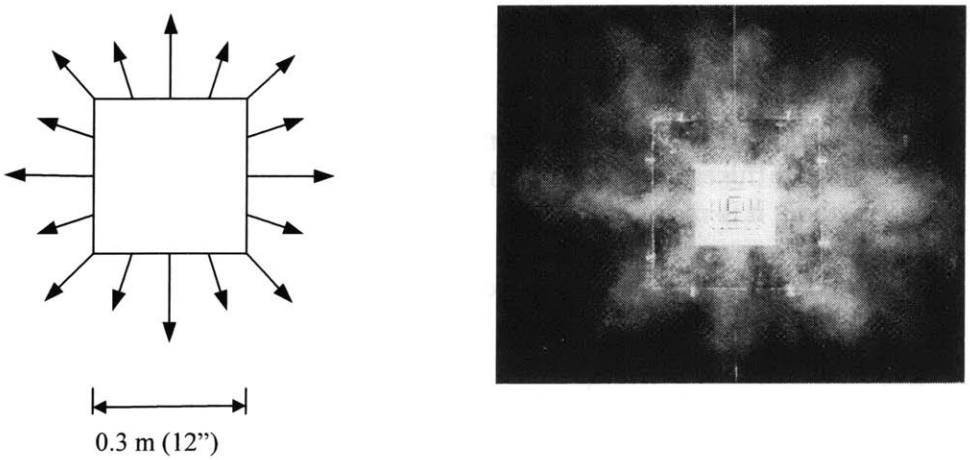

Figure 4.39 Flow sketch and smoke visualization for the square ceiling diffuser

The simulation of the square diffuser used both the momentum and box methods. Figure 4.40 shows schematically how the diffuser is simulated with the two methods: the flow direction needs to be described for the momentum method (Figure 4.40(a)) and the box size (Figure 4.40(b)). The box method requires high effort because it specifies flow information in four surfaces while the momentum method requires information in only one surface. Since the jets from the diffuser are very thin (around 0.05 m or 2 in), the measurements are more difficult due to the sharp velocity gradient. In this case, the box method used 40 measured velocities and a uniform temperature obtained from the heat balance for the box boundaries. On the other hand, the momentum method used a discharge velocity for the entire diffuser surface as the momentum source. The discharge velocity is an averaged maximum velocity measured at the perimeter of the diffuser. The flow direction specified in the momentum method was obtained from the smoke visualization. The air temperature used is the same as the supply air temperature in the duct.

Figure 4.41 compares the measured and calculated air velocities with the two methods at five positions in the room. It seems that the two methods gave similar results, although the momentum methods performed better in areas near poles 5 and 4 that are close to the diffuser. Also, the box method over-predicted the air velocity along the jet region.

Because of that over-predicted velocity in the jet region, the corresponding temperature predicted with the box method is lower than the measured one as shown in

Figure 4.42. Anyway the two methods can correctly predict the air temperature in the occupied zone. This is not surprising since the room airflow is well mixed and the energy balance ensures a correct mean air temperature.

The validation of the computed tracer gas concentration by the experimental data is illustrated in Figure 4.43. The computed results are only for the momentum method. The agreement between the computed results and the experimental data is very good. The box method can also be used to calculate the tracer gas concentration distribution with species balance. Since it is a well-mixed condition, a similar result is anticipated as indicated in the temperature prediction.

In conclusion, both the momentum and box methods predicted good results for the square ceiling diffuser. Since it is simpler to specify the boundary conditions for the momentum method, it is recommended.

This study has also used another diffuser from a different manufacturer to measure air velocity and air temperature. The purpose of the study is to identify whether the results obtained for the first diffuser are universal. In the measurement with the second diffuser, all the flow and thermal boundary conditions are identical to those used for the first diffuser. Figure 4.44 and Figure 4.45 compares the air velocity and air temperature measured with the two diffusers. The difference on room air velocity is within the measuring errors. The two temperature fields are nearly identical.

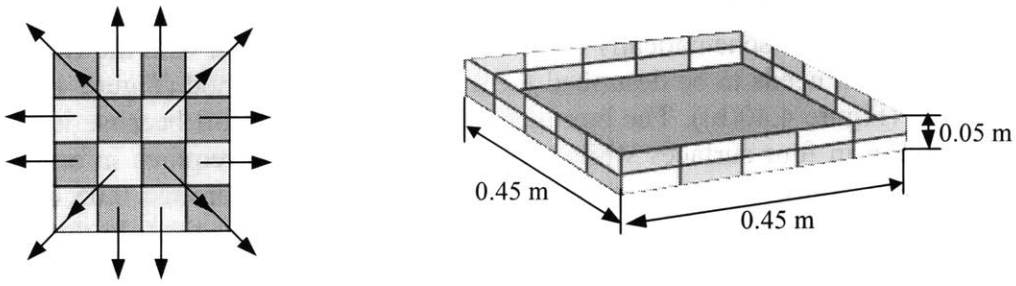

(a) (b)

Figure 4.40 Simulation of the square ceiling diffuser with
(a) the momentum method and (b) the box method

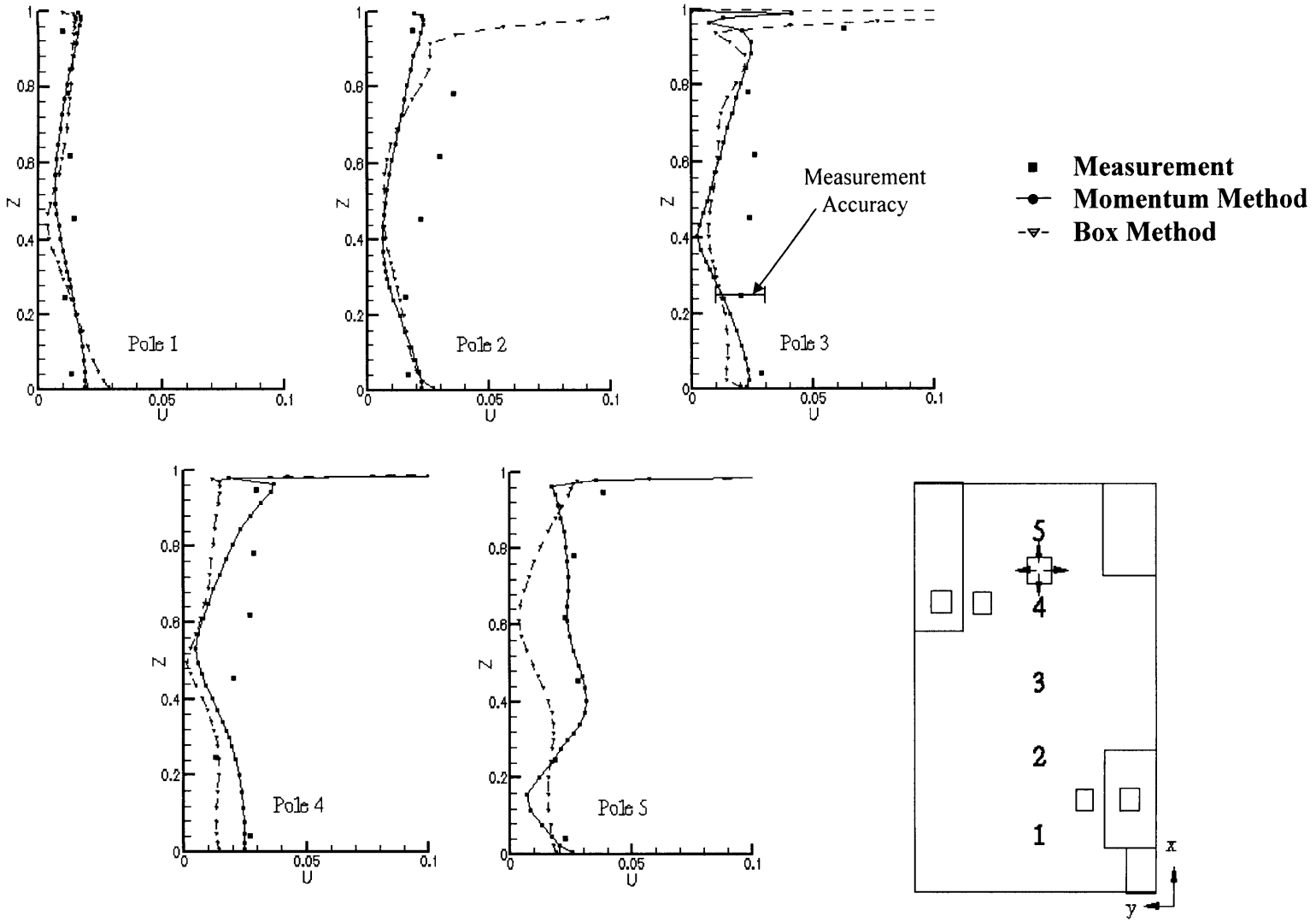

Figure 4.41 The comparison of the calculated and measured velocity profiles for the square ceiling diffuser at five positions in the room, Z=height/total room height (H), U=velocity/supply velocity (U_0), H=2.43m, U_0=5.2m/s

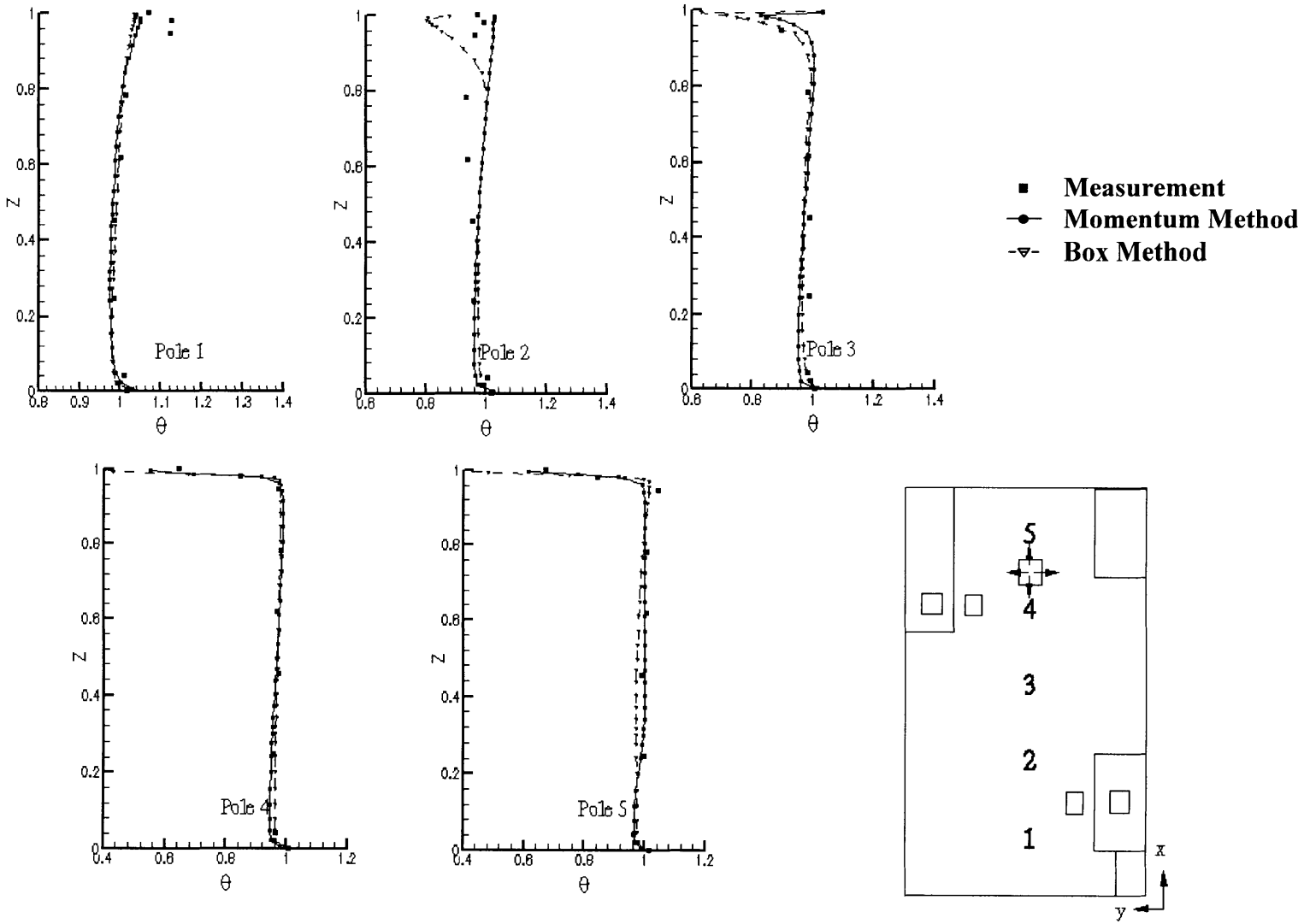

Figure 4.42 The comparison of the calculated and measured temperature profiles for the square ceiling diffuser at five positions in the room, Z=height/total room height (H), $\theta=(T-T_{in}/T_{out}-T_{in})$, H=2.43m, $T_{in}=14.5^{o}C$, $T_{out}=24.1^{o}C$

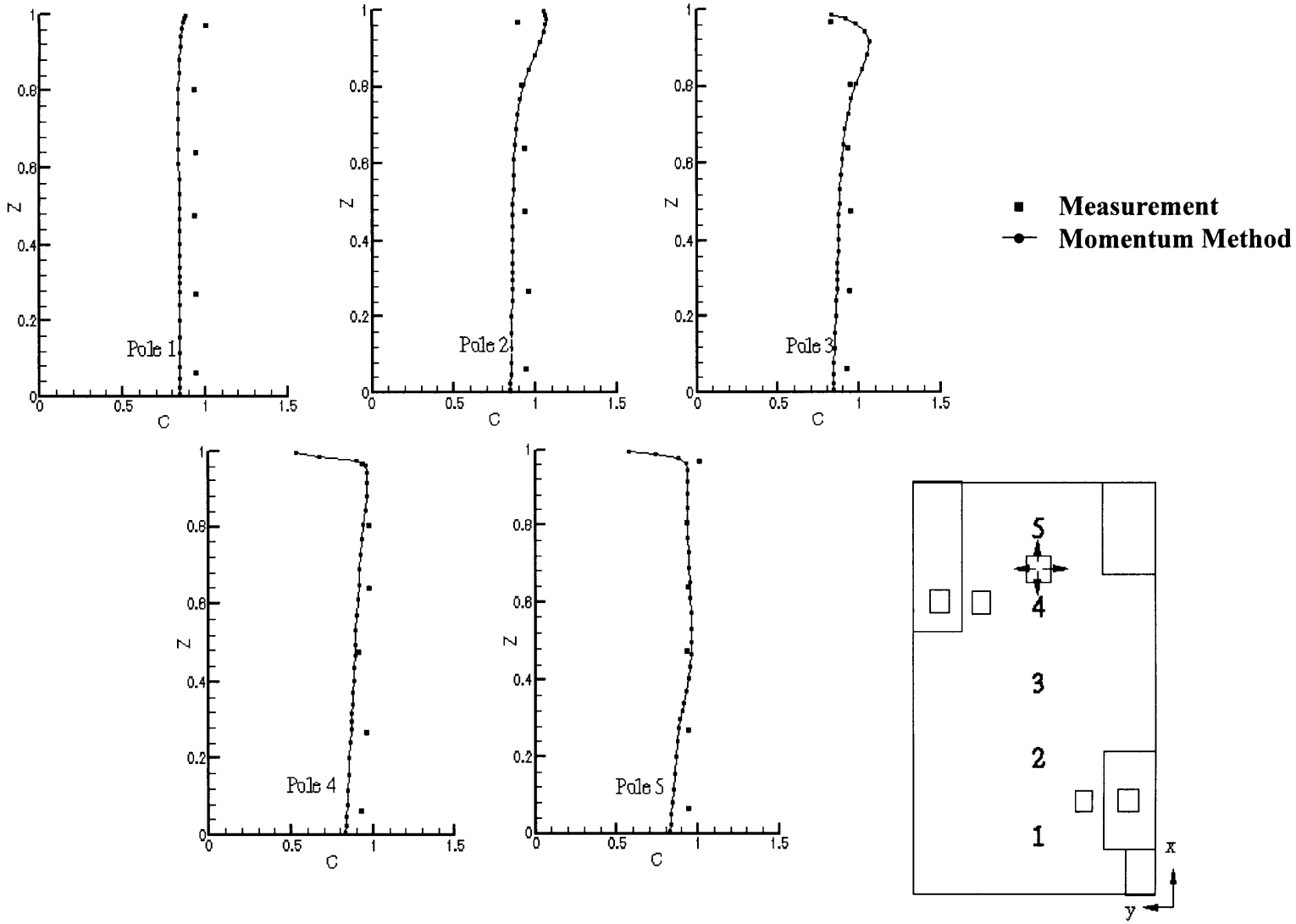

Figure 4.43 The comparison of the calculated and measured SF_6 concentration profiles for the square ceiling diffuser at five positions in the room, Z=height/total room height (H), $C=(c-c_{in}/c_{out}-c_{in})$, H=2.43m, c_{in}=0.0492 ppm, c_{out}=1.0496 ppm

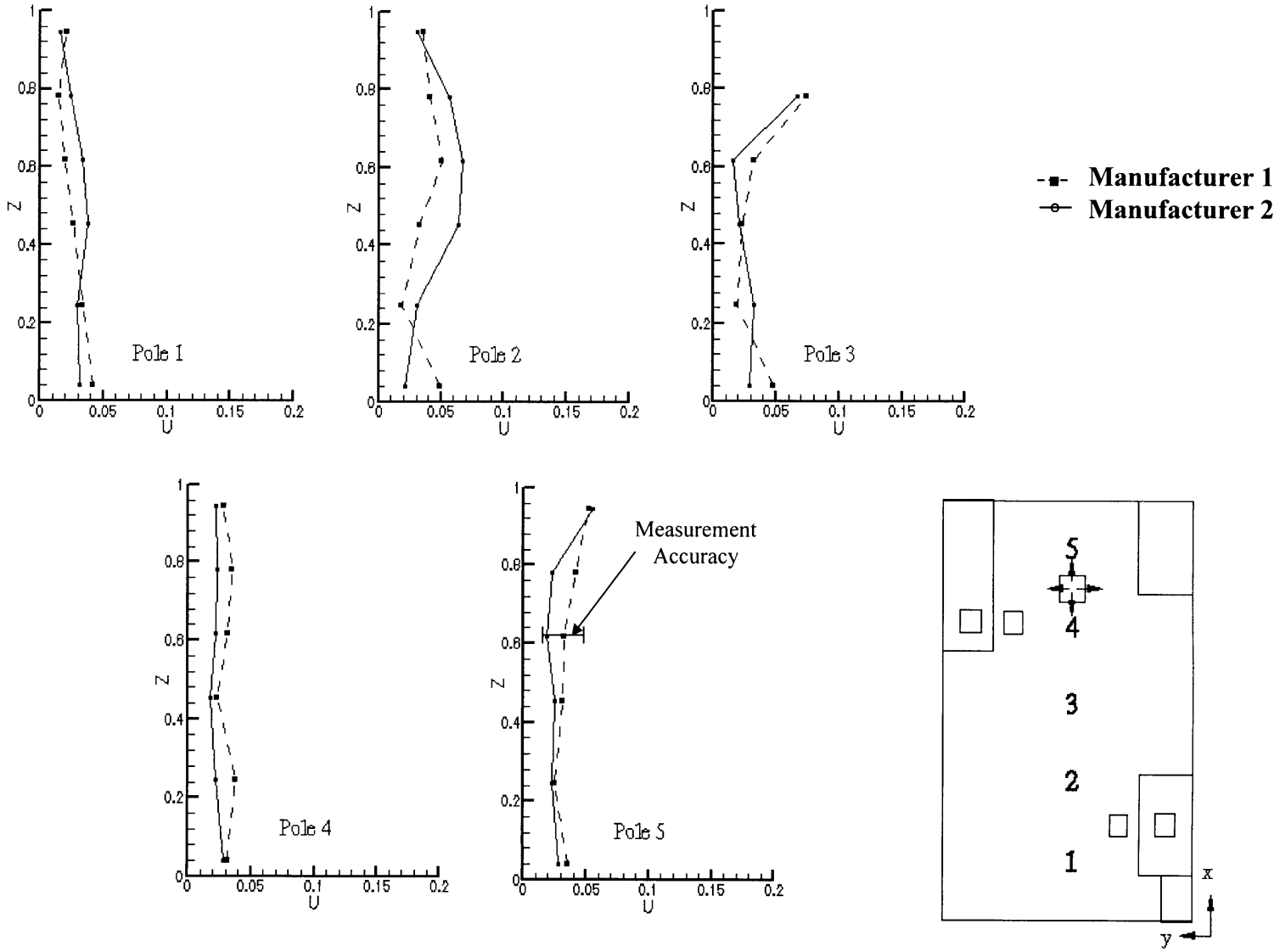

Figure 4.44 Measured air velocities with the two different square ceiling diffusers at five positions in the room

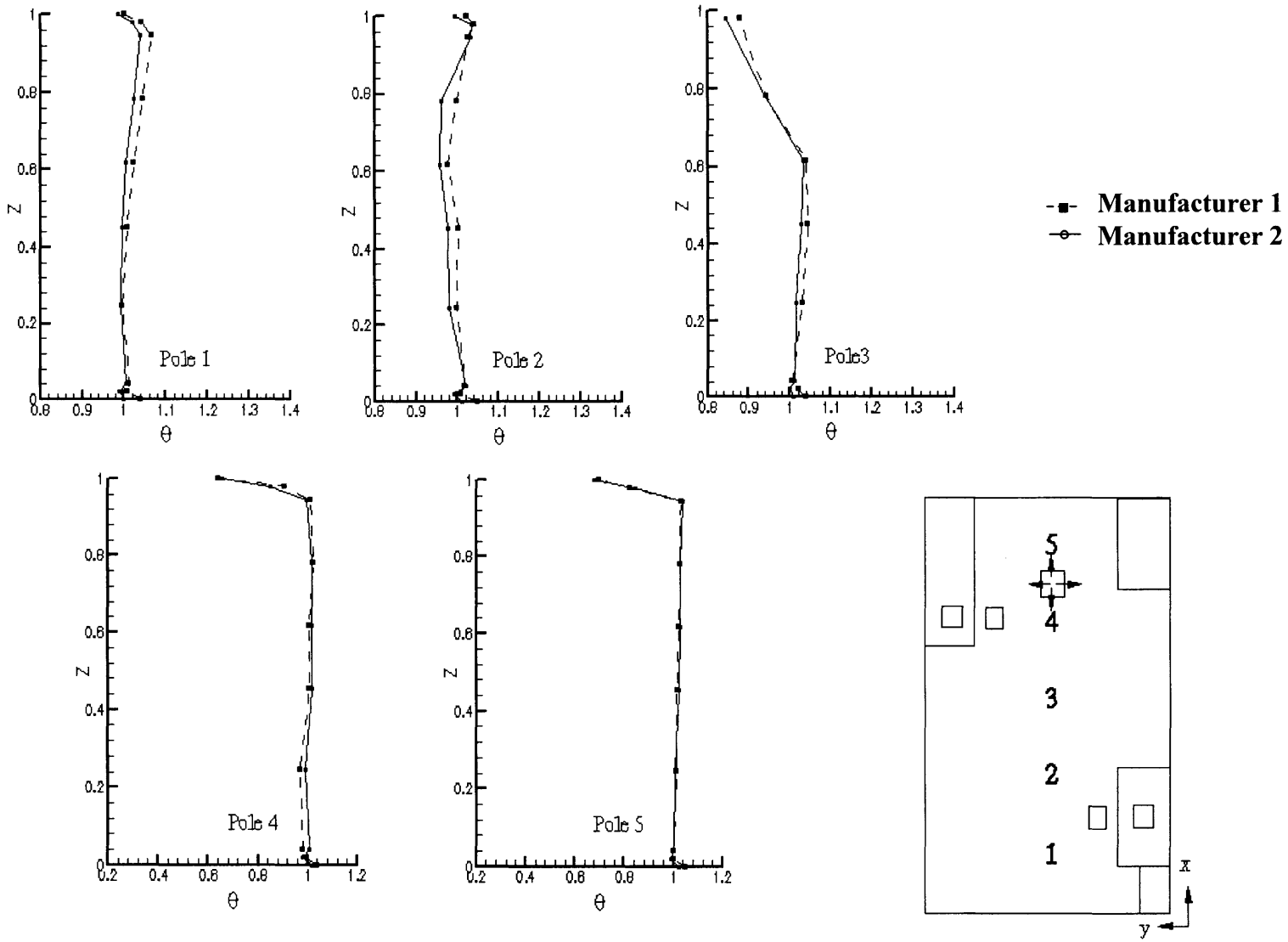

Figure 4.45 Measured air temperatures with the two different square ceiling diffusers at five positions in the room

4.5.6 Round Ceiling Diffuser

This section discusses the simulation of the round ceiling diffuser. The diffuser discharges a radial jet attached to the ceiling in a very thin layer (around 0.05 m or 2 in). The jet is similar to the one created by the square ceiling diffusers. Based on our experience with the square ceiling diffusers, the momentum method is used for the round ceiling diffuser, because the method gave the results as good as those with the box method. In addition, the momentum method is simpler than the box method.

Cartesian coordinates have difficult describing the geometry of the round diffuser, as shown in Figure 4.46(a). It is possible to specify the mass flow rate according to the ratio of the actual diffuser area over the cell size. However, we found that the specification can be further simplified. For example, the study shown in this section uses a half of the mass flow in four corner cells as marked with dash lines. All other cells covered by the diffuser are with 100% flow rate. These cells are marked with dashed lines. In addition to the mass flow rate, the discharge velocity components, air supply temperature, tracer gas concentration and turbulent properties have also been specified for the diffuser.

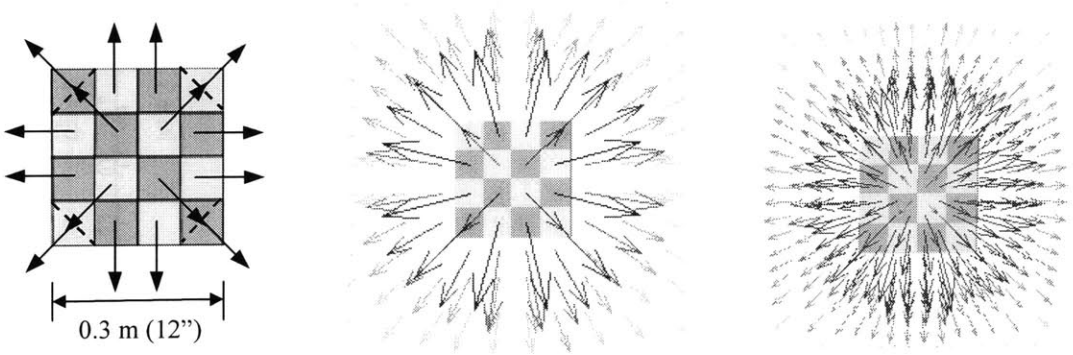

(a) (b) (c)

Figure 4.46 Simulation of the round ceiling diffuser with the momentum method (a) Discharge velocity specified, (b) the calculated results with coarse grids, and (c) the calculated results with fine grids

Different grids have been used to examine the sensitivity of grid number used for the diffuser on the results with the momentum method. In general, a finer numerical grid system is preferred since it reduces numerical diffusion and gives more accurate results. For the simulation of the radial jet, the numerical diffusion in the jet region can even produce wrong (non-radial) airflow pattern. Figure 4.46(b) shows that the resulting flow in the middle cross sections has a tangential component of velocity, although the input sets only a normal velocity component. This could be attributed to the numerical diffusion. Heikkinen and Piira (1994) studied this phenomenon and recommended the use of 8×8 patches to simulate a circular plate diffuser. Our study found that the numerical diffusion is reduced if more grids are used, as illustrated in Figure 4.46(c).

Figure 4.47 presents the calculated velocity profiles in the chamber with three different grid distributions. In general, the momentum method can predicted the air velocity in the chamber well, if the measuring errors are considered. Unlike in the slot diffuser case, the grid dependency in this case is not significant. The jet thickness predicted by the three grid systems is nearly the same.

The temperature profiles predicted with the momentum method under the three grid systems agree well with the measured data (Figure 4.48). Since this is a mixing ventilation case, the temperature in the chamber is uniform, except in the near diffuser region close to the ceiling. The case is not sensitive to the grid number.

Figure 4.49 shows that the profiles of tracer gas concentration. The momentum method slightly under-predicted the concentration in the chamber. The reason is difficult to identify. Perhaps, the concentration at the diffuser supply was higher than measured.

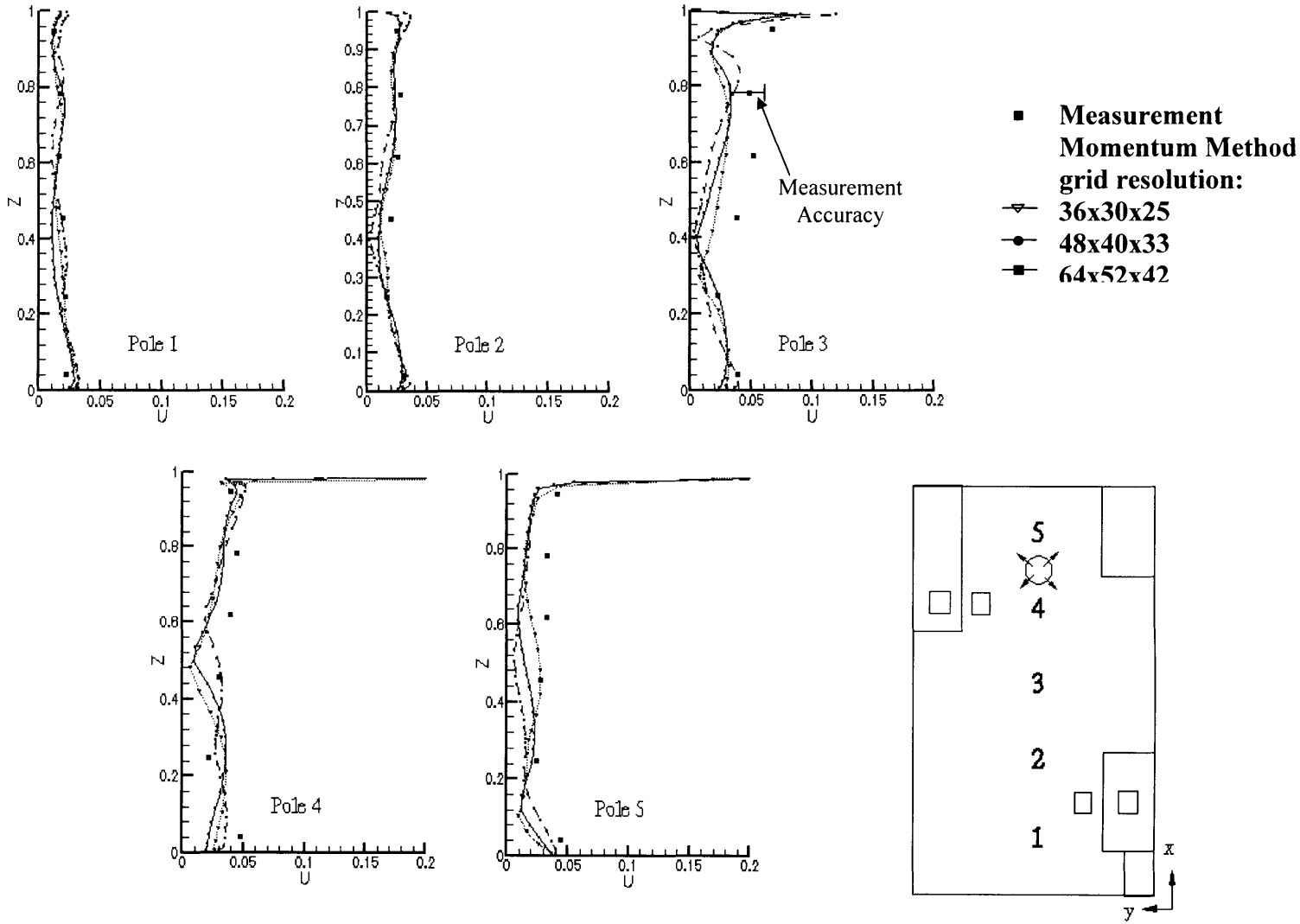

Figure 4.47 The comparison of the calculated and measured velocity profiles for the round ceiling diffuser at five positions in the room Z=height/total room height (H), U=velocity/supply velocity (U_0), H=2.43m, U_0=3.58m/s

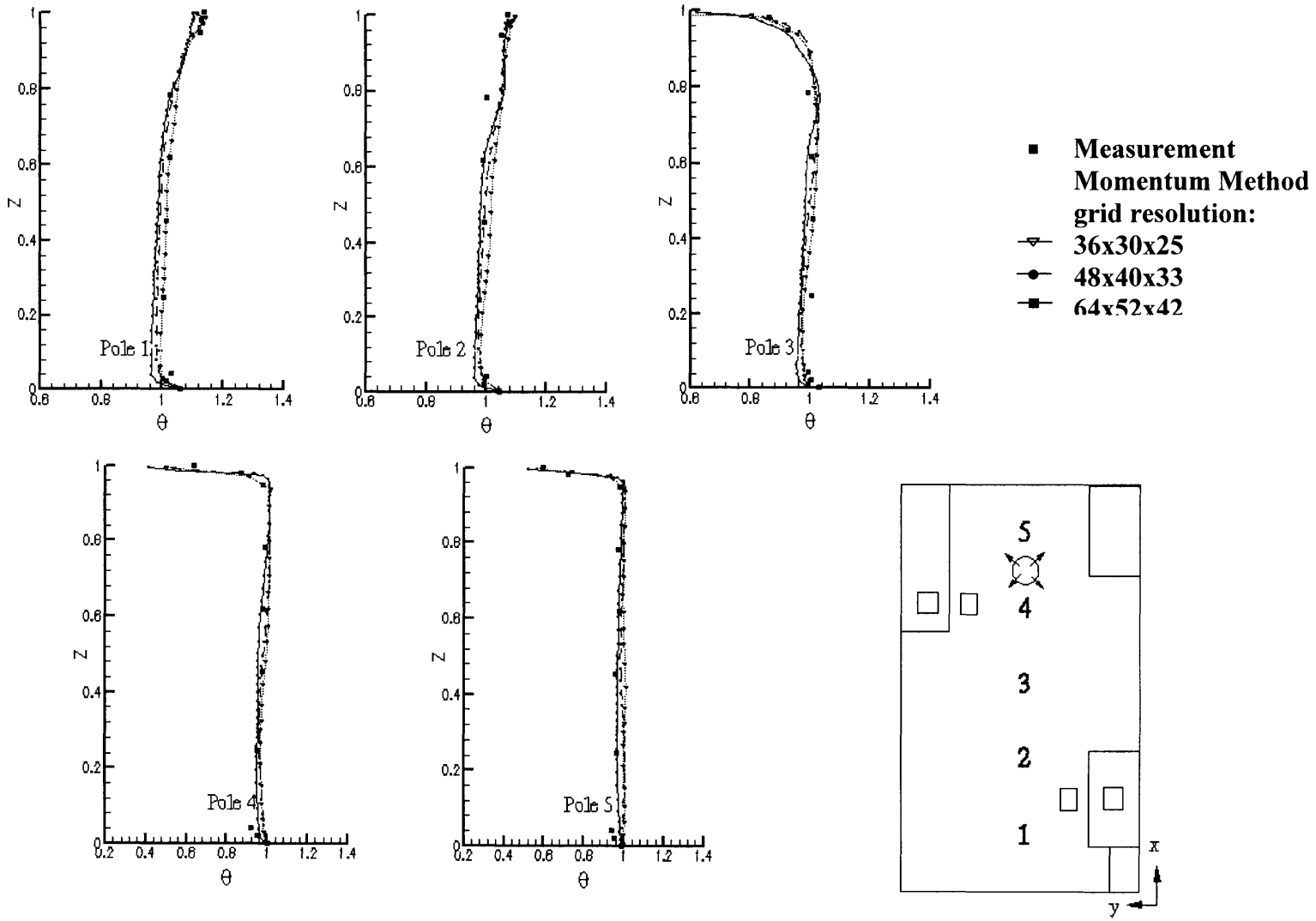

Figure 4.48 The comparison of the calculated and measured temperature profiles for round ceiling diffuser at five positions in the room, Z=height/total room height (H), $\theta=(T-T_{in}/T_{out}-T_{in})$, H=2.43m, $T_{in}=16.06^{o}C$, $T_{out}=24.8^{o}C$

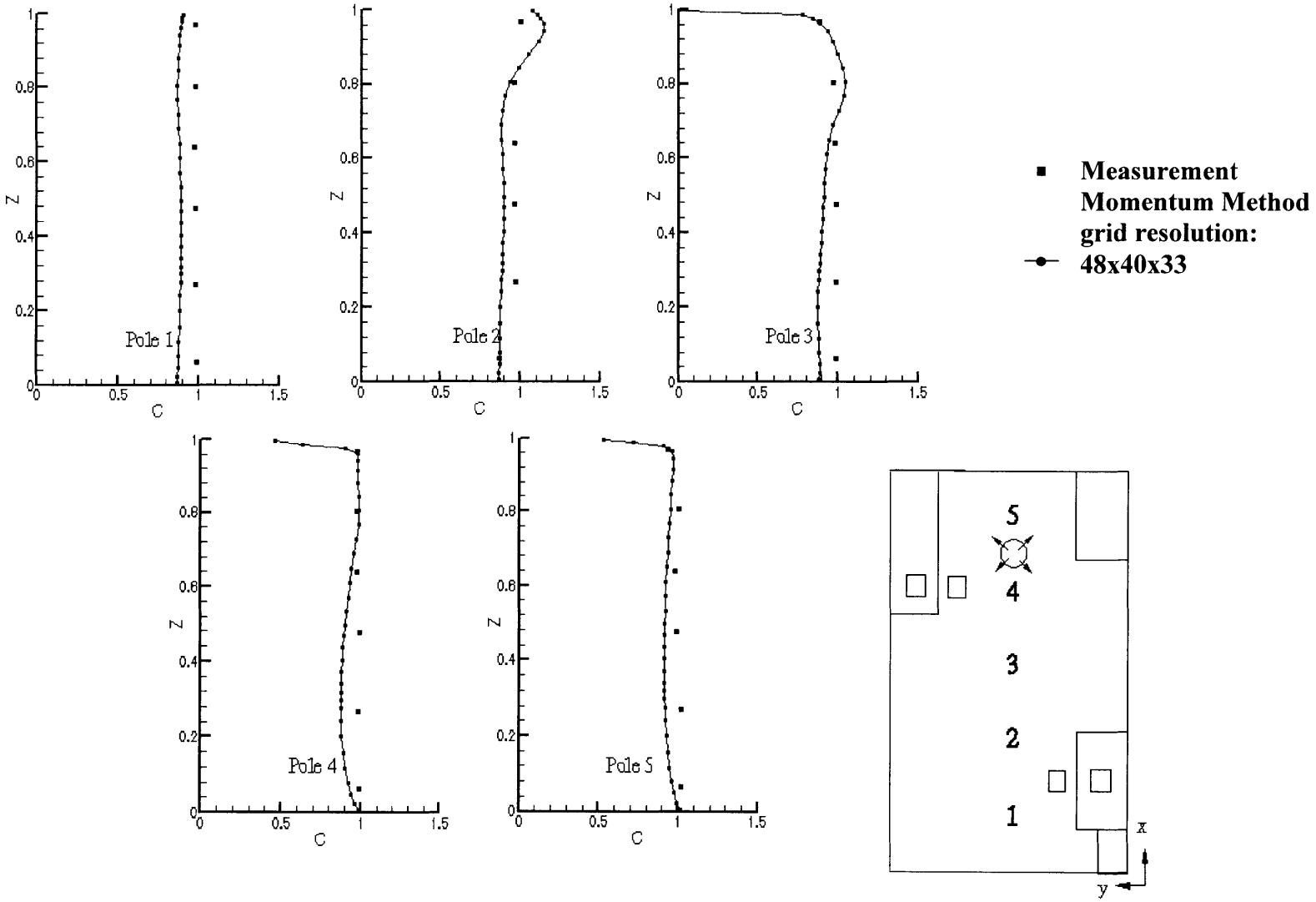

Figure 4.49 The comparison of the calculated and measured concentration (SF_6) profiles for round ceiling diffuser at five positions in the room, Z=height/total room height (H), $C=(c-c_{in}/c_{out}-c_{in})$, H=2.43m, c_{in}=0.027 ppm, c_{out}=1.0078 ppm

4.5.7 Vortex Diffuser

The vortex diffuser tested in this investigation discharges a swirl jet that entrains more room air than the circular ceiling diffuser. The higher entrainment causes faster jet velocity decay. The jet swirl is the strongest close to the diffuser, and the jet was attached to the ceiling. An experimental study (Shakerin and Miller 1996) found that the swirl disappears within three diffuser diameters, and the flow becomes radial. Our experiment confirms their conclusions. The distance at which the jet loses its tangential component depends on the airflow rate and diffuser geometry. Figure 4.50 shows a smoke visualization result from a manufacturer's catalogue. Our study used the same diffuser. The tangential angle at the edge of the diffuser shown in the figure is larger than what we have observed because the airflow rate used in the product catalogue was probably higher.

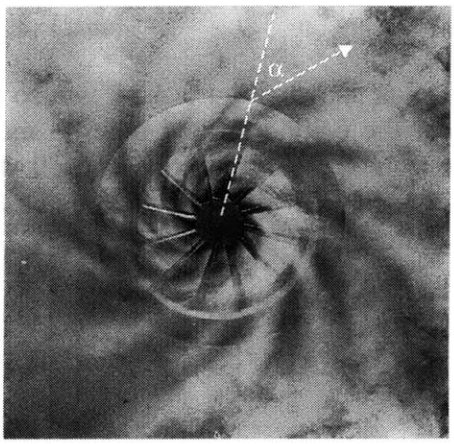

Figure 4.50 Smoke visualization for the vortex diffuser from manufacturer's catalogue

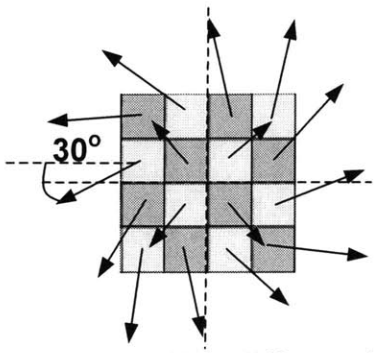

Figure 4.51 Simulation of the vortex ceiling diffuser with the momentum method

The tangential angle is very important because it is used to set the boundary conditions for the CFD simulation of the swirl jet. Figure 4.51 shows the flow directions (the tangential angle) used for the simulation. The investigation used only the momentum

method since the airflow pattern is expected to be similar to the other two ceiling diffusers that created attached jets as discussed in the previous sections.

The computed air velocity profiles in the chamber with the vortex diffuser are presented in Figure 4.52. Compared with the experimental data, the performance of the momentum method is acceptable. Although the vortex diffuser has a very complicated geometry, the momentum method can reasonably represent the diffuser. This can be confirmed if the results are compared with those for the square and round ceiling diffusers. Figure 4.52 shows discrepancies between the computed and measured velocities at the area around poles 2 and 3. Please note that our measurements with the hot-sphere anemometers have a large uncertainty when the velocity is low.

As in the previous cases, the momentum method can well present the temperature distribution in the chamber as shown Figure 4.53. First, it is easy to measure accurately the temperature distribution in the room. The temperature distribution was very stable, unlike the flow motion. The large difference on the upper part around pole 2 is due to the low velocity predicted by the momentum method.

The computed SF_6 concentration profile as shown Figure 4.54 is also in good agreement with the data except in the area near the ceiling around poles 2 and 3. The explanation used for the temperature can be used for the concentration as well. The very good agreement in the occupied zone is partly attributed to the mixing that can really eliminate the discrepancies between the computation and experiment.

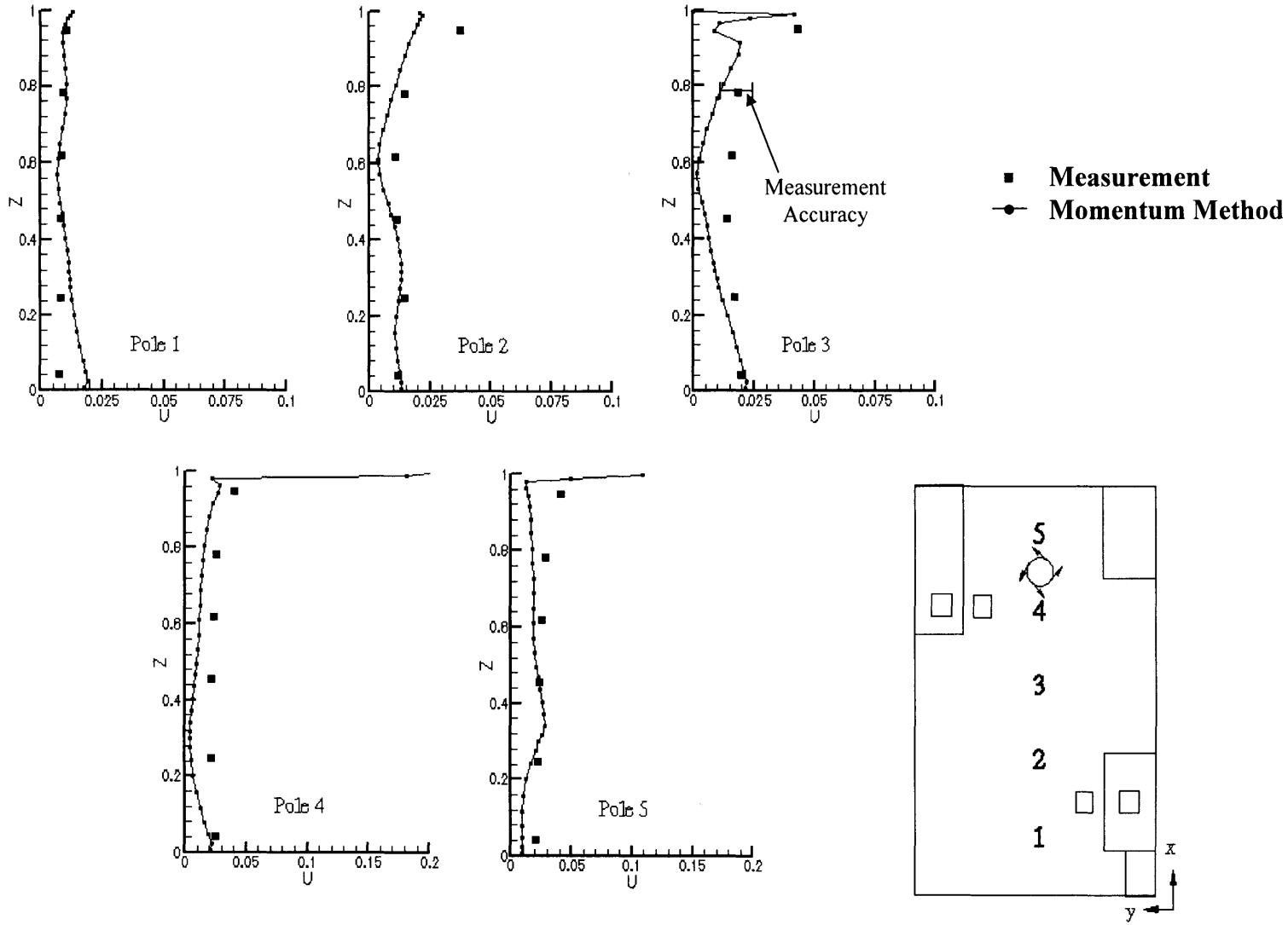

Figure 4.52 The comparison of the calculated and measured velocity profiles for the vortex ceiling diffuser at five positions in the room Z=height/total room height (H), U=velocity/supply velocity (U_0), H=2.43m, U_0=7.5m/s

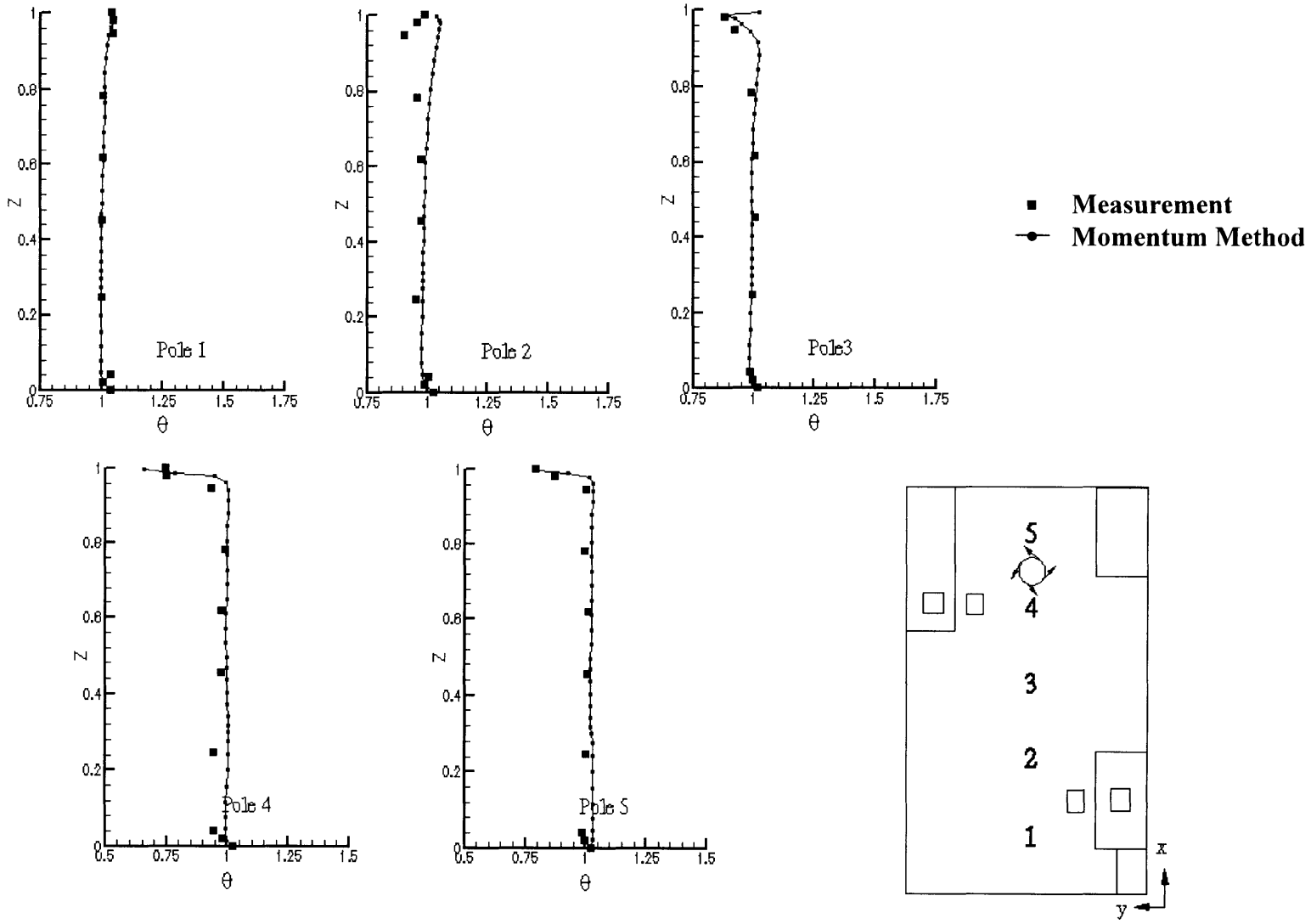

Figure 4.53 The comparison of the calculated and measured temperature profiles for the vortex ceiling diffuser at five positions in the room, Z=height/total room height (H), $\theta=(T-T_{in}/T_{out}-T_{in})$, H=2.43m, $T_{in}=16.35^{o}C$, $T_{out}=24.8^{o}C$

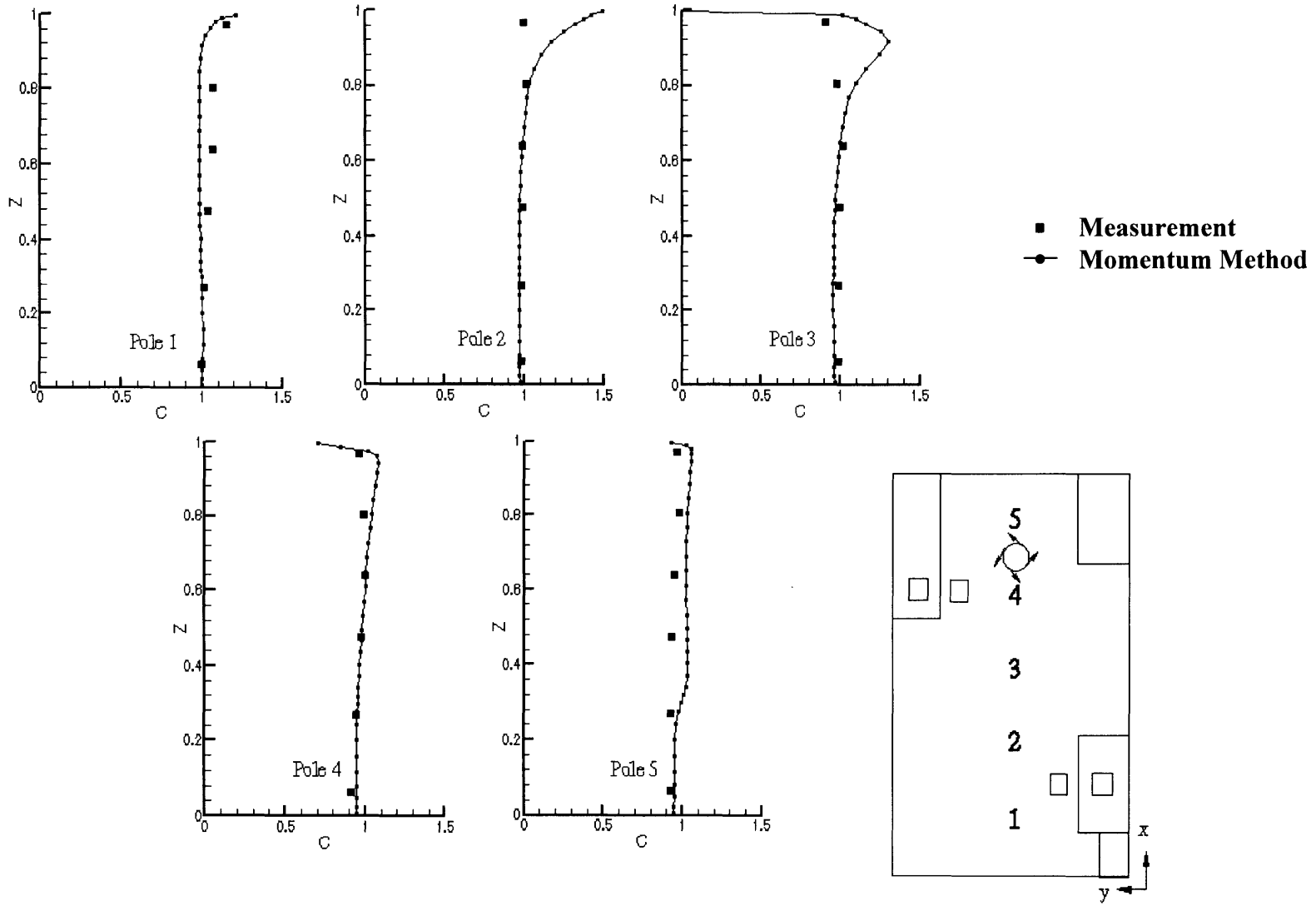

Figure 4.54 The comparison of the calculated and measured SF_6 concentration profiles for the vortex ceiling diffuser at five positions in the room, Z=height/total room height (H), $C=(c-c_{in}/c_{out}-c_{in})$, H=2.43m, c_{in}=0.0335 ppm, c_{out}=0.9773 ppm

4.5.8 Grille Diffuser

The last type of diffusers studied is a grille diffuser as shown Figure 4.55. The grille diffuser creates a jet that is neither free nor attached. Therefore, the jet formulae could not be used to predict the jet parameters, such as velocity and temperature profiles and decay. The vanes in the grill diffuser studied have been adjusted to discharge a jet normal to the grille surface. However, the resulting jet was shifted 5^{o} in the horizontal plane toward the side wall, as shown in Figure 4.55 (a). The reason for the deflection is probably due to a very short straight duct behind the diffuser that did not allow the full development of the flow in the duct. Another reason is probably from the impact of the asymmetric room geometry.

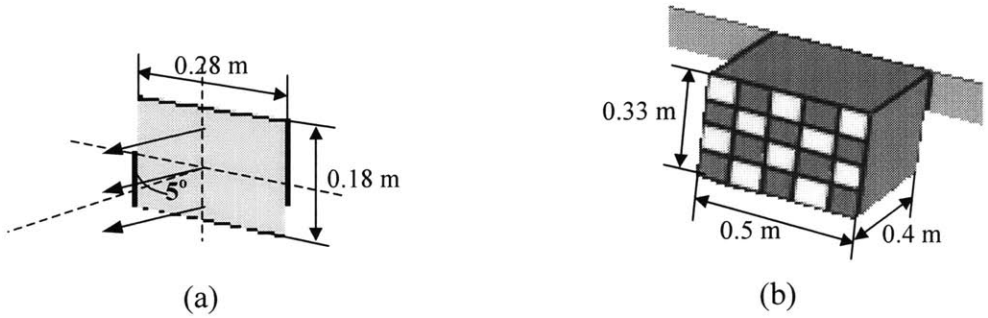

Figure 4.55 Simulation of the grille diffuser
with (a) the momentum method and (b) the box method

The simulations have used both the momentum and box methods for the diffuser. Figure 4.55(b) presents schematically the box size and patches used in the box method. The calculated and measured velocities are presented in Figure 4.56 for both methods. The results show that the maximum velocity at the jet region in the middle section is under-predicted with the box method. However, the calculated velocity profile, presented for pole 1 that is only 10 cm (4 in) away from the middle plane, shows much higher maximum jet velocity. In fact, the measured jet velocity profile in that area is asymmetric due to the possible asymmetric discharge angle.

Figure 4.57 presents calculated and measured temperature profiles. The calculated jet temperature profiles at pole 1 and 2 have the same thickness as the measured ones. However, the measured jet was closer to the ceiling than the calculated one. It is possible that the measured jet also had a small asymmetric discharge angle towards the ceiling.

The prediction of the tracer gas concentration with the momentum method is good as shown in Figure 4.58. In the middle of pole 5, the calculated data shows a small peak that was not measured. The SF_6 was released to a small box, while the CFD cell for the source is significantly larger. The difference can cause a large error near the source. Otherwise, the agreement between the measured data and the computed results is acceptable.

The results with the momentum method are better than those with the box method. The accuracy of the box method depends on the velocity direction obtained from the smoke visualization. The flow direction with such a small deflection angle (5-10^{o}) is difficult to observe. On the other hand, the measurements for the slot diffuser did not have such a problem since the jet deflection angles were much larger (30-60^{o}). It is more reliable to estimate the jet discharge angles at diffuser surface for the momentum method than to present the angels at the surfaces for the box method.

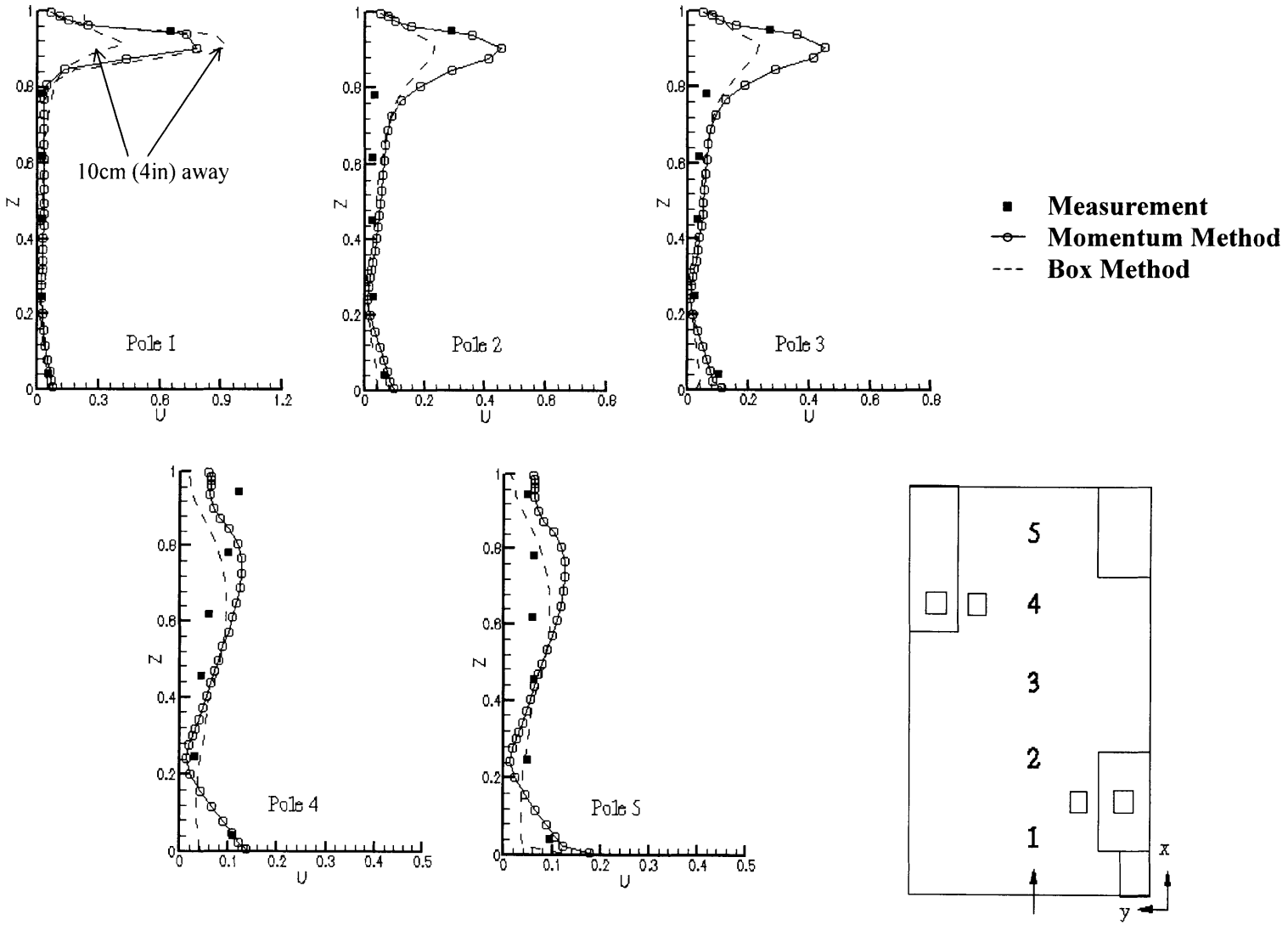

Figure 4.56 The comparison of the calculated and measured velocity profiles for the grille diffuser at five positions in the room Z=height/total room height (H), U=velocity/supply velocity (U_0), H=2.43m, U_0=1.4m/s

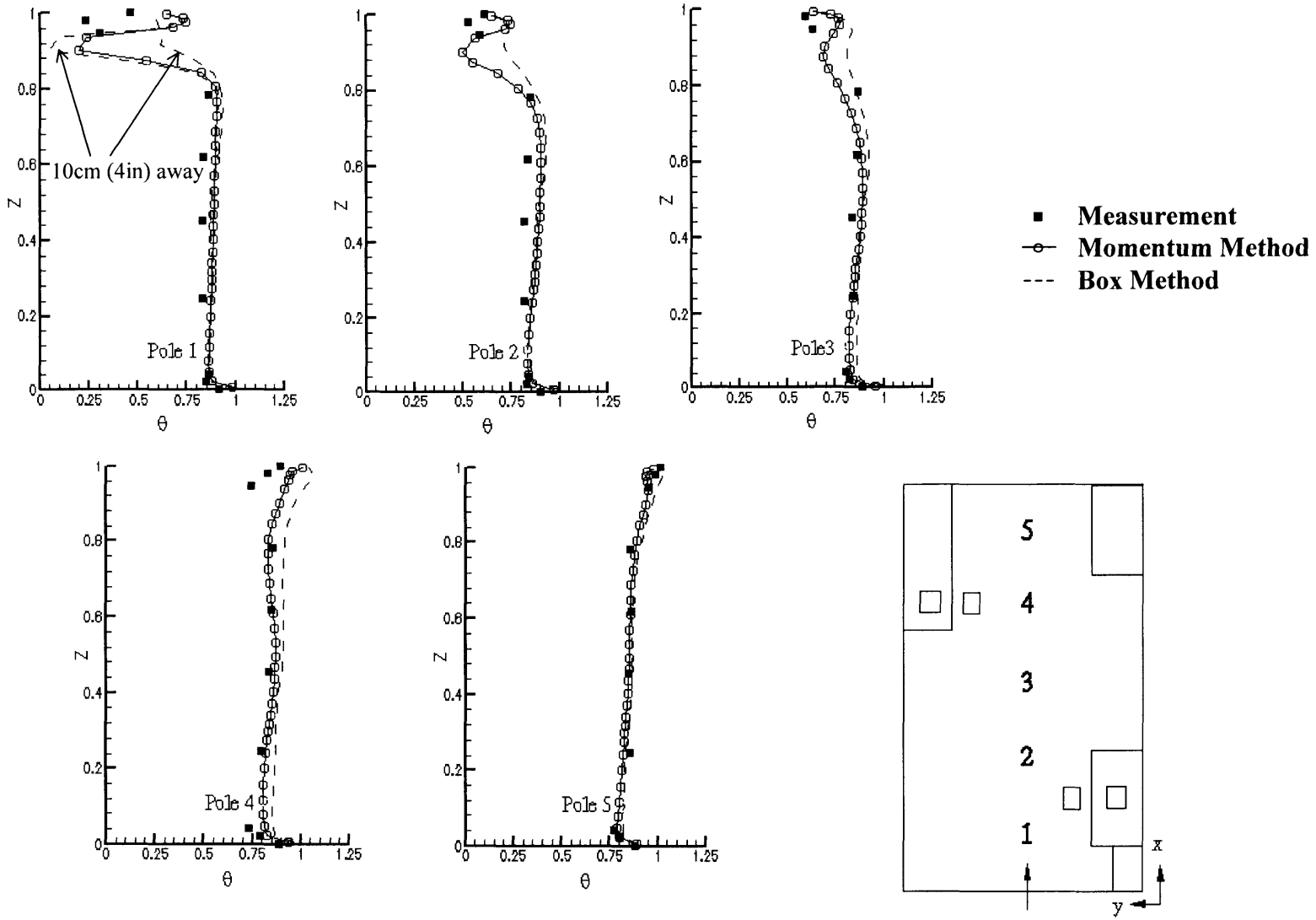

Figure 4.57 The comparison of the calculated and measured temperature profiles for the grille diffuser at five positions in the room, Z=height/total room height (H), $\theta=(T-T_{in}/T_{out}-T_{in})$, H=2.43m, $T_{in}=15.1^{o}C$, $T_{out}=24.5^{o}C$

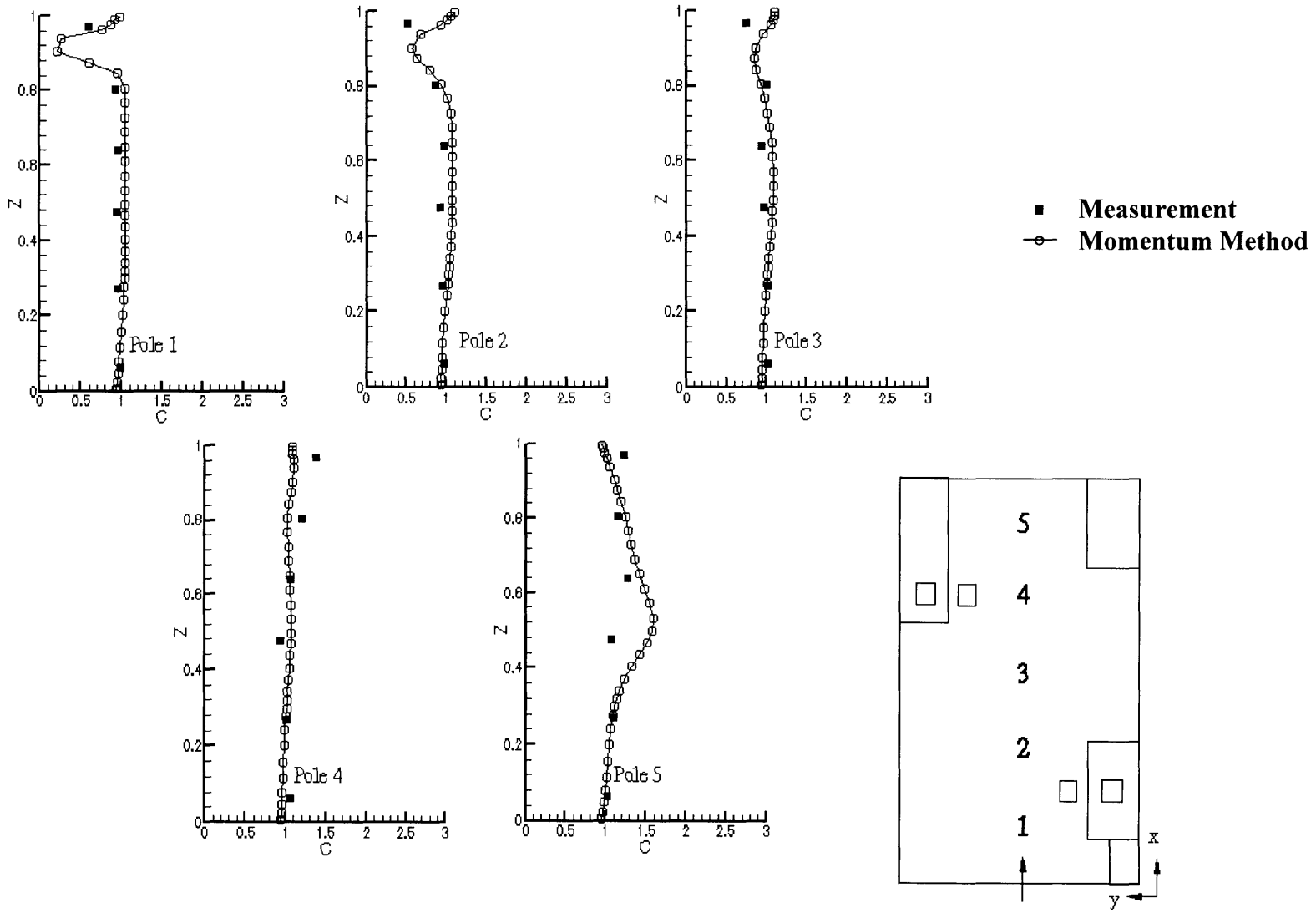

Figure 4.58 The comparison of the calculated and measured SF_6 concentration profiles for the grille diffuser at five positions in the room, Z=height/total room height (H), $C=(c-c_{in}/c_{out}-c_{in})$, H=2.43m, c_{in}=0.048 ppm, c_{out}=0.992 ppm

4.6 Method of Test (MOT)

From our experience with the simulations of the eight complex diffusers, the momentum and box methods can give reliable results. With the methods, there is no need to specify the detailed diffuser geometry. The data used in the methods are diffuser geometry that is normally available from diffuser manufacturer catalogues and the flow field in the diffuser vicinity. More specific, the momentum method requires the discharge velocity, and the box method needs the distribution of the jet velocity on the box surface. The discharge velocity and jet velocity distributions on the box surface are not available in the current catalogues. They need to be obtained through measurements. The following section describes a method of test on how to obtain the discharge velocity and jet velocity distribution.

4.6.1 Effective Diffuser Area for the Momentum Method

ASHRAE Standard 70-1991 Method of Testing for Rating Performance of Air Outlets and Intakes specifies a procedure, a test chamber and instruments for the measurements of the diffuser jet throw, pressure drop, and discharge velocity. The test procedure defines how to measure the discharge velocity. From the measurements of the discharge velocity and flow rate, manufacturers calculate an effective diffuser area called the area factor. In fact, the area factor is a function of the airflow rate. If the area factor changes with the flow rate more than 5%, the manufacturers should report the change. Only a few manufacturers provide information on the area factor, but not the measuring positions. Therefore, it is difficult to use the area factor to determine the discharge velocity for the use in the momentum method.

The measurements for the nozzle diffuser (Skovgaard et al. 1990) found that the area factor depended on the Reynolds number, i.e. flow rate. This further complicates the problem. In order to confirm that the area factor is a function of the flow rate, we have further tested the grille diffuser. The nozzle diffuser and the grille diffuser represent the two extreme of the geometry complexity among the eight diffusers studied here: the nozzle is most complex and the grille is the simplest.

The flow rate tested for the grille diffuser was 3, 5 and 8 ACH, respectively. Figure 4.59 presents the measured discharge jet velocities in front of the diffuser. The mean discharge velocity $U_{in,\,mean}$ is an average of the nine measured values in front of the diffuser. The results show that the effective area changes slightly (4-5%) with the three flow rates as shown in Table 4.4. Note that the area factor measured A_o is not the same as that calculated from the geometry of the diffusers A_{og}. For the nozzle diffuser, the difference between the two is about 10%, but for the slot diffuser it can be more than 100%. This seems independent on the effective area ratio, ε, that ranges from 0.072 for the nozzle diffuser to ε=0.96 for the grille diffuser.

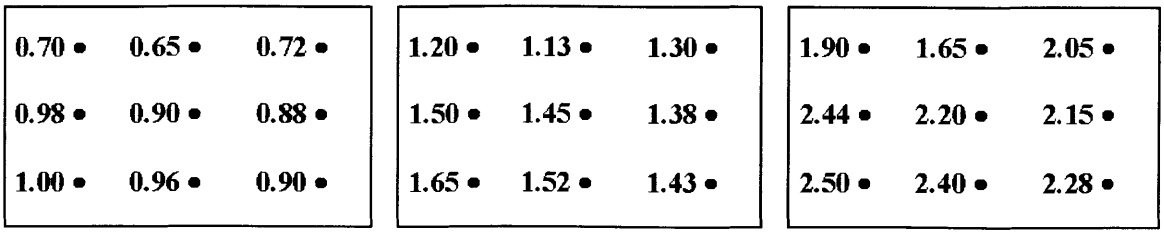

n=3 ACH, $U_{in,\ mean}$=0.86 m/s n=5 ACH, $U_{in,\ mean}$=1.40 m/s n=8 ACH, $U_{in,\ mean}$=2.18 m/s

Figure 4.59 The measured discharged jet velocities (m/s) in front of the grille diffuser for different airflow rates

Cheong et al. (1999) studied a square diffuser and found that the results are better if the measured discharge velocity was used than if the calculated discharge velocity from the diffuser geometry was employed. This confirms again that the area factor cannot be correctly estimated from the diffuser geometry. Therefore, it is very important that diffuser manufacturers measure the area factor and the corresponding measuring positions along with other parameters described in the ASHRAE Standard 70-1991. The area factor is needed not by the momentum method, but also the jet formulae for the box method.

The measured data for the grille diffuser shows further that the discharge velocity is not uniform. The jet had a higher momentum in the lower left corner of the diffuser. Since it is the intention of the project to use realistic ducting in the study, the straight duct behind the diffuser is less than 10 times the equivalent diffuser diameter. As a result, the non-uniformity of the velocity is approximately ± 18% for the flow rates studied. The non-uniformity of the discharge velocity has been observed in other diffusers and test facilities. Figure 4.60 shows the discharge velocity distribution with a round ceiling diffuser installed in the same chamber as the grille diffuser and that with a valve diffuser in another chamber.

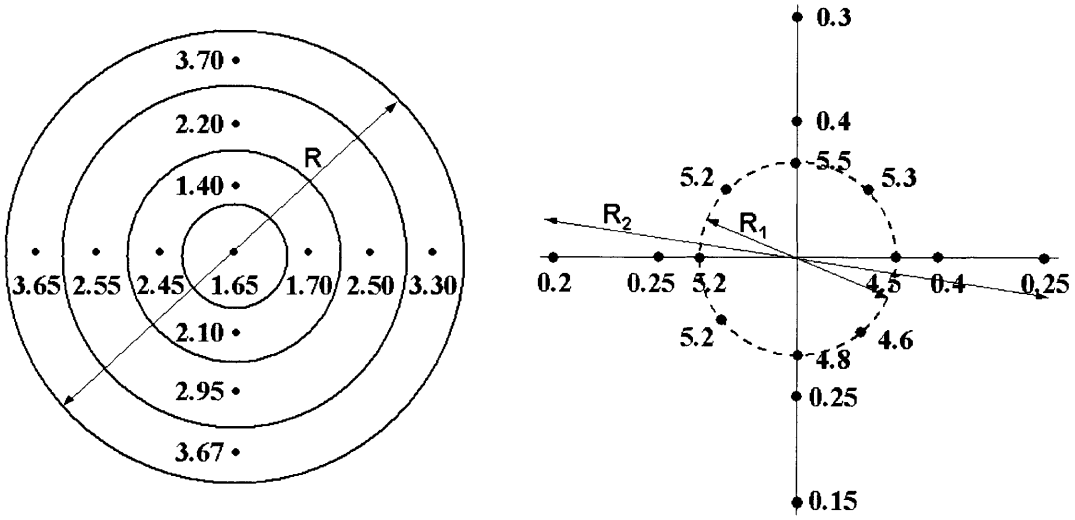

Figure 4.60 The discharge velocities (m/s) measured with (a) the round ceiling diffuser (R=35 cm or 13.5"), (b) and the valve diffuser (R_1=12 cm or 4.75", R_2=40 cm or 15.75").

Table 4.4 The measured and calculated diffuser geometry and flow parameters

Diffusers	Air exchange Rate ACH (kg/s)	Supply velocity fpm (m/s)	Gross area (A_{gross}) m^2	Area factor (A_o) * m^2	$\varepsilon=A_o/A_{gross}$ %	Geom. Area Factor (A_{og}) ** m^2
Nozzle	3.0 (0.0378)	748 (3.80)	0.71x0.17	0.0083	7	0.0092
Slot (Linear)	9.2 (0.1410)	768 (3.90)	1.15x0.1	0.0301	26	0.0690
Valve	2.1 (0.0133)	990 (5.03)	$(0.12)^2\pi/4$	0.0022	19	0.0043
Displacement	5.0 (0.0768)	70 (0.35)	1.1x0.53	0.1830	32	0.2332
Square Ceiling	4.9 (0.0750)	1024 (5.20)	0.3x0.3	0.0120	13	0.0159
Round Ceiling	5.0 (0.0768)	705 (3.58)	$(0.3)^2\pi/4$	0.0179	25	0.1101
Vortex	5.1 (0.0782)	1476 (7.50)	$(0.16)^2\pi/4$	0.0087	43	-
Grille	8.0 (0.1228)	429 (2.18)	0.28x0.18	0.0469	93	0.0336
	5.0 (0.0768)	276 (1.40)	0.28x0.18	0.0457	91	0.0336
	3.0 (0.0456)	169 (0.86)	0.28x0.18	0.0442	88	0.0336

* The measured area factor

** The area factor calculated from the diffuser geometry

On the other hand, correct measurement of the area factor requires a precise measurement of the airflow rate, because the discharge velocity is a function of the area factor and flow rate. Our experience indicates that it is more precise to measure the airflow rate with a constant, step-up, or step-down tracer-gas method than with anemometers or Pitot tubes.

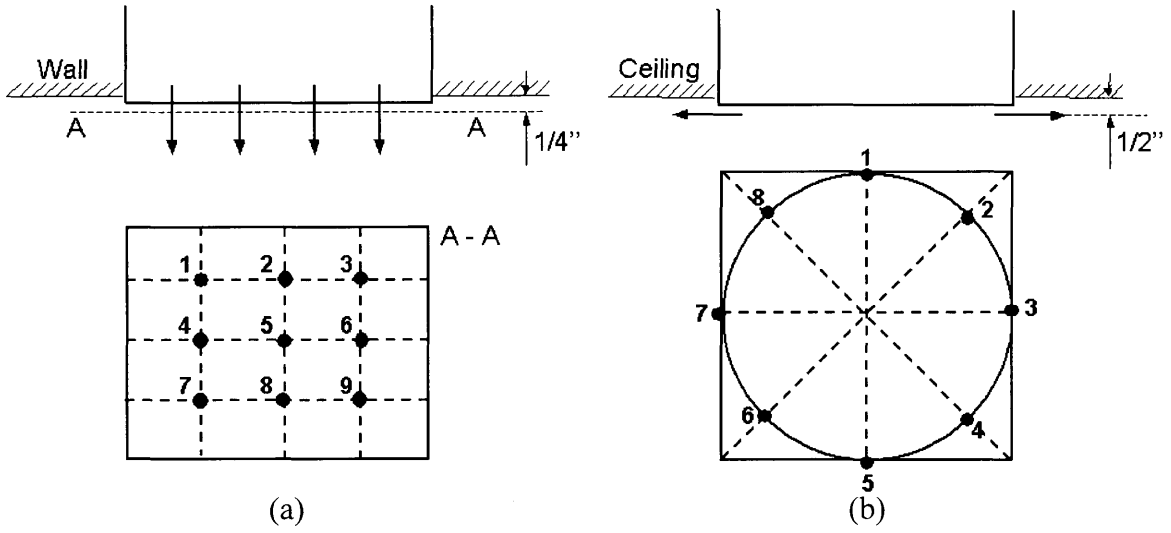

Figure 4.61 Recommended positions for measurements of the discharge velocity

As discussed in the previous section, the momentum method works for the displacement, square, round, vortex, and grille diffusers. In order to measure the discharge velocity (or area factor), Figure 4.61 recommends where the discharge velocity should be measured. Figure 4.61(a) is for the displacement and grille diffusers and Figure 4.61(b) for the other three types of the diffusers. Measurements in the multiple points are suggested in actual room installations because of the possible asymmetry on the flow distribution. In manufacturers' laboratories, the measuring points can be reduced if their system can produce a uniform distribution.

In addition to the installation of the diffuser and different manufacturing processes can have an influence on the effective area factor as reported by Nielsen (1991), Knappmiller (1994), Shakerin and and Miller (1991). A careful adjustment after installation can help to avoid the asymmetry of flow discharge.

4.6.2 Boundary conditions for the Box Method

The box method seems the only practical alternative in the simulations of complex diffusers if the momentum method fails. This type of diffusers includes the valve and nozzle diffusers. The box method is also suggested for the slot diffuser because the momentum method cannot accurately predict the flow in the jet region due to its numerical diffusion.

The original box method (see chapter 3.7) requires measured data for all the simulated variables in order to set the diffuser boundary conditions. If a simulation is isothermal, only the velocity distribution needs to be measured for the box method. However, if the simulated space needs information on temperature and concentration distributions, the temperature and concentration profiles need to be measured on the box surface. This is not a trivial job. Figure 4.62 shows the SF_6 distribution in front of the grille diffuser (n=5 ACH). This concentration measurement requires a significant labor effort and expensive equipment. Consequently, the box method, although powerful, is not widely used in practice.

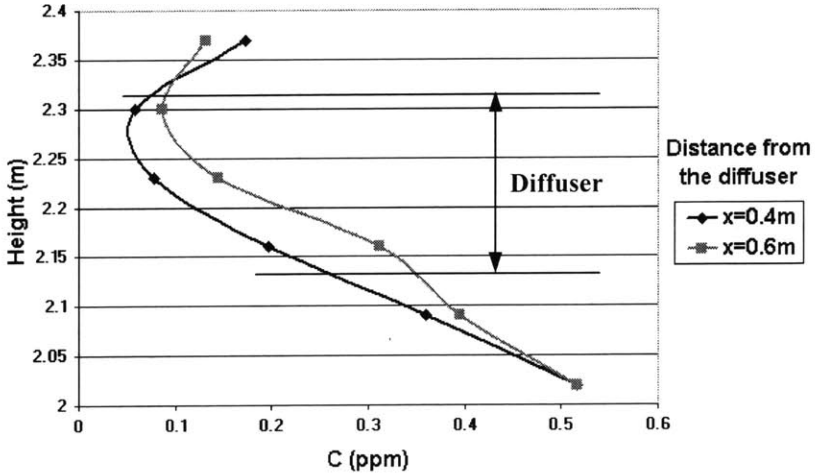

Figure 4.62 The SF_6 distribution at 0.4m (1.3 ft) and 0.6 m (2.0 ft) in middle front of the grille diffuser

We have found that the resulting distributions of air temperature and tracer gas concentration in a room are not very sensitive to the profiles of the temperature and concentration at the box surface. The use of the average temperature and concentration values is a more practical approach to impose boundary conditions for the box method. This implies that only the velocity profile needs to be specified in the box method, and the other parameters are set as uniform. The uniform air temperature T_{box} and tracer gas concentration C_{box} can be determined from the mass, energy and concentration balance at the box boundaries:

$$\dot{m}_{\text{sup }ply} + \Delta\dot{m} = \dot{m}_{box} \tag{4.3}$$

$$\dot{m}_{\text{sup }ply} T_{\text{sup }ply} + \Delta\dot{m}\, T_{exhaust} = \dot{m}_{box} T_{box} \tag{4.4}$$

$$\dot{m}_{\text{sup }ply} C_{\text{sup }ply} + \Delta\dot{m}\, C_{exhaust} = \dot{m}_{box} C_{box} \tag{4.5}$$

where $T_{exhaust}$ and $C_{exhaust}$ are temperature and concentration at the room exhaust. Figure 4.63 shows a sketch of the mass balance for the box boundaries.

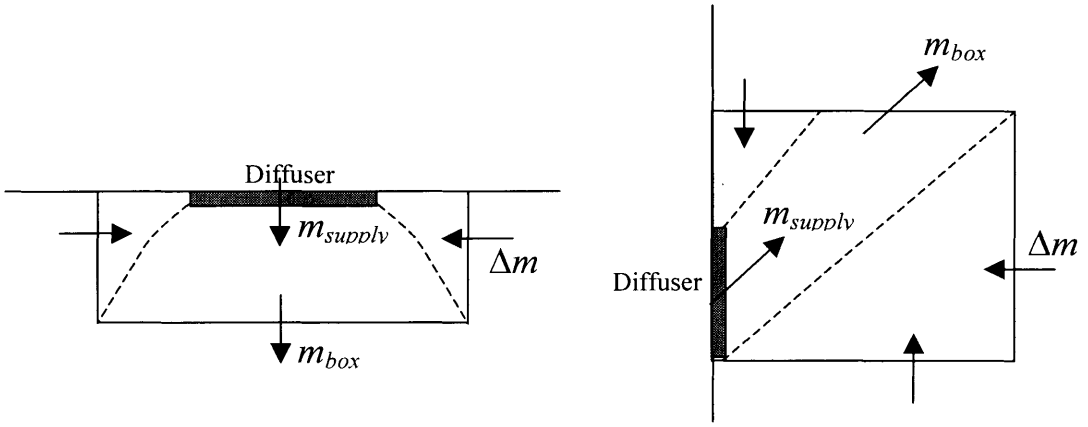

(a) (b)

Figure 4.63 Sketch of the mass balance at the box boundaries for (a) a downward free jet and (b) an inclined jet

Our experience indicates that the velocity distribution at the box surface cannot be assumed to be uniform, otherwise the box method cannot correctly predict air parameters in the jet region (see chapter 4.5.2). With the velocity distribution and uniform temperature and tracer gas concentration at the box surface, the temperature and tracer gas concentration distributions in the jet region can be correctly predicted.

Since the boundary conditions for air temperature and tracer gas concentration can be specified as uniform, the measurements needed to obtain the velocity profile can be performed under isothermal conditions. The measured velocity distribution needs to be

measured at quite a few points (six to fifteen at least) in the jet discharge direction. The measurements should be performed with low-velocity anemometers as described in ASHRAE Standard 70-1991. The standard gives a test method for rating the performance of air outlets and inlets based on the jet throw. Our method of test for the box boundary conditions complies with ASHRAE requirements for velocity measurements. In addition, smoke visualization is needed to determine jet flow direction at the box surface.

The measurements with hot sphere/wire anemometers and smoke visualization are sufficient to impose reliable boundary conditions for a diffuser with the box method. Measurements with more sophisticated equipment such as LDA are expensive and are not a standard measurement technique in diffuser manufacturers' laboratories. In fact, our calculations for the nozzle diffuser indicate that the smoke visualization provides a more important source of information than the measurements with LDA (see Chapter 4.5.1). The box size is more important than the detailed velocity data on the box surfaces.

The box size should be in the region where the diffuser jets have merged, if the diffuser discharges multiple jets (see Figure 4.1). The RANS equations with turbulence modeling have difficulty to simulate flow in the region before the jets have merged. The minimal box size can be roughly estimated from the momentum method or smoke visualization. On the other hand, the box size should not be too large since a large box may cover a portion of the domain that is important for thermal plumes, room size, and obstacles in the room, due to a strong buoyancy effect and effect of contained flow.

Although the box data gathered under isothermal conditions can be applicable for non-isothermal conditions, the box size should be selected in such a way that the buoyancy force is negligible compared to the momentum force at the box surface. A practical criterion to compare those forces is the local Archimedes number Ar_x (Grimitlyn and Pozin 1993). If the local Archimedes number is smaller than a certain value then jet is weakly non-isothermal and can be modeled by the isothermal jet formulae (see Chapter 3.5.1). From the definition of the Ar_x, we have derived a critical distance x_c where the jet velocities are still predominately influenced by the momentum forces. Within that distance the jet velocities obtained from the isothermal experiment can be used as the boundary conditions in non-isothermal simulations.

The box size should be smaller than x_c from the diffuser in the jet discharge direction:

- Plane (linear) jets

$$x_c \le H_0 \left(\frac{K_1^2}{K_2} \frac{0.15}{\mathrm{Ar}_0} \right)^{2/3} \tag{4.6}$$

- Axisymmetric and radial jets

$$x_c \le K_1 \left(\frac{0.1}{K_2} \frac{A_0}{\mathrm{Ar}_0} \right)^{1/2} \tag{4.7}$$

where K_1 is the centerline velocity decay constant, and K_2 is the centerline temperature decay constant, Ar_0 is the Archimedes number based on the air supply parameters and defined by Equation (3.10) (see chapters 3.3.2 and 3.5.1 for more details).

This criterion implies that the box method is not suitable for low Reynolds number flows such as displacement ventilation. For displacement ventilation, the buoyancy force strongly influences the jet development from its discharge. The jet from the displacement diffuser changes very rapidly its profile shape and position in front of the diffuser (Figure 3.7). On the other hand, in case of the mixing ventilation, the criterion should be easy to satisfy with a relatively small box.

For example, the grille diffuser has K_1=5.7 and K_2=3.4. The calculated x_c is 1.0 m (3.3 ft) for 5 ACH, and 0.56 m (1.8 ft) for 3 ACH. Our calculation set the box size to be 0.4 m (1.3 ft). The x_c is very small because the buoyancy is very strong at 3 ACH. The corresponding air supply temperature is 10.62 °C (51 °F). In fact, the jet would separate from the ceiling at a very short distance in such a condition. Therefore, the box size should be very small. On the other hand, the slot diffuser (K_1=2.2, K_2=1.7) has x_c = 7.3 m. The box size can be very large. For most mixing ventilation systems, the x_c is very large because of its relative high discharge jet velocity. The buoyancy force can be safely neglected in the diffuser vicinity.

Based on the above analysis, the MOT for obtaining boundary conditions for the box method can be summarized as follows:

- The room size should comply with ASHRAE Standard 70-1991 for the throw test
- The required equipment is low velocity anemometers and smoke visualization devices
- The test can be performed under isothermal conditions
- Air velocities should be measured for 6-15 points in the jet region at the box surface where the jet impinges as shown in Figure 4.63
- The box surface should be in the region where jets have merged (Figure 4.1)

The data from the MOT and the following procedure is necessary to set boundary conditions for a diffuser in CFD simulations:

- Check if the jet is weakly non-isothermal in the box surface (Equations (4.6) and (4.7))
- Use the balance equations to determine T_{box} and C_{box} (Equations (4.3) to (4.5))
- Calculate the supply turbulence properties (Equations (4.1) and (4.2))
- Define box patches with uniform velocities and set other supply air parameters

4.7 Performance of the Momentum and Box Methods

The jet flow from the diffusers that can be successfully simulated with the momentum method is:

- Jets with a low Reynolds number such as that from the displacement diffuser

- Attached ceiling jets such as those from the square, circular, and vortex ceiling diffusers
- Compact jets with a small discharge angle such as that from the grille diffuser

The box method with measured data from MOT is a robust modeling method. The momentum from the induced jet flow in other surfaces of the box boundary can be safely neglected with little impact on the accuracy of flow field. The reason is that the high jet momentum on the box surface normal to the jet is mainly responsible for the most of the mass, energy, and species transport. Also, the averaged velocity for each patch is sufficient as boundary conditions for the diffuser. Therefore, there is no need to measure in great detail the velocity profiles on the box surface. The box method is better for the mixing diffusers with which the local Archimedes number is low. However, the method is not suitable for the displacement diffuser because of the high Archimedes number.

The momentum method can correctly describe boundary conditions for some mixing diffusers and the displacement diffuser. With the momentum method, it is easier to specify boundary conditions than that with the box method. Also, the momentum method only needs a discharge velocity for specifying the boundary conditions, while the box method requires the jet velocity distribution at the box surface.

Note that the attached ceiling jets studied are very thin (about 0.05 m or 2 in.), and the gradients for all air parameters in the jet region are very large. Therefore, accurate measurements to obtain data for the box method are very tedious, and the flow directions may not be easily determined with smoke visualization due to the high velocity. Also, the specification of box boundary conditions is time consuming since the jets spread in all radial directions from a diffuser. Therefore, the momentum method is preferred and recommended over the box method for design applications.

Table 4.5 Summary for the simplified diffuser modeling

Diffusers	Momentum Method	Box Method	Recommended Method
Nozzle	Poor	Good	Box
Slot (Linear)	Poor	Good	Box
Valve	Poor	Good	Box
Displacement	Good	Poor	Momentum
Square Ceiling	Good	Good	Momentum
Round Ceiling	Good	Good	Momentum
Vortex	Good	Good	Momentum
Grille	Good	Good	Momentum

Table 4.5 shows the recommended method for different diffusers. For the nozzle, slot and valve diffusers, the box method can simulate the boundary conditions better than the momentum method. This is because the flow mixing is too complex for the momentum method to handle. The flow develops, merges, and combines (see Figure 4.1)

in front of the diffusers to form a developed jet. The momentum method may not be appropriate. To properly simulate this flow, very fine grid resolution is required. Even though, in case of the nozzle diffuser, a very fine grid resolution may not provide a correct prediction of the airflow pattern (Emvin and Davidson 1996). Therefore, the box method is recommended to simulate these complex diffusers.

Jet flows with a low Reynolds number but with strong buoyancy effect such as displacement diffuser cannot be easily simulated with the box method. The reason is that the buoyancy force plays an important role in jet development from its discharge. The jet flow and temperature change rapidly in the diffuser vicinity. The measurements would have to be performed under non-isothermal conditions. If the measurements were performed for non-isothermal conditions, the data could be used only to simulate the diffuser in a room with the same thermal conditions as the measured ones. Any change in room geometry and/or heat sources could have a significant influence on the data. The application would be very limited. Therefore, the box method is not recommended for the displacement diffuser.

The performance of the box and momentum methods has been investigated for the eight commonly used air supply diffusers. This study concludes that the simplified diffuser simulation methods can produce reliable results.

CHAPTER 5

VALIDATION OF THE FLOW PROGRAM

5.1 Introduction

With the CFD equations and simulation techniques described in Chapter 2 and the method for complex diffuser modeling reported in Chapter 3 and 4, this Chapter presents the simulated results of indoor environment for several complex indoor spaces. Currently, most CFD simulation uses the standard two-equation k-ε turbulence model or the RNG k-ε model that requires intensive computing. The simulations presented in this chapter uses the zero-equation turbulence model to reduce the computing time. The use of the zero-equation model may make the combined CFD simulation with energy analysis possible. The combined study will be detailed in Chapter 6.

Chen and Xu (1998) developed the zero-equation model used. They have validated the model with the experimental data for a number of simple indoor airflows:

- Natural convection (Olson et al. 1990)
- Forced convection (Nielsen et al. 1978)
- Mixed convection (Schwenke 1975)
- Displacement ventilation (Chen 1988)

The first three cases used for validation, although they are two-dimensional, represent basic elements for indoor airflows. The displacement ventilation is more complex since it contains all the three basic flow elements and is a three-dimensional case of displacement. The results showed that the zero-equation model gave similar results to those with the k-ε models.

In order to ensure the zero-equation model having a general applicability for indoor airflow simulation, it is important to validate the model further for more complex indoor airflows with sound experimental data.

5.2 Validation of the Flow Program

This section reports further validation of the zero-equation model for three more complicated indoor airflows (Srebric et al. 1999):

- Room airflow with infiltration and a baseboard heater (Infiltration case)
- Room airflow with forced convection and a partition wall (Partition case)
- Room with displacement ventilation (Displacement ventilation case).

Note that the displacement ventilation case used in this section is different from the one used by Chen and Xu. Our case is with higher quality experimental data and complicated indoor geometrical and thermal conditions.

Each case is simulated with the flow program and validated with the measured data. The experimental data have been obtained from the environmental chamber at MIT as described in Chapter 3. The room air velocities and temperatures are measured at about 30 to 70 points and wall temperatures in about 25 to 35 points depending upon the case. The experiment layout, air supply velocities and temperatures, internal heat sources and validation are presented in the following subsections.

The flow program calculated the flow field parameters (pressure, velocity, and temperature) with specified wall temperatures as boundary conditions. For simplicity, the temperatures are the mean values of the measurements at different locations on each room enclosure surface. This applies to all the cases presented in this chapter.

5.2.1 The infiltration case

This case evaluates the zero-equation model for a room with strong buoyancy. The case is similar to winter heating with a baseboard heater under the window, as shown in Figure 5.1. In order to create large temperature stratification in the room, cold air due to infiltration was introduced from the wall opposite to the heater. The infiltration was simulated by using a large diffuser with a very low air inflow. The outlet is at the ceiling. Table 5.1 and Table 5.2 show more information about the geometrical, thermal, and flow boundary conditions in the room.

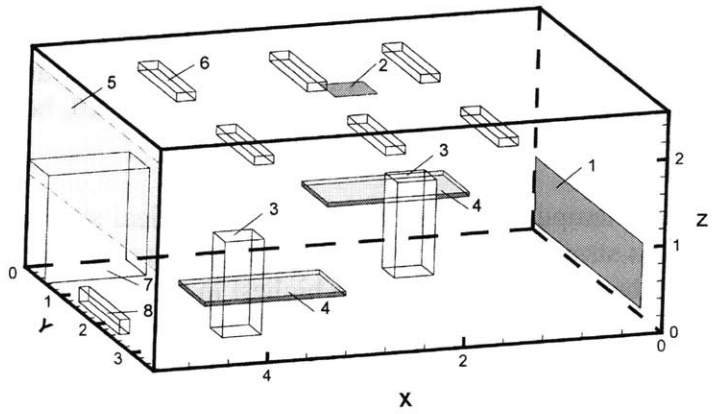

Figure 5.1 The layout of the infiltration cases simulated and tested in the chamber (inlet -1, outlet -2, person -3, table -4, window -5, fluorescent lamps -6, cabinet -7, baseboard heater -8)

Table 5.1 The geometrical, thermal, and flow boundary conditions for the diffuser and window

Infiltration case			
Inlet diffuser	Size: 3.05 m x 0.75 m (10ft x 2.5 ft)	Temperature: 13.2°C (55.8°F)	Velocity: 0.017 m/s (3.5 fpm)
Window	Size: 3.65 m x 1.16 m (12 ft x 3.8 ft)	Temperature: 20.7°C (69.3°F)	

Table 5.2 The size and capacity of the heat sources

Heat source	Size	Power
Baseboard heater	1.2 x 0.1 x 0.2 m^3 (3.9 x 0.3 x 0.7 ft^3)	1500 W (5,118 Btu/hr)
Person	0.4 x 0.35 x 1.1m^3 (1.3 x 1.15 x 3.6 ft^3)	75 W (256 Btu/h)
Overhead lighting	0.2 x 1.2 x 0.15 m^3 (0.7 x 3.9 x 0.5 ft^3)	34 W (116 Btu/h)

Figure 5.2 shows the CFD results with the zero-equation model. The results are available for all three-dimensions. However, the figure illustrates the results in only two sections: a vertical section at the center plane of the room and a horizontal section just above the infiltration diffuser. Figure 5.2(a) shows the velocity distribution. The infiltration from the diffuser falls down to the floor due to the negative buoyancy of the cold air and moves further along the floor to the front wall (the wall with the window). The baseboard heater generated a very strong plume that brought the air to the ceiling level. The exhaust extracted some of the flow and the rest moves further along the ceiling to form a large circulation in the room.

However, the flow in this room was not two-dimensional. Figure 5.2(b) illustrates that the air moves downward along the walls and the window at a location away from the heater, because the wall and window surface temperature is lower than the room air temperature. The two people generate weak plumes at the height where the velocity vector was plotted, because the buoyancy effect was not strong enough at that height.

Figure 5.2(c) gives the temperature distribution in the vertical section. In the vicinity of the diffuser, air temperature is stratified because the infiltration has a low momentum and mixes immediately with room air. The air temperature is the highest in the area close to the heater.

Figure 5.2(d) presents the flow paths by the particle tracking technique from the computed air velocity field. The results are for two particles, one at the infiltration inlet and the other close to one of the occupants. The particle tracks confirm the airflow pattern shown in Figure 5.2(a). It happens in this example that both particles are extracted through the outlet at the ceiling.

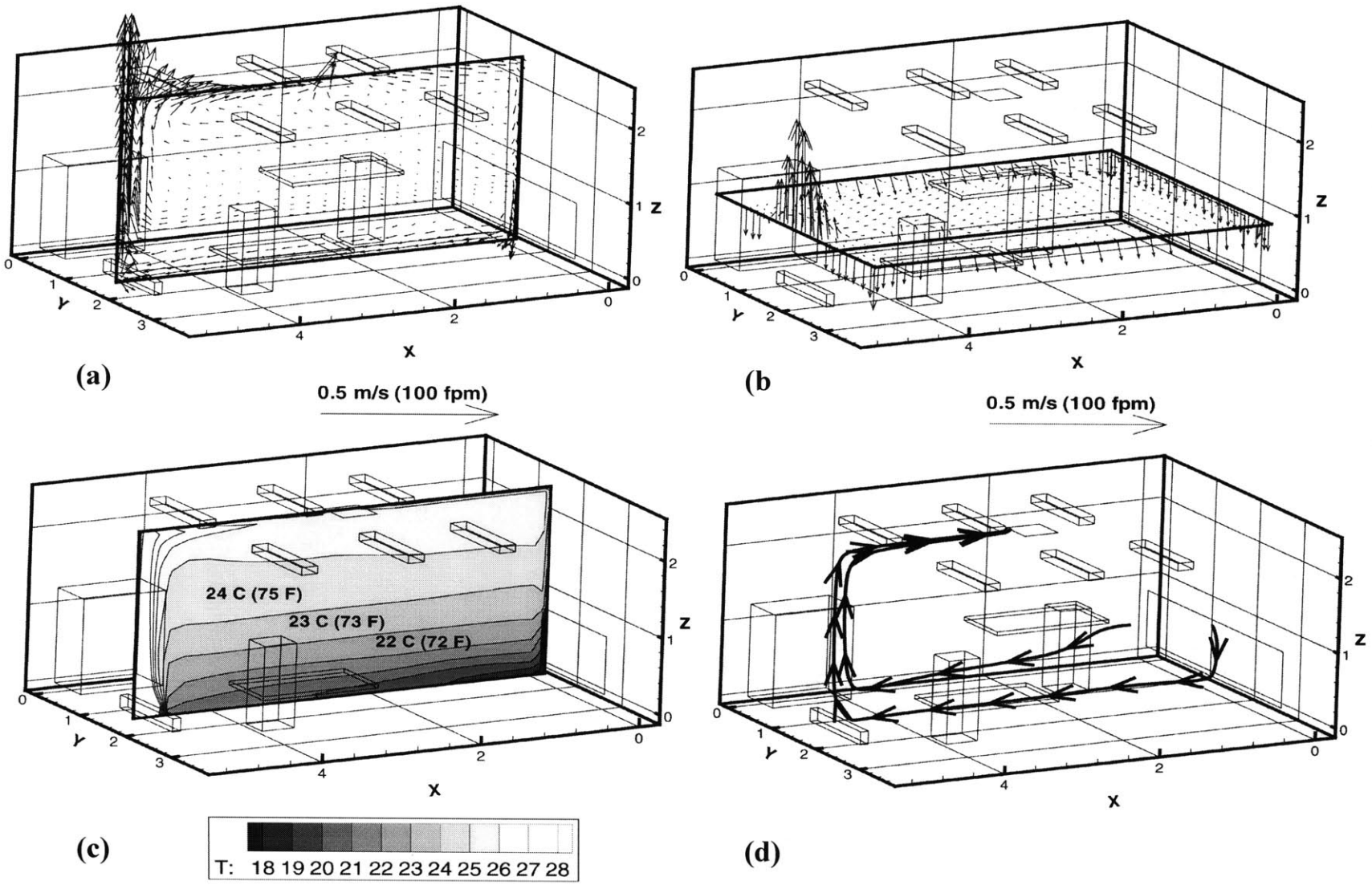

Figure 5.2 The computed air distribution for the infiltration case (a) air velocity in a middle section, (b) air velocity in a horizontal section, and (c) air temperature in a middle section (d) particle tracks

Figure 5.3 shows the quantitative comparison of the calculated air velocity with the measured data. The air velocity was measured at six different heights in five locations in the room (see right bottom figure in Figure 5.3). The figure is a plan view where position 1 is close to the infiltration diffuser and position 5 close to the baseboard heater. The calculated velocity profiles in the vertical direction agree reasonably with the measured data in most points, although there are significant discrepancies in some locations. In the figure, z = 0 ft (0 m) is the floor surface and z = 8 ft (2.43 m) is the ceiling surface. As mentioned in Chapter 3, the hot-sphere anemometer has some uncertainties in measuring low air velocities. The error bars in the two middle figures illustrate the uncertainties. In addition, there were wires and other small obstacles on the floor. These obstacles blocked the airflow near the floor. As a result, the measured air velocities near the floor tend to be smaller than those without the obstacles. The computer simulation did not consider those obstacles and, therefore, predicted higher air velocities near the floor. Nevertheless, the calculated results show the same trend as the measured data.

The agreement between the computed temperature and the experimental data is excellent, as shown in Figure 5.4. The agreement is not as good in the upper part of the room. One possible reason is that the thermal plumes from the two occupants disturbed the airflow in the upper part and the airflow may not be stable. The unstable flow is difficult to compute. Another reason is the simulation method for the lighting. The computation used boxes to simulate the lighting geometry but actually the lighting geometry was cylindrical.

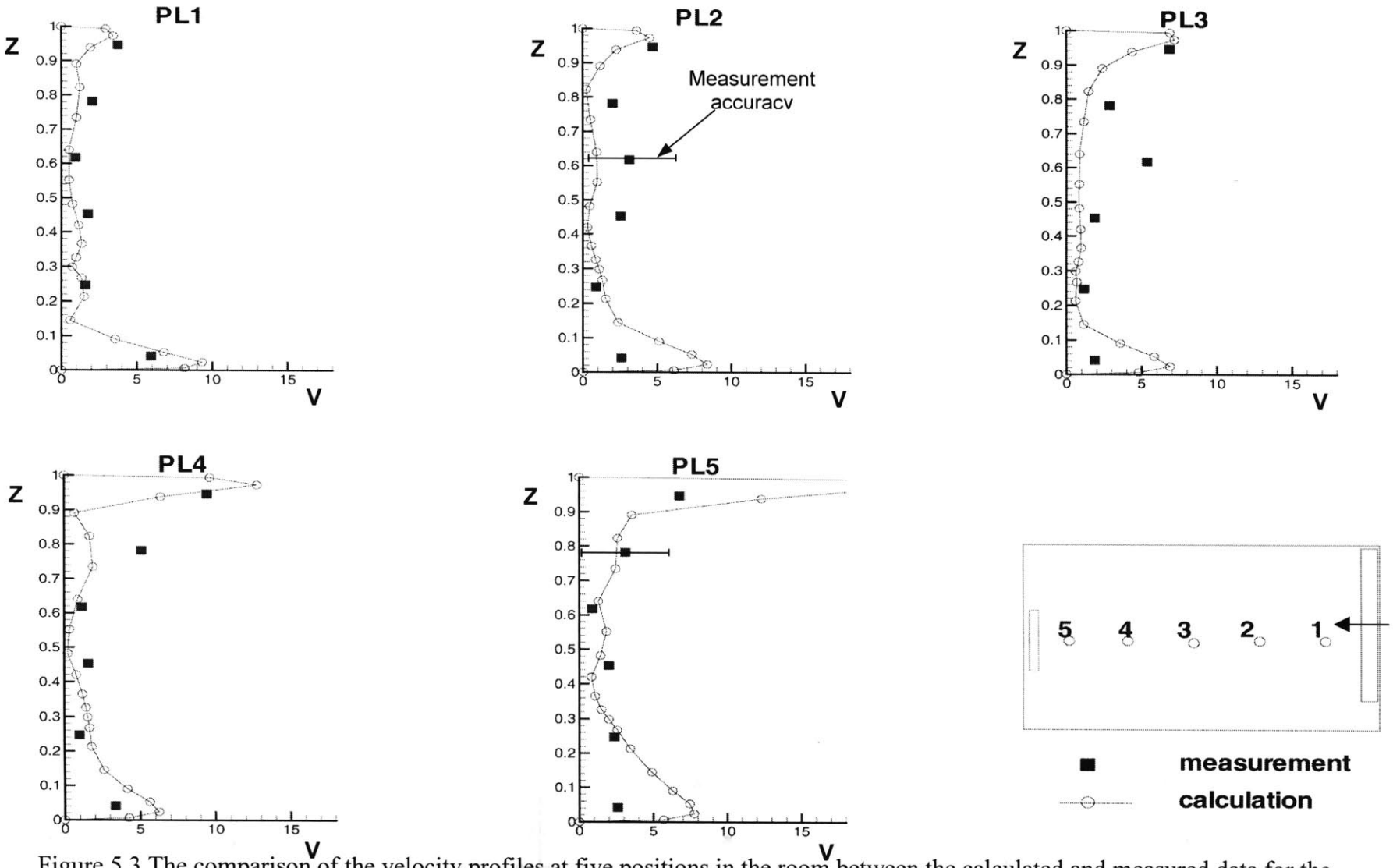

Figure 5.3 The comparison of the velocity profiles at five positions in the room between the calculated and measured data for the infiltration case, Z=height/total room height (H), V=velocity/inlet velocity (V_{in}), H=2.43m, V_{in}=0.017m/s

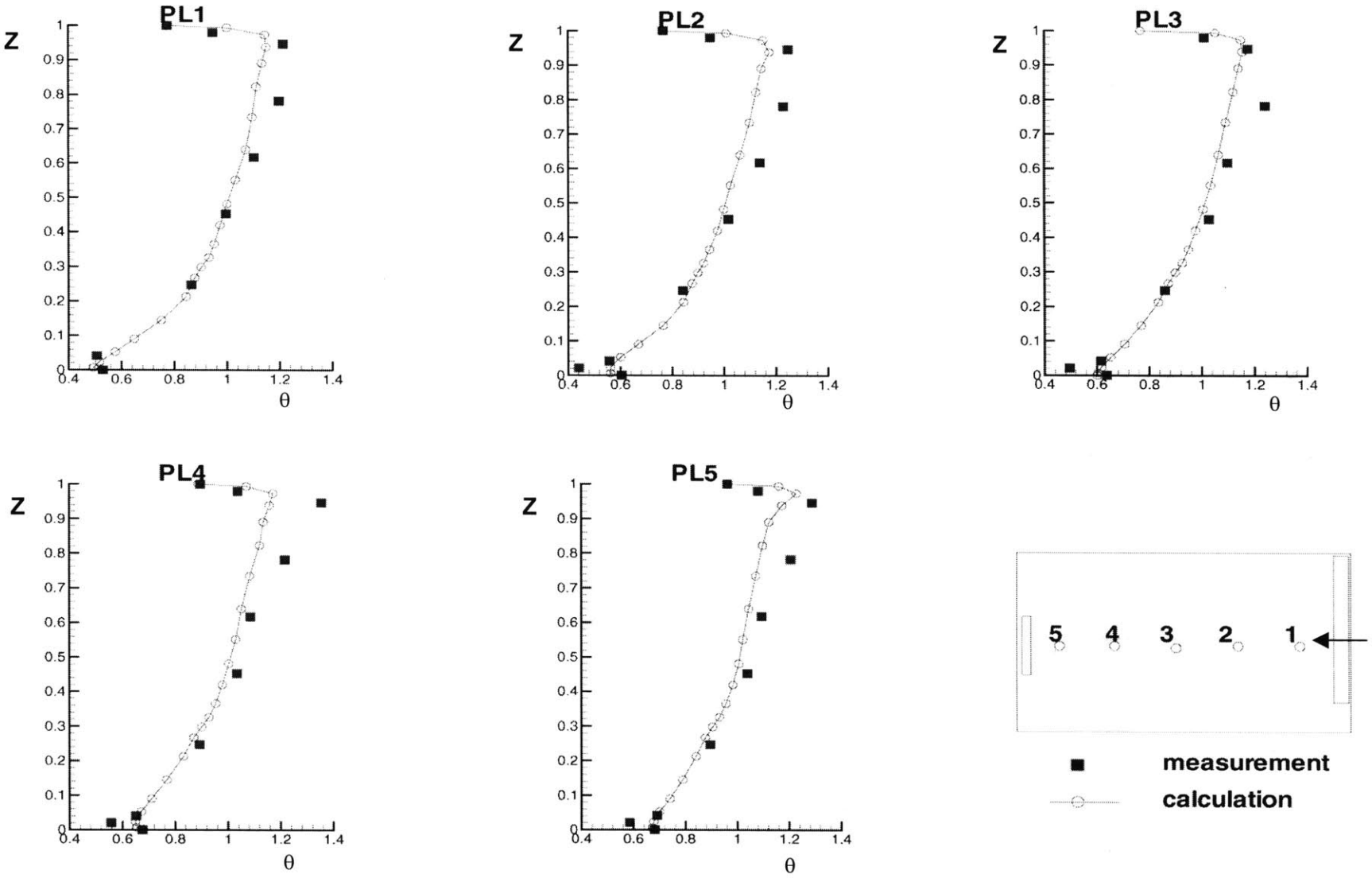

Figure 5.4 The comparison of the temperature profiles at five positions in the room between the calculated and measured data for the infiltration case, Z=height/total room height (H), $\theta=(T-T_{in}/T_{out}-T_{in})$, H=2.43m, $T_{in}=13.2^{o}C$, $T_{out}=24.0^{o}C$

5.2.2 The partition case

The partition case was designed to test the ability of the zero-equation flow program to study a non-uniform, room to room, complex mixing ventilation. A partition wall was extended from the floor to ceiling, as shown in Figure 5.5. The width of the opening in the partition wall was 3.8 ft (1.15 m). In this study, the inlet opening was on the rear wall near the ceiling and the return outlet was on the rear wall near the floor. The heat sources used in this case were a baseboard heater, two persons, six fluorescent lamps, and two computers. Table 5.3 and Table 5.4 provide more detailed geometrical, thermal, and flow boundary conditions.

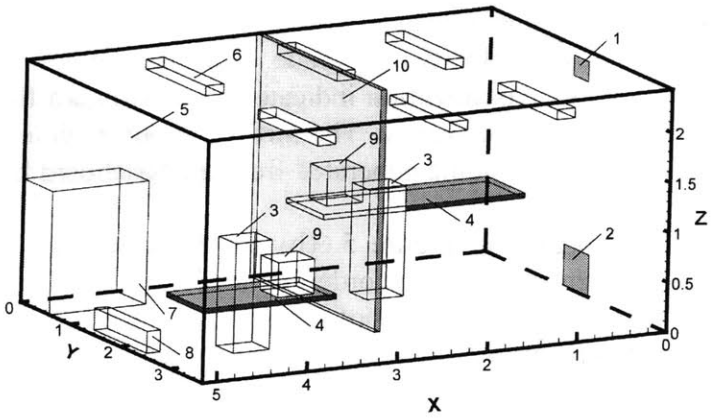

Figure 5.5 The layout of the partition cases simulated and tested in the chamber (inlet -1, outlet -2, person -3, table -4, window -5, fluorescent lamps -6, cabinet -7, baseboard heater -8, computer -9, partition wall -10)

Table 5.3 The geometrical, thermal, and flow boundary conditions for the diffuser and window

Partition case			
Inlet diffuser	Size: 0.2 m x 0.3 m (0.7 ft x 1.0 ft)	Temperature: 13.5°C (56.3°F)	Velocity: 0.85 m/s (170 fpm)
Window	Size: 3.65 m x 1.16 m (12 ft x 3.8 ft)	Temperature: 30.9°C (87.6°F)	

Table 5.4 The size and capacity of the heat sources

Heat source	Size	Power
Baseboard heater	1.2 x 0.1 x 0.2 m^3 (3.9 x 0.3 x 0.7 ft^3)	1500 W (5,118 Btu/hr)
Person	0.4 x 0.35 x 1.1m^3 (1.3 x 1.15 x 3.6 ft^3)	75 W (256 Btu/h)
Computer 1	0.4 x 0.4 x 0.4m^3 (1.3 x 1.3 x 1.3 ft^3)	108 W (368 Btu/h)
Computer 2	0.4 x 0.4 x 0.4m^3 (1.3 x 1.3 x 1.3 ft^3)	173 W (590 Btu/h)
Overhead lighting	0.2 x 1.2 x 0.15 (0.7 x 3.9 x 0.5 ft^3)	34 W (116 Btu/h)

The airflow in this case is very complicated. Figure 5.6(a), Figure 5.6(b), and Figure 5.6(c) show the computed air velocity distributions in three different sections of the room, but it is difficult to obtain a complete picture from the results. Although the air supply and return were in the rear space, there is mass exchange between the two spaces. Figure 5.6(a) indicates clearly that the flow at the lower part of the opening at the partition wall is from the rear space to the front space and vice versa at the upper part. Since the air supply inlet and return outlet are in the same space and the supply air temperature is low, some of the air short-circuits near the rear wall (Figure 5.6(b). The baseboard heater in the front space generated a strong plume that is the main force drawing the air from the rear space, as shown in Figure 5.6(c). The plume brought the air to the ceiling level and moved further back to the rear space. The computed airflow pattern is the same as the one observed by using smoke visualization (Figure 5.6(e)). The arrow length shown in Figure 5.6(e) is proportional to the velocity magnitude. Since the window temperature is lower than the air temperature, the smoke visualization indicates the downward flow on the two sides of the window is due to the negative buoyancy. The airflow in the middle of the window was upward, because of the strong thermal plume generated from the baseboard heater.

Figure 5.6(f), Figure 5.6(g), and Figure 5.6(h) are the computed particle tracks. The particles were released at different positions in order to obtain a general picture of the airflow pattern. The particle tracks show the complexity of the airflow, especially in the region close to the partition wall. The comparison between the computed and visualized airflow patterns confirms that the zero-equation model is capable of handling complicated airflow.

The temperature field in the Figure 5.6(d) reveals that two parts of the room have different temperatures. The air temperature in the front space was approximately 2°C (4°F) higher than that in the rear space. The partition wall blocked the flow and created the non-uniform temperature distribution along the horizontal section. The results show clearly that the air temperature near the inlet was lower and near the baseboard heater the temperature was higher than the average temperature.

The study also compared the computed air velocity and temperature distribution with the experimental data obtained from the chamber. The air velocity and temperature were measured in five positions in the chamber as shown in the right bottom figure in Figure 5.7 and Figure 5.8. In the figures, position 1 is close to the inlet and outlet and position 5 is close to the baseboard heater.

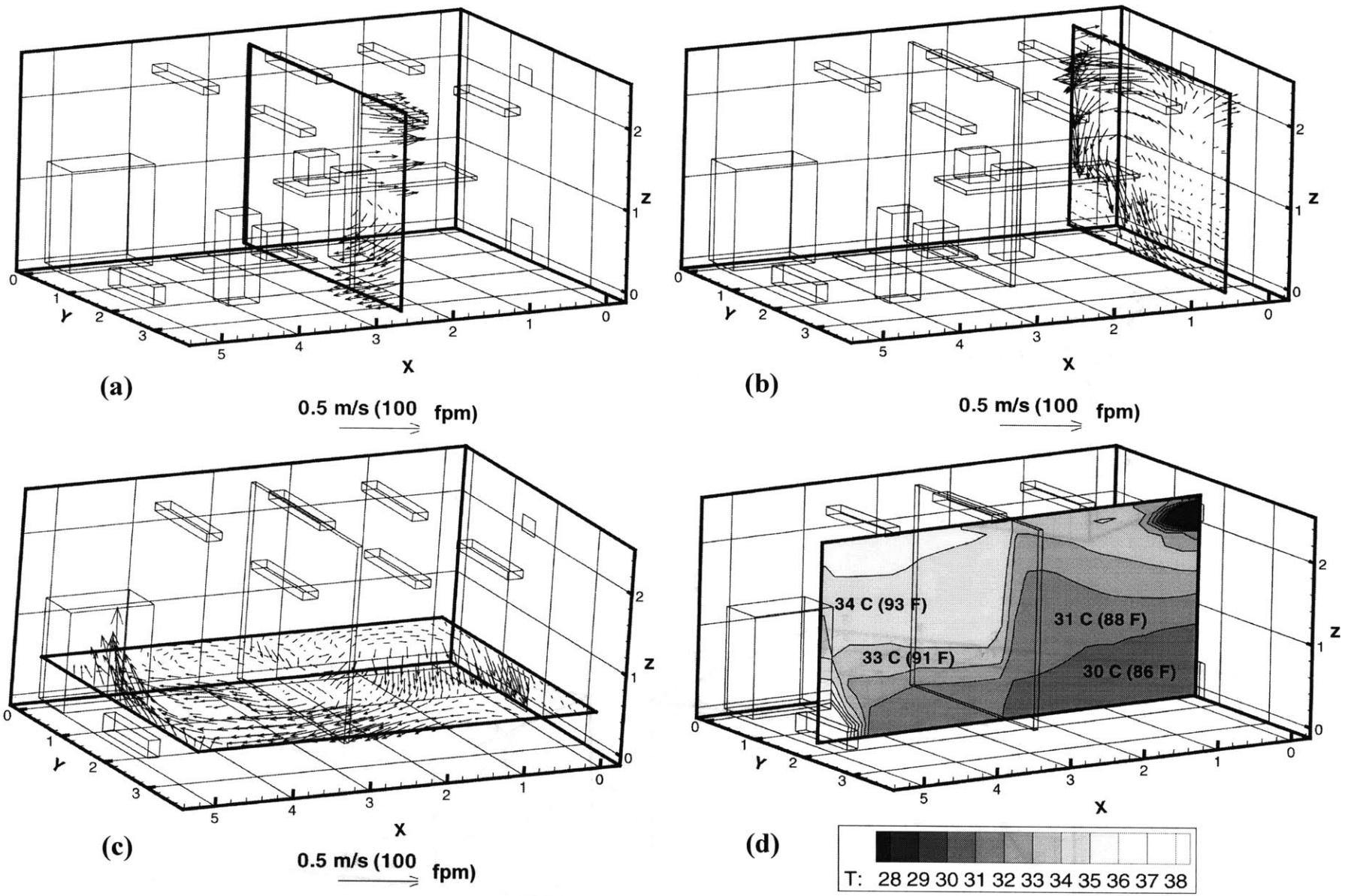

Figure 5.6 The computed and observed air distribution for the partition case. (a) air velocity at the partition opening, (b) air velocity in front of the inlet opening, (c) air velocity in the horizontal section, (d) air temperature in the middle section

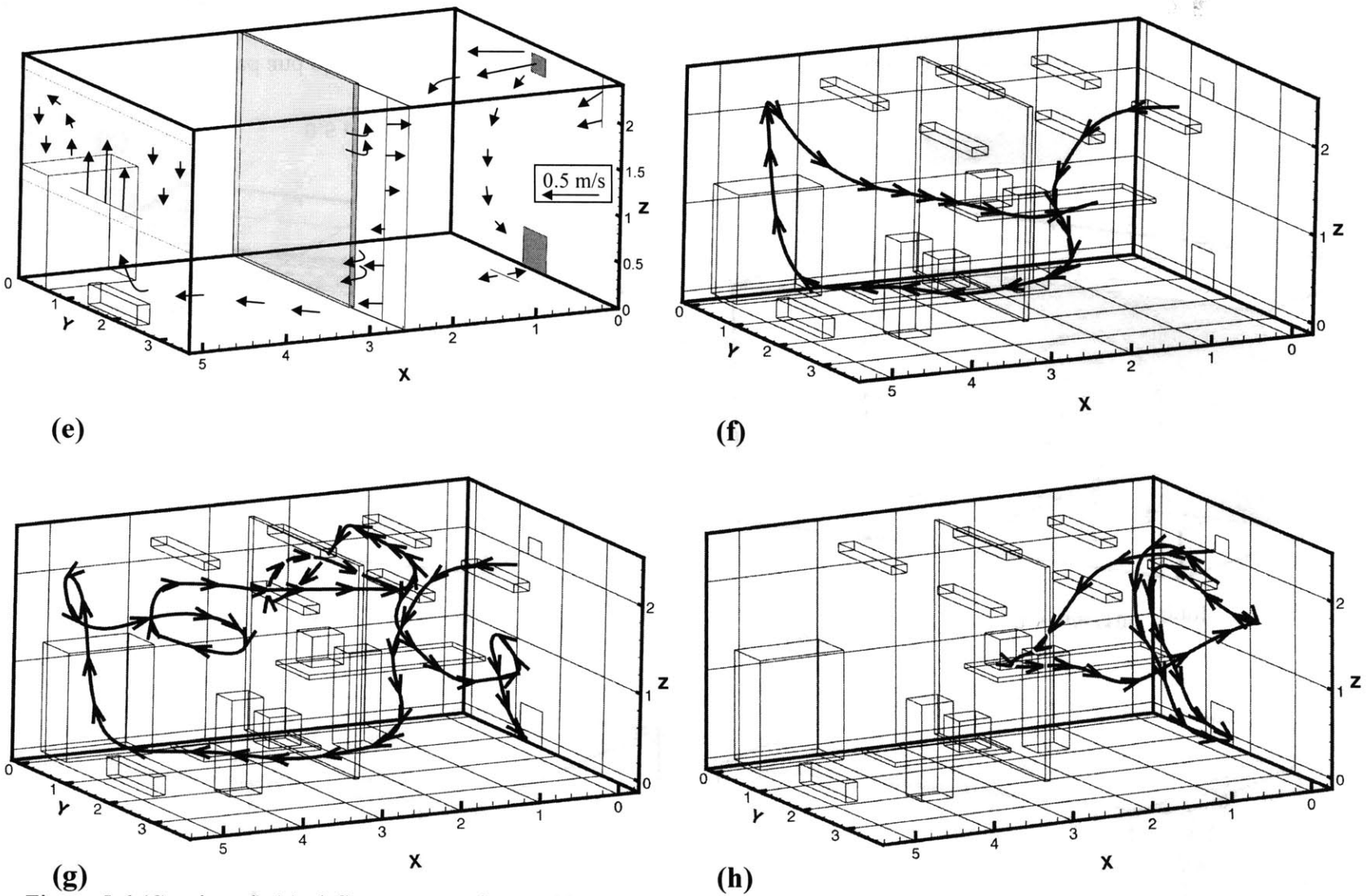

Figure 5.6 (Continued) (e) airflow pattern observed by smoke visualization, (f), (g), and (h) computed particle tracks in different positions

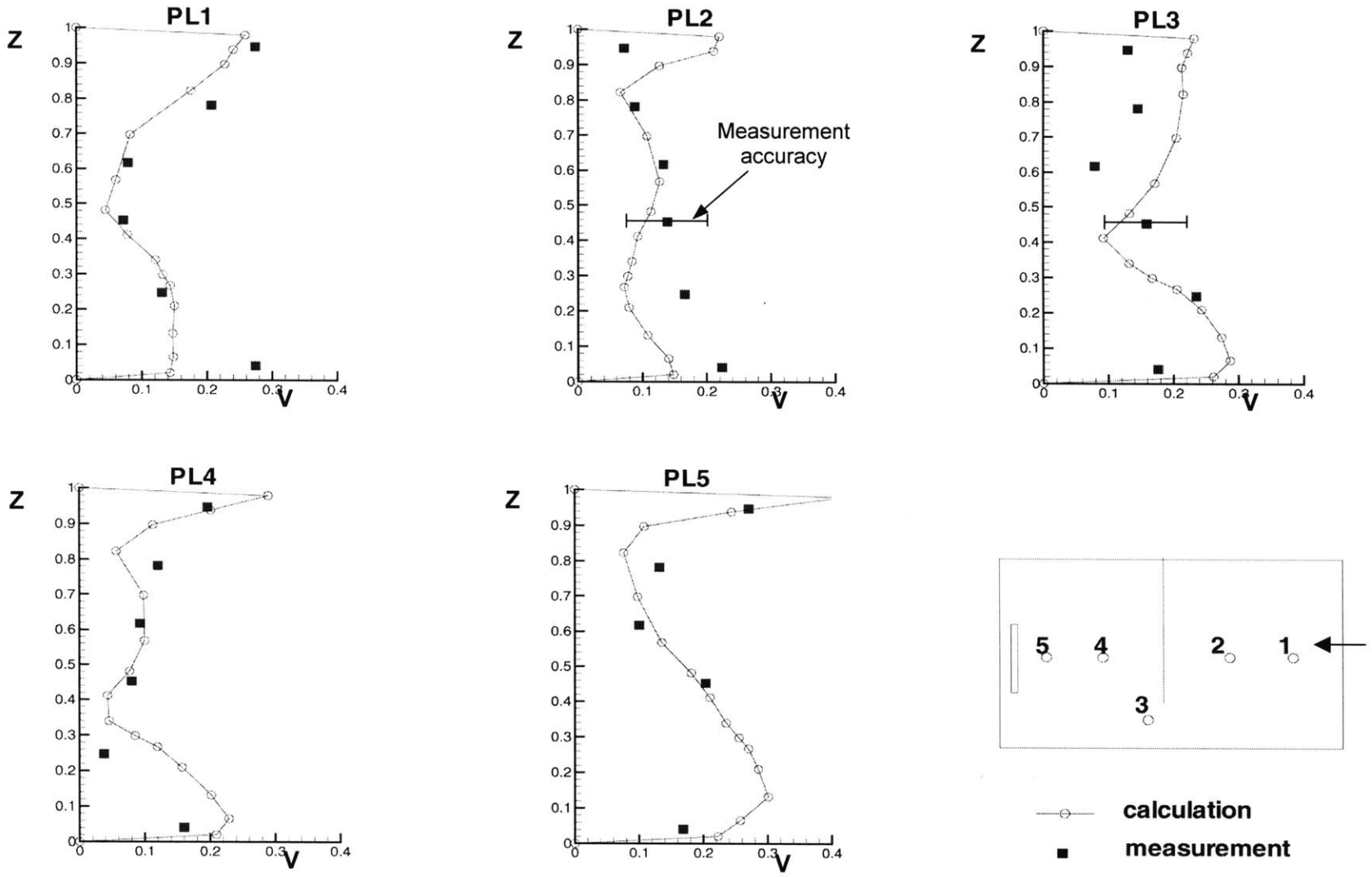

Figure 5.7 The comparison of the velocity profiles at five positions in the room between the calculated and measured data for the partition case. Z=height/total room height (H), V=velocity/inlet velocity (V_{in}), H=2.43m, V_{in}=0.85m/s.

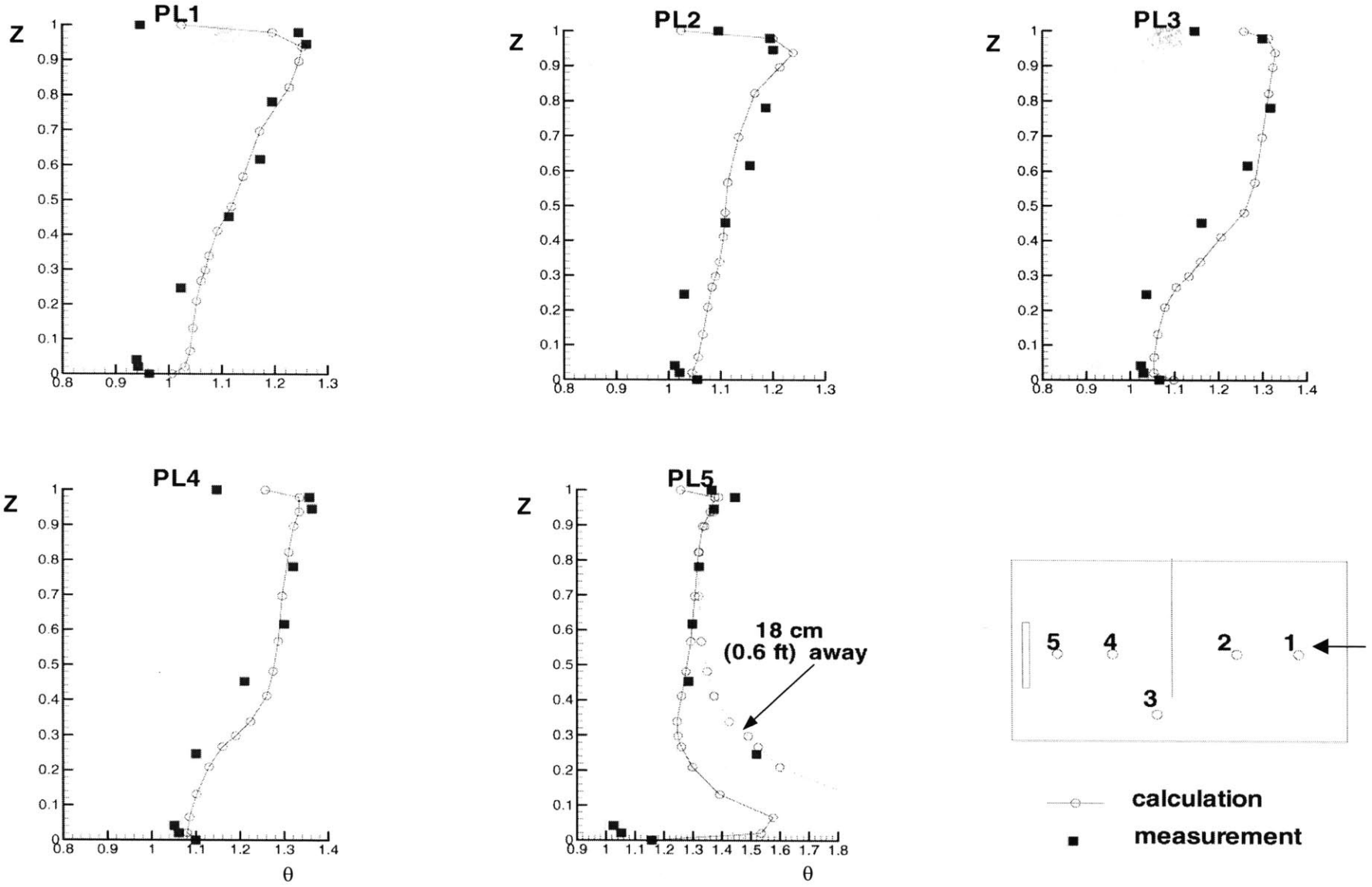

Figure 5.8 The comparison of the temperature profiles at five positions in the room between the calculated and measured data for the partition case, Z=height/total room height (H), $\theta=(T-T_{in}/T_{out}-T_{in})$, H=2.43m, $T_{in}=13.5^{o}C$, $T_{out}=29.8^{o}C$.

Figure 5.7 shows the vertical profiles of the computed and measured air velocity at five different locations in the room. The agreement between the computed results and measured data is acceptable for design purposes, but it is not as good as the previous case. In the lower part of the rear space, such as PL1 and PL2, the flow visualization shows many vortexes and the flow was swirling. It is difficult to measure and calculate such a flow. The same phenomenon was also observed in the upper part of the opening next to the partition wall (PL3). Figure 5.6(g) clearly illustrates the swirl. Therefore, the computed air velocity does not agree very good with the data in those areas.

The agreement between the computed profiles of the air temperature and the measured data is much better than that for velocity, as shown in Figure 5.8. However, the discrepancy is very large in the area near the baseboard heater (PL5). Since the heater was very hot, there was a large temperature gradient near the heater. The low temperatures measured near the floor on PL5 show that cold air coming in front of the heater would be rapidly heated in the area very close to the heater. The figure for PL5 shows that the agreement between the computed and measured temperatures is much better if we use the computed temperature at the position 0.6 ft (0.18 m) closer to the heater (the dashed line in the figure). This new position is one grid node closer to the heater. It seems that the grid distribution was too coarse for such strong temperature gradient. Probably, to catch all details in this region, one should have a finer grid than one used for the calculation.

The performance of the zero-equation model for the prediction of the computed air velocity and temperature distributions seems to be poorer in the partition case than for the infiltration case. The results from Chen and Xu (1998) also indicated that the model gives poorer results for forced convection. In the partition case, the flow includes an impinging jet that is difficult to simulate. Even with a more complicated k-ε model, the over-prediction of the turbulent energy in the impinging region would give an unacceptable discrepancy in velocity distribution (Murakami 1998). The airflow in the partition case consists of impinging jet, separation, free shear layer, vortex shedding, etc. With such a simple zero-equation model, it is unrealistic to expect that the model can predict the flow field precisely. In addition, the experimental measurements have uncertainties as well. In fact, repeated measurements did not always lead to the same results.

5.2.3 The displacement ventilation case

The study has also selected displacement ventilation as another test case. Displacement ventilation has been the subject of considerable studies in the past decade, including one sponsored by ASHRAE (Yuan et al. 1999). It can generate a stratified flow and represents a typical mixed convection case. Together with the infiltration case (natural convection) and the partition case (forced convection), the present study covers a wide range of complicated flows.

In displacement ventilation systems for cooling applications, conditioned air with a temperature slightly lower than the desired room air temperature in the occupied zone is supplied from air outlets at low air velocities (100 fpm or 0.5 m/s or less). The outlets are located at or

near the floor level, and the supply air is directly introduced to the occupied zone. The most common supply configuration is horizontal discharge from a low side wall position. Returns are located at or close to the ceiling through which the warm room air is exhausted from the room as shown in Figure 5.9. The supply air is spread over the floor and then rises as it is heated by the heat sources in the occupied zone. Heat sources (e.g., persons, computers) in the occupied zone create upward convective flows in the form of thermal plumes. These plumes remove heat and contaminants that are less dense than air from the surrounding occupied zone.

The displacement ventilation case simulated here with the zero-equation model is one of the cases used for the ASHRAE displacement ventilation project (Chen et al. 1998). Figure 5.9, Table 5.5 and Table 5.6 provide more detailed information of the geometrical, thermal, and flow boundary conditions.

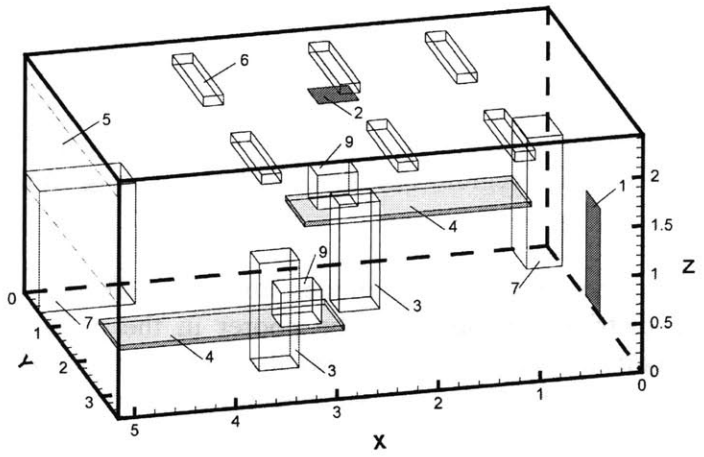

Figure 5.9 The layout of the displacement ventilation simulated and tested in the chamber (inlet -1, outlet -2, person -3, table -4, window -5, fluorescent lamps -6, cabinet -7, computer -9)

Table 5.5 The geometrical, thermal, and flow boundary conditions for the diffuser and window

Displacement ventilation case			
Inlet diffuser	Size: 0.53 m x 1.1 m (1.7 ft x 3.6 ft)	Temperature: 17.0°C (62.6°F)	Velocity: 0.086 m/s (17.5 fpm)
Window	Size: 3.65 m x 1.16 m (12 ft x 3.8 ft)	Temperature: 27.7°C (81.9°F)	

Table 5.6 The size and capacity of the heat sources

Heat source	Size	Power
Baseboard heater	1.2 x 0.1 x 0.2 m^3 (3.9 x 0.3 x 0.7 ft^3)	1500 W (5,118 Btu/hr)
Person	0.4 x 0.35 x 1.1m^3 (1.3 x 1.15 x 3.6 ft^3)	75 W (256 Btu/h)
Computer 1	0.4 x 0.4 x 0.4m^3 (1.3 x 1.3 x 1.3 ft^3)	108 W (368 Btu/h)
Computer 2	0.4 x 0.4 x 0.4m^3 (1.3 x 1.3 x 1.3 ft^3)	173 W (590 Btu/h)
Overhead lighting	0.2 x 1.2 x 0.15 (0.7 x 3.9 x 0.5 ft^3)	34 W (116 Btu/h)

Figure 5.10(a) and Figure 5.10(b) show the calculated air velocity plotted in two sections in the room. Figure 5.10(d) illustrates the airflow distribution by smoke visualization. The computed results are in very good agreement with the flow pattern observed. The recirculation in the lower part of the room is also well captured by the computation. The velocity distribution in the horizontal section (Figure 5.10(b)) shows the upward plumes due to positive buoyancy generated from the heat sources (the hot window, two computers, and two persons) as well as the downward inlet jet flow due to negative buoyancy. The computed particle tracks shown in Figure 5.10(e) and Figure 5.10(f) further reveal the flow pattern in the room. Figure 5.10(e) shows that the fresh but cold air from the inlet stayed at the lower part of the room while it moved to the front wall. The air then gradually moved up by various heat sources and is eventually removed from the room through the exhaust. The heat sources in the room, such as the computers and the occupants, generated upward thermal plumes as shown in Figure 5.10(f).

The comparison between measured and calculated velocity and air temperature is given in the Figure 5.11 and Figure 5.12, respectively. This case has more detailed experimental data than the previous two cases. The right bottom picture in Figure 5.11 and Figure 5.12 shows the floor plan of the room where the measurements were carried out at nine positions. Very similar to the previous cases, the computed results are compared with the experimental data in different vertical sections in the room. Figure 5.11 shows a very good agreement between the computed and measured results. Although the geometry of the room is not simpler than that of the infiltration and partition cases, the flow with displacement ventilation is very stable. The zero-equation model can easily predict a stable flow. On the other hand, it is also easier to measure stable flow. Figure 5.12 further compares the measured and computed temperature profiles. The agreement is excellent.

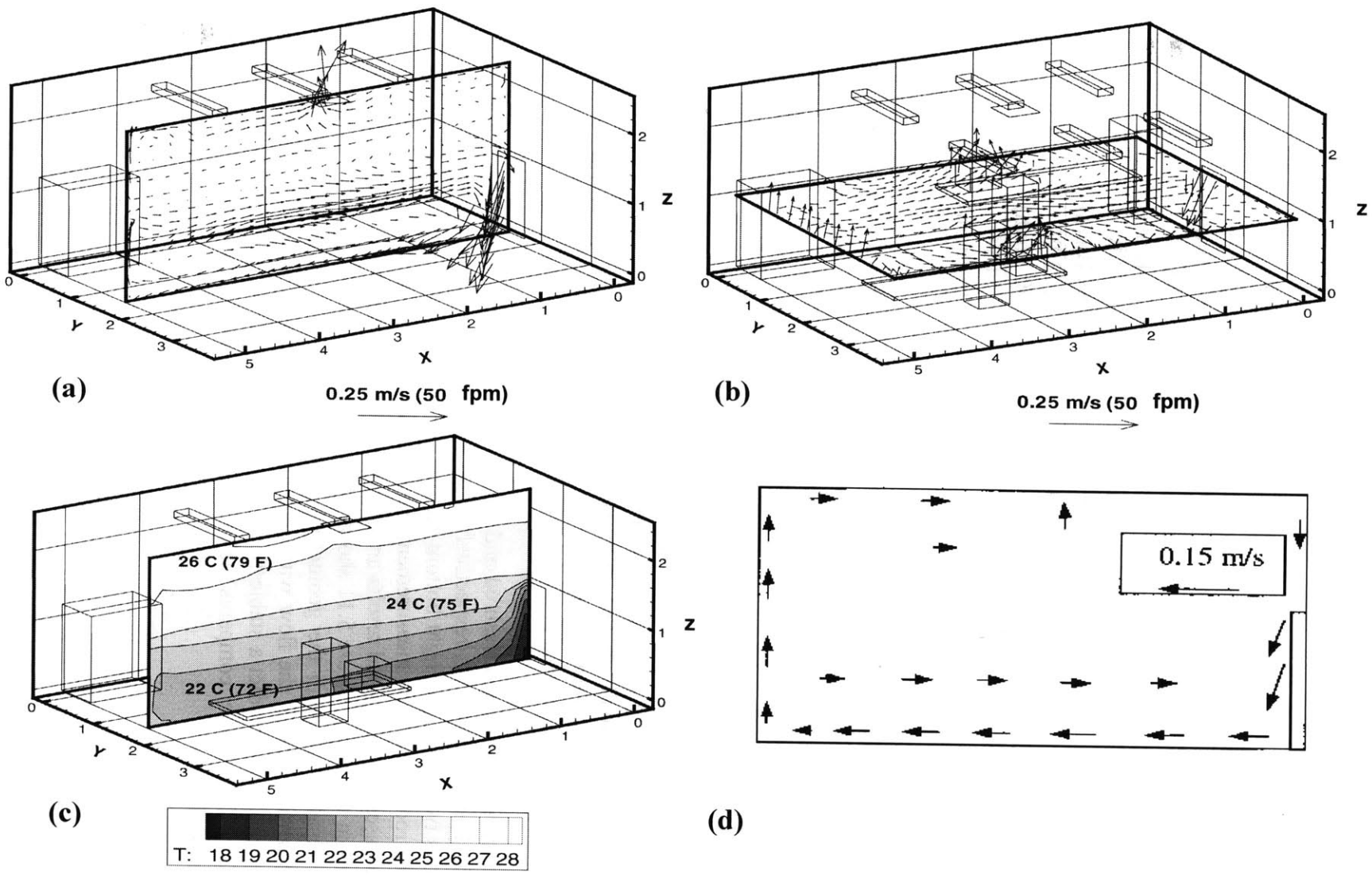

Figure 5.10 The air distribution for the displacement ventilation case. (a) computed velocity in a middle section, (b) computed velocity in a horizontal section, (c) computed temperature in a middle section, and (d) airflow pattern observed by smoke visualization in a middle section

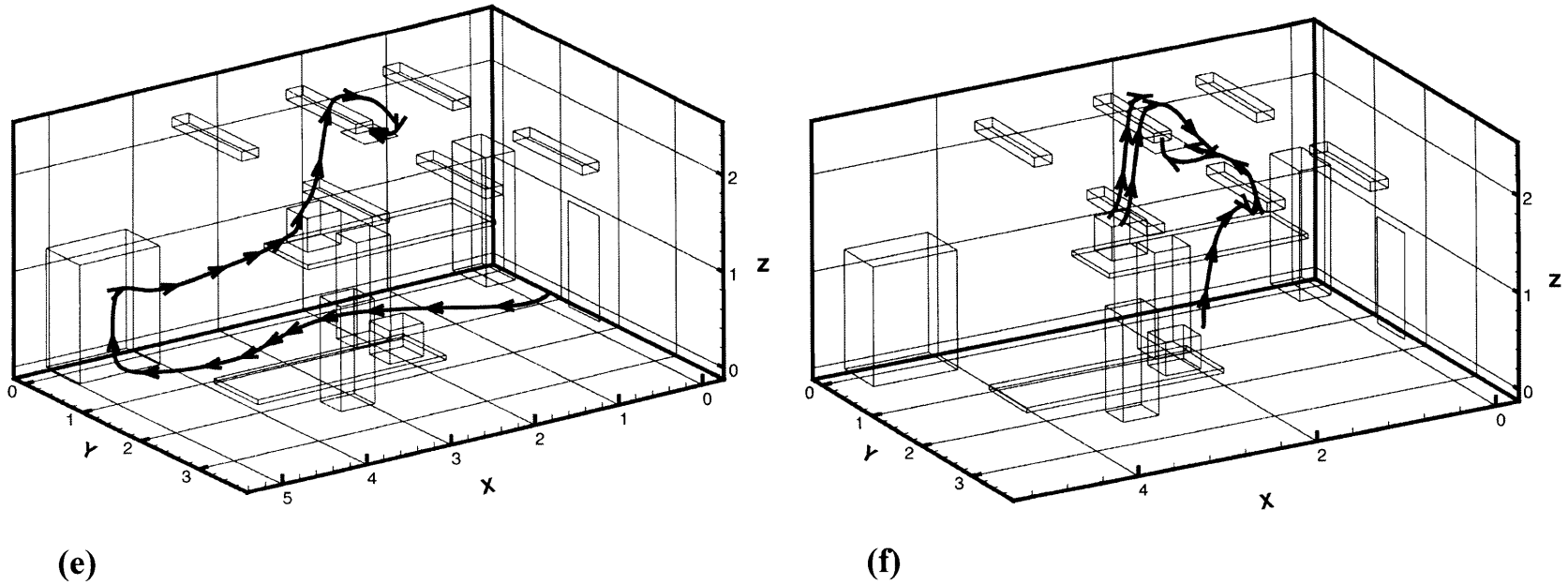

Figure 5.10 (Continued) (e) and (f) computed particle tracks at different positions.

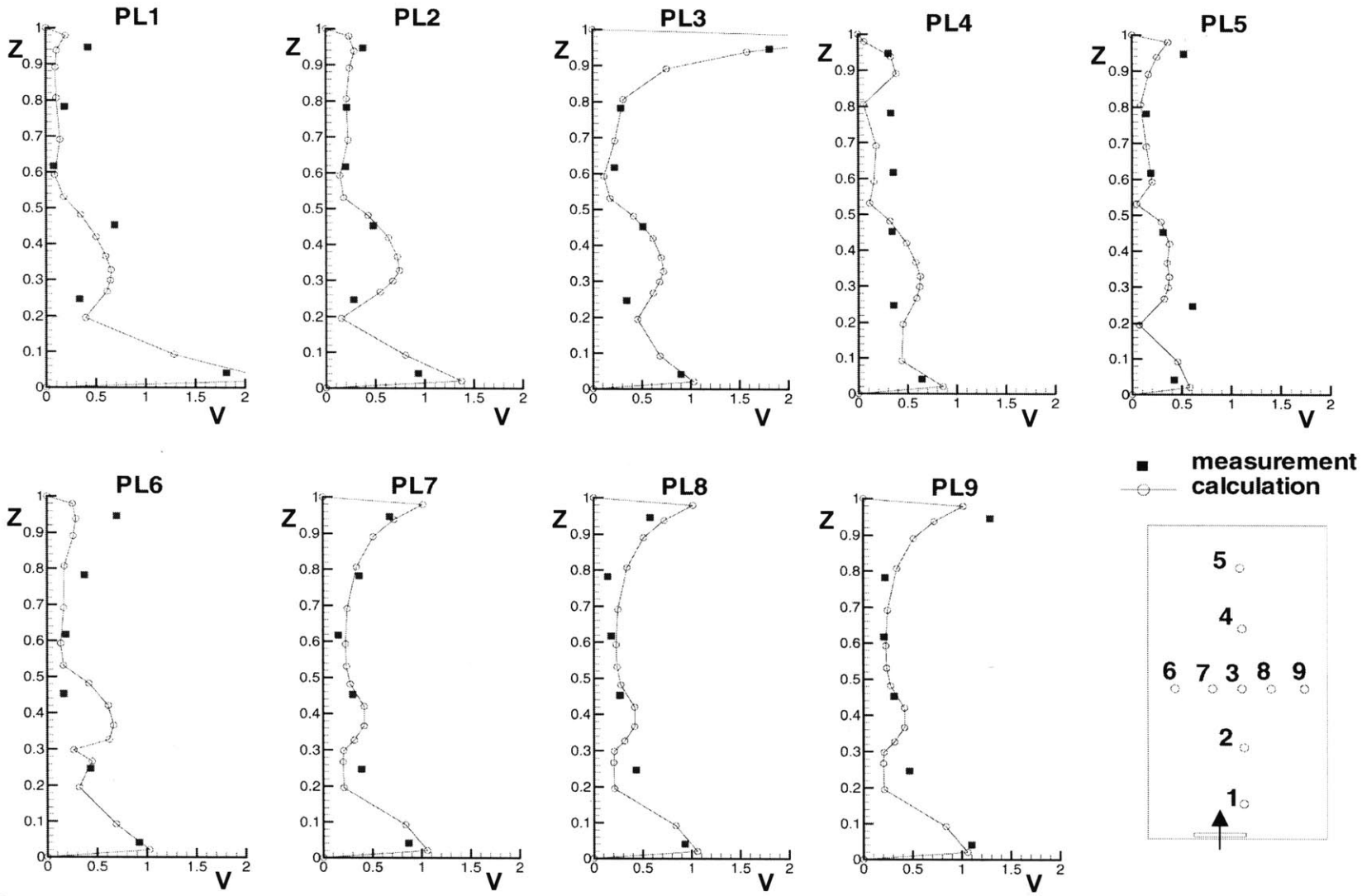

Figure 5.11 The comparison of the velocity profiles at nine positions in the room between the calculated and measured data for the displacement ventilation case. Z=height/total room height (H), V=velocity/inlet velocity (V_{in}), H=2.43m, V_{in}=0.086m/s

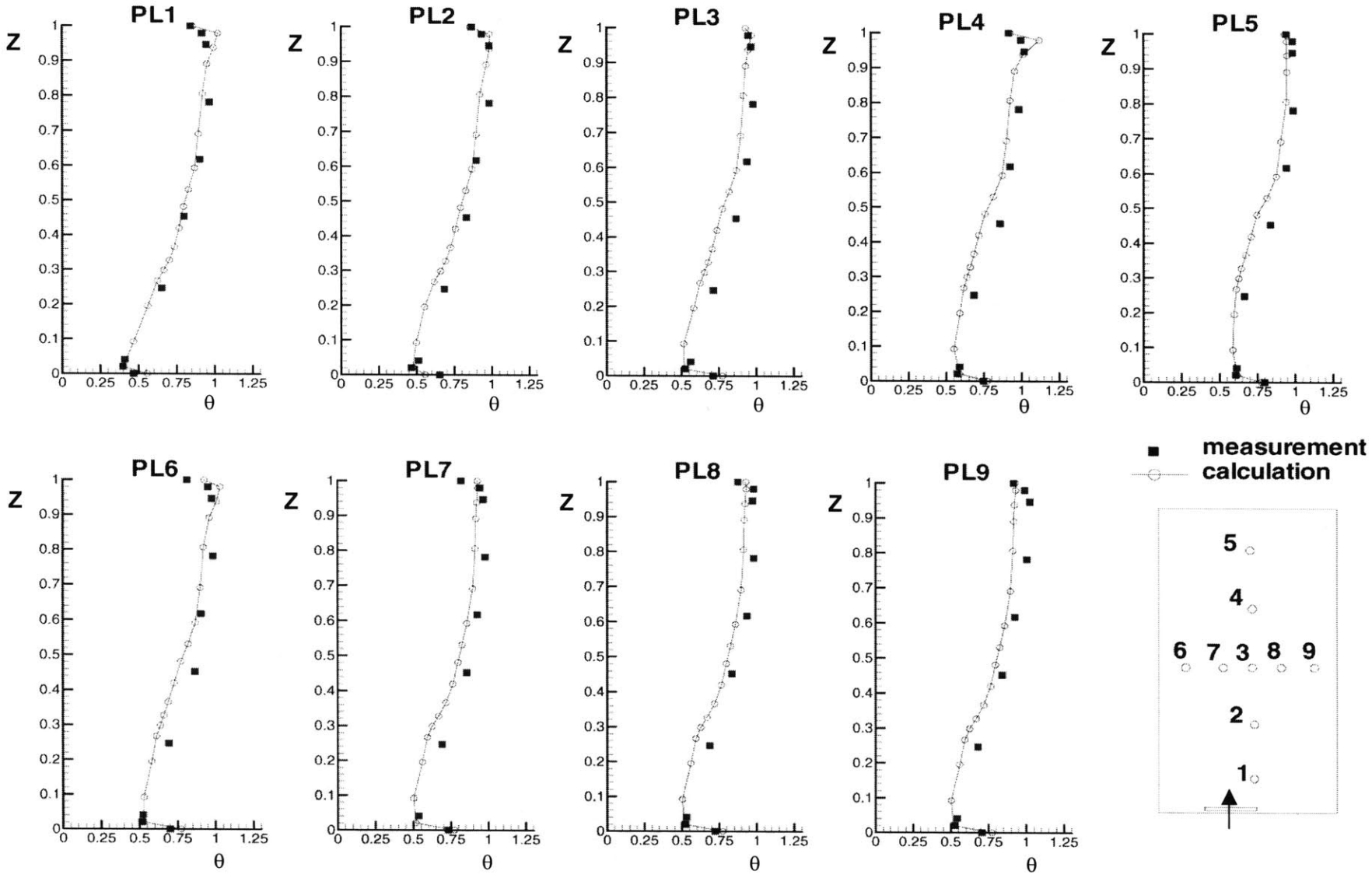

Figure 5.12 The comparison of the temperature profiles at nine positions in the room between the calculated and measured data for the displacement ventilation case. Z=height/total room height (H), $\theta=(T-T_{in}/T_{out}-T_{in})$, H=2.43m, T_{in}=17.0°C, T_{out}=26.7°C

5.2.4 Discussion and Summary

All the computations in this section used measured surface temperature as the boundary conditions. Since the zero-equation CFD program does not compute the heat conduction in the building enclosure, the surface temperature needs to be specified. In addition, the flow program does not have a radiation model. If the room surface temperature is unknown, the flow program must be combined with an energy program to perform a correct simulation. This will be described in Chapter 6.

Moreover, the current investigation did not consider the absorption and emission by moisture in the air. This is acceptable because the spaces studied are small and the impact of the moisture absorption and emission can be neglected. However, for large spaces, like atria, lobbies, aircraft hangars, etc., the absorption and emission are important for the calculation of the air temperature and total heat flux at the walls (Glicksman and Chen 1998).

Table 5.7 gives the computing time and the grid number used for the simulations in these three cases. The appendix B presents details of the measured data used for the simulations and validations for each case. The grid number used for the calculations is generally coarser than that normally used with the standard k-ε model. Since the zero-equation model is intended for design, it is crucial to reduce the computing time. However, the computed results are accurate enough for the purposes of design.

The zero-equation model does not solve for the turbulent contributions by transport equations and the model is numerically stable. This can greatly reduce the computing costs normally used by the standard k-ε model. The computing time for those three dimensional problems is under seven minutes per case. The calculations have been done on a PC Pentium II - 350 MHz.

Table 5.7 The grid number and computing time used for the three cases

Case	Grid number	Total Grid Number	Computing time [min:sec]
Infiltration	27x22x20	11,880	6:46
Partition	26x20x15	7,800	6:11
Displacement Ventilation	25x18x16	7,200	4:41

We have done the grid-density study for the displacement ventilation case. Table 5.8 shows the computing time and the grid number for the three different grid densities. The computing time shows approximately a linear dependency with the grid number as our previous study already showed (Chen and Xu 1998). The relationship between the total grid number and the computing time is also presented in Figure 5.13.

Figure 5.14 and Figure 5.15 give the comparison between the measured and calculated air velocities and temperatures for the three different grid distributions for displacement ventilation. The velocity profiles are similar for the two denser grids. However, the velocity and temperature

profiles for the coarsest grids do not agree reasonably with the measured data. In that case, due to the very coarse grid, the objects, such as the furniture, could not be presented in the numerical model and the calculation gave a much poorer result, because the heat transfer from the objects was neglected. On the other hand, the temperature profiles for the two denser grids almost coincide, although the grid number used in the second case was only half of that for the first case. The results show that good results can be obtained even with a very coarse grid distribution as soon as the grid system can describe the most important boundary conditions, such as the heat sources and furniture. The displacement ventilation case can be correctly calculated within two minutes and sixteen seconds.

Table 5.8 The different grid density and computing time for displacement ventilation

Case	Grid number	Total Grid Number	Computing time [min:sec]
Displacement Ventilation 1	25x18x16	7,200	4:41
Displacement Ventilation 2	19x15x11	3,315	2:16
Displacement Ventilation 3	14x11x8	1,232	0:49

The minimal grid number suitable for a simulation is determined by boundary conditions in that particular case, such as people, objects, inlets, outlets and non-adiabatic wall areas. The grid distribution can be uniform as well as non-uniform. We recommend use of the non-uniform grid distribution since it enables a user to create a coarser grid system, and gives more freedom in positioning the heat sources and other boundary conditions. Generally, area with large gradients (near the walls, inlets, furniture and other objects) should have a finer grid distribution than the rest of the space.

The indoor areas with particularly high gradients are around supply diffusers. The simplified techniques as discussed in Chapter 4 can significantly reduce the necessary grid for simulation of supply diffusers. The techniques have been proved to be useful.

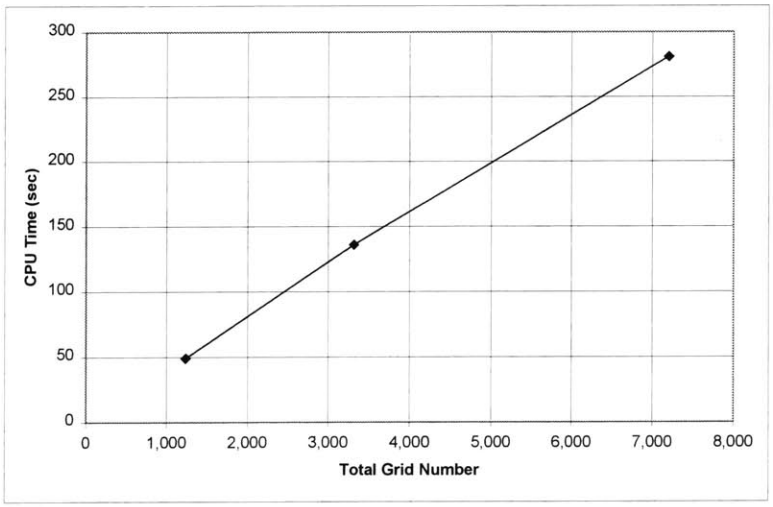

Figure 5.13 Relationship between total grid number and calculation time for the displacement ventilation simulated with the zero-equation model

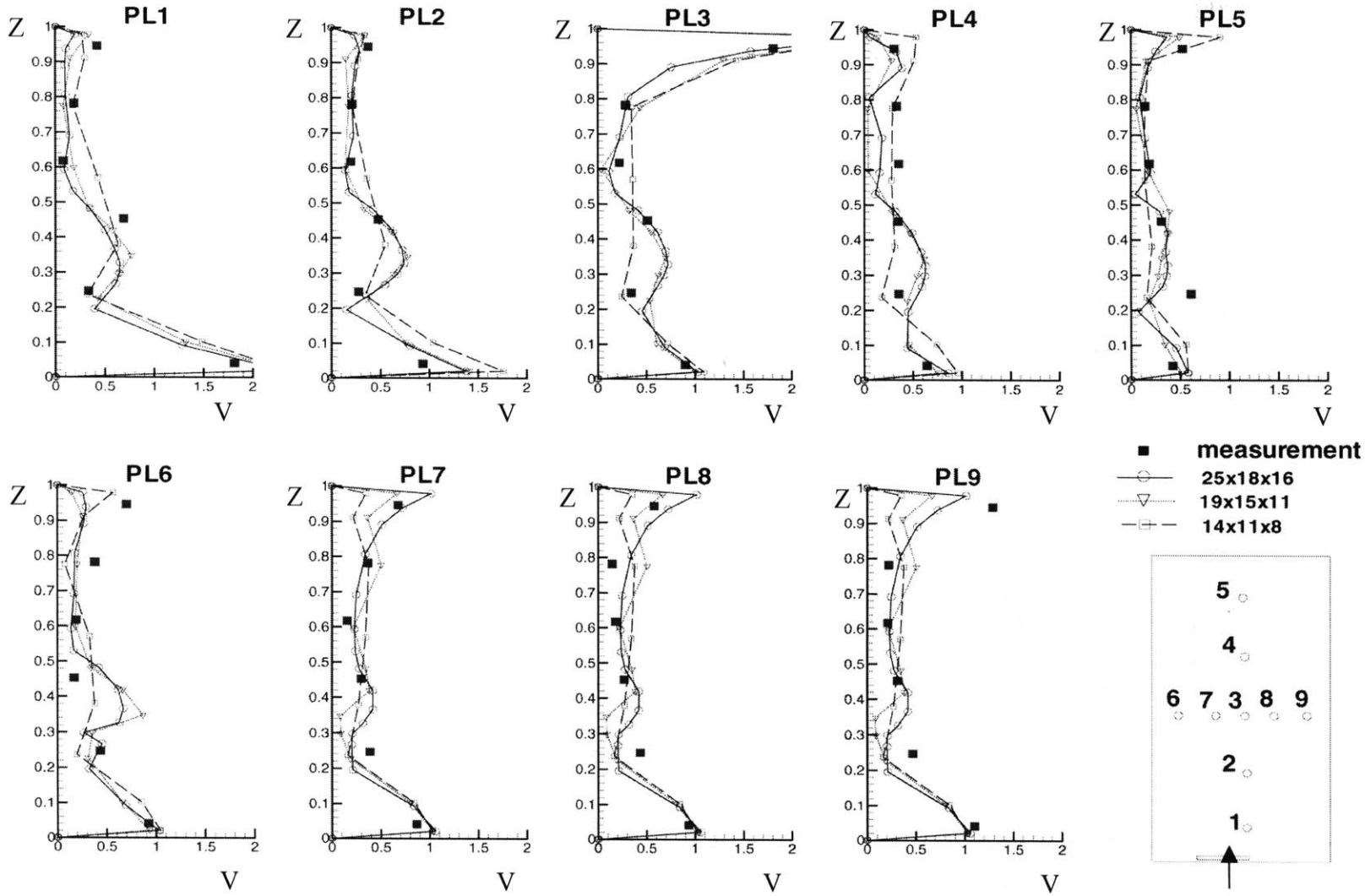

Figure 5.14 The comparison of the velocity profiles at nine positions in the room between the calculated and measured data for the three displacement ventilation calculations. Z=height/total room height (H), V=velocity/inlet velocity (V_{in}), H=2.43m, V_{in}=0.086m/s

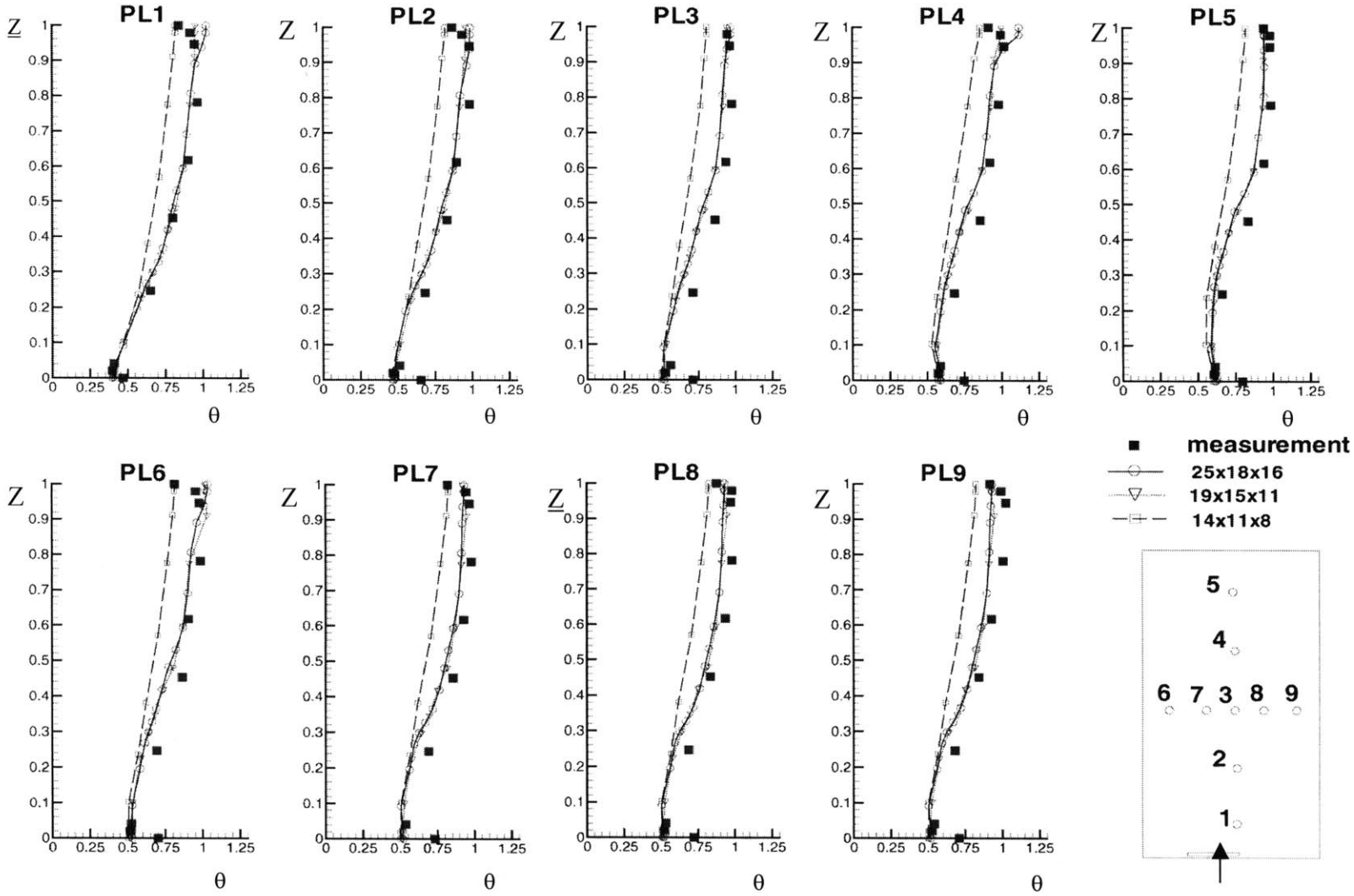

Figure 5.15 The comparison of the temperature profiles at nine positions in the room between the calculated and measured data for the three displacement ventilation calculations. Z=height/total room height (H), $\theta=(T-T_{in}/T_{out}-T_{in})$, H=2.43m, $T_{in}=17.0^{o}C$, $T_{out}=26.7^{o}C$

CHAPTER 6

COUPLING BETWEEN THE FLOW PROGRAM AND AN ENERGY ANALYSIS PROGRAM

One very important objective of this study is to demonstrate how the flow program can be combined with an energy simulation program and to calculate the coupled energy/thermal comfort/air movement situations by analyzing five heating and cooling system designs. The goal of these examples is to ensure that the simplified model produces realistic results that are representative of field conditions. The investigation used the energy analysis program ACCURACY (Chen and Kooi 1988). The energy program has been extensively used to analyze energy consumption in buildings with different room air temperature distributions (Niu 1994).

6.1 Coupling between the Flow Program and an Energy Analysis Program

Coupling between a flow program and an energy analysis program relates the governing flow equations (Chapter 2) in the flow program to the energy balance equation of room air in the energy program. The energy balance equation of room air is:

$$\sum_{i=1}^{N} q_{i,c} A_i + Q_{lights} + Q_{people} + Q_{appliances} + Q_{infiltration} - Q_{heat\_extraction} = \frac{\rho V_{room} c_p \Delta T}{\Delta t} \qquad (6.1)$$

where $\sum_{i=1}^{N} q_{i,c} A_i$ is the convective heat transfer from enclosure surfaces to room air, N is the number of enclosure surfaces, A_i is the area of surface i, Q_{lights}, Q_{people}, $Q_{appliances}$, and $Q_{infiltration}$ are the cooling loads of lights, people, appliances and infiltration, respectively, $Q_{heat\_extraction}$ is the heat extraction via HVAC device, $\frac{\rho V_{room} c_p \Delta T}{\Delta t}$ is the room air energy change, ρ is the air density, V_{room} is the room volume, c_p is the air specific heat, ΔT is the temperature change of room air, and Δt is the sampling time interval.

A flow program can be extended to solve the heat conduction in the solid building enclosure. In that way, the flow program includes the capacity of an energy program. The method is known as the conjugate-heat-transfer method. Chen et al. (1995) have applied the method to calculate the room thermal response. It is extremely expensive to use in terms of computing effort, although the method is powerful.

A feasible method for design is to couple a flow program with an energy program. This method uses the outputs from a flow program, such as room air temperature distribution and convective heat transfer coefficients, as the inputs of an energy program. Also, the outputs from the energy program, such as enclosure surface temperatures and air-conditioning load, are the inputs of the flow program.

The coupling between the flow program and an energy analysis program requires proper exchange of the data between the two programs. This study uses the energy program, ACCURACY, as an example. Figure 6.1 shows the basic scheme for the data exchange and the calculation procedure (Srebric et al. 2000a).

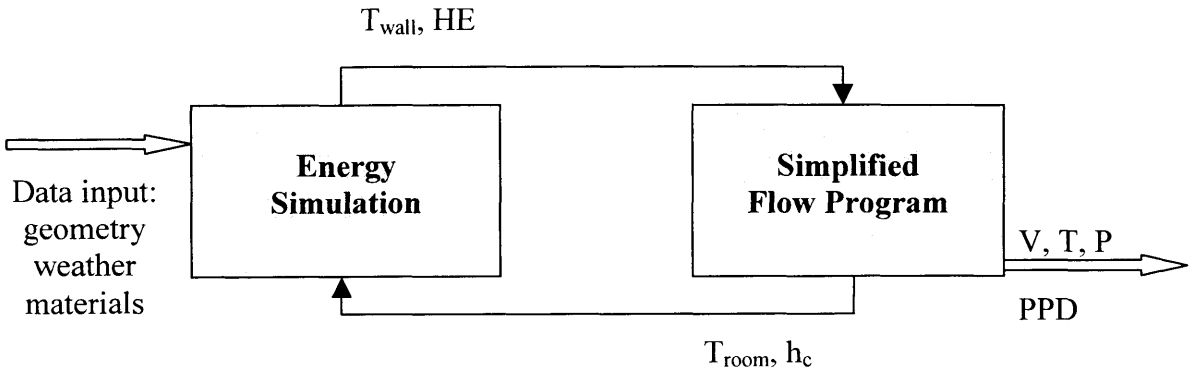

Figure 6.1 Data exchange between the programs for energy /airflow/thermal comfort simulation

The calculation starts with the energy simulation for the current hour. The wall surface temperatures (T_{wall}) and the heat extraction rate (HE) are the results of the energy simulation. The heat extraction rate is the rate at which the energy is removed or added to the space by the HVAC system.

The results from the energy program are used as the boundary conditions for the flow program to determine the air temperature and thermal comfort for the current hour. More specifically, the heat extraction is used to determine the inlet velocity for the room with a variable-air-volume ventilation system or the inlet temperatures for the room with a constant-air-volume ventilation system. The boundary conditions for non-adiabatic walls in the flow program use the wall surface temperatures from the output of the energy program.

The flow program then calculates the convective heat transfer coefficients for all non-adiabatic walls and the distributions of air temperature, velocity, pressure, and overall viscosity. The convective heat transfer coefficients are based on the wall surface temperature and the air temperature near the walls (the air temperature in the closest grid cell to the wall). These distributions are then further used to calculate the thermal comfort distribution in the room.

It is easy to determine the air temperature near the walls from the air temperature distribution. Then the air temperature near the walls and the corresponding convective heat transfer coefficients are used in the energy analysis program to determine the wall surface temperature and the heat extraction for the next hour.

The outputs from the flow and energy simulation were used to determine the distribution of thermal comfort with the ASHRAE comfort model (ASHRAE 1997):

$$PPD = 100 - 95\exp(-0.03353PMV^4 - 0.2179PMV^2) \ [\%] \qquad (6.2)$$

where PPD is the predicted percentage dissatisfied, and PMV is the predicted mean vote.

The predicted mean vote, PMV, in the equation is determined by:

$$PMV = 3.155\,[0.303\,\exp(-0.114\,M) + 0.028]\,L \quad \text{(I-P)} \quad (6.3)$$

$$PMV = [0.303\exp(-0.036M) + 0.028]\,L \quad \text{(SI)} \quad (6.4)$$

where M is the metabolism, and L the load.

The M and L are the functions of air temperature, air velocity, and environmental temperature. The flow program calculates the distributions of air temperature and velocity, and an energy simulation program the environmental temperature distribution. Then the flow program calculates the distribution of PPD in any position in a space. Figure 6.1 illustrates a complete diagram of the coupled energy /airflow/thermal comfort program.

6.2 Simulation Exercises

The study carried out five simulation exercises for the energy /airflow/thermal comfort program:

- a home (Hanibuchi and Hokoi 1996)
- an atrium (Hiramatsu et al. 1996)
- an aircraft hanger (Notarianni and Davis 1993).
- a large office with partition walls (Chen et al. 1998)
- a factory with individual workstations (Chen et al. 1998)

Those cases are carried out with experimental data or with detailed CFD simulation with a k-ε model. Therefore, those cases can further validate the simplified flow model developed. Further validation will enhance our research quality and provide more evidence about the performance of the simplified program.

All the dynamic simulations of the coupled flow and energy programs have been carried out under both winter and summer outdoor conditions. This allows us to demonstrate the coupling between the simplified flow program and the energy program, ACCURACY. Note that all the measurements were not done under dynamic conditions. It is therefore impossible to validate the combined program for the dynamic conditions. The simulations for the dynamic conditions are exercises to show the capacity of the combined program.

The following sections present the results for the three of five cases: the home, the atrium, and the large office with partition walls. The other two examples are available in the more detailed report (Chen et al. 1999).

6.2.1 The Home

The home shown in Figure 6.2 was a small house within a climate chamber. This was to achieve controlled outdoor thermal boundary conditions. The home was 6.0 m (20 ft) long, 4.0 m (13 ft) wide, and 2.5 m (8 ft) high. The climate chamber was controlled at 2.0 °C (35.6 °F) to simulate a winter condition. The house was empty and without partitions. The materials used for the ceiling, floor, walls were different and with a thermal conductance shown in the following table.

Table 6.1 Materials used in the house in the experimental setup

Enclosure	Thermal conductance
Wall-1, Wall-3	0.55 $W/m^2 K$
Wall-2, Wall-4	0.27 $W/m^2 K$
Floor	0.60 $W/m^2 K$
Ceiling	0.32 $W/m^2 K$
Windows	4.51 $W/m^2 K$

An air-conditioner, shown in Figure 6.3, was used to heat the house. The air-conditioner was installed above the window on Wall-3. The air supply temperature was 38.2°C (100 °F) and the heat supply was 1.99 kW (6824 Btu/hr). The air return outlet is located above the supply outlet. The air temperature at the return outlet was 24.7 °C (77 °F).

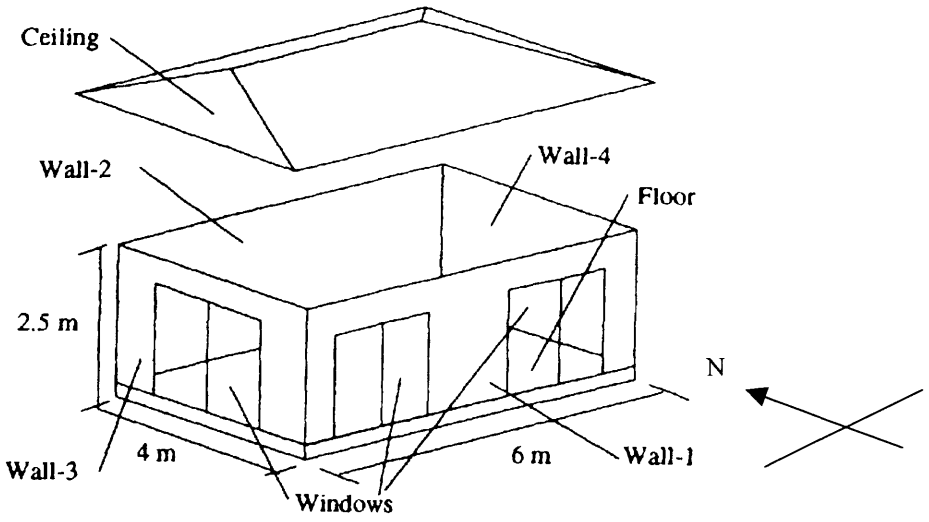

Figure 6.2 Test home placed in a climate chamber (Hanibuchi and Hokoi 1996)

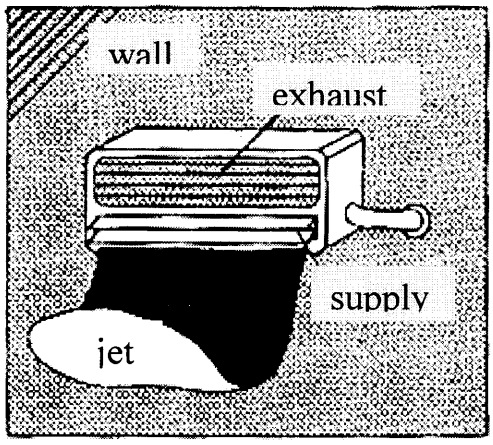

Figure 6.3 Air-conditioner used for the heating of the test house

The experiment measured the air and surface temperature, and the air velocity in the house. Figure 6.4 shows the air velocity and temperature distributions at two sections in the house. Although the air temperature from the air-conditioner was warm, the high downward momentum pushes the air towards the floor to form a mixing type of airflow pattern.

Figure 6.5 shows that the computed air velocities near the floor (the top two figures) are much smaller than the measured data. It seems that the computed air jet is not as strong as the one found in the experiment. Since the geometry of the air outlet is complicated, it is very difficult to simulate such an air-supply device. The momentum method was used to simulate the supply jet flow since the data for the box method are not available.

Figure 6.6 compares the measured and computed air temperatures in the house. The vertical coordinate is for the house height. The agreement between the computed results and the measured data is good, except near the floor area. Near the floor area, the computation under-predicted the air temperature due to the poor simulation of the air supply device.

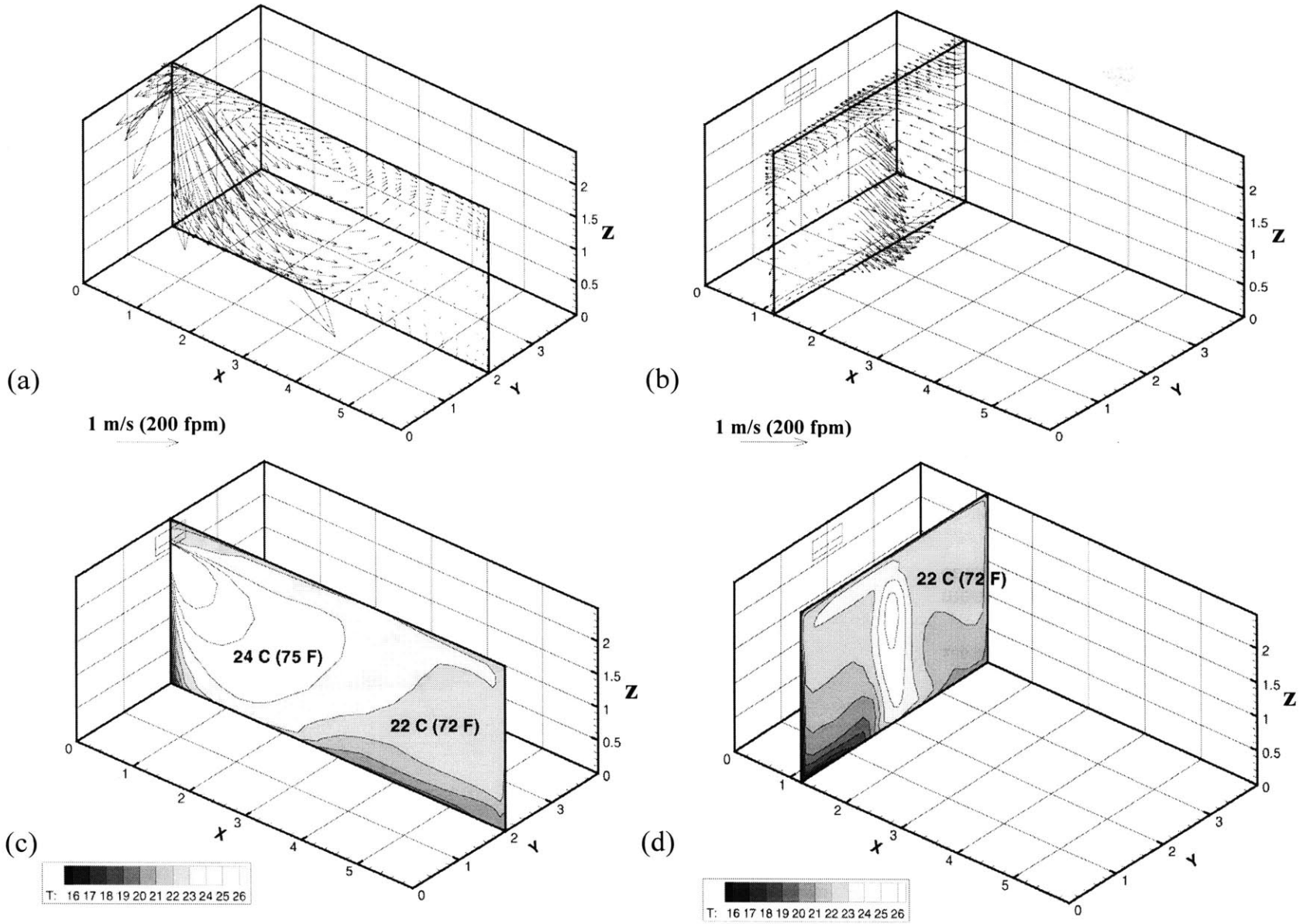

Figure 6.4 The computed air distributions for the home. (a) air velocity in a middle section, (b) air velocity in a vertical section, (c)air temperature in a middle section, and (d) air temperature in a vertical section

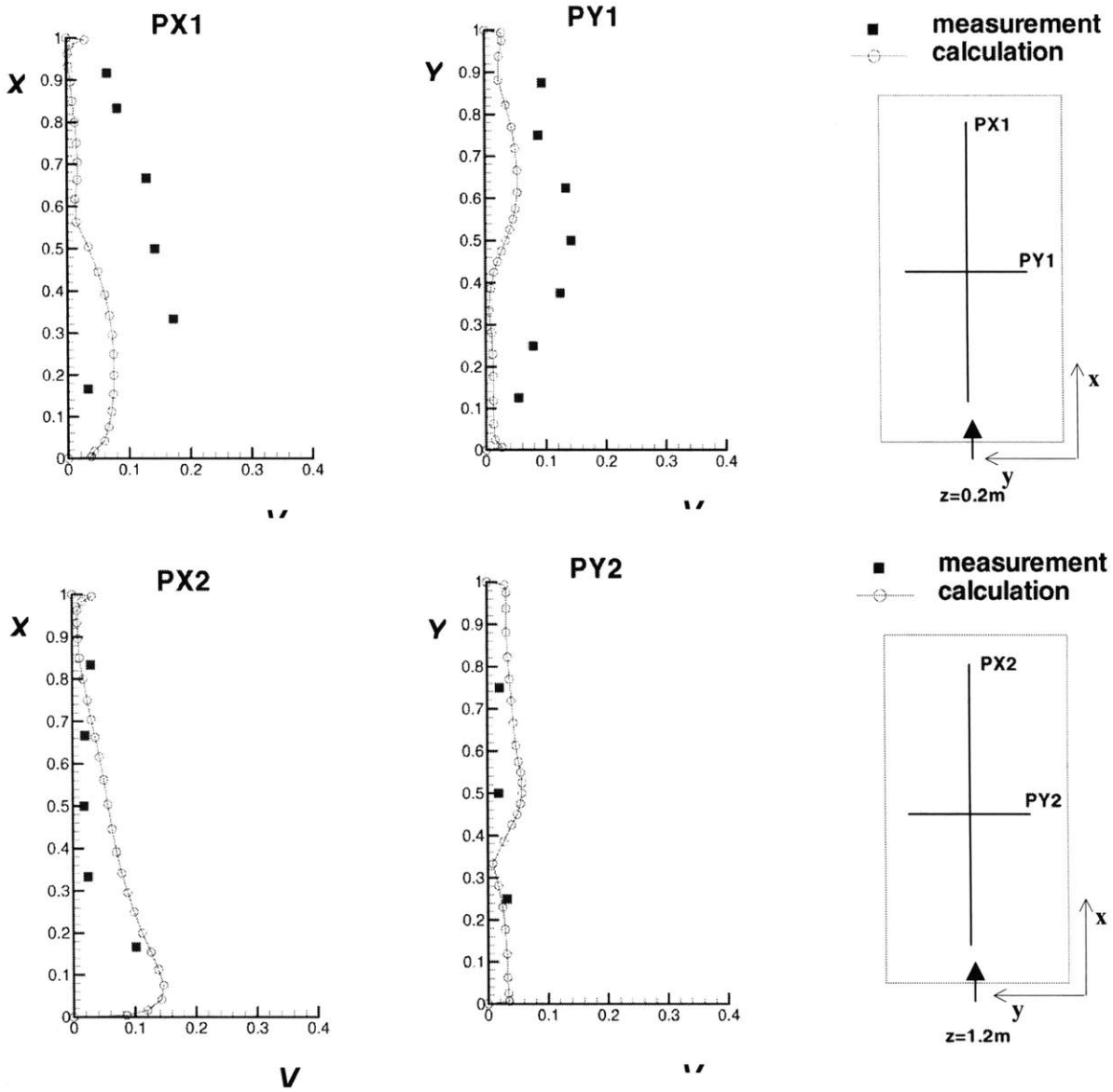

Figure 6.5 The comparison of the computed and measured velocity profiles at five positions, X=length/total room length (L), Y=width/total room width (W), V=velocity/inlet velocity (V_{in}), L = 6.0 m (20 ft), W= 4.0 m (13 ft),V_{in}= 6.1 m/s (1220 fpm)

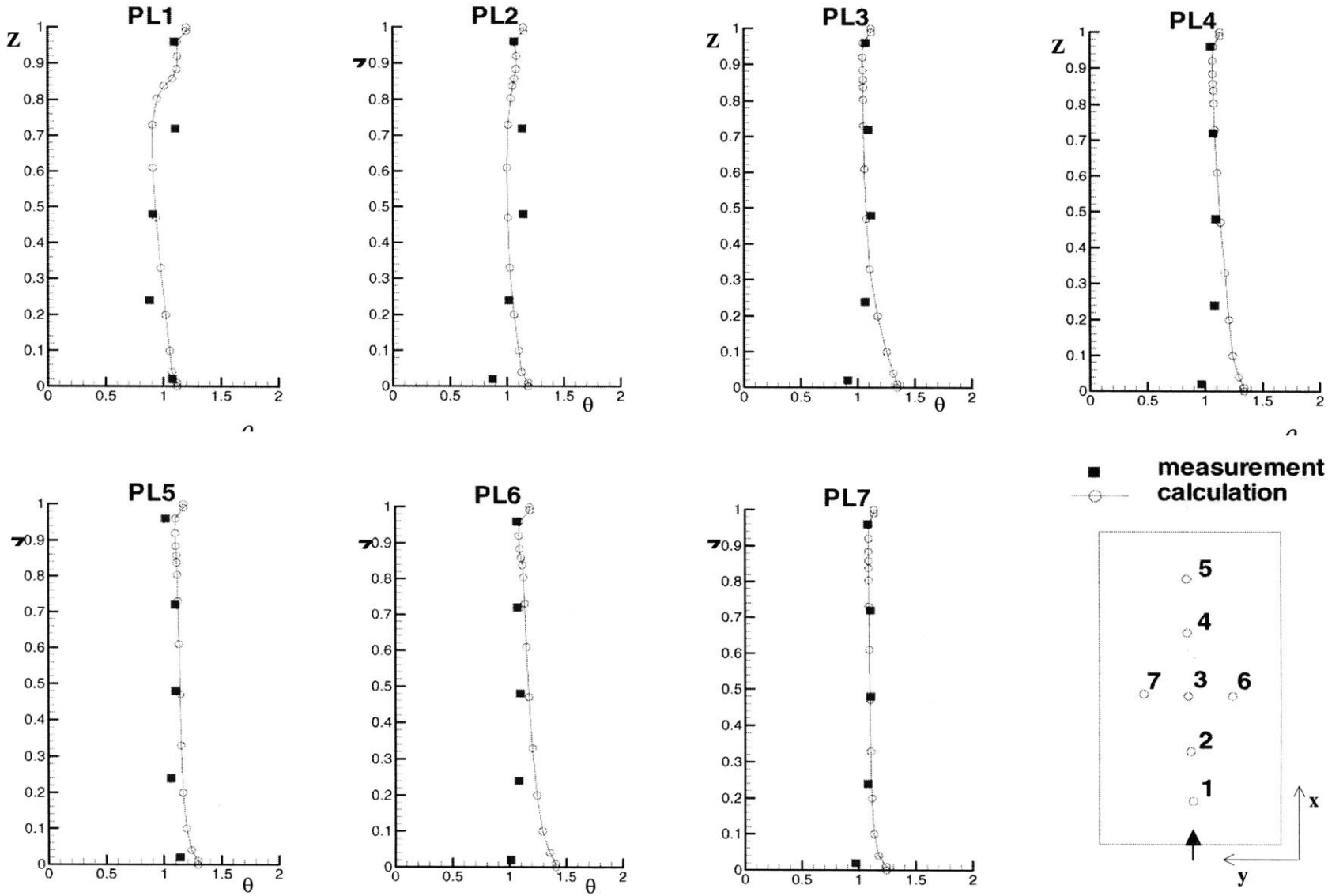

Figure 6.6 The comparison of the calculated and measured temperature profiles at seven positions in the room. Z=height/room height (H), $\theta = (T-T_{in}) / (T_{out}-T_{in})$, H = 2.5m (8.2 ft), T_{in}=38.2°C (100°F), T_{out}=24.7°C (76.5°F)

For the analysis of the dynamic performance of the coupled flow and energy program, the study used typical meteorological year (TMY) data sets derived from the 1961 - 1990 national solar radiation database. Since the purpose of the study is to demonstrate how the simplified program couples with the energy program ACCURACY, the investigation used Boston weather data and focused on only two typical days in a year: January 7 in winter and July 8 in summer. Figure 6.7 show the outdoor air temperature and solar radiation on the two typical days.

The calculation assumed that the house was conditioned 24 hours per day and the indoor air temperature was set at 25 °C (77 °F). The materials used in the house are shown in Table 6.2. The inlet boundary conditions for the calculations are presented in Table 6.3. The simulations used constant air volume system with variable inlet air temperature. The inlet air temperature depends on the heat extraction in each hour.

Table 6.2 The materials used in the calculation for the house.

Enclosure	Layer	Thickness (m)	Specific heat (J/kg K)	Density (kg/m^3)	Conductivity (W/m K)
Floor	1	0.10	840	2243	1.731
Ceiling	3	0.10	840	1600	0.52
		0.10	500	190	0.046
		0.01	1215	545	0.12
Walls	3	0.10	840	2082	1.3
		0.10	1210	55	0.027
		0.01	840	721	0.72
Windows	2 (double-glazing)	The reflection index of the glass is 1.52, the thickness of the glass is 6 mm, and the absorptivity of the glass is 0.018.			

The windows had no shading device. The house had no internal heat gain/loss. The infiltration was assumed to be zero and the air temperature in the basement to be 20°C (68°F) all year around.

Table 6.3 The inlet boundary conditions used in the calculation for the house

	Winter day (01/07)		Summer day (07/08)	
Time (hours)	Inlet temperature (°C)	Mass flow rate (kg/s)	Inlet temperature (°C)	Mass flow rate (kg/s)
4am	33.6	0.14	25.9	0.14
8am	32.0	0.14	23.8	0.14
12pm (noon)	27.8	0.14	18.2	0.14
4pm	28.4	0.14	13.9	0.14
8pm	29.6	0.14	22.6	0.14
12am	30.0	0.14	24.8	0.14

Figure 6.7(b) shows the heat extraction (positive means cooling and negative implies heating) for the house. During the winter day, the house needs heating all the time. The solar radiation in the daytime reduces the heating load on the winter day, but it increases the cooling load in the summer day. During the summer afternoon, the cooling load increases significantly due to the solar radiation from the west window. Figure 6.7(c) shows the total amount of direct and diffuse solar radiation received on a horizontal surface during the 60 minutes preceding the hour indicated.

Figure 6.8 and Figure 6.9 show the air velocity and temperature distributions in the house during the winter day. Although the simulation was done hour by hour, the results shown in the figures are for every four hours. Figure 6.10 presents the PPD distribution at 8 am, 12 noon, and 4 pm in the day. Figure 6.11 and Figure 6.12 illustrate the air velocity and temperature distributions in the house during the summer day. The computation was quasi-steady to save computing time. The surface temperature and heat extraction were used to calculate the air temperature and heat transfer coefficients for the current hour. The air temperature and heat transfer coefficient for the current hour were used to determine the surface temperature and heat extraction in the next hour.

In this particular case, the airflow patterns in the winter and summer are similar. It is clear that the room air is not perfectly mixed and the air velocity is large in some part of the house. The air temperature distributions are rather uniform, unless the absolute value of the heat extraction is large. The comfort level in the house is generally good. Except in the area near the air conditioner, the PPD is less than 10% in most parts of the house for both summer and winter.

Note that the uniform air velocity and temperature distributions can have a significant impact on the heat extraction. Chen and Kooi (1988) found that the heat extraction that accounts for temperature stratification was 30% lower than the heat extraction calculated with the uniform indoor air temperature. Also, the heat extraction based on the non-uniform temperature has an excellent agreement with the measured data. It is therefore very important to combine an airflow program with an energy analysis program to obtain more accurate results. This is very important for designing a suitable cooling or heating system in a space.

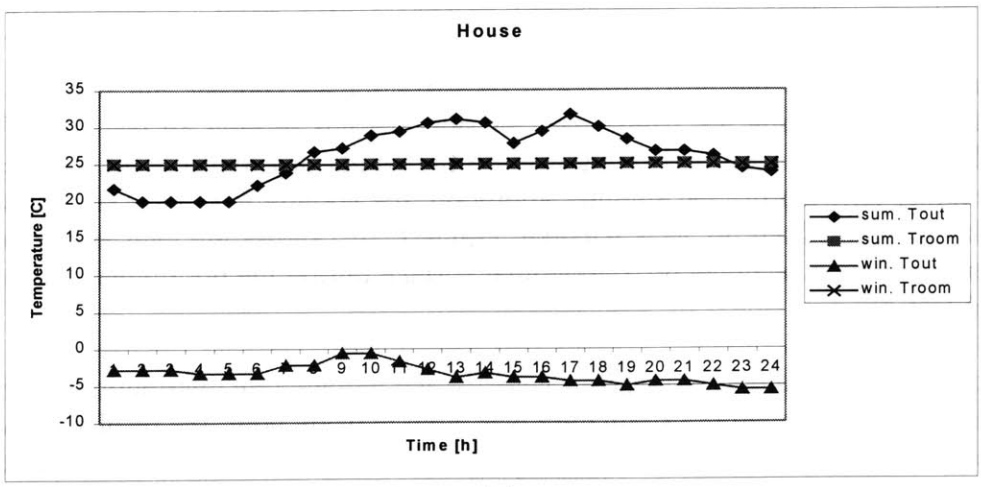

(a)

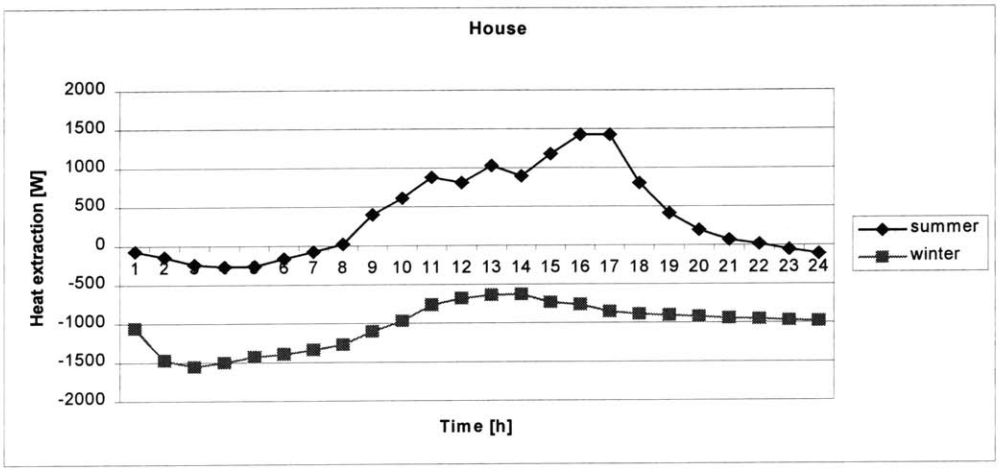

(b)

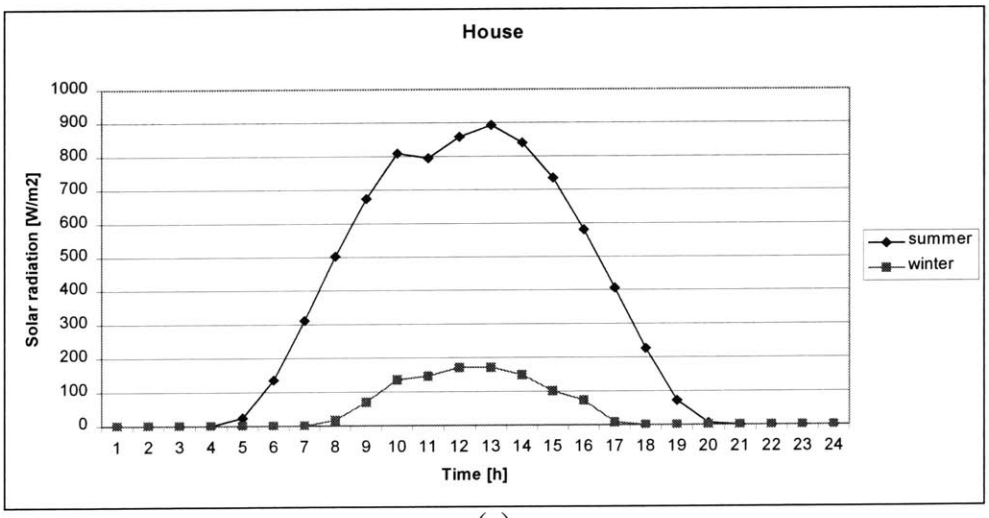

(c)

Figure 6.7 Outputs from the energy program ACCURACY for the house during the winter and summer days. (a) Indoor and outdoor air temperature (b) heat extraction, (c) outdoor solar radiation

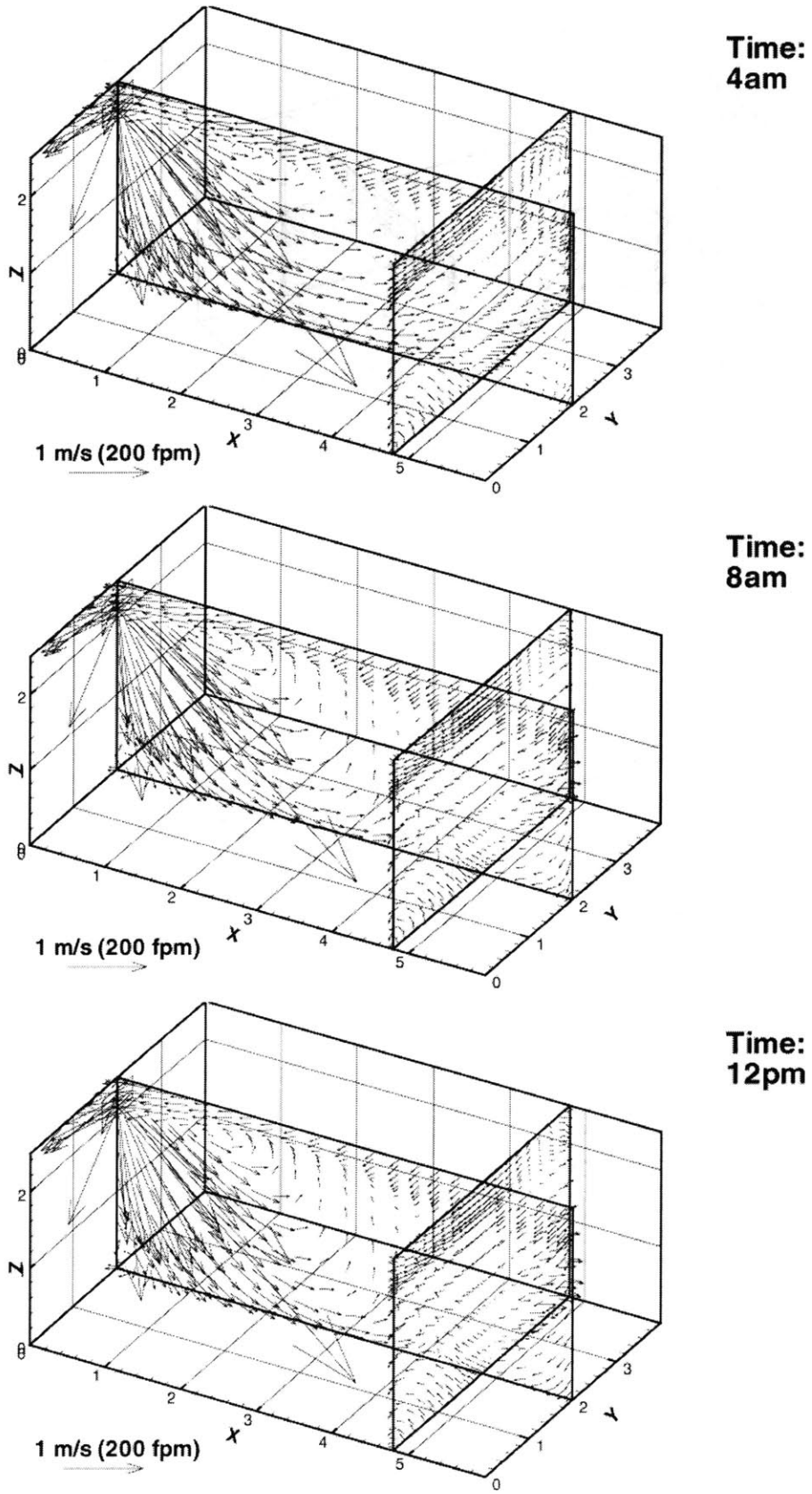

Figure 6.8 The computed air velocity distributions for the home during the winter day

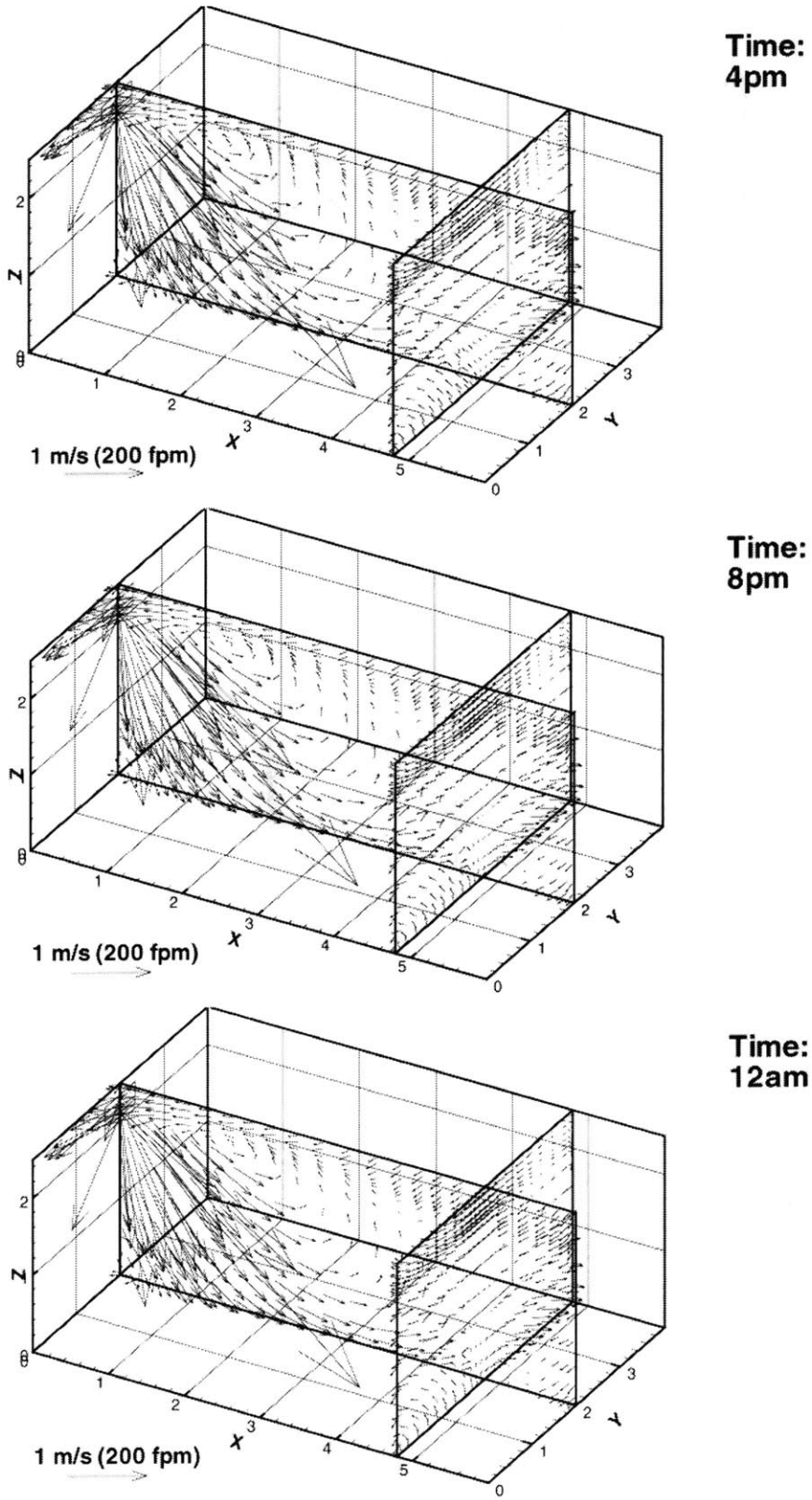

Figure 6.8 (Continued) The computed air velocity distributions for the home during the winter day

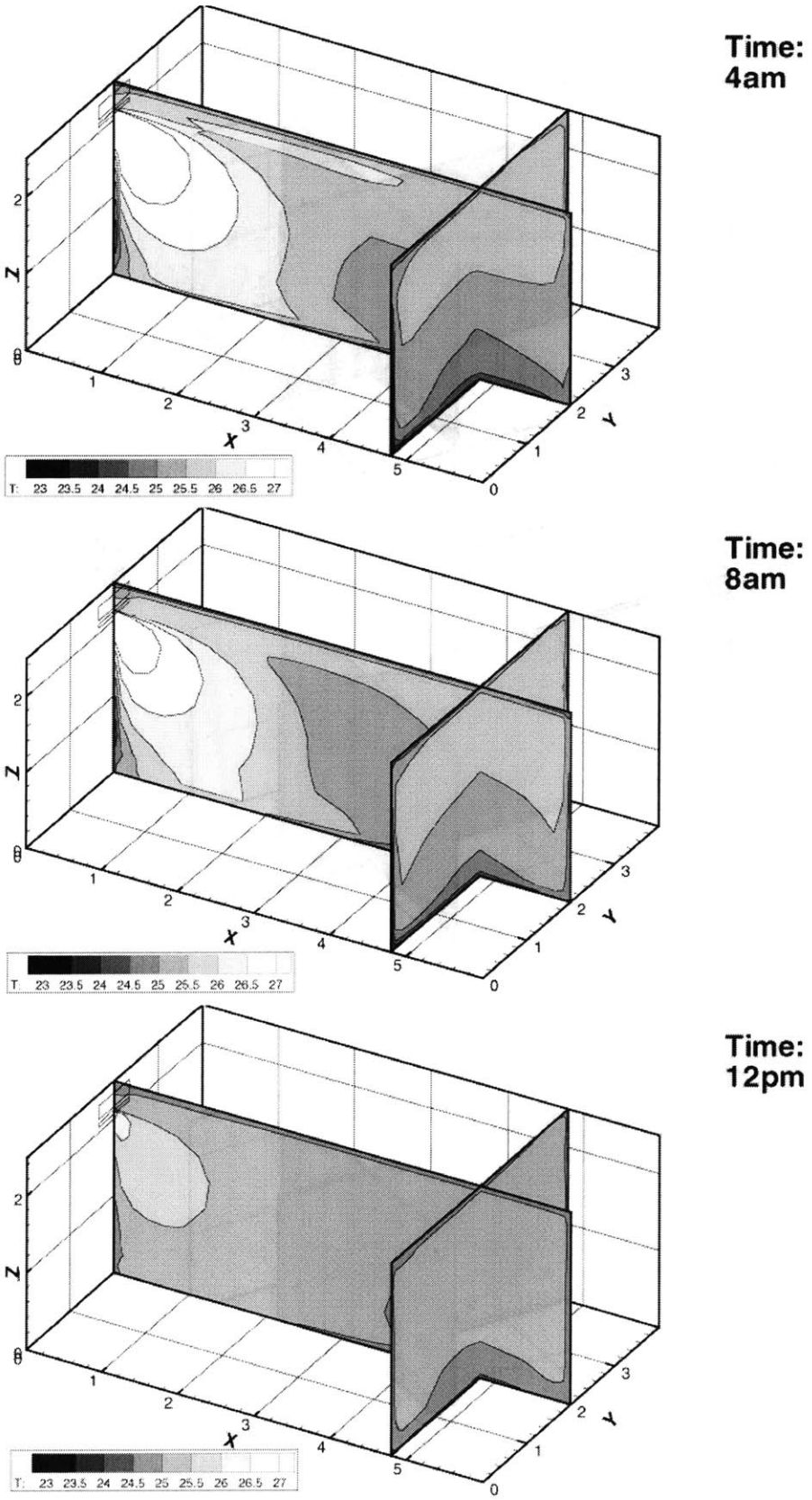

Figure 6.9 The computed air temperature distributions for the home during the winter day

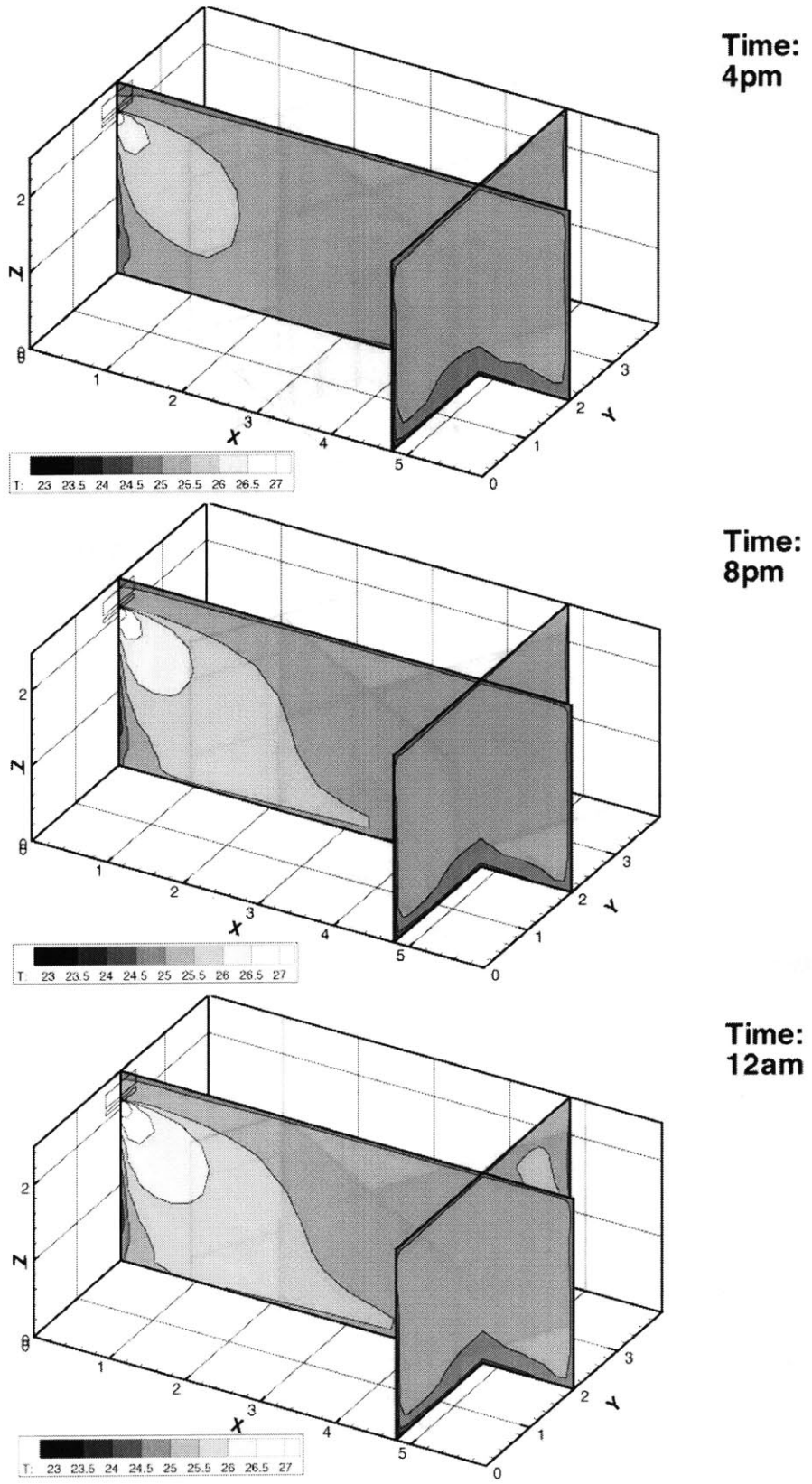

Figure 6.9 (Continued) The computed air temperature distributions for the home during the winter day

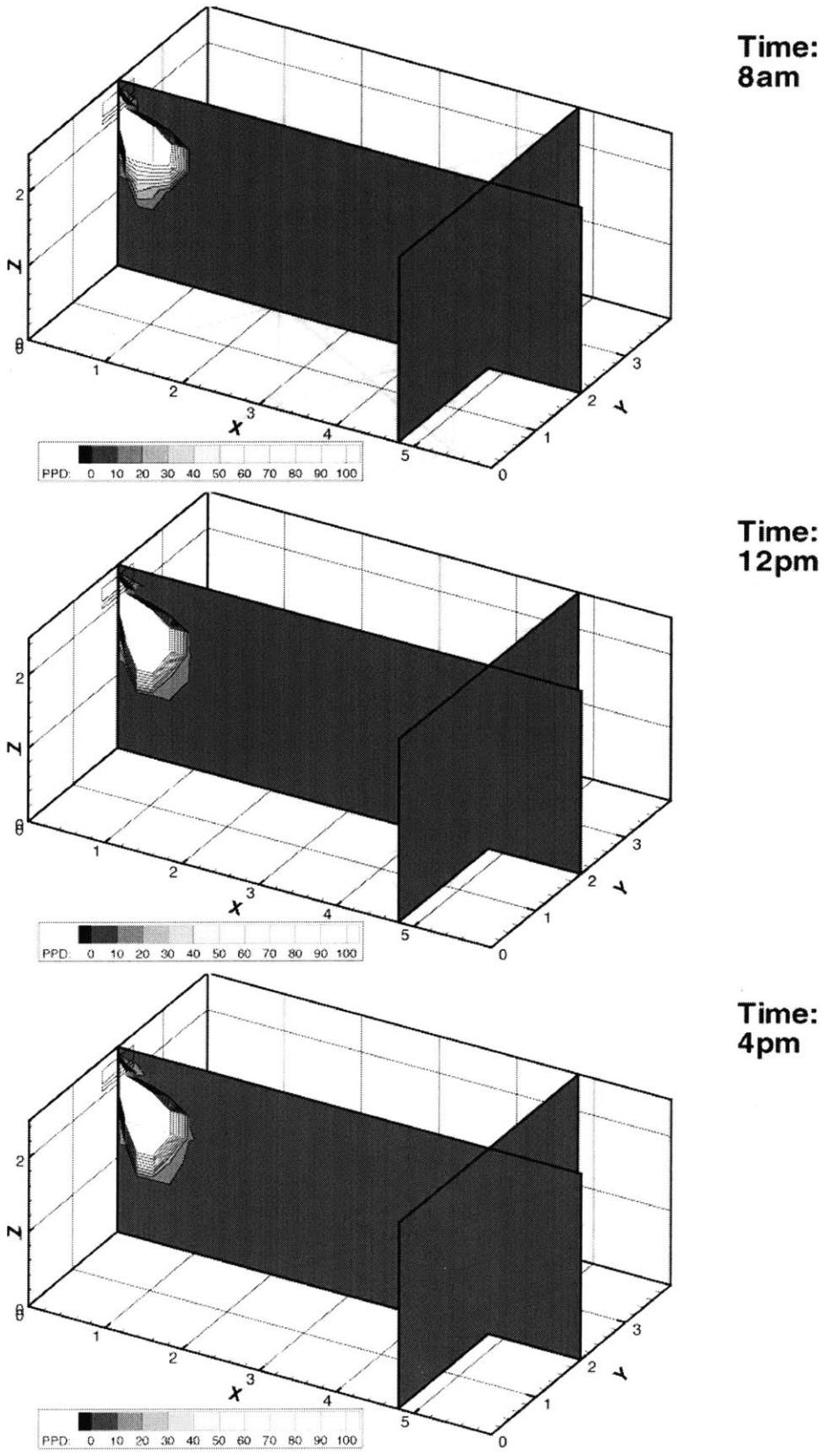

Figure 6.10 The PPD distribution in the home during the winter day

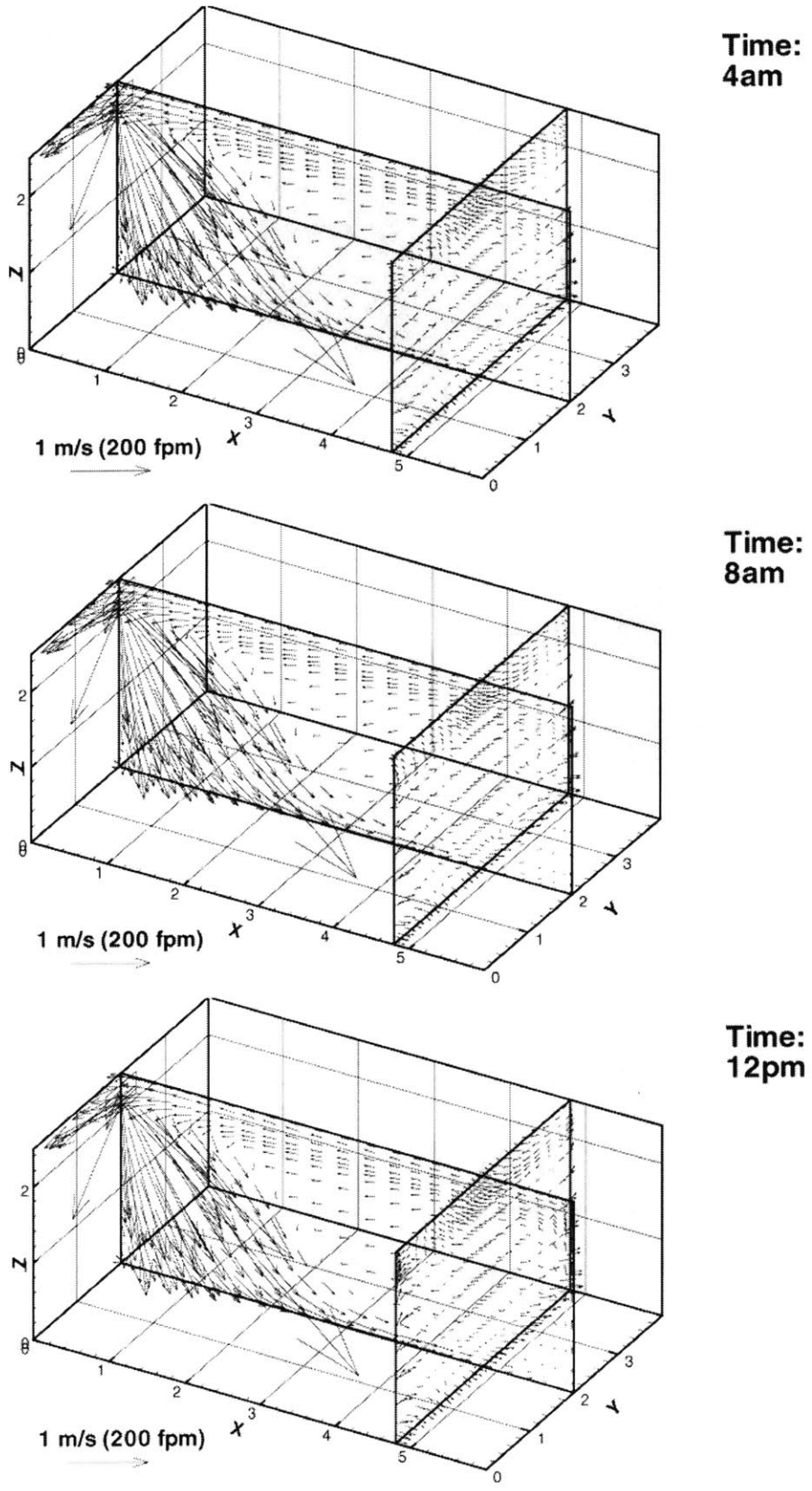

Figure 6.11 The computed air velocity distributions for the home during the summer day

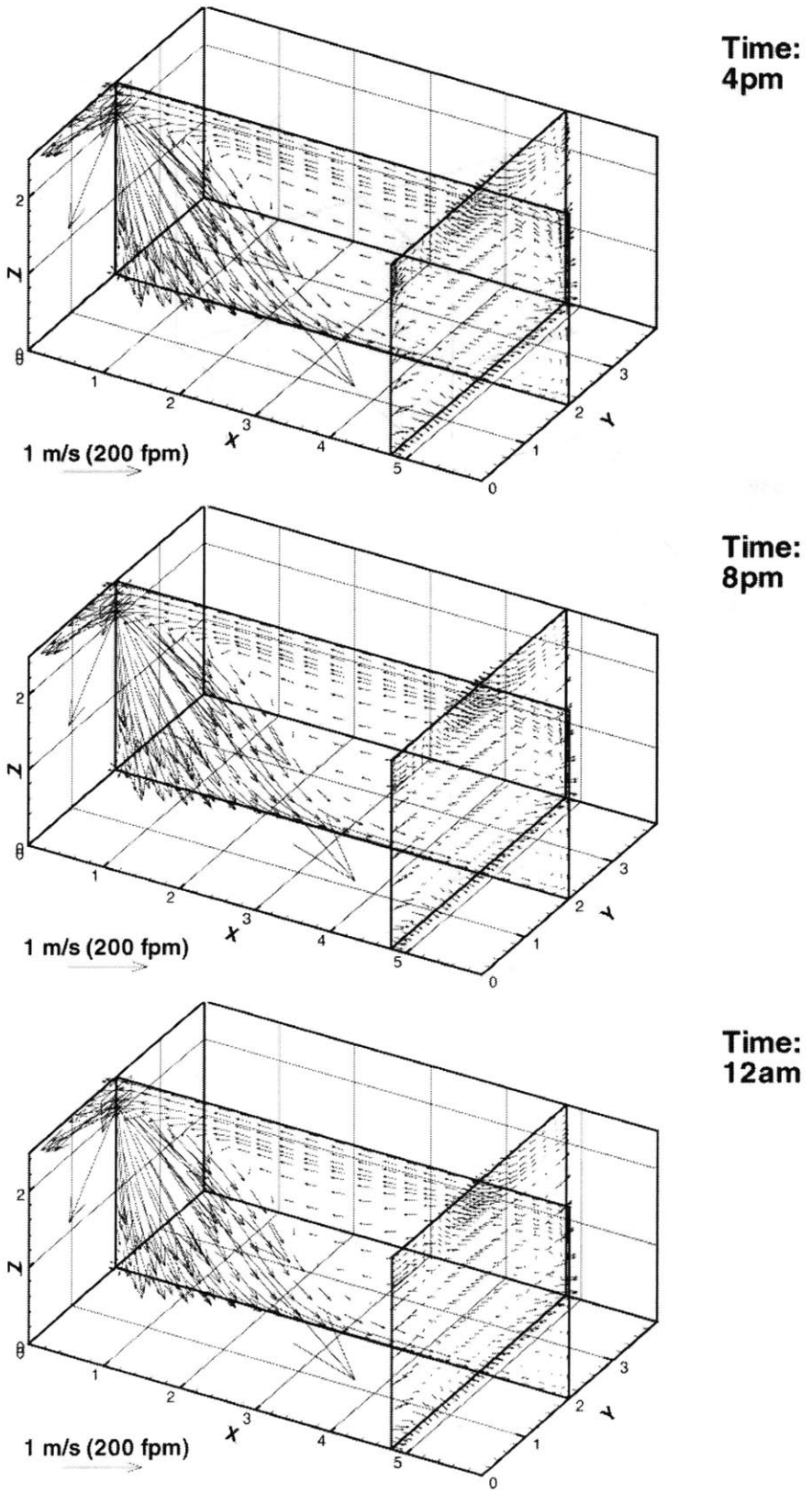

Figure 6.11 (Continued) The computed air velocity distributions for the home during the summer day

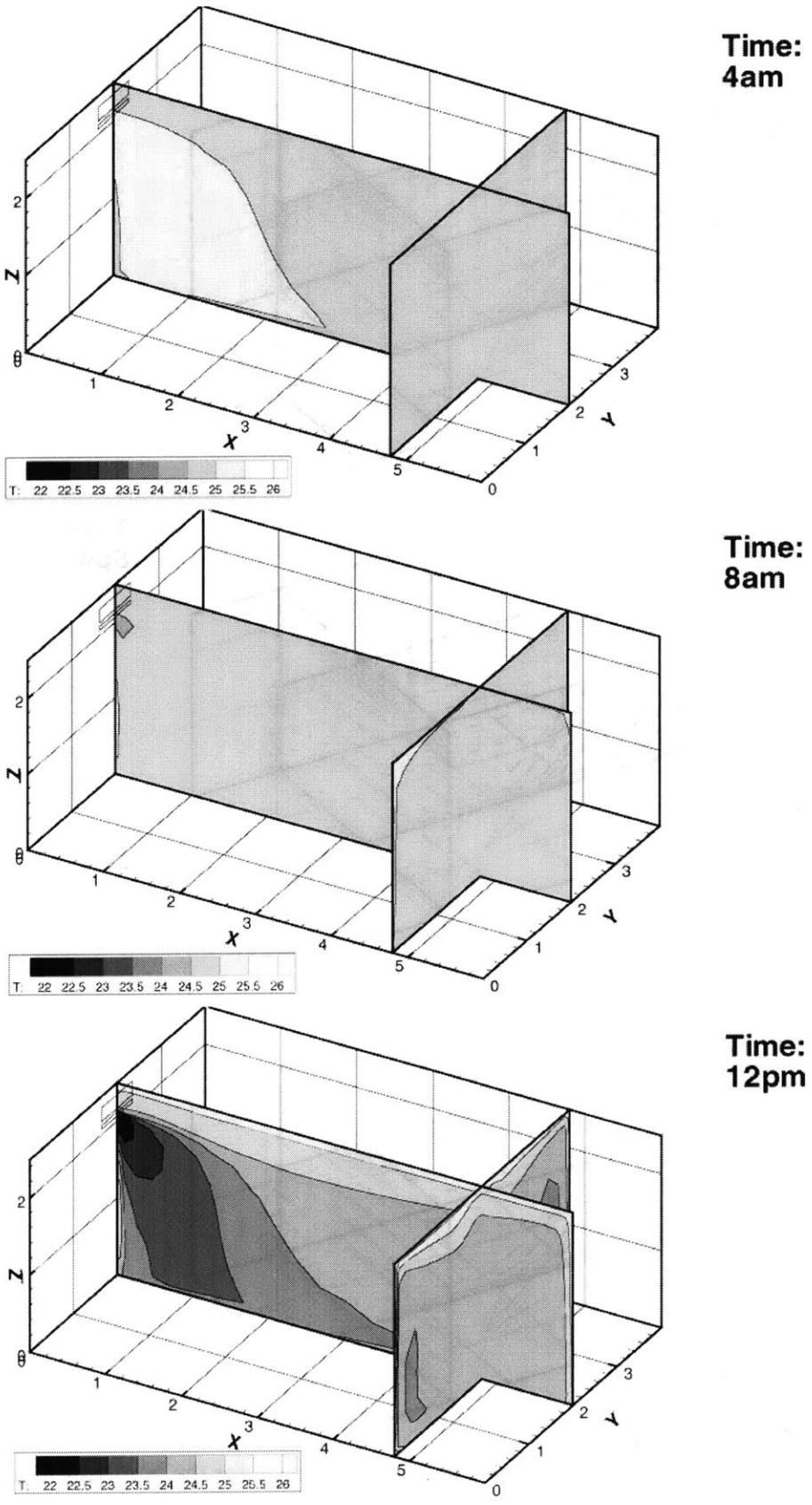

Figure 6.12 The computed air temperature distributions for the home during the summer day

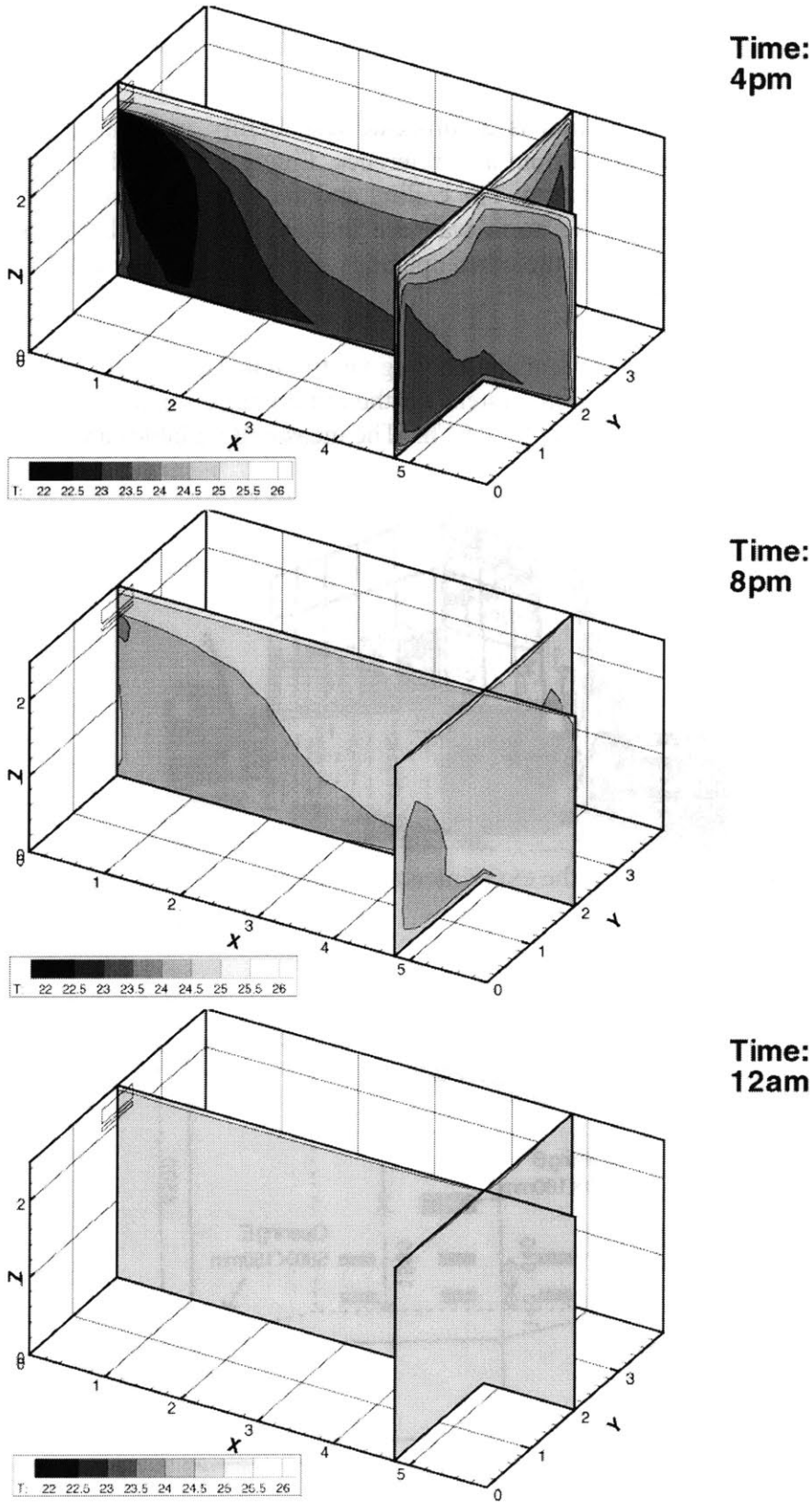

Figure 6.12 (Continued) The computed air temperature distributions for the home during the summer day

6.2.2 The Atrium

The atrium used for simulation is a full-scale test facility in Japan (Hiramatsu et al. 1996). Many studies have used this atrium as a reference. Figure 6.13 and Figure 6.14 illustrate the appearance and the size of the atrium. The ceiling and the south, west and east walls of the atrium are glazed. The floor and the north wall are insulated. Our simulation used the inlet opening A and outlet opening B. All the other openings were closed (Figure 6.14). The atrium was empty and had no partitions.

The original study was for natural and cooling ventilation. The present investigation used only the cooling conditions. The cooling system for the atrium has a maximum power of 32 kW and the maximum air supply volume of 4050 m^3/hr. The measured variables are:

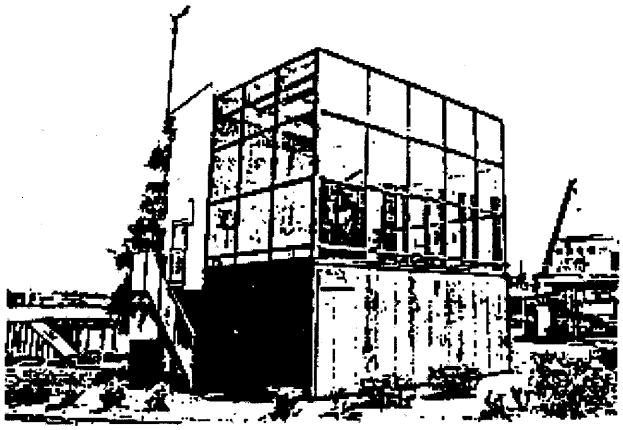

Figure 6.13 The appearance of the experimental atrium Japan (Hiramatsu et al. 1996)

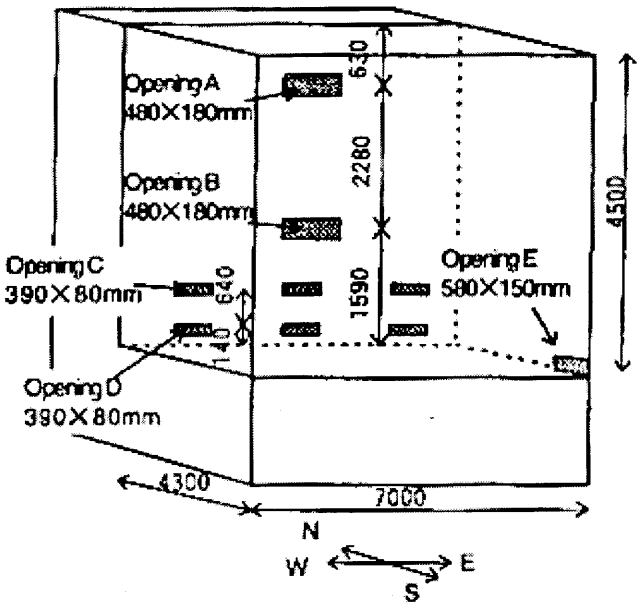

Figure 6.14 The atrium size and openings (dimensions given in mm)

- solar radiation
- outdoor air temperature
- outdoor wind speed and direction
- indoor air temperature at 27 points
- inner surface temperature at 42 points
- solar radiation transmitted through each glass wall
- indoor air velocity at 9 points

The temperature was measured by copper-constantan thermocouples with an accuracy of 1.0 K (2°F). The air velocity was measured by a three-dimensional supersonic anemometer. The experiment also measured the cooling load (2.3kW or 7847 Btu/hr).

Figure 6.15 presents the computed air velocity and temperature distribution in the atrium. The jet from the air diffuser was not strong enough to reach to the opposite glass façade. The falling jet may lead to draft in the atrium. The room air is not well mixed. During the measurement, the corresponding cooling load was not very high. However, there was temperature stratification in the atrium.

Figure 6.16 compares the computed velocity profiles with those measured. Since too few experimental data were available, the discrepancies between the computation and measurement are very significant. Off et al. (1996) found a similar problem, when they tried to compare their CFD results by the k-ε model with the experimental data. As this is a real atrium, it would be very difficult to control the thermal boundary conditions. The measurements may also have a greater uncertainty. Therefore, it is difficult to conclude anything from the comparison.

The predicted air temperature distribution agrees with the experimental data as shown in Figure 6.17. However, the discrepancies in some locations are still significant. It is difficult to find a convincing reason, because both the computation and experiment have some uncertainties.

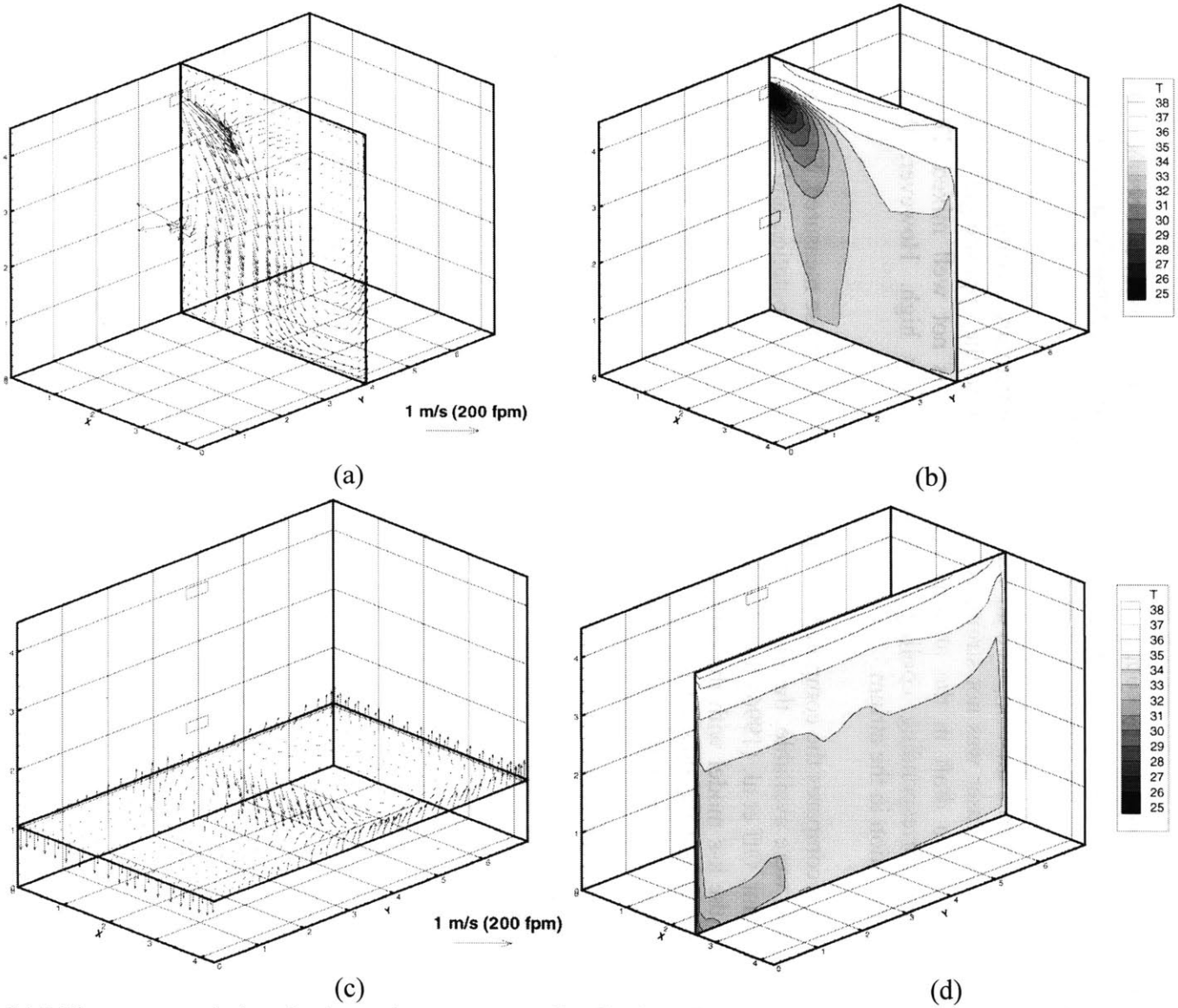

Figure 6.15 The computed air velocity and temperature distributions for the atrium (a) and(c) in a section through the inlet and outlet, (b) and (d) in a vertical section

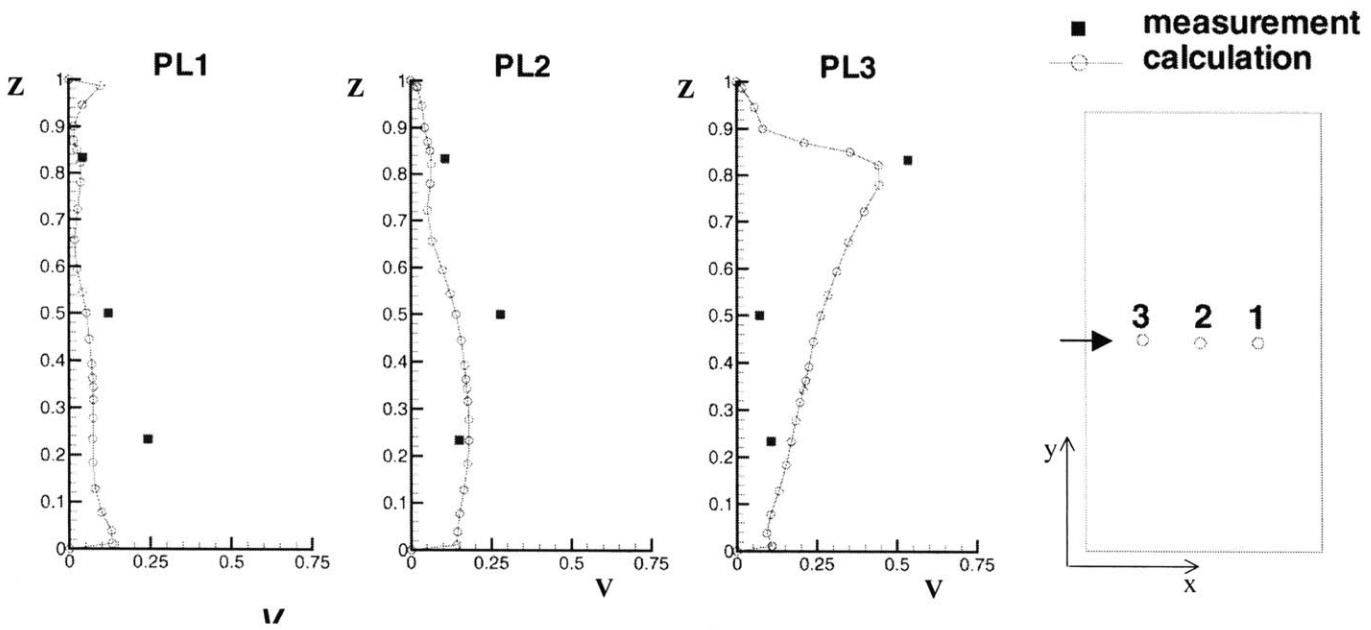

Figure 6.16 The comparison of the calculated and measured velocity profiles at three positions in the atrium Z=height/total room height (H), V=velocity/inlet velocity (V_{in}), H=4.5m (14.8 ft), V_{in}=1.4m/s (280 fpm)

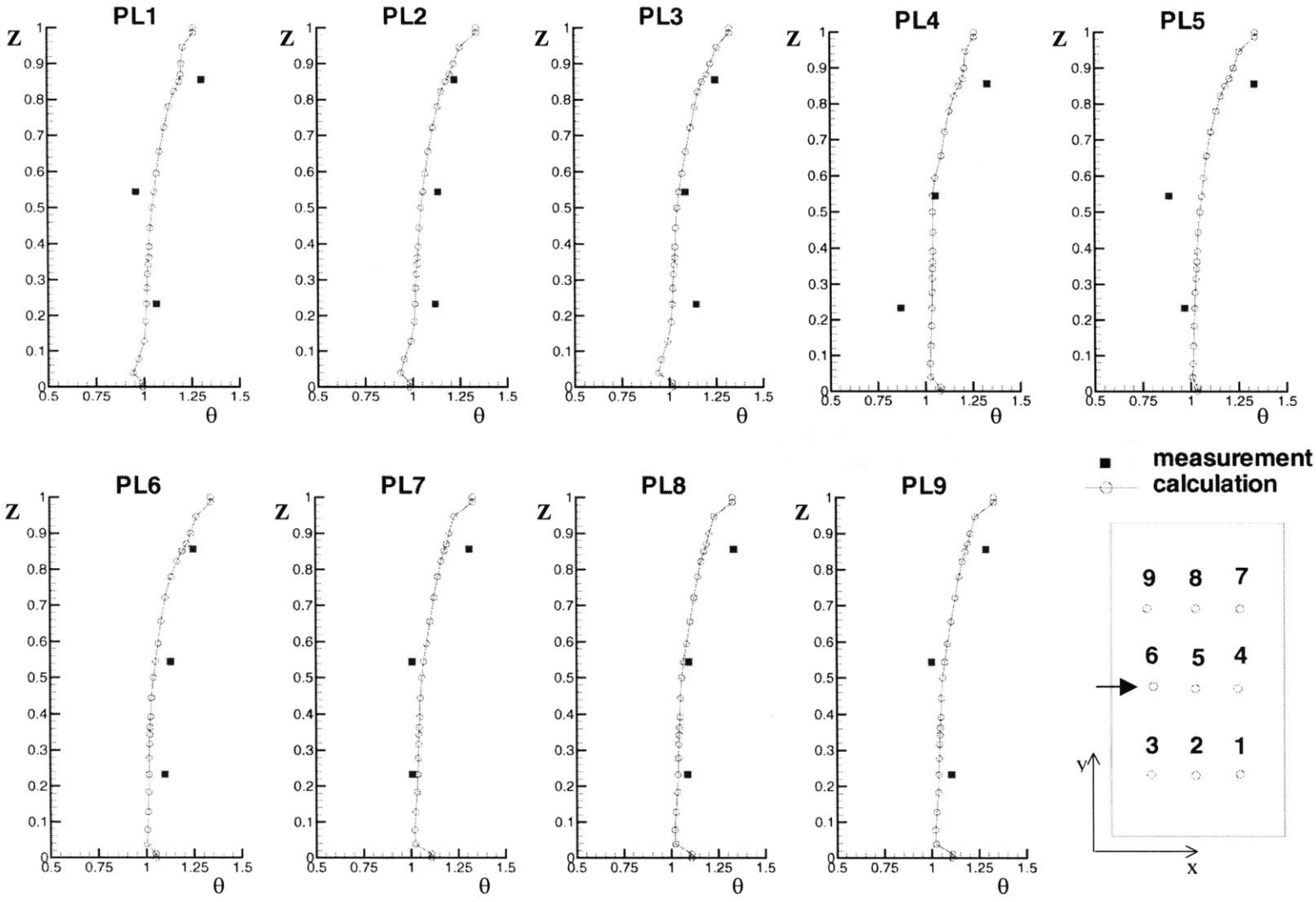

Figure 6.17 The comparison of the calculated and measured temperature profiles at nine positions in the atrium
Z=height/total room height (H), $\theta=(T-T_{in})/(T_{out}-T_{in})$, H=4.5m, $T_{in}=20.6^{o}C$, $T_{out}=33.1^{o}C$

The calculations of the airflow, thermal comfort, and energy with the combined airflow and energy program used the following materials for the atrium as shown in Table 6.4.

Table 6.4 The materials used in the calculations for the atrium

Enclosure	Layer	Thickness (m)	Specific heat (J/kg K)	Density (kg/m^3)	Conductivity (W/m K)
Floor	1	0.10	840	2243	1.731
North wall	3	0.10 0.10 0.01	840 1210 840	2082 55 721	1.3 0.027 0.72
Ceiling glazing	1	The reflection index of the glass is 1.52, the thickness of the glass is 6 mm, and the absorptivity of the glass is 0.018.			
South, east, and west glazing	1	The same as the ceiling.			

The atrium had no internal heat gain/loss and infiltration. The atrium was only conditioned between 7 am and 6 pm. The air temperature was controlled at 23 °C (73.4 °F) in the winter day and 25 °C (77 °F) in the summer day, as illustrated in Figure 6.18(a). Table 6.5 shows the inlet boundary conditions used for the calculations. The system used for the air-conditioning has a constant air flow rate and variable inlet temperature. Since the heat extraction from this space is very large, the inlet temperatures are extremely high in the winter and extremely low in the summer.

Table 6.5 The inlet boundary conditions used in the calculation for the atrium

	Winter day (01/07)		Summer day (07/08)	
Time (hours)	Inlet temperature (°C)	Mass flow rate (kg/s)	Inlet temperature (°C)	Mass flow rate (kg/s)
4am	-	-	-	-
8am	48.2	0.145	16.5	0.145
12pm (noon)	79.4	0.145	-55.3	0.145
4pm	101.4	0.145	-59.9	0.145
8pm	-	-	-	-
12am	-	-	-	-

Figure 6.18(b) shows the heat extraction (positive means cooling and negative implies heating) for the atrium. Obviously, both the solar radiation and outdoor air temperature have a major contribution to the heat extraction. Figure 6.18(c) shows total amount of direct and diffuse solar radiation received on a horizontal surface during the 60 minutes preceding the hour indicated.

Figure 6.19 and Figure 6.20 show the air velocity and temperature distributions in the atrium during the winter day. Since this is a heating situation, the warm air moves upwards and forms a large temperature stratification in the atrium during the conditioned period. However, the air velocity is small and the temperature is uniform during the unconditioned period. The air velocity is higher in the evening than that in the early morning hours, because there is a temperature difference between the wall and floor surfaces and the glazing surface. The temperature difference is due to the thermal capacity of the wall and floor.

The PPD distributions are not uniform at all during the conditioned period, as shown in Figure 6.21. The major contribution to the non-uniform PPD during the winter day is from the air temperature. In the summer, although the results are not shown here, the air velocity also contributes to the non-uniform distribution of the PPD. The PPD at the floor level can be as high as 60%, since the air temperature is low there. Although the mean temperature was controlled at a reasonable value (23 ^{o}C or 73.4 ^{o}F), the warm air in the upper part of the room does not go to the lower part.

In the summer, the air throw becomes much shorter because of the negative buoyancy from the cool jet. This is especially evident when the heat extraction is high as illustrated at 12 pm and 4 pm in Figure 6.22. Figure 6.22 further indicates that the air distribution is poor. Very similar to the winter case, Figure 6.23 shows the vertical temperature gradient is large when the heat extraction is high. The air in the atrium does not mix well with the diffuser jet.

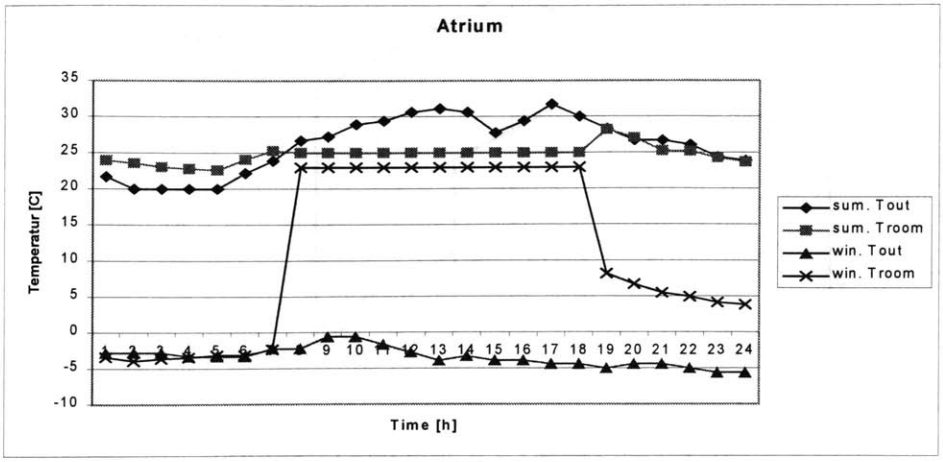

(a)

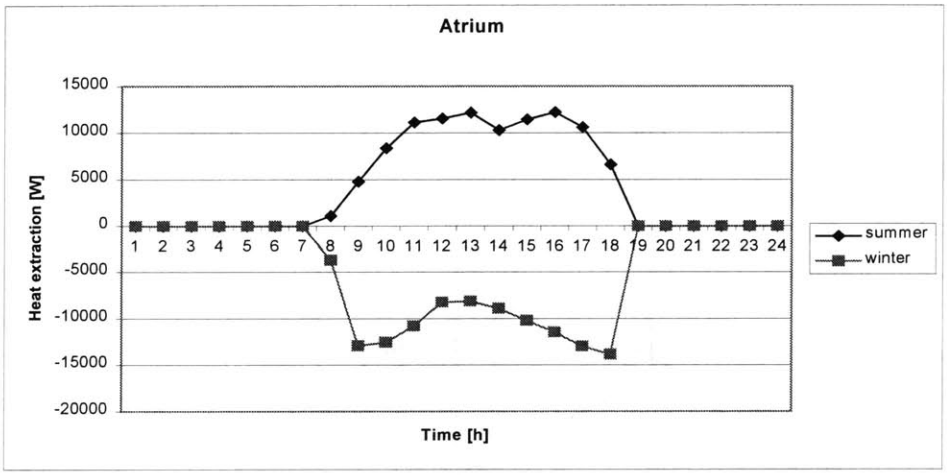

(b)

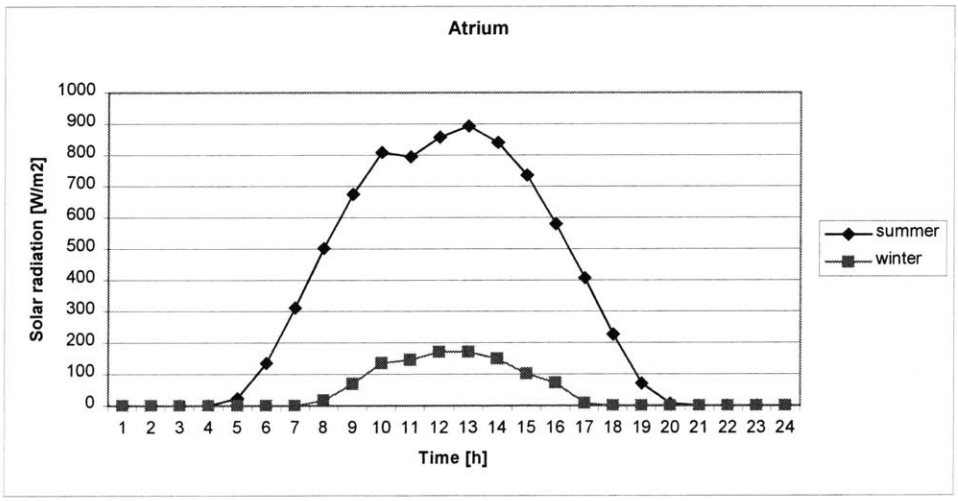

(c)

Figure 6.18 Outputs from the energy program ACCURACY for the atrium for the winter and summer days. (a) Indoor and outdoor air temperature (b) heat extraction , (c) outdoor solar radiation

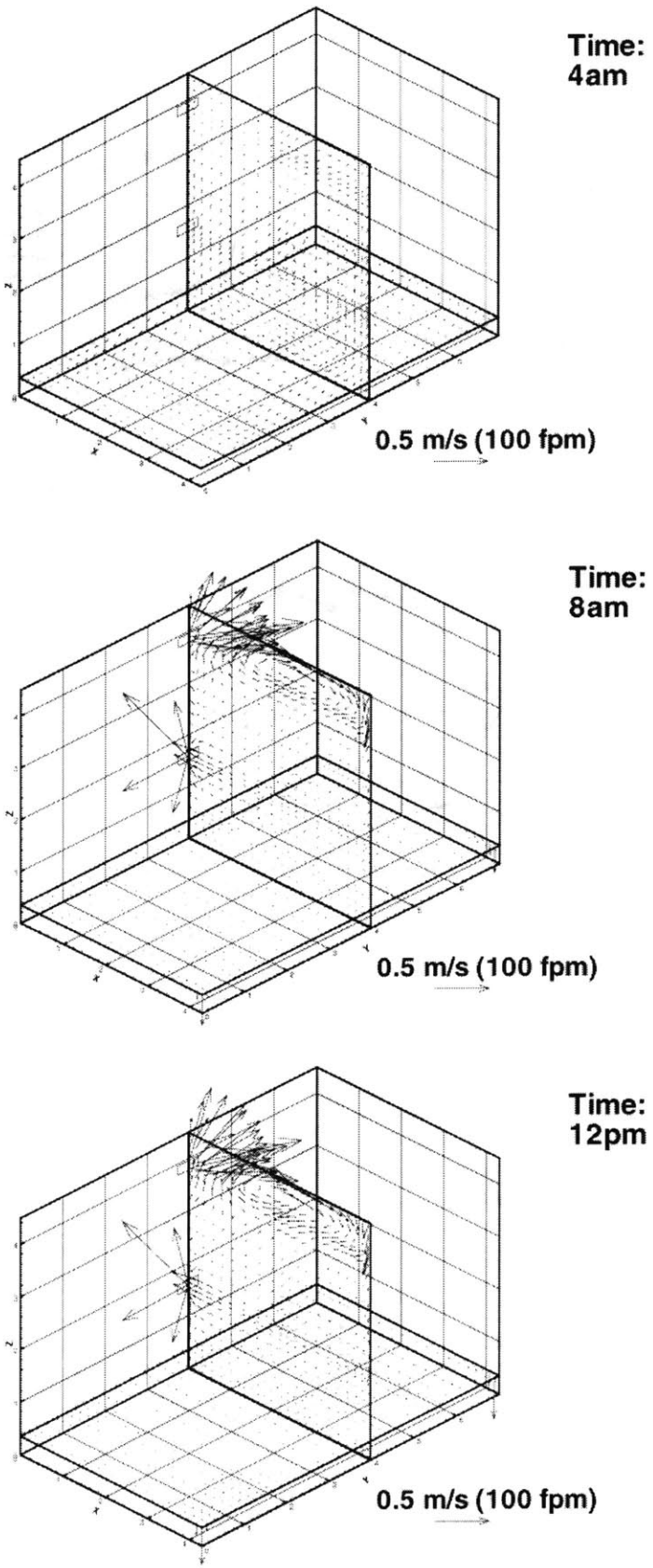

Figure 6.19 The computed air velocity for the atrium during the winter day

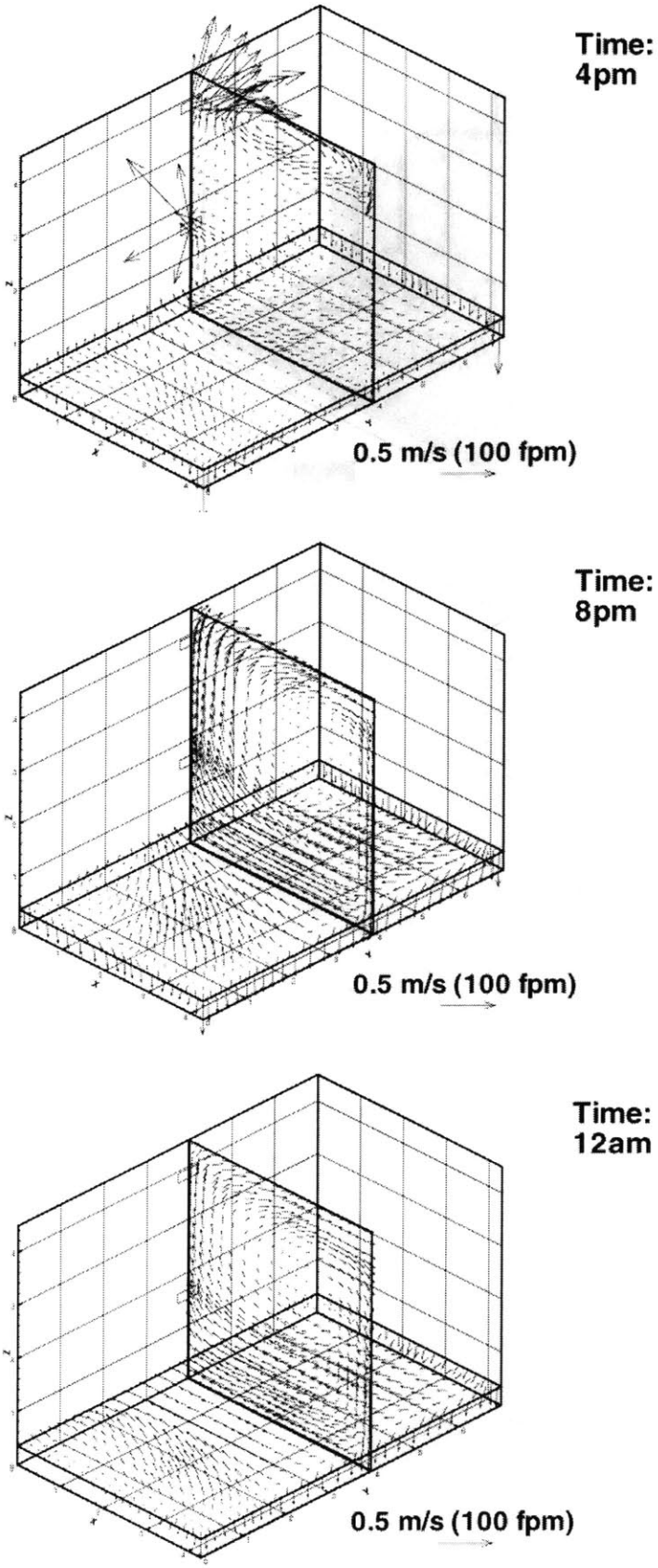

Figure 6.19 (Continued) The computed air velocity for the atrium during the winter day

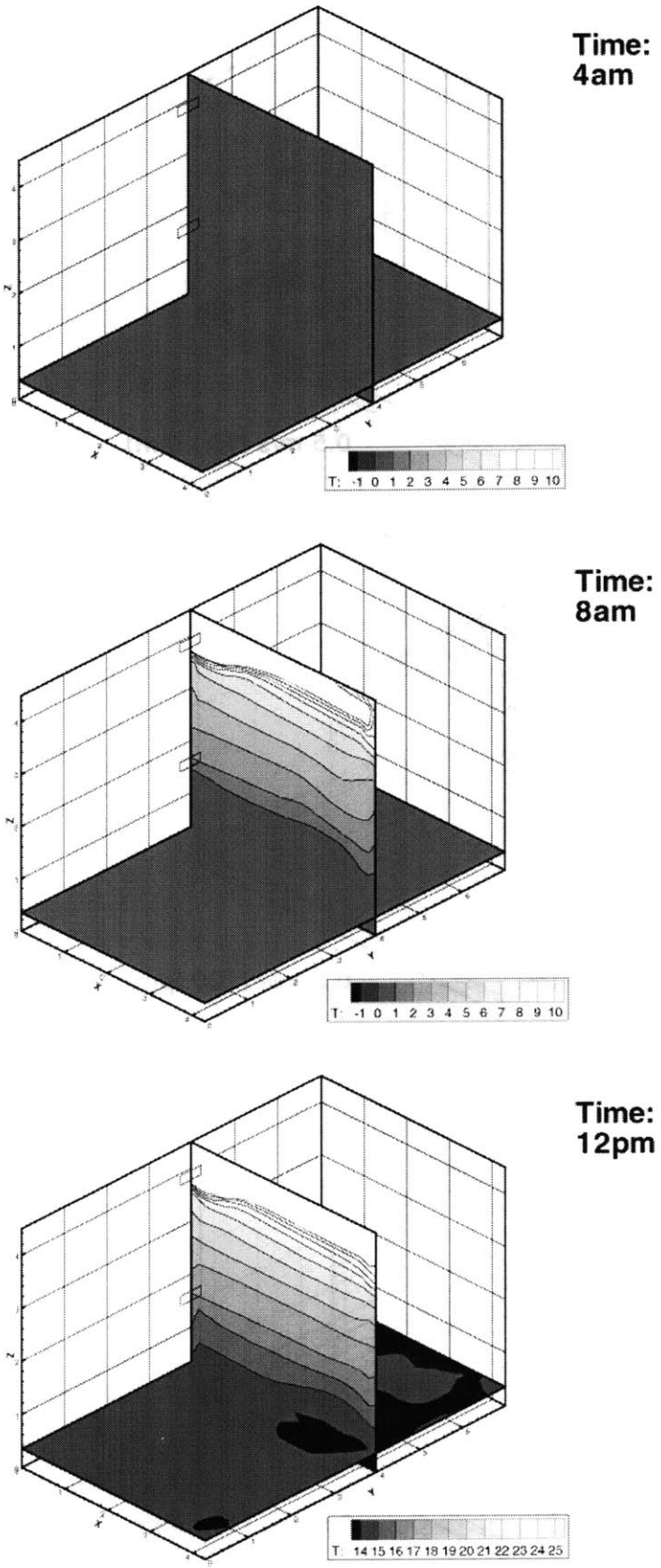

Figure 6.20 The computed air temperature for the atrium during the winter day

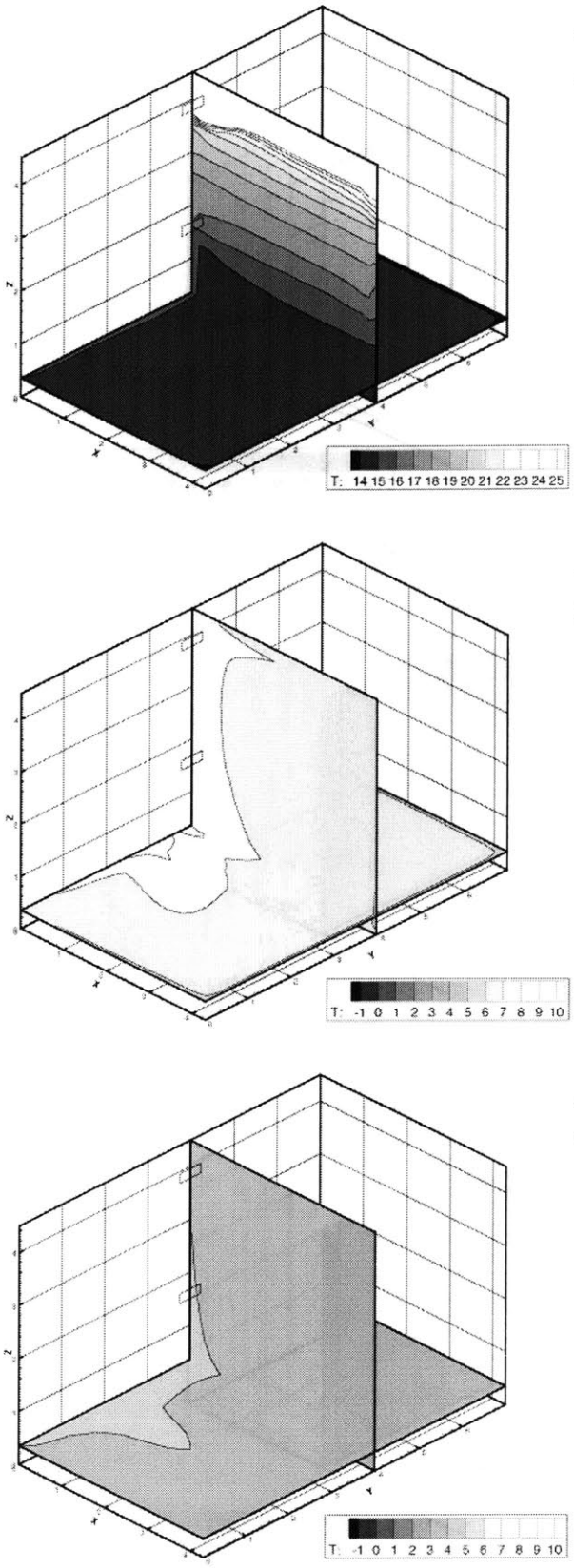

Figure 6.20 (Continued) The computed air temperature for the atrium during the winter day

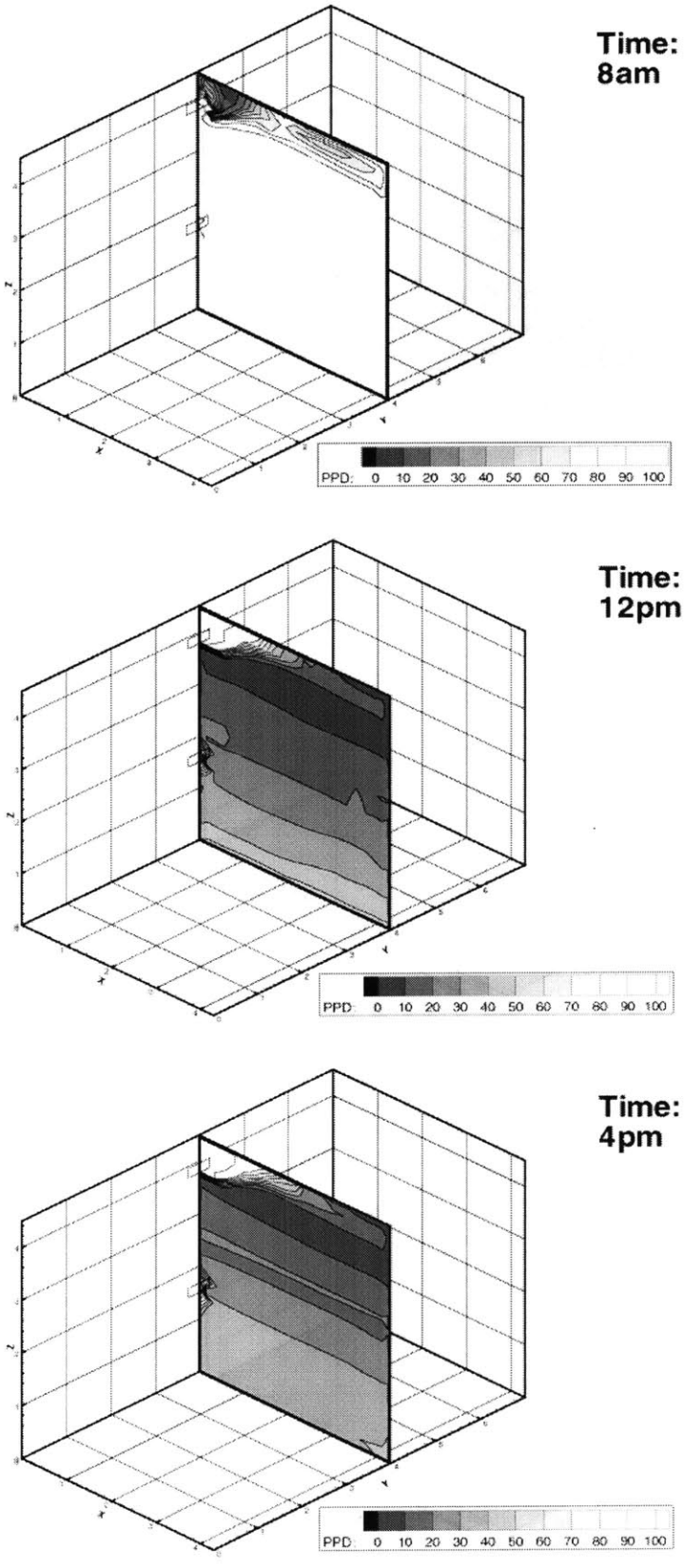

Figure 6.21 The PPD distribution in the atrium during the winter day

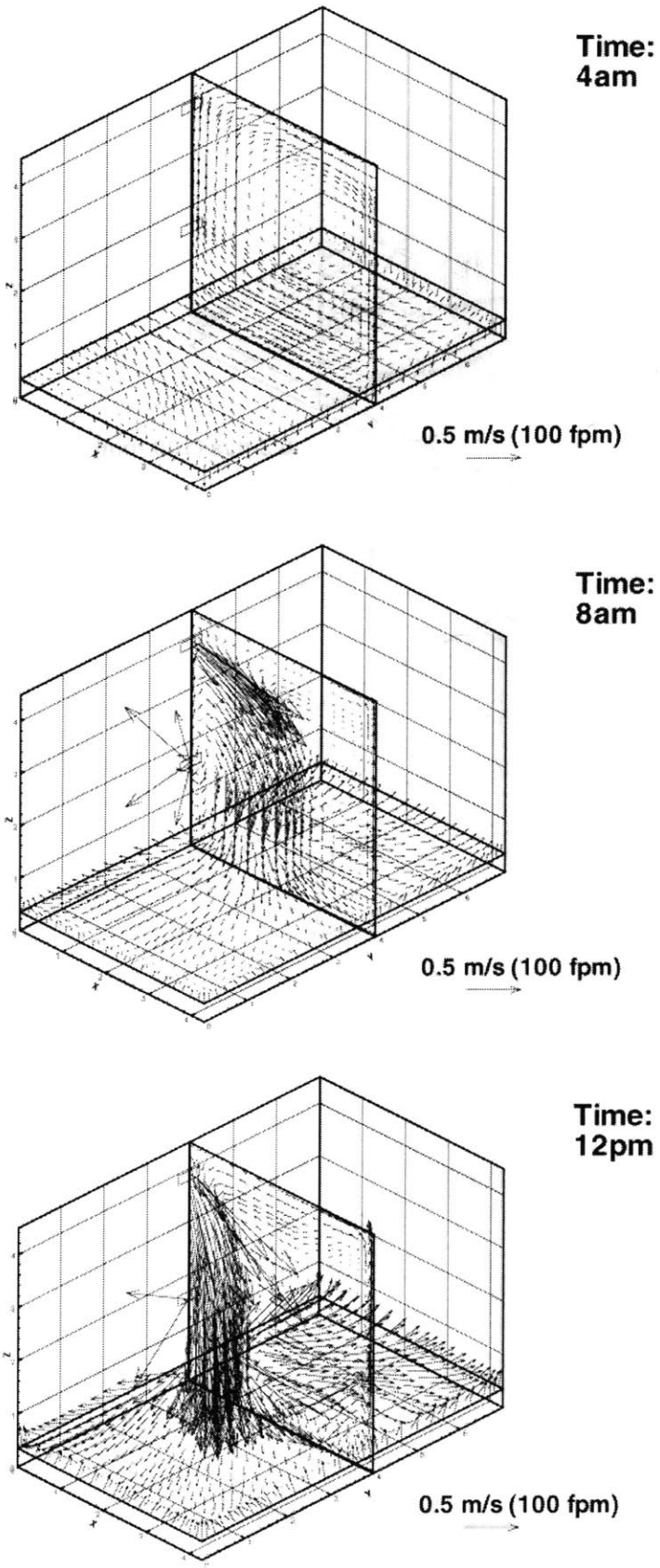

Figure 6.22 The computed air velocity for the atrium during the summer day

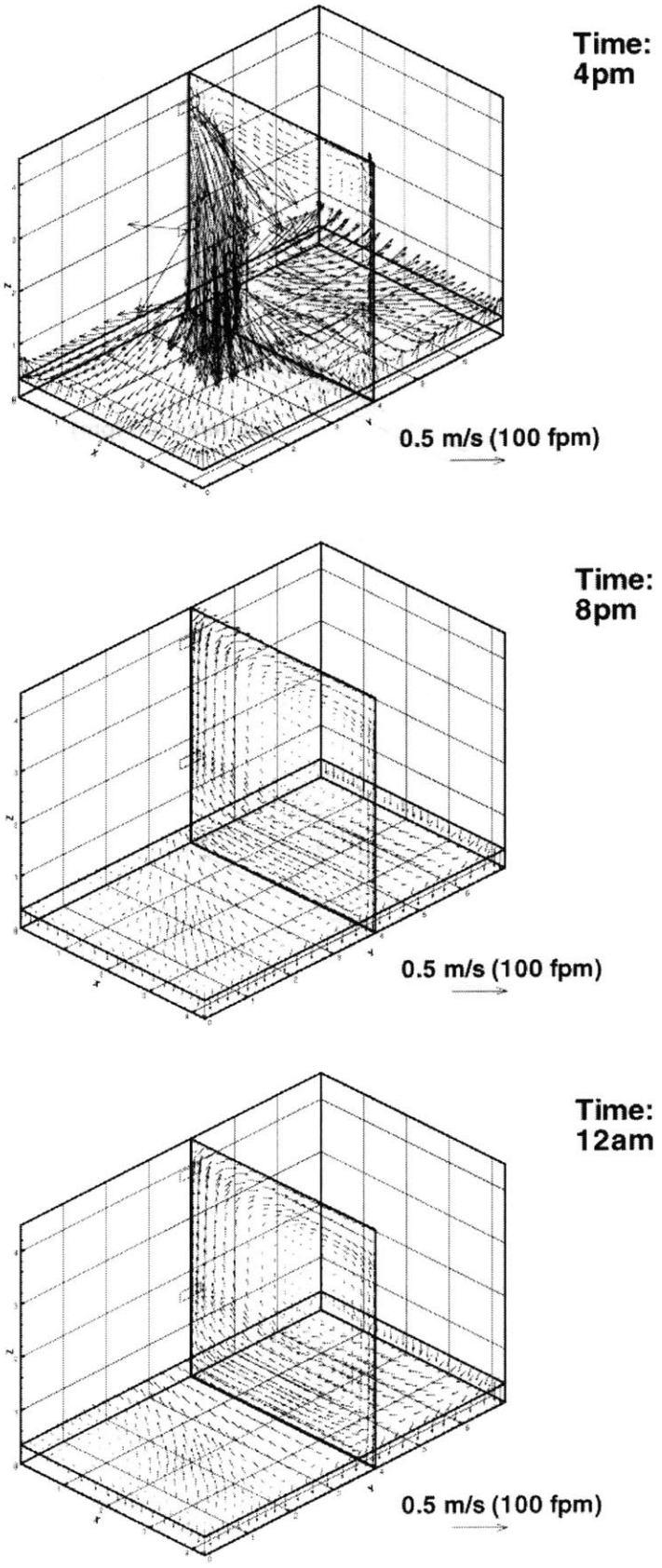

Figure 6.22 (Continued) The computed air velocity for the atrium during the summer day

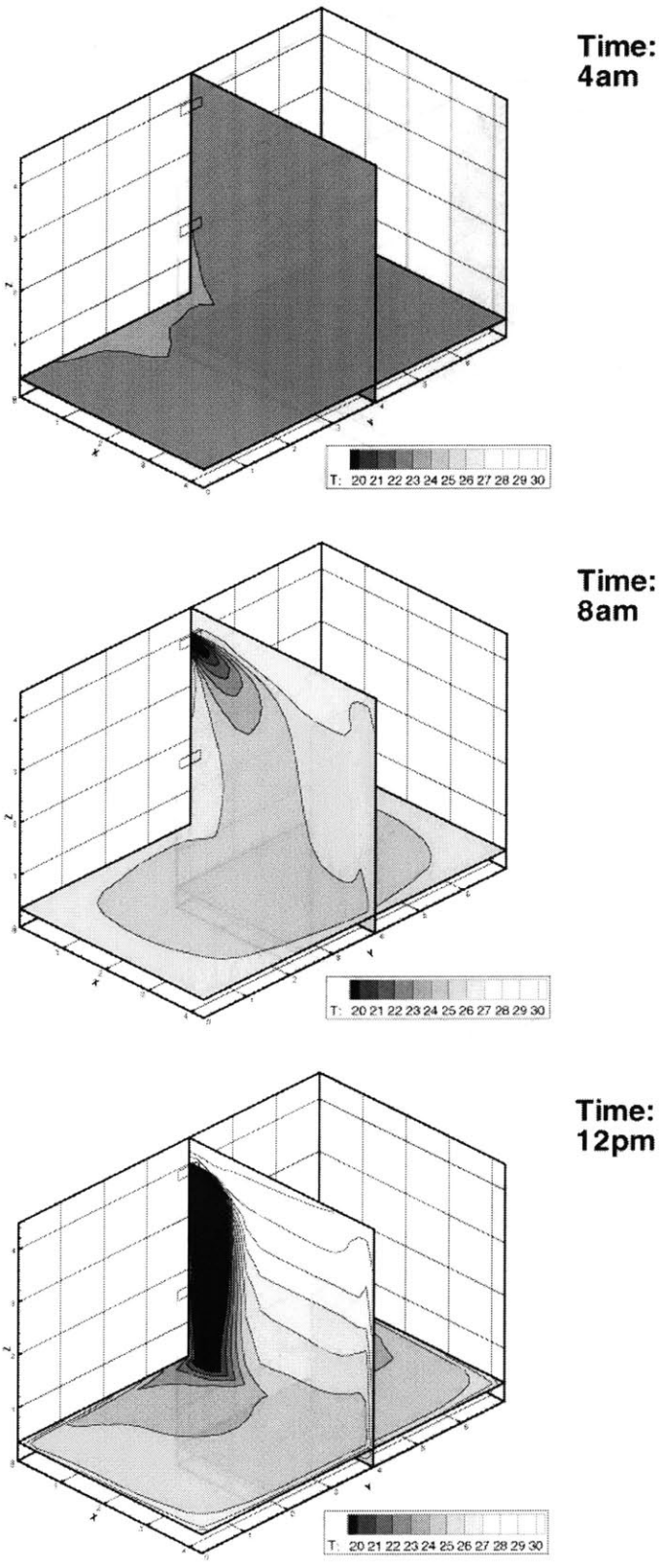

Figure 6.23 The computed air temperature for the atrium during the summer day

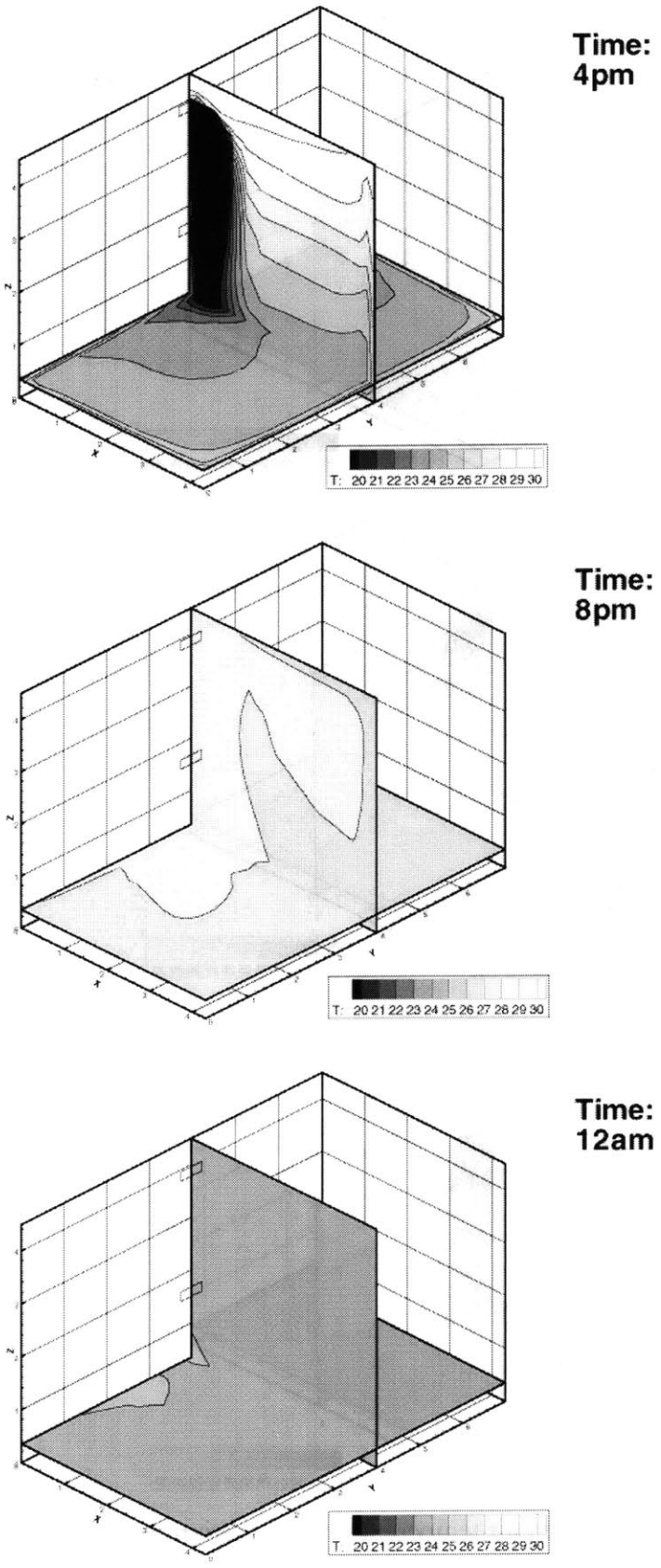

Figure 6.23 (Continued) The computed air temperature for the atrium during the summer day

6.2.3 The Large Office with Partition Walls

The study has used a large office with partitions (Chen et al. 1998) shown in the Figure 6.24 as another exercise example. The office uses a displacement ventilation system. The inlet diffusers are placed on the two side-walls and the outlets are on the ceiling. The office size is 23.2 m × 15.8 m × 3.3 m (76 ft × 52 ft × 9.9 ft) with 32 occupants.

Each occupant generates 75 W of sensible heat. Each occupant has a personal computer that generates 110 W of heat. In addition, there is overhead lighting, solar radiation through the windows, and heat conduction from the outside to inside through the building enclosure. The heat sources per floor area are

- occupants 6.45 W/m^2 (2.07 Btu/(hr ft^2))
- computer 9.6 W/m^2 (3.04 Btu/(hr ft^2))
- overhead lighting 12 W/m^2 (3.8 Btu/(hr ft^2))
- solar radiation 10 W/m^2 (3.17 Btu/(hr ft^2))
- heat conduction through the building enclosure 9.6 W/m^2 (3.04 Btu/(hr ft^2))

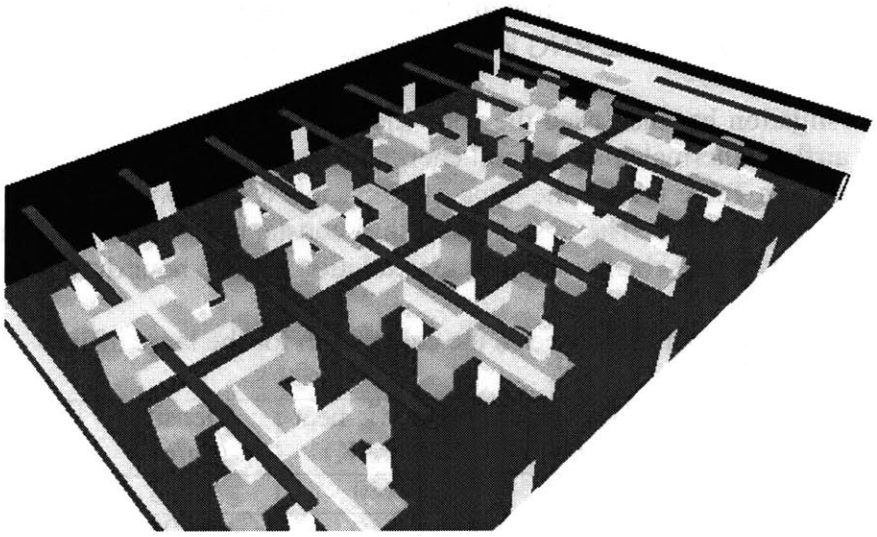

Figure 6.24 The large office with partition walls

ASHRAE RP-949 computed the distributions of air velocity and temperature by a CFD program with the RNG k-ε model (Chen et al. 1998). The CFD program was validated by detailed experimental data. The agreement between the computed results and the measured data is excellent for an office. Therefore, the computed results are regarded as reliable and can be used as a benchmark for the comparison of the computed results.

Since the large office is symmetric, Chen et al. (1998) conducted the CFD simulation for a quarter of the office. In order to compare the results in the same format, the current study calculates the airflow distribution also for a quarter of the office.

Figure 6.25 shows the airflow pattern in the large office at three different planes, at the ankle level and at two sections. The corresponding results computed by another CFD program with the RNG k-ε model are shown in Figure 6.26 for comparison. The agreement between the two computer simulations is very good. The latter used a finer computer grid distribution. The grid location is therefore closer to a warm surface, such as the occupant surface. Since the air velocity is higher close to a warm surface, the arrows in the figure are larger. In fact, the air velocities at the same location are the same between the two simulations.

Figure 6.27 presents the air temperature distributions in the large office at three different planes. Compared with the results computed with the RNG k-ε model (Figure 6.28), the zero-equation model used in the present study gives a smaller vertical temperature gradient. The air temperature near the floor is about 2 K (3.5 °F) higher in the present study than that reported by Chen et al. (1998). The major discrepany occurs in the area near the air supply inlet. Furthermore, the zero-equation model predicted consistent results for the factory with individual workstations that is also a large space with the displacement ventilation (Chen et al. 1999). We suspect the discrepancies in this office case may be attributed to the RNG k-ε model used by Chen et al. (1998).

The investigation has also used the combined flow and energy analysis program to calculate the airflow, thermal comfort, and energy in the large office. The analysis uses the materials shown in Table 6.7 for the large office. Table 6.8 shows the inlet boundary conditions for the large office. The system is with a constant air volume, and the inlet temperature changes with the change of the hate extraction in each hour during day.

Table 6.7 The materials used in the calculation for the large office

Enclosure	Layer	Thickness (m)	Specific heat (J/kg K)	Density (kg/m^3)	Conductivity (W/m K)
Floor	1	0.10	840	2243	1.731
Ceiling	3	0.10	840	1600	0.52
		0.10	500	190	0.046
		0.01	1215	545	0.12
Walls	3	0.10	840	2082	1.3
		0.10	1210	55	0.027
		0.01	840	721	0.72
Windows	2	The reflection index of the glass is 1.52, the thickness of the glass is 6 mm, and the absorptivity of the glass is 0.018.			

The large office is conditioned from 7 am to 6 pm, Monday through Friday. During these conditioned periods, the heat generated by the occupants is 2,400 W, by the computers 3,520 W, and by the overhead lighting 1,360 W for the whole office. There is no infiltration in the large office during both conditioned and unconditioned periods. The room temperature is controlled at 24 ± 1 °C (75 ± 2 °F).

Since the building is well insulated and has a high internal heat load and solar radiation, the large office needs a small amount of cooling in the late afternoon during the winter day. This can be seen from Figure 6.29(b). Figure 6.29(a) also shows that, when the outdoor temperature is below the freezing point, the indoor air temperature is above 17 °C (63 °F) before the air conditioning system starts to heat the building in the morning. Figure 6.29(c) shows total amount of direct and diffuse solar radiation received on a horizontal surface during the 60 minutes preceding the hour indicated.

Table 6.8 The inlet boundary conditions used in the calculation for the large office

	Winter day (01/07)		Summer day (07/08)	
Time (hours)	Inlet temperature (°C)	Mass flow rate (kg/s)	Inlet temperature (°C)	Mass flow rate (kg/s)
4am	-	-	-	-
8am	30.4	0.406	19.9	0.406
12pm (noon)	27.9	0.406	15.8	0.406
4pm	24.5	0.406	17.0	0.406
8pm	-	-	-	-
12am	-	-	-	-

Figure 6.30 and Figure 6.31 show the air velocity and temperature distributions in a quarter of the large office during the winter day. Since the large office uses a displacement ventilation system, the warm air moves upward when the system heats the air, as shown in the figure at 8 am. The airflow pattern in the room changes when the ventilation system works in the cooling mode. The air temperature is rather uniform during the unoccupied hours.

Figure 6.32 illustrates the PPD distribution in the large office. In general the PPD is less than 10%. This is because the heating load and the cooling load are small during the winter day, and the temperature difference between the room air and supply air is small.

The air velocity and temperature distributions during the summer day are presented in Figure 6.33 and Figure 6.34. The room needs to be cooled on the summer day. The airflow pattern during the air-conditioned period is similar. Since the heat extraction during the summer day is high, the vertical temperature gradient is large on the summer day. This would lead to a non-uniform distribution of thermal comfort.

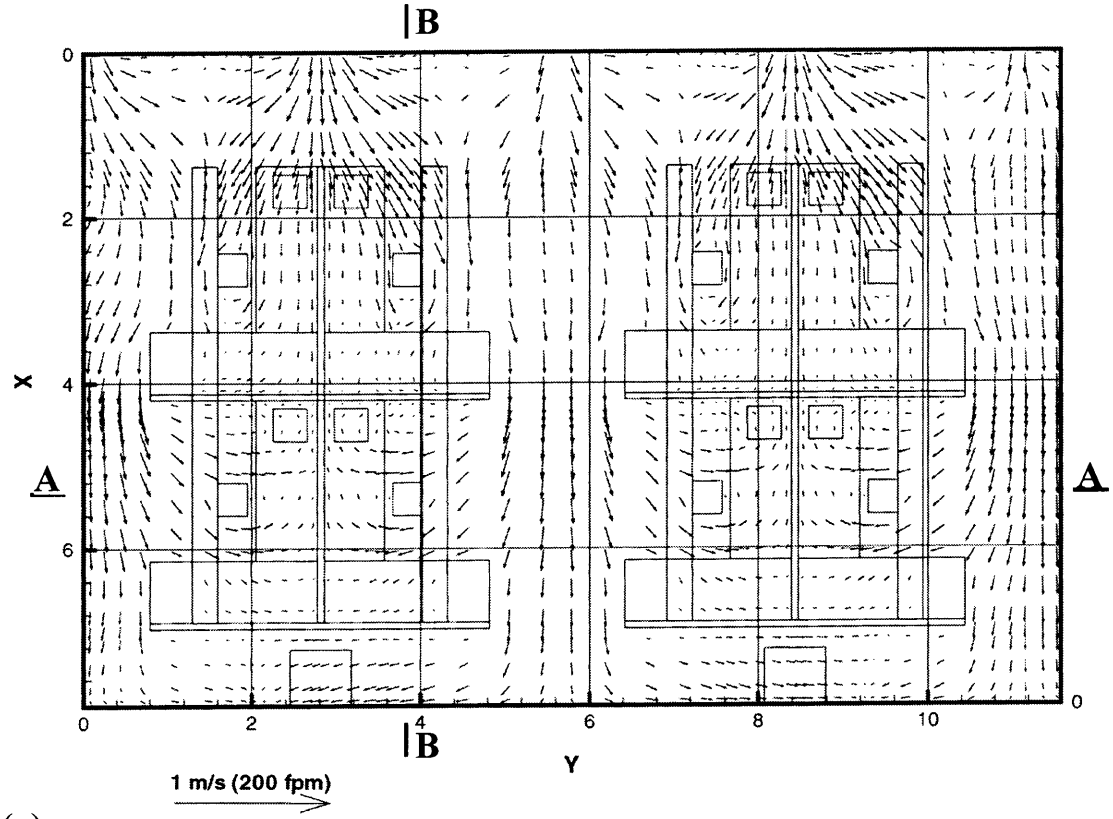

(a)

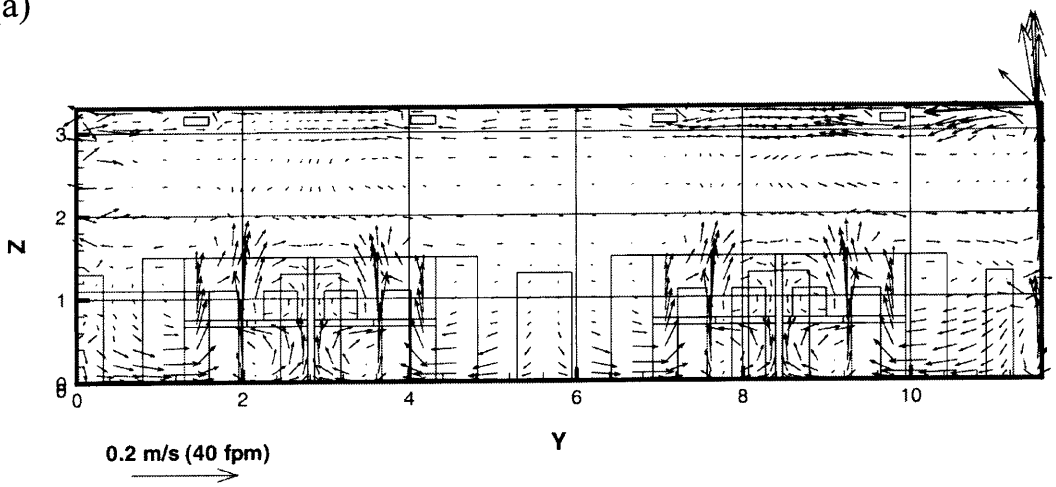

(b)

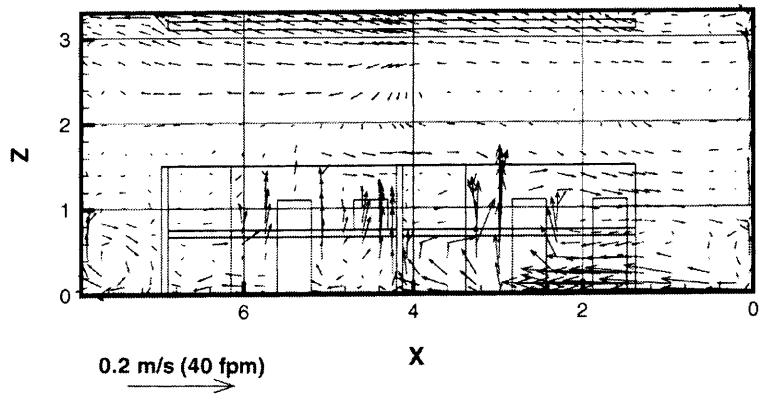

(c)

Figure 6.25 The computed air velocity for the large office with partitions (a) near the ankle level, (b) in section A-A, and (c) in section B-B

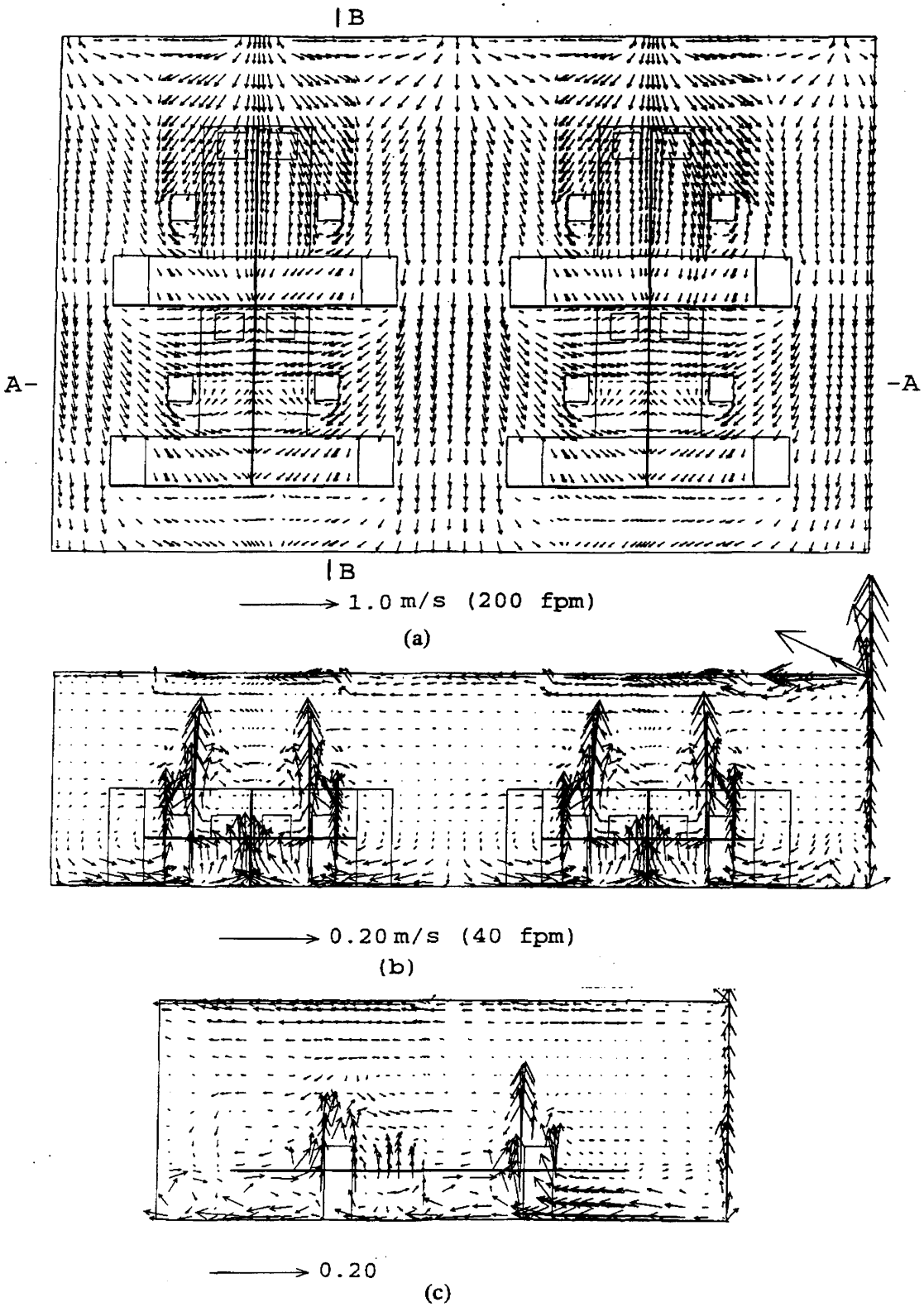

Figure 6.26 The air velocity for the large office with partitions computed by the RNG k–ε model (Chen et al. 1998) (a) near the ankle level, (b) in section A-A, and (c) in section B-B

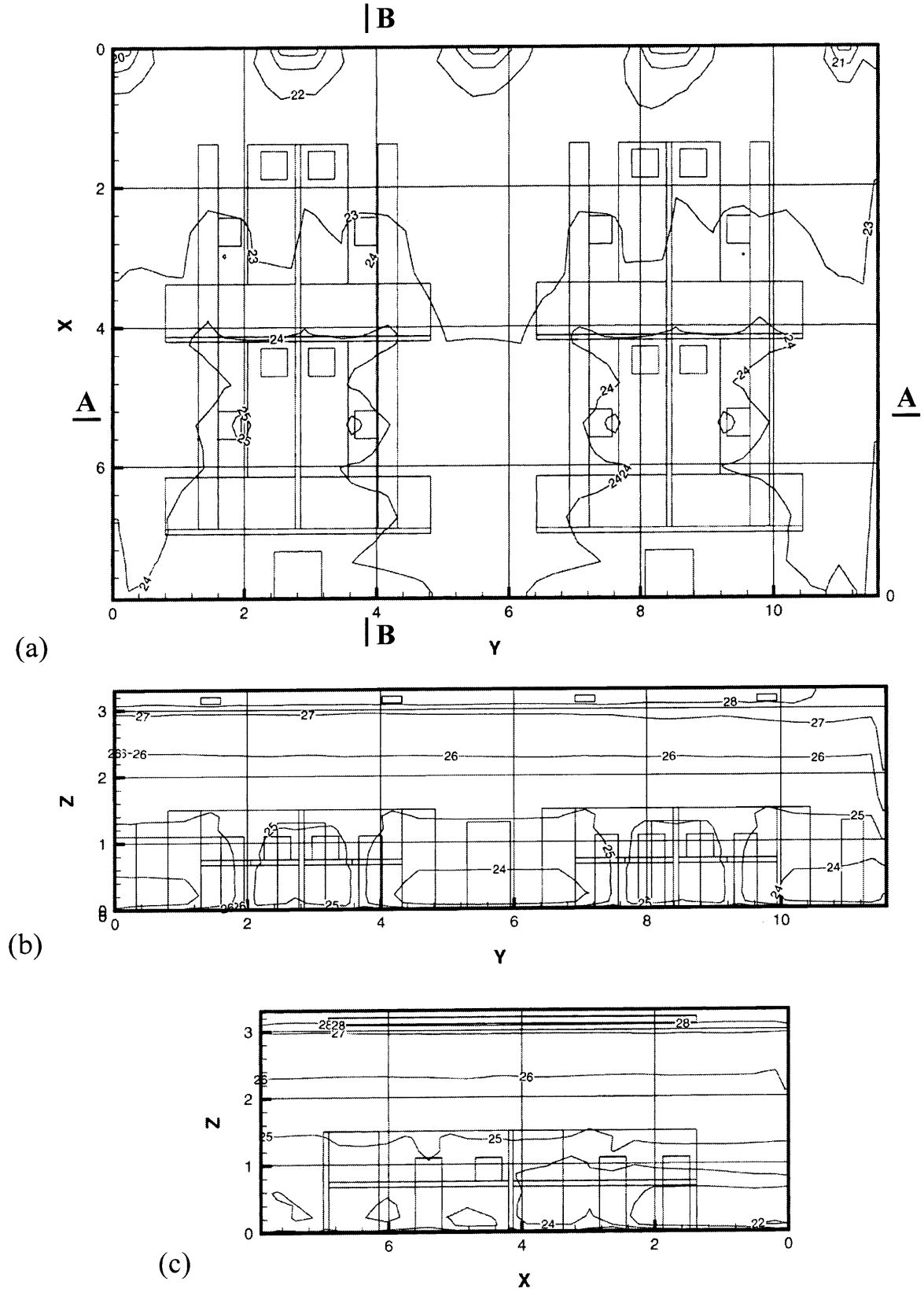

Figure 6.27 The computed air temperature for the large office with partitions. (a) near the ankle level, (b) in section A-A, and (c) in section B-B.

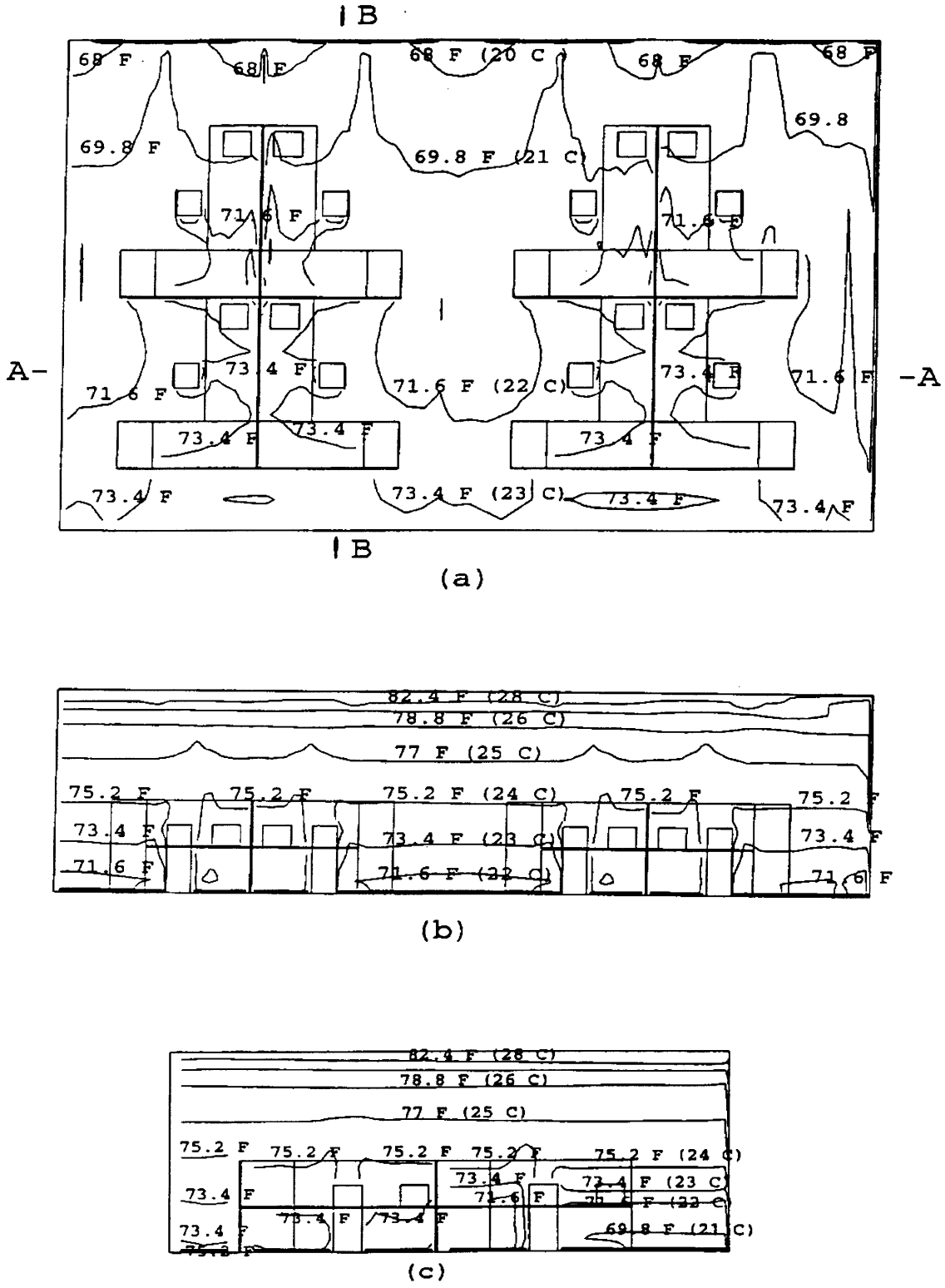

Figure 6.28 The air temperature for the large office with partitions computed by the RNG k–ε model (Chen et al. 1998) (a) near the ankle level, (b) in section A-A, and (c) in section B-B

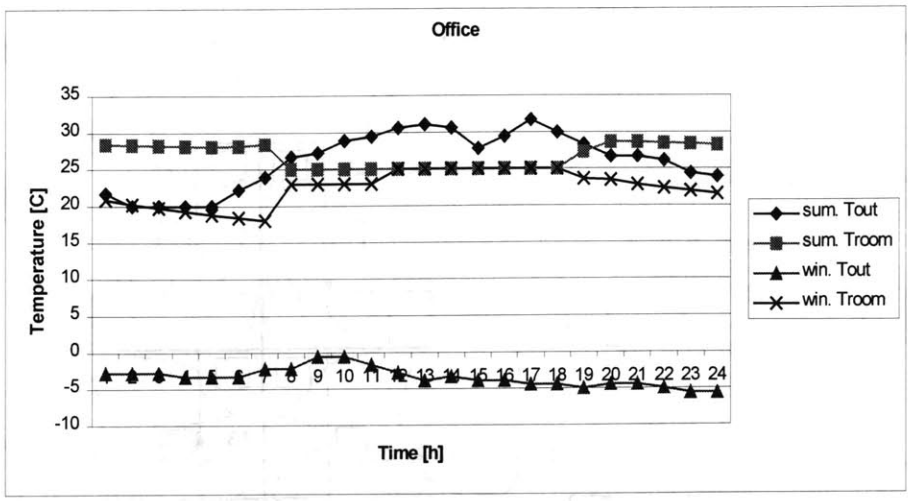

(a)

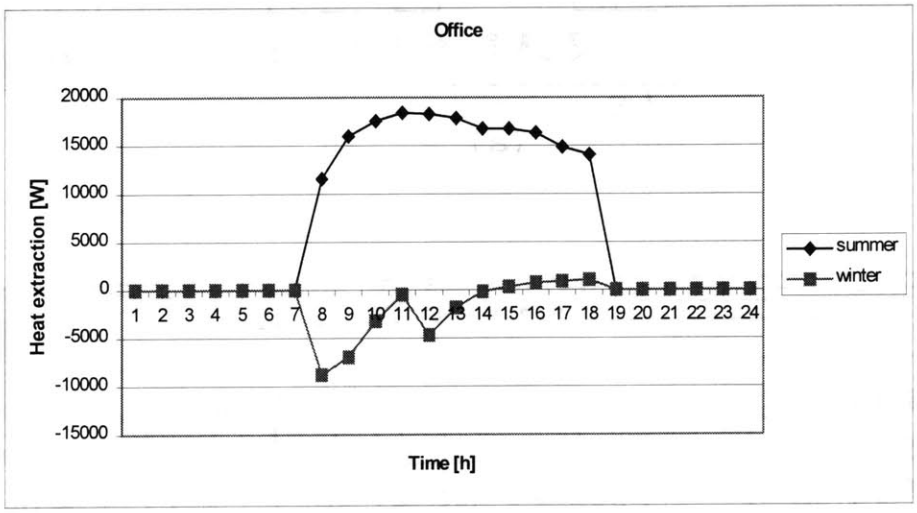

(b)

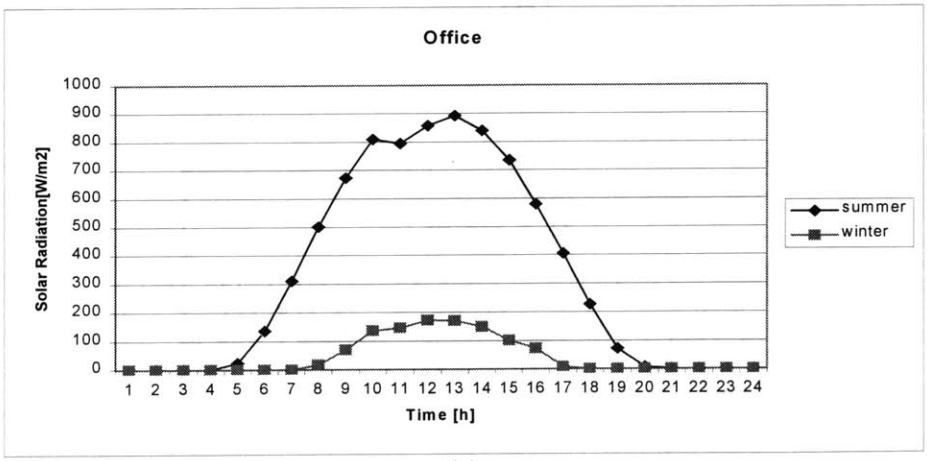

(c)

Figure 6.29 Outputs from the energy program ACCURACY for the large office for the winter and summer days. (a) Indoor and outdoor air temperature (b) heat extraction, (c) outdoor solar radiation

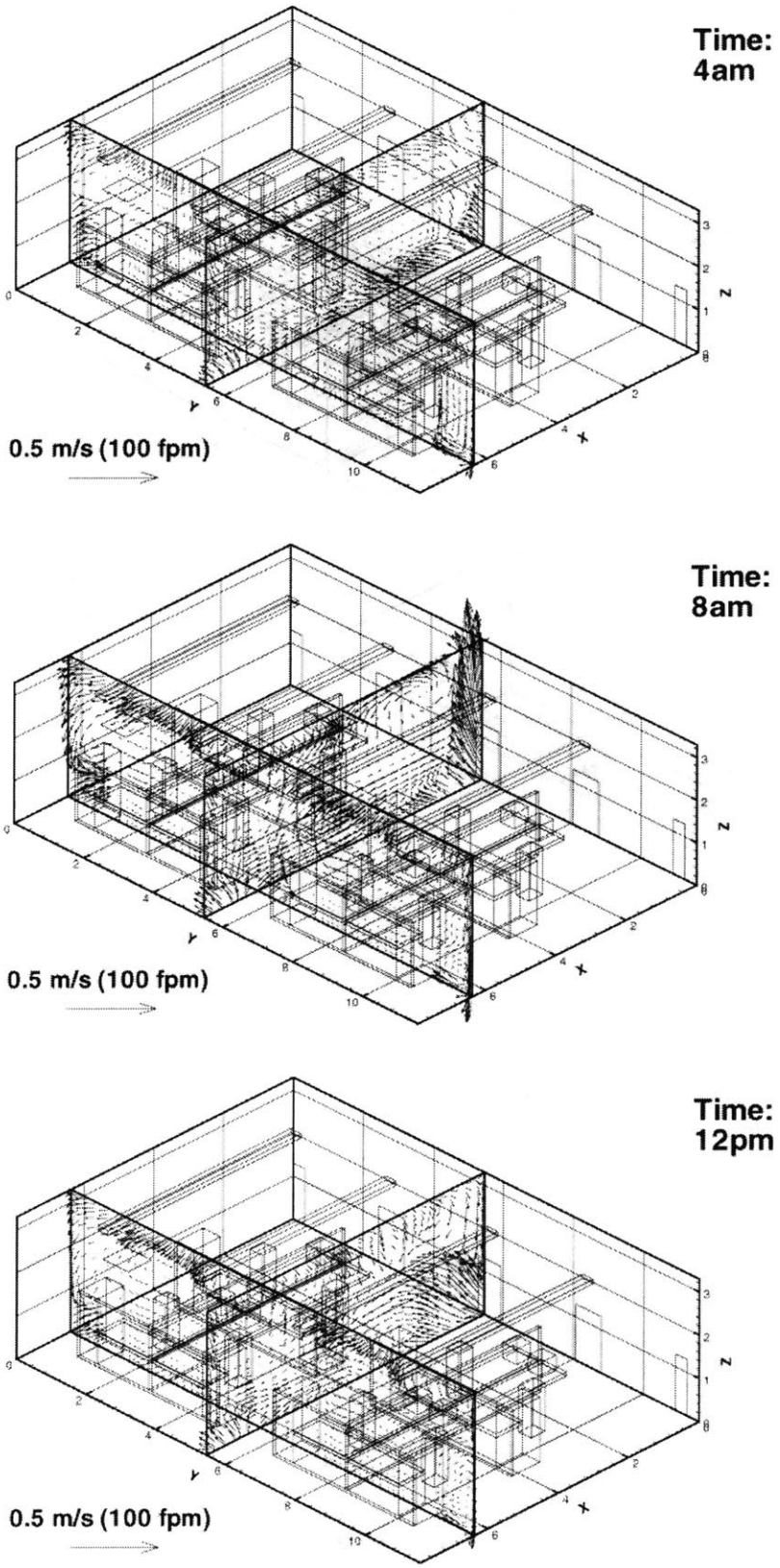

Figure 6.30 The computed air velocity distributions in the large office with partitions for the winter day

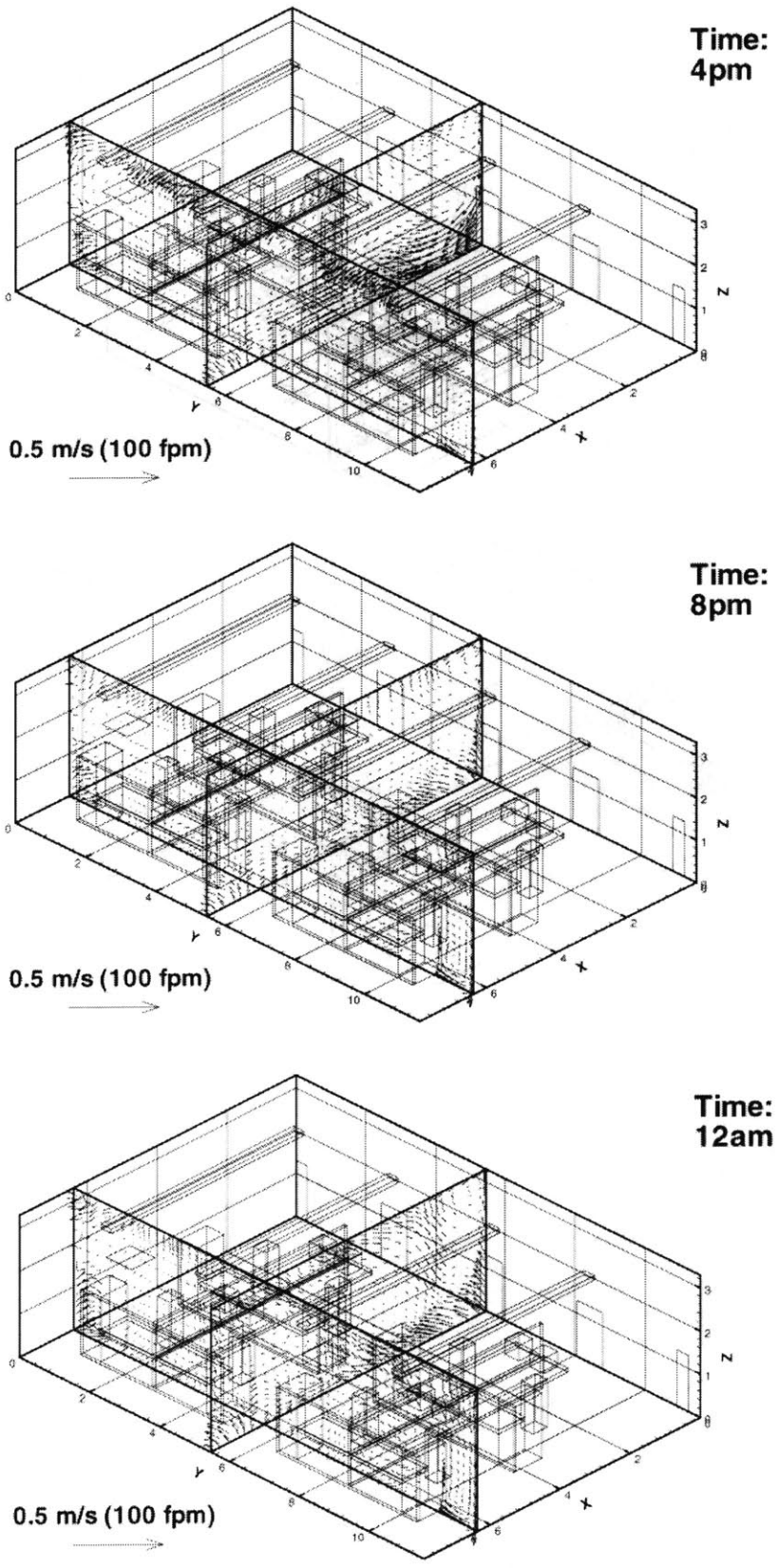

Figure 6.30 (Continued) The computed air velocity distributions in the large office with partitions for the winter day

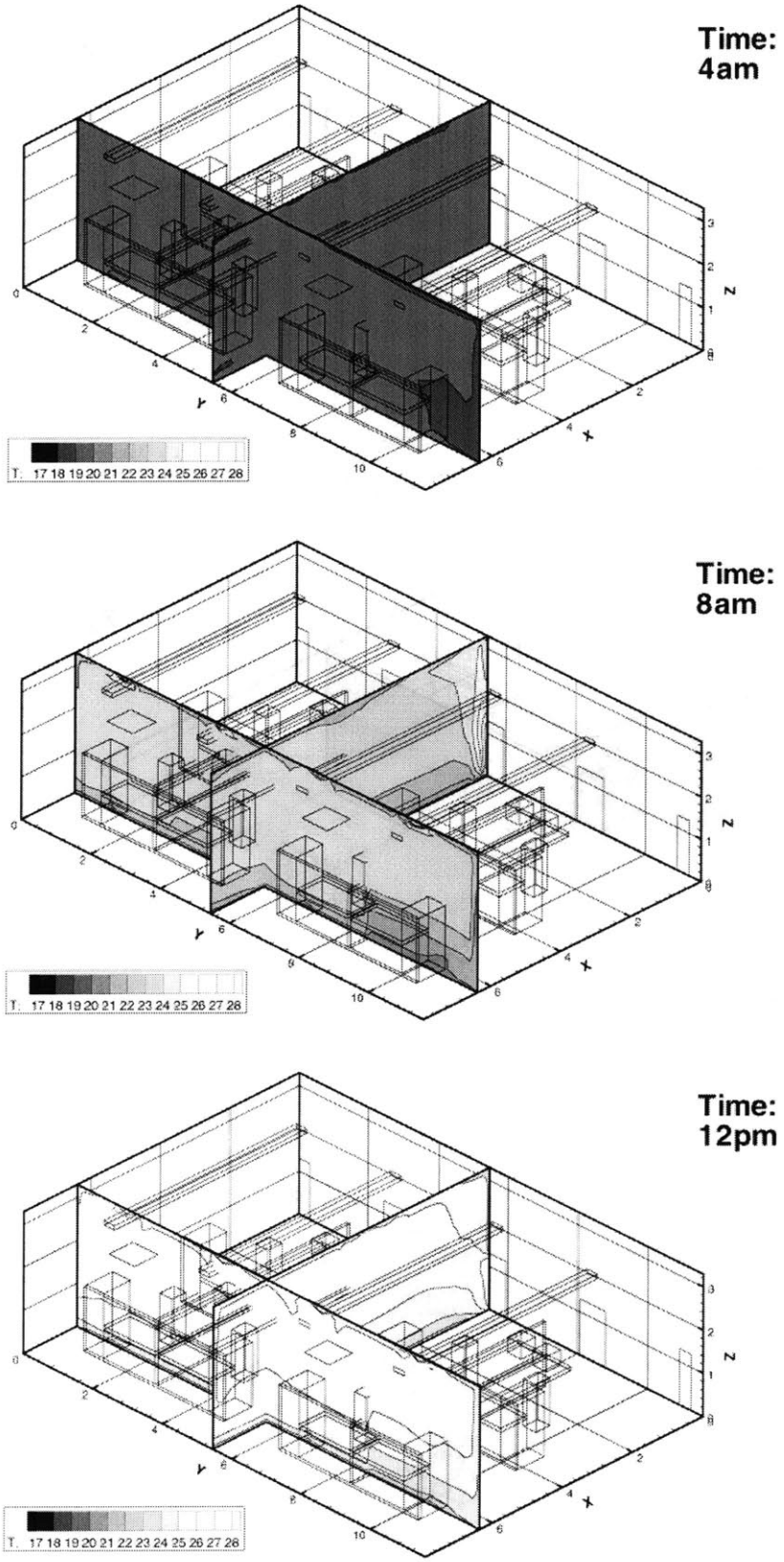

Figure 6.31 The computed air temperature distributions in the large office with partitions for the winter day

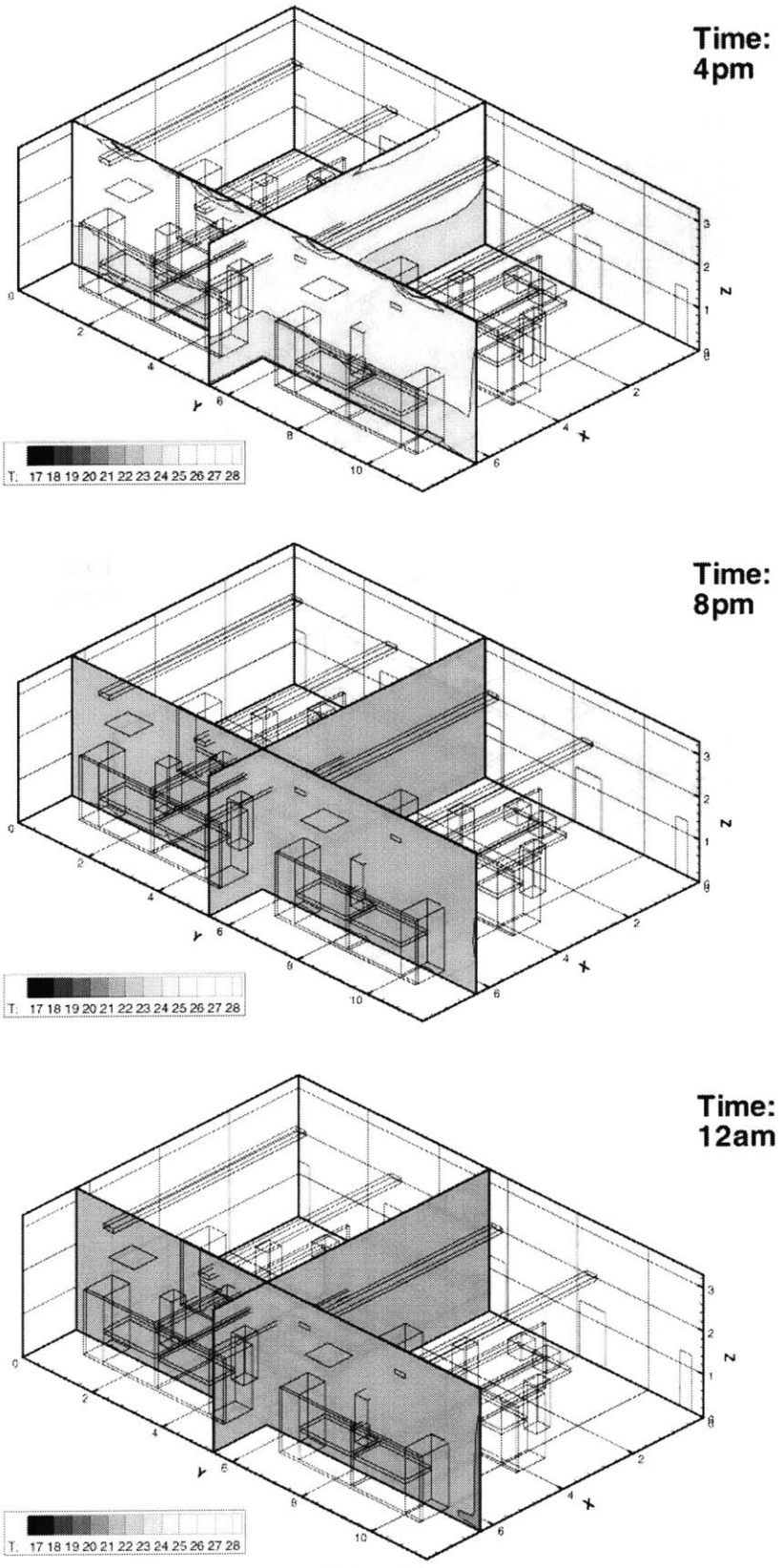

Figure 6.31 (Continued) The computed air temperature distributions in the large office with partitions for the winter day

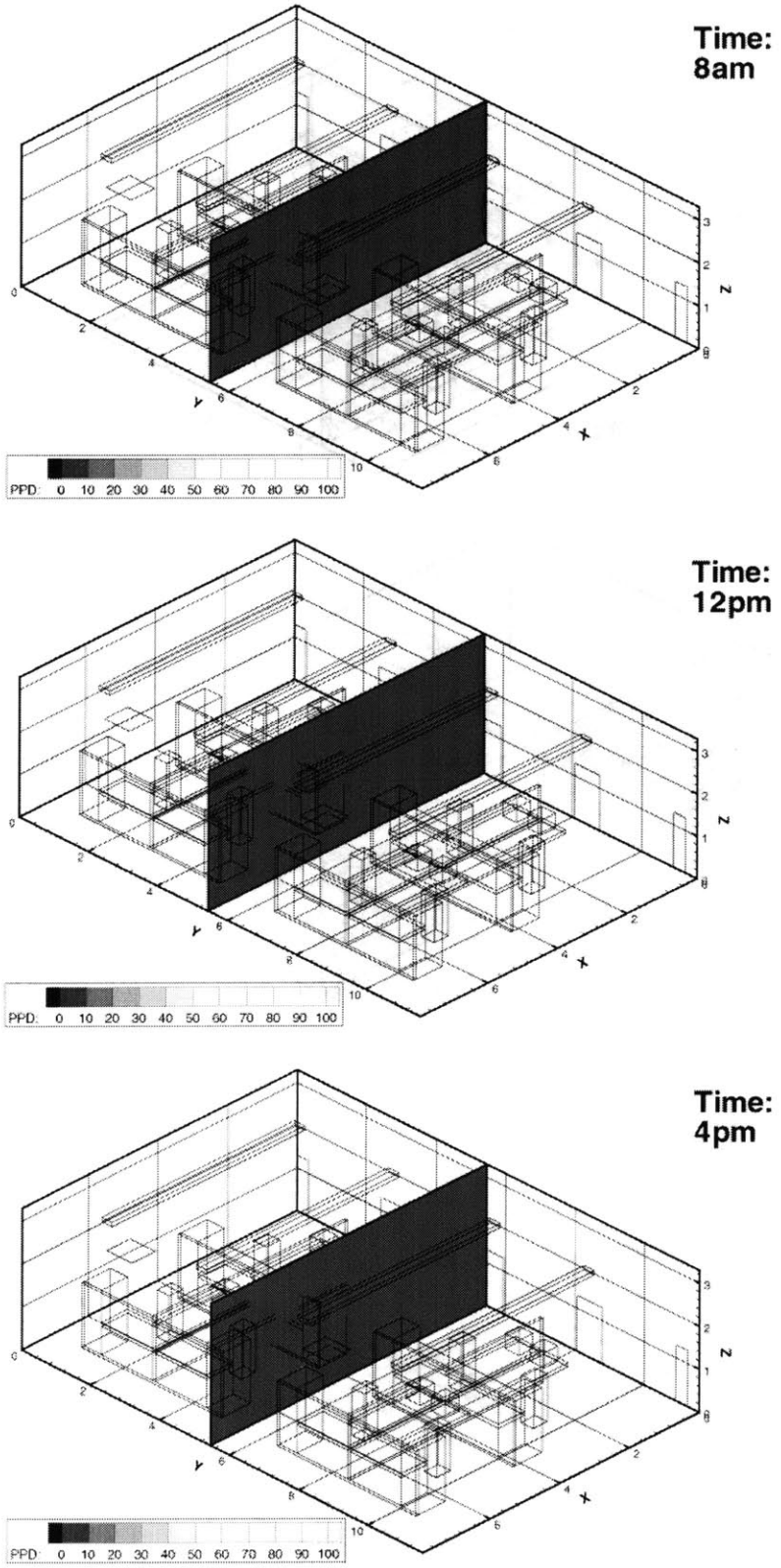

Figure 6.32 The PPD distribution in the large office with partitions under the winter conditions

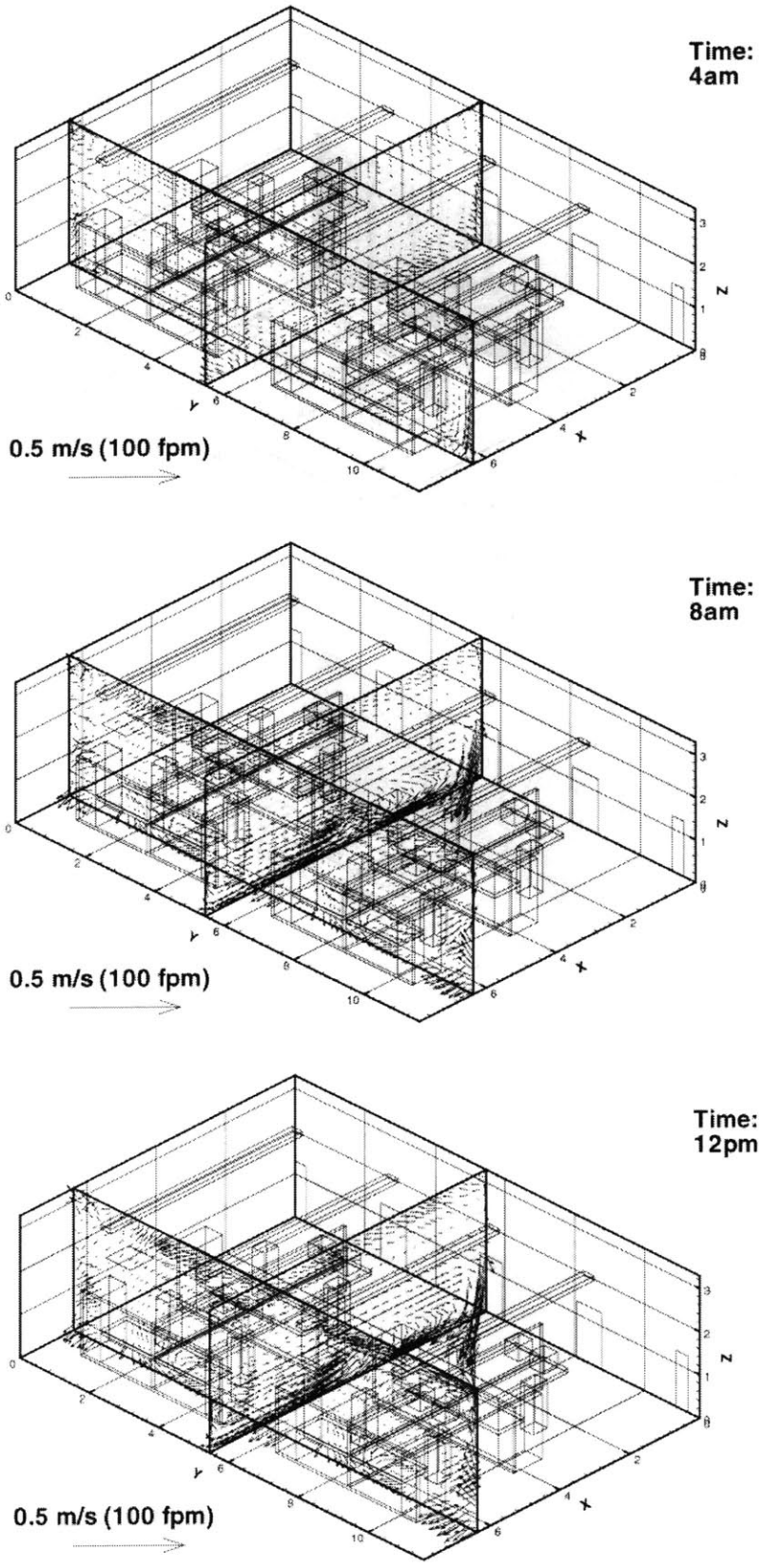

Figure 6.33 The computed air velocity distributions in the large office with partitions for the summer day

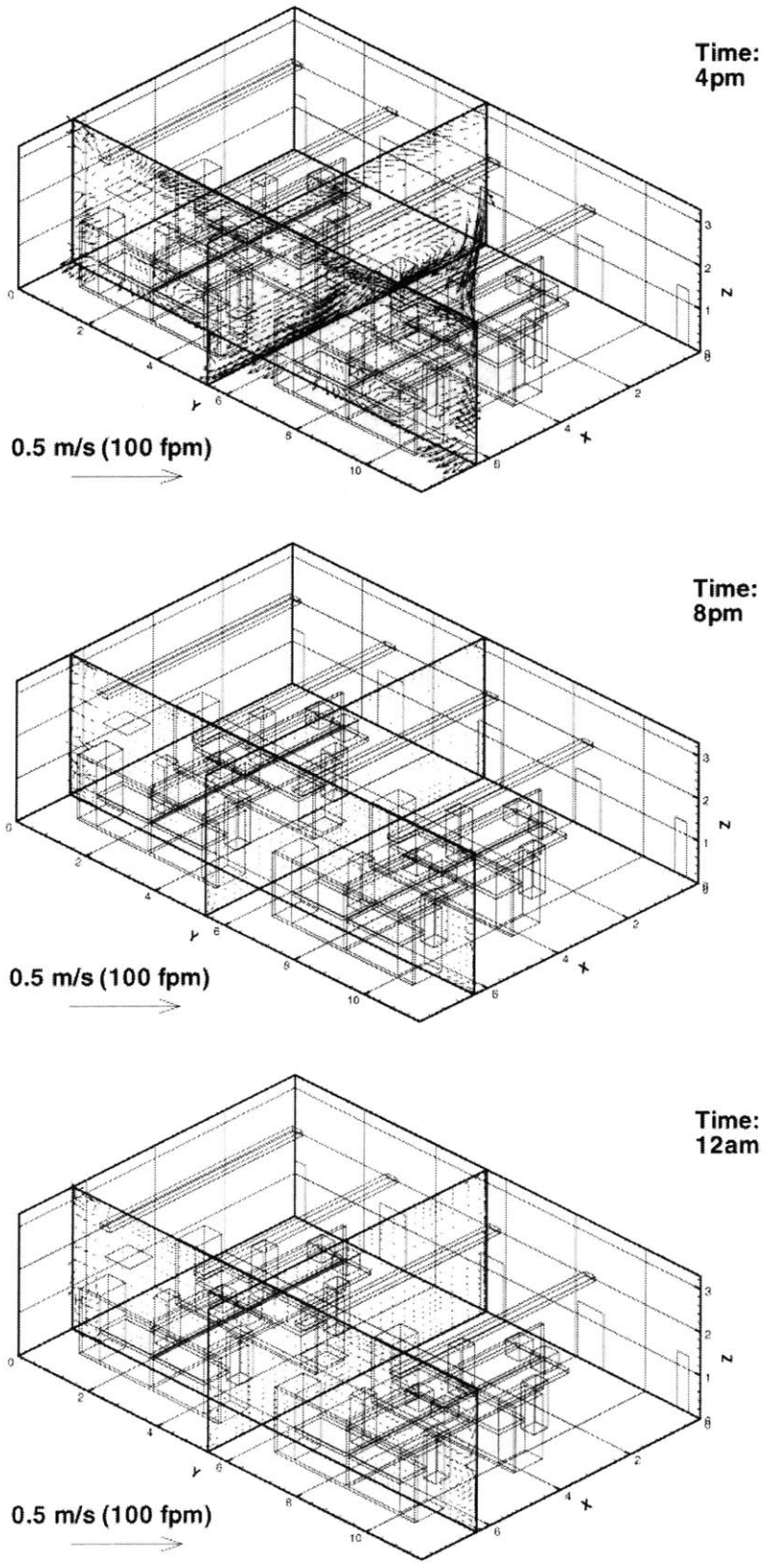

Figure 6.33 (Continued) The computed air velocity distributions in the large office with partitions for the summer day

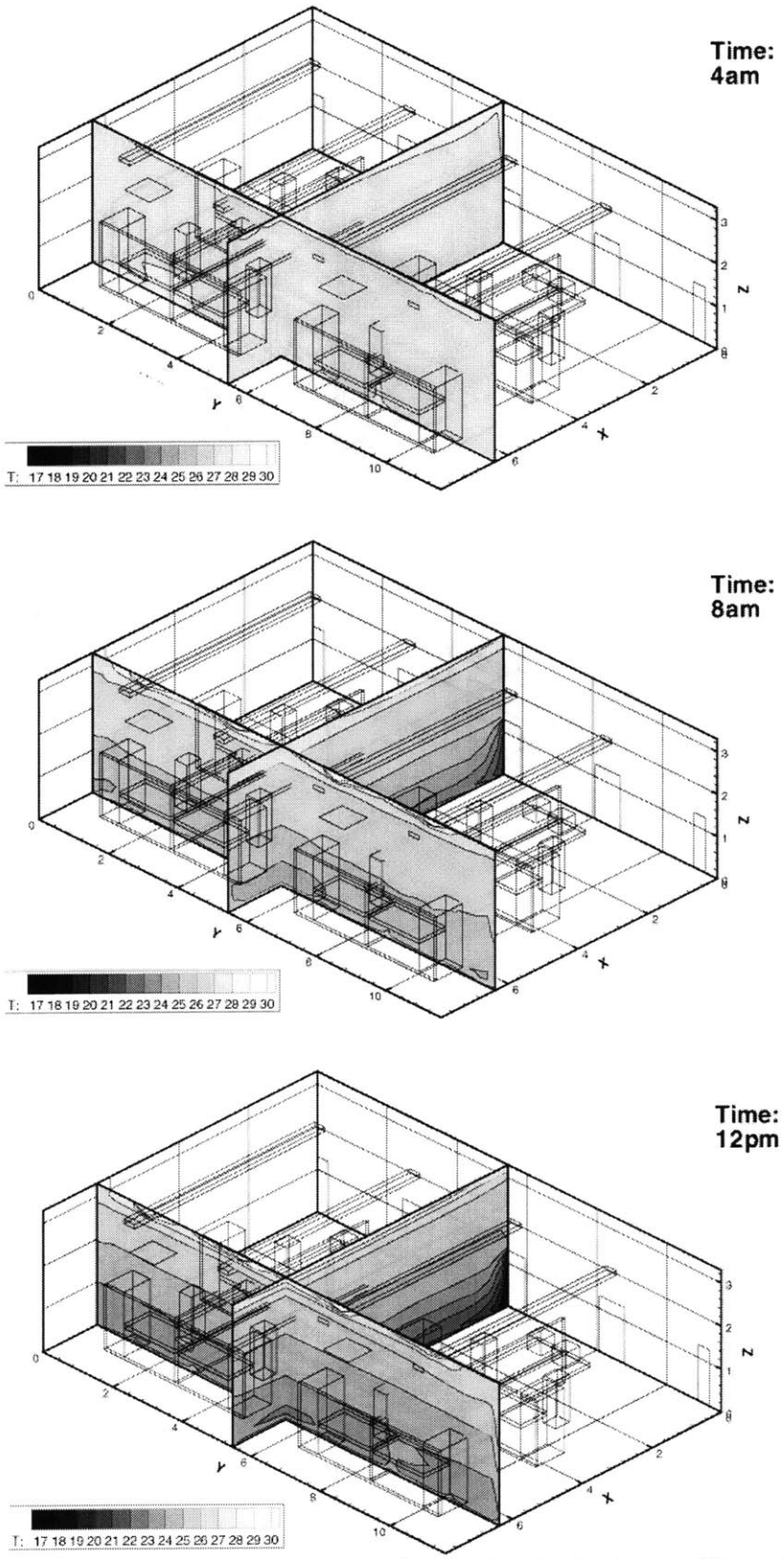

Figure 6.34 The computed air temperature distribution in the large office with partitions for the summer day

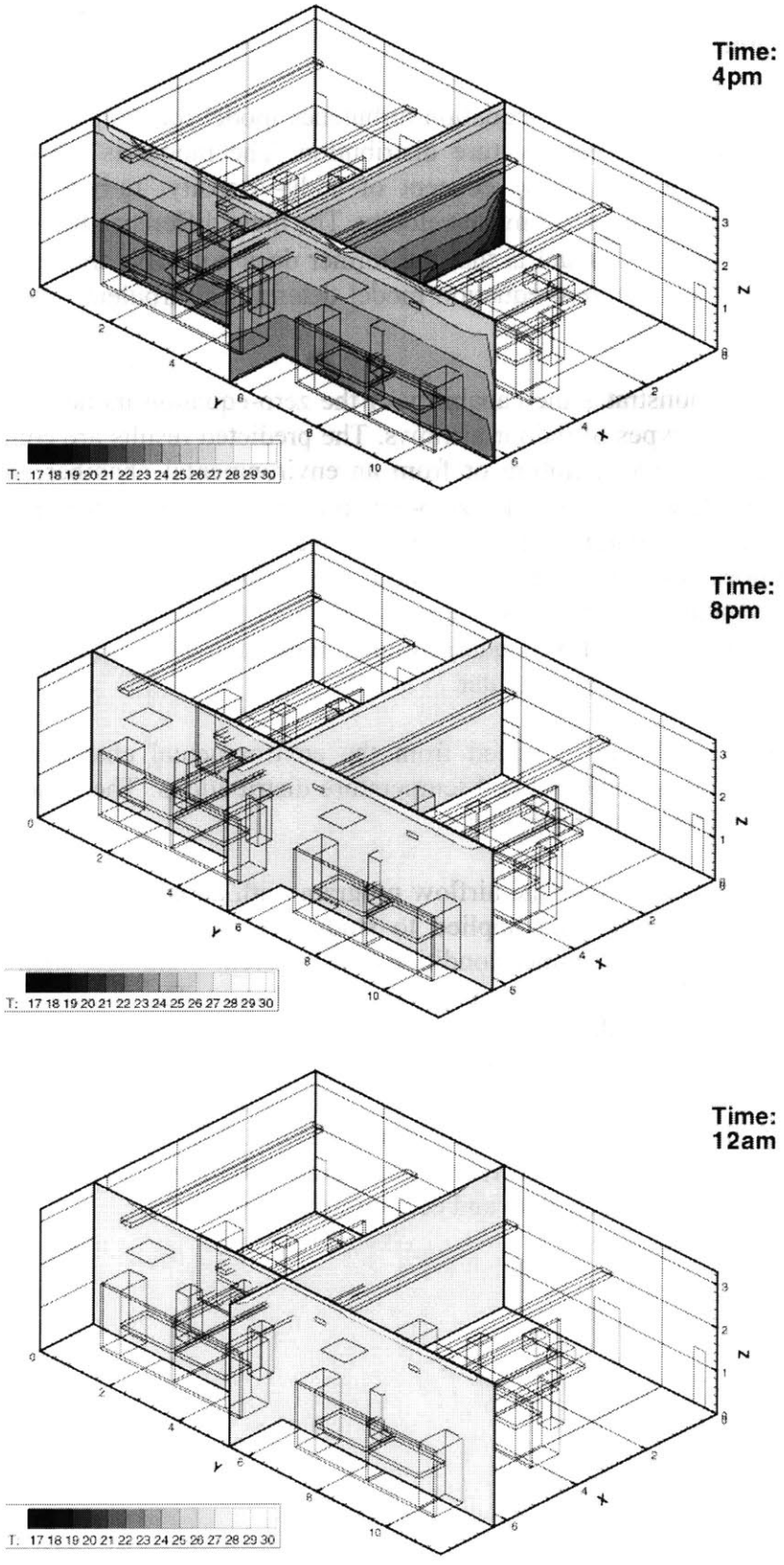

Figure 6.34 (Continued) The computed air temperature distributions in the large office with partitions for the summer day

6.3 Discussion and Summary

This study used a new zero-equation turbulence model for the prediction of room airflow patterns and the air temperature distribution. The model is derived from the Navier-Stokes equations. Using the concept of eddy-viscosity, turbulent viscosity is approximated by a length scale and mean velocity. The main difference between the zero-equation model and the k-ε model is that the former does not solve transport equations for turbulent quantities. The zero-equation model determines turbulent quantities by an algebraic equation.

The study demonstrates the capability of the zero-equation model by applying it to predict the different types of indoor airflows. The predicted results are compared with experimental data from the literature or from an environmental chamber and with the results from the RNG k-ε model. The zero-equation model can predict indoor airflow patterns and the air temperature distributions with reasonable accuracy. Since the zero-equation model does not solve transport equations for turbulence, the computer memory needed is much smaller, and the convergence speed is 10 times faster than that with the k-ε model. With the zero-equation model, simulation of a three-dimensional airflow in a room can be made in a personal computer.

The experimental data obtained from the environmental chamber include the airflow pattern and the air velocity and temperature distributions. The data can be used for the validation of other flow programs.

The investigation couples the airflow program with an energy analysis program. The combined program has been applied to study the airflow, energy, and thermal comfort for both winter and summer conditions for different buildings, such as a home, an atrium, an aircraft hangar, a large office, and a workshop. The results show that the combined program is capable of studying the dynamic airflow, energy, and thermal comfort simultaneously in a building on a personal computer.

The thermal comfort in most cases is not uniform. This has to be considered in designing radiative, convective, and hybrid heating and cooling systems for a building. The combined program is an effective and economical design tool.

CHAPTER 7

CONCLUSIONS AND RECOMMENDATIONS

7.1 Conclusions

This chapter presents the main conclusions and results from the research done for this thesis. The thesis objective was to develop a simplified methodology for indoor environment design. The methodology should be simple, but can be used to obtain detailed information on indoor environment parameters such as distributions of air velocity, air temperature and contaminant concentrations. These parameters are important to determine indoor air quality, thermal comfort, and energy consumption that enable design of energy efficient and healthy indoor environments. However, current design does not use this approach since the detailed calculations or measurements of indoor air parameters are very expensive in terms of labor effort and equipment. Therefore, the simplified modeling should provide answers to design questions in a reliable, fast and cost effective manner.

This study developed a simplified program for modeling indoor environment. The development had three phases, which are described in Chapter 4, 5 and 6. The first phase is the simplified modeling of diffuser jet flow, which is the key flow element in mechanically ventilated spaces. The second phase is simplified turbulence modeling of indoor air distribution that uses a zero-equation turbulence model. To test the turbulence model, a simplified airflow program was developed. Finally, in the third phase, the simplified airflow program was coupled with an energy analysis program. The coupled program is a tool that simultaneously analyzes the impact of the heat transfer through the building envelope, the indoor heat transfer and the air movement on the thermal comfort within a space.

Each phase of the simplified tool development employed models validated with measured data in order to assess their accuracy and reliability. By using a state-of-the-art experimental facility at MIT, we have obtained data of indoor airflow, thermal comfort and indoor air quality. The data were used to validate our airflow program. Also, the validation of the airflow program used data from the literature. The following paragraphs summarize experiences and conclusions for each phase in development of the simplified modeling tool.

Our observations, conclusions, and recommendations with modeling diffuser jet flow can be summarized as following:

- Jet flow from complex diffusers normally used to supply air to indoor environments may be modeled with the jet formulae in special cases. The special cases are diffusers that develop either free or attached jets and have decay coefficients available. This investigation found that most applications do not comply with these requirements and recommend numerical simulations to study jet flows as a more general approach.

- Numerical simulations of the diffusers can use simplified modeling technique by using the resultant momentum from the diffusers without the detailed diffuser geometry representation. The modeling of the resultant momentum can be at the diffuser surface with the momentum method or in front of the diffuser in the direction of jet discharge with the box method. The momentum method is simpler than the box method in terms of the effort to specify the data for modeling.

- The momentum method is recommended for the displacement diffuser and the mixing diffusers that discharge combined jets. The mixing diffusers that discharge several jets that are merging and combining in front of them should use the box method since the momentum method gives incorrect results.

- The mixing diffusers produced the uniform temperature distribution and dispersion of the tracer gas throughout the chamber, while the displacement diffuser created stratified temperature and tracer gas distribution. The recommended simplified diffuser simulation methods can predict the distributions of indoor parameters.

The simplified diffuser modeling requires experiment to measure some of the parameters necessary for the simulations. A method of test (MOT) was developed in order to provided necessary data. The following are observations, conclusions, and recommendations for MOT:

- The method of test can use isothermal boundary conditions to obtain discharge jet velocity for the momentum method, and the distribution of jet velocity for the box method. The velocity measurements can use low-velocity anemometers to collect data with satisfactory accuracy, and the smoke visualization to determine the flow direction.

- The measured velocities at the box surface are used to define mass, energy and specie balance for the box boundaries. In such a way, the measured velocities under isothermal conditions can be used to set diffuser boundary conditions for temperature and concentration calculations. Therefore, the recommended diffuser testing defines the box boundary conditions for many different applications (different heat and contaminant sources).

- Current ASHRAE Standard 70-1991 describes the procedure for testing air supplies (diffusers) and one of the measured parameters is the diffuser area factor, which is the diffuser effective area. The area factor could be used to determine diffuser discharge velocity if more precise guidelines for measurement positions and measured velocity averaging are appended to the current version of the standard.

The simplified diffuser boundary conditions enable simulations of diffuser jet flow to save computing time as well as effort in setting a numerical model. Further, more significant savings in computing time have been achieved with simplified turbulence modeling of indoor airflow. The simplified model had been previously tested with the data from literature for several simple airflows, and we tested the model for more realistic

and complex scenarios. Our observations and conclusions from measurements and calculations are:

- A simplified flow program has been developed to test the performance of the zero-equation turbulence model. The program was first validated with the data from the literature, and the simulations correctly predicted airflow for those two-dimensional room airflow cases.

- The zero-equation model and the airflow program have been further validated with three additional complex airflows. The tested cases contain elements of natural, mixed and forced convection. The predicted airflow patterns are correct and the agreement between the measured and calculated data is good.

- The calculations of indoor airflow are very fast, although the computing times for different cases are slightly different. In general, the calculation is within several minutes, which is much faster than with other programs with "standard" k-ε model, although the results obtained with our program have similar accuracy as those obtained by the other program. The computing time was measured on a low-end personal computer with a Pentium II 350 MHz processor. With the current computing technology, the calculation time would be much shorter. Therefore, for the design purpose the zero-equation model is more suitable than the standard k-ε model since the results can be obtained much faster.

-

The airflow program calculates air motion and convective heat transfer within a space that is a needed parameter in building energy simulation. On the other hand, an energy simulation would provide heat transfer through the building façade and radiation within the space that is required in flow simulation. Hence, a natural extension is to couple the airflow program with an energy analysis program to make an integrated building energy, thermal comfort, and indoor air quality study. Our observations and conclusions on the coupled program are:

- The coupled program can be used to obtain hour-by-hour indoor thermal comfort for a typical day in a season. The program is an effective and economical design tool.

- The program validation uses five cases with experimental data found in the literature. The data were used to validate the airflow part of the program. The overall agreement between the measured and calculated data is good, but less than for the cases measured in our full-scale chamber. The possible reason is that the information regarding the boundary conditions in the literature is not sufficiently detailed .

7.2 Recommendations for Future Research

The developed modeling tool can be further improved and validated. Some of the areas where further improvement can be achieved are:

- The zero-equation model should be tested and further developed for outdoor airflow. The validation for the outdoor flow should enable fast and reliable simulations of the wind flow around buildings that may be further applied to study natural ventilation inside buildings.

- Our calculations for the indoor airflow in large spaces show discrepancies between measured and calculated data larger than for the simulations in small spaces. The discrepancies could be attributed to the zero-equation turbulence model. However, more data with well defined and controlled boundary conditions are needed.

- For large spaces such as atria, large offices, workshops, and hangars, the gas absorption for radiation plays an important role. Therefore, the radiation model in the energy analysis part of the program should be extended to incorporate the absorption of radiation by the moist air.

- A dynamic validation of the coupled energy / airflow / thermal comfort program should be done to assess the reliability of the coupled program. The dynamic validation requires weather data measured hour by hour with the simultaneously measured indoor air parameters.

The recommended further validations and research should provide insight in different airflows from the studied ones and strengthen the reliability of the dynamic simulations. The extensive validation should enable the design of different ventilation systems only by using the computer simulations.

REFERENCES

Abramovich, G.N. 1963. "The theory of turbulent jets," *The M.I.T. Press*, Cambridge, Massachusetts.

Ameri, A.A. and Arnone, A. 1994. "Prediction of turbine blade pass heat transfer using a zero and a two-equation turbulence model," *ASME Proceedings of the International Gas Turbine and Aeroengine Congress and Exposition.* Paper 94-GT-122, June 13-16, Hugus, Neth ASME, New York, pp. 1-8.

Amiri, S., Sandberg, M., and Moshfegh, B. 1996. "Effects of cooling loads on warm plane air jet," *Proc. of ROOMVENT '96*, Vol. 1, pp. 407-414.

ASHRAE. 1991. "Method of testing for rating the performance of air outlets and inlets," *ANSI/ASHRAE Standard 70 - 1991*, ASHRAE, Atlanta.

ASHRAE. 1992. "Thermal environmental conditions for human occupancy," *ANSI/ASHRAE Standard 55 - 1992*, ASHRAE, Atlanta.

ASHRAE. 1997. "ASHRAE Handbook - Fundamentals," *ASHRAE*, Atlanta, Ch.31.

ASHRAE. 1999. "Ventilation for acceptable indoor air quality," *ANSI/ASHRAE Standard 62 - 1999*, ASHRAE, Atlanta.

Awbi, H.B. 1991. "Ventilation of Buildings," *Chapman & Hall*, London.

Balandina, L.Y. 1996. "Distribution of air in the working zones," *Indoor Air '96*, Vol. 1, pp. 865-870.

Baldwin, B.S. and Lomax, H. 1978. "Thin-layer approximation and algebraic models for separated turbulent flows," *AIAA Paper*, Huntsville, AL, pp. 78-257.

Baturin, V.V. 1972. "Fundamentals of industrial ventilation," *Pergamon Press,* Oxford.

Cebeci, T. and Smith, A.M.O. 1974, "Analysis of turbulent boundary layers," *Ser. In Appl. Math & Meth*, XV, Academic Press, 1974.

Chen, Q. 1995. "Comparison of different k-ε models for indoor airflow computation," *Numerical Heat Transfer*, Part B, Fundamentals, 28: 353-369.

Chen, Q. 1997. "Computational fluid dynamics for HVAC: successes and failures," *ASHRAE Transactions*, 103(1), 178-187.

Chen, Q., and Kooi, J. v. d. 1988. "ACCURACY - a computer program for combined problems of energy analysis, indoor airflow and air quality," *ASHRAE Trans.* 94(2): 196-214.

Chen, Q., and Jiang, Z. 1996. "Simulation of a complex air diffuser with CFD technique," *Proc. of ROOMVENT '96*, Vol. 1, pp. 227-234.

Chen, Q., and Moser, A. 1991. "Simulation of a multiple-nozzle diffuser," *Proc. of 12th AIVC Conference*, Vol. 2, pp. 1-14.

Chen, Q., and Srebric, J. 2000. "Simplified Diffuser Boundary Conditions for Numerical Room Airflow Models," *Final Report for ASHRAE RP-1009*, MIT, Cambridge.

Chen, Q., and Xu, W. 1998. "A zero-equation turbulence model for indoor airflow simulation, " *Energy and Buildings,* 28(2): 137-144.

Chen, Q., Srebric, J., and Glicksman, L.R. 1999. "Simplified methodology to factor room air movement and the impact on thermal comfort into design of radiative, convective and hybrid heating and cooling systems," *Final Report for ASHRAE RP-927*, MIT, Cambridge.

Chen, Q., Glicksman, L.R., Yuan, X., Hu. S., Hu, Y., and Yang, X. 1998. "Performance evaluation and development of design guidelines for displacement ventilation," *Final Report for ASHRAE RP-949*, MIT, Cambridge, MA.

Cheong, K.W.D., Sekhar, S.C., Tham, K.W., and Djunaedy, E. 1999. "Airflow pattern in an air-conditioned seminar room," *Indoor Air '99*, Vol.2, pp.54-59.

Chyou, S.-W., and Sheicher, C.A. 1992. "Can one- and two-equation models be modified to calculate turbulent heat transfer with variable properties?" *Industrial and Engineering Chemistry Research*, 31(3): 756-759

Clauser, F.H. 1956. "The turbulent boundary layer," *Advances in Applied Mechanics*, IV, Academic Press, New York, 1-51.

Corrsin, S., and Kistlter, A.L. 1954. "The free-stream boundaries of turbulent flows," NACA TN 3133.

Deardorff, J.W. 1970. "A numerical study of three-dimensional turbulent channel flow at large Reynolds numbers," *Journal of Fluid Mechanics*, Vol. 42: 453-480.

Dorgan, C.B., Dorgan, C.E., Kanarek, M.S., and Willman, A.J. 1998. "Health and productivity benefits of improved indoor air quality," *ASHRAE Trans.*, 104(1): no. 4161.

Emvin, P. and Davidson L. 1996. "A numerical comparison of the diffuse in case E1 Annex20," *Proc. of ROOMVENT '96*, Vol. 1, pp. 219-226.

Escudier, M.P. 1966. "The distribution of mixing-length in turbulent flows near walls," *Heat Transfer Section Report*, TWF/TN/12, Imperial College.

Esmen, T. 1985. "The status of indoor air pollution," *Environmental Health Perspectives*, Vol. 62, pp. 259-265.

Ewert, M., Renz, U., Vogl, N., and Zeller, M. 1991. "Definition of the flow parameters at the room inlet devices - measurements and calculations," *Proc. of 12th AIVC Conference*, Vol. 3, pp. 231-237.

Fan, Y. 1995. "CFD modeling of the air and contaminant distribution in rooms," *Energy and Buildings*, 1995, No.23, pp. 33-39.

Ferziger, J.H., and Peric, M. 1996. "Computational methods for fluid dynamics," *Springer-Verlag*, New York.

Glicksman, L.R., and Chen. Q. 1998. "Interaction of radiation absorbed by moisture in air with other forms of heat transfer in an enclosure," *Proc. of ROOMVENT '98*, Vol. 2, pp. 111-118.

Godish, T. and Spengler, J.D. 1996. "Relationship between ventilation and indoor air quality: a review," *Indoor Air,* 6:135-145.

Grimitlyn, M.I. and Pozin G.M. 1993. "Fundamentals of optimizing air distribution in ventilated spaces," *ASHRAE Trans.*, 99(1): 1128-1138.

Grimitlyn, M.I. 1996. "Fundamental and the ways of development of design calculations for air distribution in Russia," *Indoor Air '96*, Vol. 1, pp. 835-840.

Hanibuchi, H., and Hokoi, S. 1996. "An analysis of velocity and temperature fields in a room heated by a room air-conditioner," *Proc. of ROOMVENT '96,* Vol. 1, pp. 445-452.

Hassani, V., and Miller, P.L. 1998. "Thermal comfort and cold air distribution," *ASHRAE Trans.*, 104(1): 1763-1772.

Haymore, O., and Odom, R. 1993. "Economic effects of poor IAQ," *EPA Journal*, Vol. 19 (4), pp. 28-29.

Heikkinen, J. 1991. "Modeling of a supply air terminal for room air flow simulation," *Proc. of 12th AIVC Conference*, Vol. 3, pp. 213-230.

Heikkinen, J., and Piira, K. 1994. "CFD computation of jets from circular ceiling diffusers," *Proc. of ROOMVENT '94*, Vol. 1, pp. 329-344.

Heiselberg, P. 1994. "Interaction between flow elements in large enclosure," *Proc. of ROOMVENT '94*, Vol. 1, pp. 363-376.

Heiss, A. 1987. "Numerische und experimentelle Untersuchungen der laminaren und turbulenten Konvektion in einem geschlossenen Behatter," *Ph.D. Dissertation*, Technische Universitat Muenchen.

Hiramatsu, T., Harada, T., Kato, S., Murakami, S., and Yoshino, H. 1996. "Study of thermal environment in experimental real-scale atrium," *Proc. of ROOMVENT '96,* Vol. 1, pp. 523-529.

Hu, S.C., Barber, J.M., and Chiang, H. 1998. "Comparison of room airflow characteristics in a full scale environment chamber with cold air distribution," *Proc. of ROOMVENT '98*, Vol. 2, pp. 71-78.

Huo, Y., Zhang, J., Shaw, C., and Haghighat, F. 1996. "A new method to describe the diffuser boundary conditions in CFD simulation," *Proc. of ROOMVENT '96*, Vol. 2, pp. 233-240.

IEA. 1993. "Annex 20: Room air and contaminant flow, evaluation of computational methods," Subtask-1, Summary report, ed. A. D. Lemaire, *TNO Building and Construction Research*, Delft.

IEA. 1998. "Annex 28: Case studies of low energy cooling technologies," *Swiss Federal for materials testing and research*, Dubendorf, Switzerland.

Inard, C., Bouia, H., and Dalicieux, P. 1996. "Prediction of air temperature distribution in buildings with a zonal model," *Energy and Buildings*, 24: 125-132.

Jacobitz, F., Sarkar, S., and Van Atta, C.W. 1997. "Direct numerical simulations of turbulence evolution in a uniformly sheared and stably stratified flow," *Journal of Fluid Mechanics*, Vol. 342, pp. 231-261.

Jacobsen, T.V., and Nielsen, P.V. 1992. Velocity and temperature distribution in flow from an inlet device in rooms with displacement ventilation," *Proc. of ROOMVENT '92*.

Joubert, P., Sandu, A., Beghein, C. and Allard, F. 1996. "Numerical study of the influence of inlet boundary conditions on the air movement in a ventilated room," *Proc. of ROOMVENT '96*, Vol. 1, pp. 235-242.

Jouini, D.B., Said, M.N., and Plett, E.G. 1994. "Measurements of room air distribution in a ventilated office environment," *Building and Environment*, 1994, Vol. 29, No. 4, pp. 511-529.

Karimipanah, T. 1996. "Turbulent jets in confined spaces," *Ph.D. Dissertation*, Center for Built Environment, Royal Institute of Technology, Galve, Sweden.

Kirkpatrick, A.T., and Elleson, J.S. 1996. "Cold air distribution - system design guide," *ASHRAE*, Atlanta.

Kirkpatrick, A.T., and Knappmiller, K.D. 1996. "The ADPI of cold air jets in an enclosure," *ASHRAE Trans.*, 102(1): 3-9.

Klebanoff, P.S. 1956. "Characteristics of turbulence in a boundary layer with zero pressure gradient," NACA, TN 3178.

Knappmiller, K.D. 1994. "The mixing and separation characteristics of cold air ceiling jets," *Ph.D. Dissertation*, Colorado State University, Fort Collins, Colorado.

Kostel, A., and Tuve, G.L. 1955. "Performance and evaluation of room air distribution systems," *ASHRAE Trans.*, 61: 533.

Lai, J.C.S., and Nasr, A. 1998. "Two parallel plane jets: comparison of the performance of three turbulence models," *Proc Instn Mech Engrs Part G J. Aerospace Engineering*, Vol. 212, pp. 379-391.

Launder, B.E., and D.B. Spalding. 1974. "The numerical computation of turbulent flows," *Computer methods in applied Mechanics and Energy*, Vol. 3: 269-289.

Lebrun, J., and Ngendakumana, Ph. 1987. "Air circulation induced by heating emitters and corresponding heat exchanges along the walls: test room results and modelling," *Proc. ROOMVENT '87*, Session 2a, Paper 6, Stockholm, Sweden.

Leonard, B.P. 1979. "A stable and accurate convective modelling procedure based on quadratic upstream interpolation," *Comput. Methods Appl. Mech. Eng.*, 19: 59-98.

Li, Y., A. Delsante, and J. G. Symons. 1998. "Upward flows in a multi-zone building with subfloor plenums and solar chimneys," *Proc. of ROOMVENT '98*, Vol. 2, pp. 429-436.

Li, Z.H., Zhang, J.S., Zhivov, A.M., and Christianson, L.L. 1993. "Characteristics of diffuser air jets and airflow in the occupied regions of mechanically ventilated rooms - a literature review," *ASHRAE Trans.*, 99(1): 1119-1127.

Liu, H., and Ikehata, M. 1994. "Computation of free surface waves around an arbitrary body by a Navier-Stokes solver using pseudocompressibility technique," *Int. J. Numerical Methods in Fluids*, 19(5): 395-413

Livchak, A. 1999. Private Communication. Halton Company, Scottsville, KY.

Livchak, A., Laurikainen, J., and Pekkinen, J. 1994. "Development and validation of a model for predicting the air distribution with adjustable flow pattern swirl diffusers," *Proc. of the 4th International Symposium on Ventilation for Contaminant Control*, 1994: 18, Part1, pp. 159-164.

Loomans, M. 1998. "The measurement and simulation of indoor air flow" *Ph.D. Dissertation*, Eindhoven University of Technology, The Netherlands.

Malmstrom, T.G., Kirkpatrick, A.T., Christensen, B., and Knappmiller, K.D. 1997. "Centerline velocity decay measurements in low-velocity axisymmetric jets," *Journal of Fluid mechanics*, Vol. 246, pp. 363-377.

McQuiston, F.C., and Parker J.D. 1994. "Heating, ventilating, and air conditioning - analysis and design," *John Wiley & Sons, Inc.*, New York.

Melikov, A.K. 2000. Private Communication. Department of Energy Engineering, Technical University of Denmark

Melikov, A.K., Popiolek, Z., Finkelstein, W., Sefker, T., and Care, I. 1998. "Requirements and guidelines for low-velocity measurements," *ASHRAE Trans.*, Vol. 104(1): SF-98-20-5.

Miller, P.L., and Nevins, R.G. 1972. "An analysis of the performance of room air distribution systems," *ASHRAE Trans.*, 78(1): 191.

Molhave, L. 1982. "Indoor air pollution due to organic gases and vapors of solvents in building materials," *Environment International*, Vol. 8, pp. 117-127.

Moser, A. 1991. "The Message of Annex 20: Air Flow Patterns within Buildings" *Proc. 12th AIVC Conference.*

Muller, D., and U. Renz. 1998. "Measurements and prediction of room airflow patterns using different turbulence models," *Proc. of ROOMVENT '98*, Vol.1, pp.109-116.

Murakami, S. 1998. "Overview of turbulence models applied in CWE-1997," *Journal of Wind Engineering and Industrial Aerodynamics,* 74-76: 1-24.

Murakami, S., Kato, S. and Nakagawa, H. 1991. "Numerical prediction of horizontal nonisothermal 3-D jet in room based on k-ε model," *ASHRAE Trans.*, 97(1).

Nasr, A., and Lai, J.C.S. 1998. "A turbulent plane offset jet with small offset ratio," *Experiments in Fluids*, 24: 47-57.

Nero, A.V. 1988. "Controlling indoor air pollution," *Scientific American*, Vol. 258, pp. 42-48.

Nielsen, J.R., Nielsen, P.V. and Svidt K. 1996. "Obstacles in the occupied zone of a room with mixing ventilation," *Proc. of ROOMVENT '96*, Vol. 3, pp. 137-144.

Nielsen, P.V. 1974. "Flow in air conditioned rooms - model experiments and numerical solution of the flow equations," *Ph.D. Dissertation* (Revised English edition), Technical University of Denmark, Lyngby, Denmark.

Nielsen, P.V. 1989. "Representation of boundary conditions at supply openings," *IEA*, Annex 20, Research item no.1.11.

Nielsen, P.V. 1991. "Models for the prediction of room air distribution," *Proc. of 12th AIVC Conference*, Vol. 1, pp. 55-71.

Nielsen, P.V. 1992. "Description of supply openings in numerical models for room air distribution," *ASHRAE Trans.*, 98(1): 963-971.

Nielsen, P.V. 1997. "The box method - a practical procedure for introduction of an air terminal device in CFD calculation," *Institute for Bygningsteknik*, Aalborg Universite, Denmark.

Nielsen, P.V. 1998. "The selection of turbulence models for prediction of room airflow," *ASHRAE Trans.*, 104(1): SF-98-10-1.

Nielsen, P.V. and Tryggvason T. 1998. "Computational fluid dynamics and building energy performance simulation," *Proc. of ROOMVENT '98.*

Nielsen, P.V., Restivo, A., and Whitelaw, J.H. 1978. "The velocity characteristics of ventilated rooms," *J. of Fluid Engineering*, 100: 291-298.

Nikitopoulos, D.E., and Michaelides, E.E. 1995. "Phenomenological model for dispersed bubbly flow in pipes," *AIChE Journal*, 41(1): 12-22.

NIOSH. 1996. "*National Occupational Research Agenda*," NIOSH, U.S. Department of Health and Human Services.

Niu, J. 1994. "Modelling of cooled-ceiling air-conditioning systems," *Ph.D. Dissertation*, Delft University of Technology, Delft, The Netherlands.

Notarianni, K.A., and Davis, W.D. 1993. "The use of computer models to predict temperature and smoke movement in high bay spaces, " *National Institute of Standards and Technology*, Report Number: NISTIR 5304.

Nottage, H.B. 1951. "Ventilation jets in room air distribution," *Ph.D. Dissertation*, Case Institute of Technology, Cleveland, Ohio.

NREL. 1998. "Buildings research - Developing energy efficiency and renewable energy technologies for buildings," *NREL Research*, Colorado.

Off, F., Moser, A., and Suter, P. 1996. "Transient numerical modelling of heat transfer by radiation and convection in atrium with thermal inertia," *Proc. of ROOMVENT '96*, Vol.3, pp. 153--162.

Olson, D.A. and Glicksman, L.R. 1991. "Transient natural convection in enclosures at high Rayleigh number," *J. Heat Transfer*, 113, 635-642.

Olson, D. A., Glicksman L.R., and Ferm. H.M. 1990. "Steady-state natural convection in empty and partitioned enclosures at high Rayleigh numbers," *ASME J. Heat Transfer,* 112: 640-647.

Patankar S.V., and Spalding, D.B. 1972. "A calculation procedure for heat, mass and momentum transport in three-dimensional parabolic flows," *Int. J. of Heat and Mass Transfer*, Vol. 15, pp.1787.

Peng, X. 1996. "Modeling of indoor thermal conditions for comfort control in buildings," *Ph.D. Dissertation*, Delft University of Technology, Delft, The Netherlands.

Popiolek, Z., Melikov, A.K., Jorgensen, F.E., Finkelstein, W., and Sefker, T. 1998. "Impact of natural convection on the accuracy of low-velocity measurements by thermal anemometers with omnidirectional sensor," *ASHRAE Trans.*, Vol. 104(1): SF-98-20-3.

Prandtl, L. 1925. "Uber die ausgebildete Turbulenz," *ZAMM*, 5: 136-139.

Rajaratnam, N. 1976. "Turbulent jets," *Elsevier Scientific Publishing Co.*, Amsterdam.

Reichardt, H. 1944. "Impuls und warmeaustausch in freier turbulenz," *ZAMM*, 24: 268-272.

Rodi, W. 1982. "Turbulent buoyant jets and plumes," *Pergamon Press*, Oxford, 1982.

Sandberg, M., Blomqvist, C., and Mattson, M. 1991. " Turbulence characteristics in rooms ventilated with a high velocity jet" *Proc. of 12th AIVC Conference*, Vol. 2, pp. 105-123.

Schlichting, H. 1979. "Boundary-layer theory," *McGraw-Hill*, New York.

Schwenke, H. 1975. "Ueber das Verhalten elener horizontaler Zuluftstrahlen im begrenzten Raum," *Luft- und Kaltetechnik*, 5: 241-246.

Shakerin, S., and Miller, P.L. 1996. "Experimental study of vortex diffusers," *ASHRAE Trans.*, 102(2): 340-346.

Sheng, Y., Shoukri, M., Sheng, G., and Wood, P. 1998. "A modification to the SIMPLE method for buoyancy-driven flows," *Numerical Heat Transfer*, Part B, 33: 65-78.

Shepelev, I. 1978. "Air dynamics of airflow in rooms," *Stroyizdat*, Moscow, 1978.

Skovgaard, M., and Nielsen, P.V. 1991. "Modelling complex inlet geometries in CFD - Applied to air flow in ventilated rooms," *Proc. of 12th AIVC Conference*, Vol. 3, pp. 183-200.

Skovgaard, M., Hyldgaard, P. and Nielsen, P.V. 1990. "High and low Reynolds number measurements in a room with an impinging isothermal jet," *Proc. of ROOMVENT '90.*

Srebric, J., Chen, Q., and Glicksman, L.R. 1999. "Validation of a zero-equation turbulence model for complex indoor airflow simulation," *ASHRAE Trans.*, 105(2): 414-427.

Srebric, J., Chen, Q., and Glicksman, L.R. 2000a. "A coupled airflow-and-energy simulation program for indoor thermal environment studies," *ASHRAE Trans.*, 106(1): 465-476.

Srebric, J., Liu, J., and Chen, Q. 2000b. "An experimental study of commonly used air supply diffusers," *Proc. of ROOMVENT 2000.*

Svidt, K. 1994. "Investigation of inlet boundary conditions for numerical prediction of air flow in livestock buildings," *Proc. of ROOMVENT '94.*

Tavakkol, S., Hosni, M.H., Miller, P.L., and Straub, H.E. 1994. "A study of isothermal throw of air jets with various room sizes and outlet configurations," *ASHRAE Trans.*, 100(1): 1679-1686.

Tennekes, H., and Lumley, J.L. 1972. "A first course in turbulence," *MIT Press*, Cambridge.

Van Doormal, J.P., and Raithby, G.D. 1984. "Enhancements of the SIMPLE method for prediction incompressible fluid flows," *Numerical Heat Transfer*, 7: 147-163.

Verhoff, A. 1963. "The two-dimensional turbulent wall jet with and without an external stream," *Report 626*, Princeton University.

Versteeg, H.K., and Malalasekera, W. 1995. "An introduction to computational fluid dymnamocs - The finite volume method," *Longman*, UK.

Walton, G.N. 1989. "Airflow network models for element-based building airflow modeling," *ASHRAE Trans*, 95(2): 611-620.

Whittle, G.E. 1986. "Room air distribution: design and evaluation," *BSRIA*, London, U.K., Technical Note 4/86.

Wilcox, D.C. 1993. "Turbulence modeling for CFD," *DCW industries, Inc.*

Wurtz, E., and Nataf, J.M. 1994. "Validation des modeles zonaux decrits par l'envirronment oriente objet SPARK," *Proc. European Conf. on Energy Performance and Indoor Climate in Buildings*, pp. 785-790, Lyon, France.

Wyon, D.P. 1996. "Indoor environmental effects on productivity," *Proc. Of IAQ '96*, ASHRAE, pp. 5-15.

Yokhot, V., and Orszag, S.A. 1986. "Renormalization group analysis of turbulence - I - Basic theory," *Journal of Scientific Computing*, 1(1): 3-51.

Yokhot, V., Orszag, S.A., Thangam, S., Gatski, T.B., and Speziale, C.G. 1992. "Development of turbulence models for shear flows by a double expansion technique," *Physics Fluids A*, 4(7): 1510-1520.

Yuan, X., Chen, Q., Glicksman, L.R., Hu, Y., and Yang, X.1999. "Measurements and computations of room airflow with displacement ventilation," *ASHRAE Trans.*, 105(1): 340-352.

Zhivov, A. 1993. "Theory and practice of air distribution with inclined jets," *ASHRAE Trans.*, 99(1): 1152-1159.

APPENDIX A

Assessment of the Errors of Mean Velocity, RMS of Velocity, Tu and Temperature Measurement by the Omni-directional Anemometers

The errors that may occur in practice during measurements by low velocity thermal anemometers were identified and their impact on the accuracy of the mean velocity and the turbulence intensity measurements was analyzed (Melikov 2000). The error sources included in the analyses were divided into two groups: primary error sources and secondary error sources. The primary error sources include: natural convection flow generated by the velocity sensor, directional sensitivity of the velocity sensor, and dynamic response of the anemometer. The impact of this group of error sources was modeled and predicted with sufficient accuracy. The second group of error sources, named secondary error sources, includes: calibration reference, conversion and reproducibility, temperature compensation, barometric pressure, humidity, temperature gradient, temperature fluctuations, velocity gradient, gaseous composition of air, aging effect, and limited spatial resolution of the velocity sensor. The impact of these error sources on the accuracy of mean velocity and turbulence intensity measured by low velocity thermal anemometer was assessed based on the existing knowledge.

A mathematical model that incorporates all significant error sources and allows assessment of their impact on accuracy of the measurements was developed and tested. The error assessment was performed in accordance with the guidelines, definitions and terminology defined in the Guide to the Expression of Uncertainty in Measurement (ISO). Based on the mathematical model, a software package was developed. The software enables the simulation of low velocity thermal anemometers based on their characteristics, such as dynamic response, directional sensitivity, free convection, etc. It also enables the performance of low velocity anemometers to be assessed under practical conditions. The following are the accuracy assessment results for the omni-directional anemometers used for the experiments in MIT's environmental chamber.

A.1 Equations for Uncertainty Calculations (Melikov 2000)

- Mean Velocity

Absolute expanded error of mean velocity measurement (95%)

$$\hat{U}(V_{mean}) = 0.0265 \text{ m/s}$$

Relative expanded error of mean velocity measurement (95%)

$$U(V_{mean}) = \hat{U}(V_{mean}) / V_{mean} = 0.0265/V_{mean}$$

- RMS of Velocity (standard deviation of velocity)

Absolute expanded error of RMS of velocity measurement (95%)

$$\hat{U}(V_{RMS}) = (0.18+0.011/ V_{mean})\cdot V_{RMS} \quad m/s$$

Relative expanded error of RMS of velocity measurement (95%)

$$U(V_{RMS}) = (0.18+0.011/ V_{mean})$$

- Turbulence intensity

Absolute expanded error of Tu measurement (95%)

$$\hat{U}(Tu) = 0.038/(Vmean+0.1) - 0.02$$

Relative expanded error of Tu measurement (95%)

$$U(Tu) = \hat{U}(Tu)/Tu = [0.038/(Vmean+0.1) - 0.02]/Tu$$

- Temperature

Absolute expanded error of temperature measurement (95%)

$$\hat{U}(t_a) = 0.5\ ^{\circ}C$$

Relative expanded error of temperature measurement (95%)

$$U(t_a) = 0.5/t_a$$

A.2 An Example of Uncertainty Assessment

Experimentally measured parameters by the low-velocity transducer are:

V_{mean}=0.185 m/s
V_{RMS}=0.087 m/s
Tu=47%
t_a=23.14°C

Uncertainty of measurement

- Mean Velocity

Absolute expanded error of mean velocity measurement (95%)

$$\hat{U}(Vmean) = 0.0265 \text{ m/s}$$

Relative expanded error of mean velocity measurement (95%)

$$U(Vmean) = \hat{U}(Vmean) / 0.185 = 0.0265/0.185 = 14.3\%$$

- RMS of Velocity (standard deviation of velocity)

  Absolute expanded error of RMS of velocity measurement (95%)

  $$\hat{U}(VRMS) = (0.18+0.011/ 0.185)\cdot 0.087 = 0.021 \text{ m/s}$$

  Relative expanded error of RMS of velocity measurement (95%)

  $$U(VRMS) = (0.18+0.011/ 0.185) = 23.9\%$$

- Turbulence intensity

  Absolute expanded error of Tu measurement (95%)

  $$\hat{U}(Tu) = 0.038/(0.185+0.1) - 0.02 = 0.113 = 11.3\%$$

  Relative expanded error of Tu measurement (95%)

  $$U(Tu) = \hat{U}(Tu)/Tu = [0.038/(0.185+0.1) - 0.02]/0.47 = 24.1\%$$

- Temperature

  Absolute expanded error of temperature measurement (95%)

  $$\hat{U}(ta) = 0.5\ ^{\circ}C$$

  Relative expanded error of temperature measurement (95%)

- $U(ta) = 0.5/23.14 = 2.16\%$

APPENDIX B

Measured Data for the Infiltration, Partition, and Displacement Ventilation Cases

This appendix presents the detailed data measured from our environmental chamber and the corresponding thermal and flow boundary conditions. The data can be used to validate other flow programs.

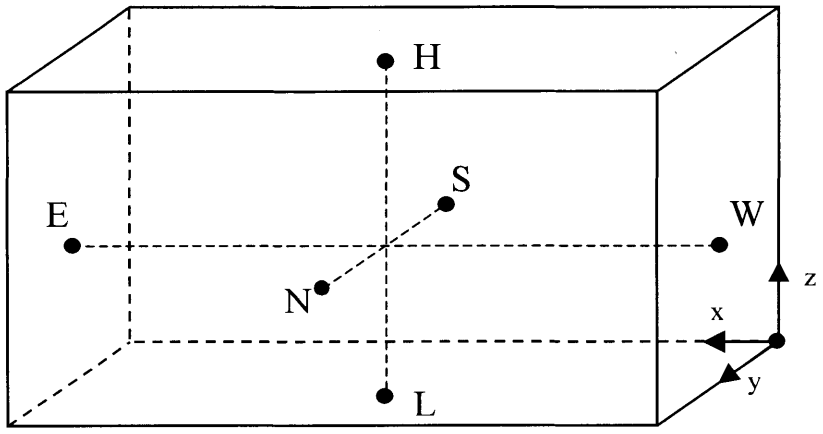

Figure B1 Notation for test room walls and coordinate axes

B.1 The Infiltration Case

Table B.1 Configuration of the infiltration case

	Size			Location			Heat
	Δx [m]	Δy [m]	Δz [m]	x [m]	y [m]	z [m]	Q [W]
Room	5.16	3.65	2.43	0.0	0.0	0.0	-
Window	0.02	3.35	1.16	5.16	0.0	0.94	-
Inlet	3.05	0.75	0.09	0.0	0.0	0.10	-
Outlet	0.43	0.43	0.0	2.365	1.61	2.43	-
Person 1	0.4	0.35	1.1	1.42	0.90	0.0	75
Person 2	0.4	0.35	1.1	3.74	2.40	0.0	75
Heater	0.07	1.22	0.17	5.02	1.21	0.0	1500
Table 1	1.45	0.75	0.01	0.9	0.0	0.74	-
Table 2	1.45	0.75	0.01	4.66	2.90	0.74	-
Lamp 1	0.2	1.2	0.15	1.03	0.16	2.18	34
Lamp 2	0.2	1.2	0.15	2.33	0.16	2.18	34
Lamp 3	0.2	1.2	0.15	3.61	0.16	2.18	34
Lamp 4	0.2	1.2	0.15	1.03	2.29	2.18	34
Lamp 5	0.2	1.2	0.15	2.33	2.29	2.18	34
Lamp 6	0.2	1.2	0.15	3.61	2.29	2.18	34
Cabinet	0.95	0.58	1.24	4.21	0.0	0.0	-

Note: - x is from west to east, y is from south to north, z is from low to high
- the heat generated includes radiation and convection.

Infiltration case - measured data

Ventilation rate n = 3 ach
Temperature
Supply air temperature: 13.2 °C
Exhaust air temperature: 24.0 °C
South wall temperature (x = 2.58 m, y = 0.0 m)

z [m]	0.1	0.6	1.1	1.8	2.38
T [°C]	19.958	20.930	21.564	22.607	22.307

East wall & window temperature (x = 5.16 m, y = 1.83 m)

z [m]	0.1	0.6	1.1	1.8	2.38
T [°C]	23.404	21.281	20.338	21.115	24.093

North wall temperature (x = 2.58 m, y = 3.65 m)

z [m]	1.1	1.8
T [°C]	21.419	22.088

West wall temperature (x = 0.0 m, y = 1.83 m)

z [m]	1.8
T [°C]	21.467

Air, floor, and ceiling temperatures
x = 0.78 m, y = 1.83 m

z [m]	0.00	0.05	0.10	0.60	1.10	1.50	1.90	2.30	2.38	2.43
T [°C]	18.92	17.17	18.67	22.54	23.95	25.10	26.13	26.30	23.42	21.55

x = 1.74 m, y = 1.83 m

z [m]	0.00	0.05	0.10	0.60	1.10	1.50	1.90	2.30	2.38	2.43
T [°C]	19.73	17.96	19.22	22.28	24.18	25.49	26.46	26.66	23.43	21.46

x = 2.7 m, y = 1.83 m

z [m]	0.00	0.05	0.10	0.60	1.10	1.50	1.90	2.30	2.38
T [°C]	20.09	18.56	19.85	22.49	24.28	25.02	26.57	25.88	24.08

x = 3.66 m, y = 1.83 m

z [m]	0.00	0.05	0.10	0.60	1.10	1.50	1.90	2.30	2.38	2.43
T [°C]	20.49	19.22	20.24	22.83	24.37	24.93	26.34	27.84	24.41	22.88

x = 4.62 m, y = 1.83 m

z [m]	0.00	0.05	0.10	0.60	1.10	1.50	1.90	2.30	2.38	2.43
T [°C]	20.56	19.52	20.66	22.87	24.42	25.01	26.22	27.11	24.87	23.59

Mean velocity
x = 0.78 m, y = 1.83 m

z [m]	0.1000	0.6000	1.1000	1.5000	1.9000	2.3000
u [m/s]	0.101	0.027	0.030	0.016	0.035	0.064

x = 1.74 m, y = 1.83 m

z [m]	0.1000	0.6000	1.1000	1.5000	1.9000	2.3000
u [m/s]	0.044	0.015	0.043	0.053	0.034	0.080

x = 2.7 m, y = 1.83 m

z [m]	0.1000	0.6000	1.1000	1.5000	1.9000	2.3000
u [m/s]	0.032	0.020	0.032	0.091	0.049	0.117

x = 3.66 m, y = 1.83 m

z [m]	0.1000	0.6000	1.1000	1.5000	1.9000	2.3000
u [m/s]	0.057	0.017	0.027	0.020	0.087	0.161

x = 4.62 m, y = 1.83 m

z [m]	0.1000	0.6000	1.1000	1.5000	1.9000	2.3000
u [m/s]	0.044	0.040	0.034	0.015	0.053	0.115

B.2 The Partition Case

Table B.2 Configuration of the partition case.

	Size			Location			Heat
	Δx [m]	Δy [m]	Δz [m]	x [m]	y [m]	z [m]	Q [W]
Room	5.16	3.65	2.43	0.0	0.0	0.0	-
Window	0.02	3.35	1.16	5.16	0.0	0.94	-
Inlet	0.0	0.30	0.20	0.0	1.675	2.11	-
Outlet	0.0	0.43	0.43	0.0	1.61	0.02	-
Partition	0.06	2.50	2.43	2.58	0.0	0.0	-
Person 1	0.4	0.35	1.1	1.63	0.90	0.0	75
Person 2	0.4	0.35	1.1	3.91	2.40	0.0	75
Heater	0.07	1.22	0.17	5.02	1.21	0.0	1500
Computer 1	0.4	0.4	0.4	1.63	0.1	0.75	108.5
Computer 2	0.4	0.4	0.4	3.91	3.15	0.75	173.4
Table 1	2.23	0.75	0.01	0.0	0.0	0.74	-
Table 2	1.45	0.75	0.01	3.71	2.90	0.74	-
Lamp 1	0.2	1.2	0.15	1.03	0.16	2.18	34
Lamp 2	0.2	1.2	0.15	2.33	0.16	2.18	34
Lamp 3	0.2	1.2	0.15	3.61	0.16	2.18	34
Lamp 4	0.2	1.2	0.15	1.03	2.29	2.18	34
Lamp 5	0.2	1.2	0.15	2.33	2.29	2.18	34
Lamp 6	0.2	1.2	0.15	3.61	2.29	2.18	34
Cabinet	0.95	0.58	1.24	4.21	0.0	0.0	-

Note: - x is from west to east, y is from south to north, z is from low to high
- the heat generated includes radiation and convection.

Partition case - measured data

Ventilation rate n = 4 ach
Temperature
Supply air temperature: 14.5 °C
Exhaust air temperature: 29.8 °C
South wall temperature (x = 2.58 m, y = 0.0 m)

z [m]	0.1	0.6	1.1	1.8	2.38
T [°C]	30.350	31.288	33.190	33.850	32.288

East wall & window temperature (x = 5.16 m, y = 1.83 m)

z [m]	0.1	0.6	1.1	1.8	2.38
T [°C]	38.140	34.493	31.007	30.790	35.908

Window temperature (x = 5.16 m, y = 2.70 m)

z [m]	1.8
T [°C]	29.030

North wall temperature (x = 2.58 m, y = 3.65 m)

z [m]	1.1	1.8
T [°C]	31.088	32.535

West wall temperature (x = 0.0 m, y = 1.83 m)

z [m]	1.8
T [°C]	31.118

Air, floor, and ceiling temperatures

x = 1.10 m, y = 1.83 m

z [m]	0.00	0.05	0.10	0.60	1.10	1.50	1.90	2.30	2.38	2.43
T [°C]	29.20	28.86	28.81	30.18	31.65	32.61	32.99	34.04	33.80	28.93

x = 2.02 m, y = 1.83 m

z [m]	0.00	0.05	0.10	0.60	1.10	1.50	1.90	2.30	2.38	2.43
T [°C]	30.69	30.14	29.99	30.29	31.58	32.35	32.85	33.08	32.98	31.37

x = 2.83 m, y = 3.15 m

z [m]	0.00	0.05	0.10	0.60	1.10	1.50	1.90	2.38	2.43
T [°C]	30.87	30.28	30.19	30.41	32.43	34.12	34.97	34.68	32.18

x = 3.80 m, y = 1.83 m

z [m]	0.00	0.05	0.10	0.60	1.10	1.50	1.90	2.30	2.38	2.43
T [°C]	31.42	30.79	30.63	31.44	33.23	34.70	35.03	35.73	35.63	32.21

x = 4.80 m, y = 1.83 m

z [m]	0.00	0.05	0.10	0.60	1.10	1.50	1.90	2.30	2.38	2.43
T [°C]	32.37	30.66	30.23	38.27	34.44	34.67	35.04	35.88	37.06	35.74

Mean velocity

x = 1.10 m, y = 1.83 m

z [m]	0.1000	0.6000	1.1000	1.5000	1.9000	2.3000
u [m/s]	0.2330	0.1110	0.0610	0.0670	0.1760	0.2330

x = 2.02 m, y = 1.83 m

z [m]	0.1000	0.6000	1.1000	1.5000	1.9000	2.3000
u [m/s]	0.1900	0.1410	0.1180	0.1130	0.0750	0.0610

x = 2.83 m, y = 3.15 m

z [m]	0.1000	0.6000	1.1000	1.5000	1.9000	2.3000
u [m/s]	0.1500	0.2000	0.1350	0.0670	0.1230	0.1100

x = 3.80 m, y = 1.83 m

z [m]	0.1000	0.6000	1.1000	1.5000	1.9000	2.3000
u [m/s]	0.1360	0.0320	0.0680	0.0790	0.1020	0.1670

x = 4.80 m, y = 1.83 m

z [m]	0.1000	0.6000	1.1000	1.5000	1.9000	2.3000
u [m/s]	0.1430	0.4830	0.1730	0.0850	0.1120	0.2300

B.3 The Displacement Ventilation Case

Table B.3 Configuration of the displacement ventilation case.

	Size			Location			Heat
	Δx [m]	Δy [m]	Δz [m]	x [m]	y [m]	z [m]	Q [W]
Room	5.16	3.65	2.43	0.0	0.0	0.0	-
Window	0.02	3.35	1.16	5.16	0.0	0.94	-
Inlet	0.28	0.53	1.11	0.0	1.51	0.03	-
Outlet	0.43	0.43	0.0	2.365	1.61	2.43	-
Person 1	0.4	0.35	1.1	1.98	0.85	0.0	75
Person 2	0.4	0.35	1.1	3.13	2.45	0.0	75
Computer 1	0.4	0.4	0.4	1.98	0.1	0.75	108.5
Computer 2	0.4	0.4	0.4	3.13	3.15	0.75	173.4
Table 1	2.23	0.75	0.01	0.35	0.0	0.74	-
Table 2	2.23	0.75	0.01	2.93	2.90	0.74	-
Lamp 1	0.2	1.2	0.15	1.03	0.16	2.18	34
Lamp 2	0.2	1.2	0.15	2.33	0.16	2.18	34
Lamp 3	0.2	1.2	0.15	3.61	0.16	2.18	34
Lamp 4	0.2	1.2	0.15	1.03	2.29	2.18	34
Lamp 5	0.2	1.2	0.15	2.33	2.29	2.18	34
Lamp 6	0.2	1.2	0.15	3.61	2.29	2.18	34
Cabinet 1	0.33	0.58	1.32	0.0	0.0	0.0	-
Cabinet 2	0.95	0.58	1.24	4.21	0.0	0.0	-

Note: - x is from west to east, y is from south to north, z is from low to high
- the heat generated includes radiation and convection.

Displacement ventilation - measured data

Ventilation rate n = 4 ach
Temperature
Supply air temperature: 17.0 °C
Exhaust air temperature: 26.7 °C
South wall temperature (x = 2.58 m, y = 0.0 m)

z [m]	0.1	0.6	1.1	1.8	2.38
T [°C]	23.311	24.406	25.725	26.023	25.776

East wall & window temperature (x = 5.16 m, y = 1.83 m)

z [m]	0.1	0.6	1.1	1.8	2.38
T [°C]	24.180	24.641	27.221	28.132	26.571

North wall temperature (x = 2.58 m, y = 3.65 m)

z [m]	1.1	1.8
T [°C]	25.051	25.949

West wall temperature (x = 0.0 m, y = 1.83 m)

z [m]	1.8
T [°C]	25.369

Air, floor, and ceiling temperatures

x = 0.78 m, y = 1.83 m

z [m]	0.00	0.05	0.10	0.60	1.10	1.50	1.90	2.30	2.38	2.43
T [°C]	21.54	20.85	20.97	23.33	24.75	25.76	26.37	26.17	25.90	25.16

x = 1.74 m, y = 1.83 m

z [m]	0.00	0.05	0.10	0.60	1.10	1.50	1.90	2.30	2.38	2.43
T [°C]	23.34	21.51	21.96	23.63	25.06	25.70	26.55	26.53	26.05	25.40

x = 2.70 m, y = 1.83 m

z [m]	0.00	0.05	0.10	0.60	1.10	1.50	1.90	2.30	2.38	2.38
T [°C]	23.90	22.10	22.44	23.91	25.38	26.10	26.49	26.36	26.19	26.19

x = 3.66 m, y = 1.83 m

z [m]	0.00	0.05	0.10	0.60	1.10	1.50	1.90	2.30	2.38	2.43
T [°C]	24.24	22.56	22.71	23.63	25.33	25.96	26.52	26.89	26.68	25.87

x = 4.62 m, y = 1.83 m

z [m]	0.00	0.05	0.10	0.60	1.10	1.50	1.90	2.30	2.38	2.43
T [°C]	24.72	22.87	22.94	23.43	25.10	26.13	26.57	26.53	26.53	26.13

x = 2.7 m, y = 0.61 m

z [m]	0.00	0.05	0.10	0.60	1.10	1.50	1.90	2.30	2.38	2.43
T [°C]	23.80	22.01	22.08	23.73	25.40	25.79	26.57	26.49	26.25	24.90

x = 2.7 m, y = 1.22 m

z [m]	0.00	0.05	0.10	0.60	1.10	1.50	1.90	2.30	2.38	2.43
T [°C]	24.11	22.19	23.71	25.30	25.99	26.49	26.38	26.16	24.95	24.95

x = 2.7 m, y = 2.44 m

z [m]	0.00	0.05	0.10	0.60	1.10	1.50	1.90	2.30	2.38	2.43
T [°C]	24.01	22.08	22.15	23.66	25.09	26.07	26.51	26.44	26.51	25.50

x = 2.7 m, y = 3.05 m

z [m]	0.00	0.05	0.10	0.60	1.10	1.50	1.90	2.30	2.38	2.43
T [°C]	23.86	22.12	22.26	23.60	25.16	25.99	26.75	26.94	26.61	25.89

Mean velocity

x = 0.78 m, y = 1.83 m

z [m]	0.1000	0.6000	1.1000	1.5000	1.9000	2.3000
u [m/s]	0.1630	0.0300	0.0620	0.0070	0.0170	0.0380

x = 1.74 m, y = 1.83 m

z [m]	0.1000	0.6000	1.1000	1.5000	1.9000	2.3000
u [m/s]	0.0840	0.0250	0.0430	0.0180	0.0190	0.0340

x = 2.7 m, y = 1.83 m

z [m]	0.1000	0.6000	1.1000	1.5000	1.9000	2.3000
u [m/s]	0.0810	0.0310	0.0460	0.0200	0.0260	0.1630

x = 3.66 m, y = 1.83 m

z [m]	0.1000	0.6000	1.1000	1.5000	1.9000	2.3000
u [m/s]	0.0580	0.0320	0.0310	0.0320	0.0300	0.0280

x = 4.62 m, y = 1.83 m

z [m]	0.1000	0.6000	1.1000	1.5000	1.9000	2.3000
u [m/s]	0.0380	0.0550	0.0280	0.0170	0.0130	0.0470

x = 2.7 m, y = 0.61 m

z [m]	0.1000	0.6000	1.1000	1.5000	1.9000	2.3000
u [m/s]	0.0830	0.0390	0.0150	0.0170	0.0340	0.0630

x = 2.7 m, y = 1.22 m

z [m]	0.1000	0.6000	1.1000	1.5000	1.9000	2.3000
u [m/s]	0.0780	0.0350	0.0270	0.0140	0.0330	0.0610

x = 2.7 m, y = 2.44 m

z [m]	0.1000	0.6000	1.1000	1.5000	1.9000	2.3000
u [m/s]	0.0840	0.0390	0.0240	0.0160	0.0130	0.0520

x = 2.7 m, y = 3.05 m

z [m]	0.1000	0.6000	1.1000	1.5000	1.9000	2.3000
u [m/s]	0.0990	0.0420	0.0280	0.0190	0.0200	0.1160

NOMENCLATURE

a_W, a_E, a_S, a_N, a_L, a_T, a_P	coefficients in the final discretization equations, -
A	area, m^2
A_0	effective diffuser area or area factor, m^2
ACH	air change per hour, h^{-1}
Ar	Archimedes number, -
Ar_0	Archimedes number based on the air supply parameters, -
Ar_x	Archimedes number at distance x from the jet source, -
c	species concentration, mg/m^3 air
c_p	specific heat at constant pressure, J/kg.K
C_μ, $C_{\varepsilon 1}$, $C_{\varepsilon 2}$, $C_{\varepsilon 3}$	coefficients in turbulence model, -
D	diffusion coefficient, m^2/s
D_W, D_E, D_S, D_N, D_L, D_T, D_P	diffusive coefficient at each face of a control volume, -
E	wall roughness parameter, -
F_W, F_E, F_S, F_N, F_L, F_T, F_P	convective flux at each face of a control volume, -
g_I	gravity vector, m/s^2
G_b	generation of turbulent energy due to buoyancy, W/m^3
h	height, m
h, h_c	convective heat transfer coefficient, $W/m^2.K$
H_0	effective width of a linear diffuser, m
k	thermal conductivity, W/m.K
k	turbulent kinetic energy per unit mass, J/kg
K_1	jet centerline velocity decay constant, -
K_2	jet centerline temperature decay constant, -
l	turbulent length scale, m
l_{mix}	mixing length, m
L	thermal load on body, W/m^2 or Btu/h
m	mass flow rate, $kg/m^2.s$
M	rate of metabolic heat production, W/m^2 or Btu/h
M_x	jet momentum at distance x from the jet source, $kg.m/s^2$
M_0	initial jet momentum, $kg.m/s^2$
N	total number of repeated measurements, -
P	pressure, Pa
ΔP	diffuser static pressure drop, Pa
P_k	production of turbulent energy due to turbulent stress, W/m^3
Pr	laminar Prandtl number, -
Pr_t	turbulent Prandtl number, -
PMV	predicted mean vote, -
PPD	predicted percentage of dissatisfied, %
q	heat flux, W/m^2
q_c	convective heat flux, W/m^2
Q	heat load, W
Q	volume flow rate, m^3/s
R	additional source term introduced in RNG k-ε model, $W/m^3.s$
Re	Reynolds Number, -

S_{ij}	magnitude of rate-of-strain, s^{-1}
Sc	laminar Schmidt number, -
Sc_t	turbulent Schmidt number, -
S_ϕ	source term for ϕ in general transport equation
t	time, s
T	temperature, °C, K, or °F
T	averaging time, s
$T_{0.25}$	jet throw, m
Ti	turbulence intensity, -
T_m	centerline or maximum jet temperature, °C or °F
T_r	average room temperature, °C or °F
ΔT	temperature difference (T_{supply} - T_{room}), °C or °F
u	flow velocity or velocity component in x direction, m/s
u_i, u_j	index notation of velocity components, m/s
u_τ	friction velocity, m/s
U_0	initial jet velocity, m/s
U_m	centerline or maximum jet velocity, m/s
v	velocity component in y direction, m/s
V	volume, m^3
x, y, z	Cartesian coordinates in three directions, m
x_i, x_j	index notation of Cartesian coordinates, m
x_s	separation distance, m
$y_{1/2Um}$	half-width of the jet spread, m
w	velocity component in z direction, m/s

Greek symbols

α	linear relaxation factor, -
β	volumetric thermal expansion coefficient, K^{-1}
β'	parameter in RNG k-ε model, -
Γ	diffusion coefficient, kg/m.s
Δ	diference, -
δ_{ij}	Kronecker delta function, -
δt_f	false-time-step relaxation factor, -
ε	rate of dissipation of turbulent kinetic energy per unit mass, J/kg.s
η_0	parameter in RNG k-ε model, -
θ	dimensionless temperature, -
κ	von Karman's constant (0.41), -
μ	dynamic viscosity, kg/m.s
ν	kinetic viscosity, m^2/s
ρ	density, kg/m^3
$\sigma_{k,\varepsilon}$	turbulent Prandtl (k, ε) number, -
τ	Reynolds stress, N/m^2
τ_w	wall shear stress, N/m^2

φ	relative humidity, %
ϕ	general fluid property

Subscripts

box	fluid parameters at the box surface
eff	effective
i, j	coordinate
m, max	maximum
mix	mixing
o	reference point
old	value of a variable at a previous time step
0	diffuser and jet properties at the diffuser supply surface
w, e, s, n, l, t	faces of a control volume
P, W, E, S, N, L, T	position of a control volume
r	room air paramter
exhaust	fluid parameters at the exhaust opening
supply	fluid parameters at the supply opening
t	turbulent
w	wall
x	jet parameters at distance x from the jet source

Superscripts

+	dimensionless variable
*	guessed turbulent parameter
–	averaged component of turbulent parameter
'	fluctuating component of turbulent parameter
~	instantaneous value of turbulent parameter
new	new value of calculated turbulent parameter

Abbreviations

ASHRAE	American Society of Heating, Refrigerating and Air-Conditioning Engineers, Inc.
CFD	Computational Fluid Dynamics
DNS	Direct Numerical Simulation
HVAC	Heating, Ventilating, and Air-Conditioning
IAQ	Indoor Air Quality
IEA	International Energy Agency
LES	Large Eddy Simulation
NIOSH	National Institute of Occupational Safety and Health
NREL	National Renewable Energy Laboratory
RANS	Reynolds Averaged Navier-Stokes
RNG	Renormalization Group
RSTM	Reynolds Stress Turbulence Model